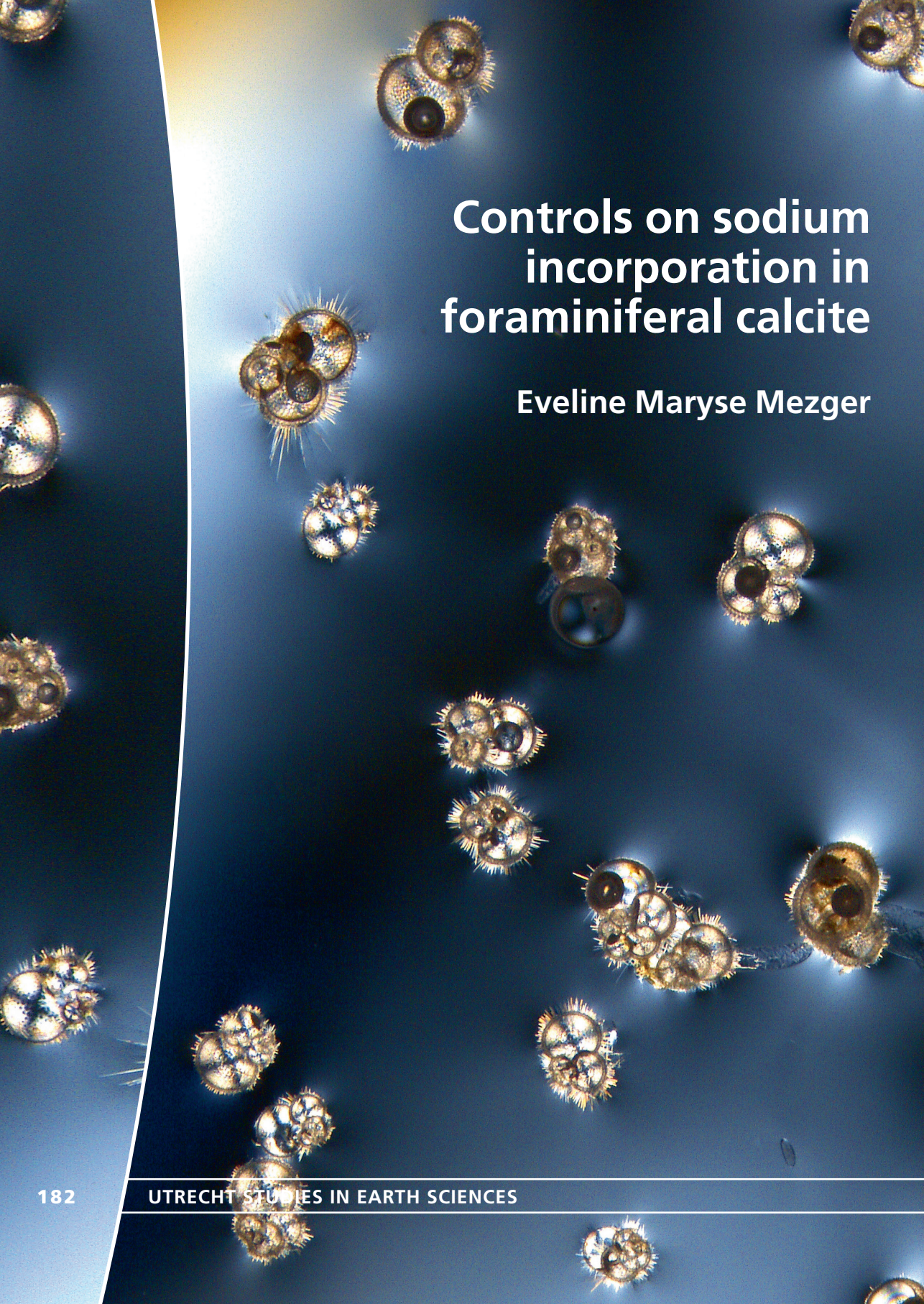

Controls on sodium incorporation in foraminiferal calcite

Eveline Maryse Mezger

182 UTRECHT STUDIES IN EARTH SCIENCES

Controls on sodium incorporation in foraminiferal calcite

Eveline Maryse Mezger

Members of the dissertation committee:

Dr. J.S. Fehrenbacher
Dr. B.A.A. Hoogakker
Prof. dr. L.J. Lourens
Prof. dr. P.R.D. Mason
Prof. dr. J..B.M. Middelburg

ISBN: 978-90-6266-536-5
Uses no. 182
Thesis lay-out: David de Groot, Persoonlijkproefschrift.nl
Cover lay-out: Margot Stoete, UU Geo C&M
Cover photo is an assemblage of the foraminiferal species used for this study, embedded in resin and polished.
Printed in the Netherlands by Ridderprint BV, Ridderkerk

Controls on sodium incorporation in foraminiferal calcite

De inbouw van natrium in de kalkschaaltjes van foraminiferen en het effect van omgevingsinvloeden

(met een samenvatting in het Nederlands)

Proefschrift

ter verkrijging van de graad van doctor aan de Universiteit Utrecht op gezag van de rector magnificus, prof.dr. H.R.B.M. Kummeling, ingevolge het besluit van het college voor promoties in het openbaar te verdedigen op

maandag 6 mei 2019 des middags te 12.45 uur

door

Eveline Maryse Mezger

geboren op 11 augustus 1989 te Nijmegen

Promotor: Prof. dr. G.-J. Reichart

Copromotor: Dr. L.J. de Nooijer

Voor Peter

Als je begrijpt, wat ik bedoel

- De heer Ollie B. Bommel, Marten Toonder

Co-author affiliations

MSc. Jacqueline Bertlich
Research unit Paleoceanography, GEOMAR Helmholtz Centre for Ocean Research Kiel, Germany

Prof. dr. Jelle Bijma
Department of Biogeosciences, Alfred-Wegener-Institut Helmholtz-Zentrum für Polar- und Meeresforschung, Germany

Ing. Wim Boer
Department of Ocean Systems, NIOZ-Royal Netherlands Institute for Sea Research, and Utrecht University, The Netherlands

Prof. dr. Geert-Jan Brummer
Department of Ocean Systems, NIOZ-Royal Netherlands Institute for Sea Research, and Utrecht University, The Netherlands
Faculty of Earth and Life Sciences, Department of Earth Sciences, VU University Amsterdam, The Netherlands

Dr. Laurent Devriendt
Department of Ocean Systems, NIOZ-Royal Netherlands Institute for Sea Research, and Utrecht University, The Netherlands

Dr. Zeynep Erdem
Department of Marine Microbiology and Biogeochemistry, NIOZ-Royal Netherlands Institute for Sea Research, and Utrecht University, The Netherlands

MSc. Marit van Erk
Department of Marine Microbiology and Biogeochemistry, NIOZ-Royal Netherlands Institute for Sea Research, and Utrecht University, The Netherlands
*Now at Max Planck Institute for Marine Microbiology, Germany

Dr. Karina Kaczmarek
Department of Biogeosciences, Alfred-Wegener-Institut Helmholtz-Zentrum für Polar- und Meeresforschung, Germany

Prof. dr. Michal Kucera
MARUM – Center for Marine Environmental Sciences, University of Bremen, Germany

MSc. Julie Lattaud,
Department of Marine Microbiology and Biogeochemistry, NIOZ-Royal Netherlands Institute for Sea Research, and Utrecht University, The Netherlands

Dr. Gernot Nehrke
Department of Biogeosciences, Alfred-Wegener-Institut Helmholtz-Zentrum für Polar- und Meeresforschung, Germany

Dr. Lennart de Nooijer
Department of Ocean Systems, NIOZ-Royal Netherlands Institute for Sea Research, and Utrecht University, The Netherlands

Prof. dr. Dirk Nürnberg
Research unit Paleoceanography, GEOMAR Helmholtz Centre for Ocean Research Kiel, Germany

MSc. Ellen Olsen
Department of Geological Sciences, University of Oregon, United States

Prof. dr. Gert-Jan Reichart
Department of Ocean Systems, NIOZ-Royal Netherlands Institute for Sea Research, and Utrecht University, The Netherlands

Prof. dr. Stefan Schouten,
Department of Marine Microbiology and Biogeochemistry, NIOZ-Royal Netherlands Institute for Sea Research, and Utrecht University, The Netherlands

Dr. Michael Siccha
MARUM – Center for Marine Environmental Sciences, University of Bremen, Germany

Prof. dr. James Watkins
Department of Geological Sciences, University of Oregon, United States

Contents

1

Chapter 1

Introduction and synopsis

1.1 Paleoclimatology and –oceanography

The Earth is covered for 71% by water, of which 96.5% is ocean. The ocean is not only large, it also plays a key role in physical, chemical and biological processes on our planet. Yet, at the same time it remains one of the least explored environments on Earth. It is an important driver of our climate system because of its role in the carbon cycle and by redistributing heat. The human imprint on the ocean increases because of pollution, overfishing and warming. In addition, since the start of the industrial revolution in the late 18th century, burning of fossil fuels resulted in the massive release of carbon dioxide (CO_2) (IPCC, 2014: Pachauri et al., 2014). Carbon dioxide has a substantial effect on ocean chemistry -so-called ocean acidification- and, being a greenhouse gas, on global climate. Associated anthropogenic global warming increases global sea level due to melting of ice sheets and thermal expansion of the ocean. The oceans also play an important role in buffering atmospheric CO_2 as they store 98% of present-day CO_2 and have taken up 30% of the anthropogenic added CO_2 until now. Earth's climate is and has always been subject to change and the ocean played a key role in these changes. Understanding the role of the ocean is hence vital for predicting the future of our planet at a time of major changes in CO_2 and climate.

Investigating past climate change (paleoclimatology) and past changes in the oceans (paleoceanography) provides valuable information on climate functioning and the role of oceans. Climate can be described as the average conditions of a region, for example by combining temperature, precipitation (e.g. snow- or rainfall) and wind, over longer (multi-annual) timescales. Climate should not be confused with 'weather', which applies to shorter fluctuations on timescales from hours to weeks. Albeit that numerical climate modeling exercises can simulate climate change, input for and verification of these models by present-day monitoring studies alone would not suffice to understand long-term effects. The range of forecasted changes is too large to compare to any variability in the existing instrumental record. Past climates, encompassing a much larger range, provide a wealth of information on climate and ocean functioning. In the absence of direct ways to measure past climate parameters such as temperature, sea-level, ice volume or salinity on pre-instrumental timescales, geologists use a variety of tools to reconstruct past climate. These so-called 'proxies' are based on material collected from sediments from the seafloor and on land, which have accumulated through time. Proxies are often based on organisms, producing shells or molecules with an isotopic or (trace-) elemental composition varying in response to environmental changes. To develop and understand these proxies, species

on which proxies are based can be collected from the modern environment and compared to the environmental parameters in which they grew. Alternatively, organisms producing proxy signals are cultured under controlled conditions to independently test the effect of different chemical or physical marine parameters.

1.2 Foraminifera

The chemical composition of marine calcifying organisms is often used as a tool to reconstruct past environmental conditions. The phylum of the Foraminifera (within the kingdom of the Protista) consists of marine unicellular eukaryotic organisms, producing shells (also referred to as 'tests') of calcite (calcareous), organic compounds ('naked' foraminifera/polysaccharides) or sediments (agglutinants). Shells of calcifying foraminiferal species were found up to ~500 million years back in the marine sedimentary record (Culver, 1991; Pawlowski et al., 2003). Due to their preservation in the fossil record and worldwide distribution, calcite foraminiferal shells are considered a valuable climate archive. First, the relative abundances of the fossil shells of specific foraminifera, ecologically linked to certain habitat preferences (e.g. light, temperature, oxygen content, reproduction depth), can be used to reconstruct changes in the paleo-environment (e.g. Rutherford et al., 1999, Van der Zwaan et al., 1990, Imbrie and Kipp, 1971). Second, foraminifera build these carbonate shells by subsequently adding chambers, with an isotopic and/or (trace) elemental composition reflecting the environment in which they calcified (e.g. Nürnberg et al., 1996; Shackleton, 1987).

During foraminiferal shell formation, different minor or trace elements are incorporated from seawater, thereby reflecting seawater element concentrations, as well as the biological and physical conditions during precipitation. During their life cycle, (calcifying) foraminifera add multiple chambers to their shell via a tightly controlled biological calcification mechanism (De Nooijer, 2009, 2014b; Erez, 2003). Chamber addition starts extra-cellularly by formation of an organic template (Erez, 2003; Hemleben et al., 1977), the primary organic sheet, with calcification occurring on both sides in a (semi-) enclosed space, often referred to as the site of calcification (SOC). The (chemical) conditions at this SOC are essentially unknown, but probably largely determined by selective ion transport (Bentov and Erez, 2006; De Nooijer, 2014b; De Nooijer et al., 2009; Nehrke et al., 2013; Toyofuku et al., 2017), possibly influenced by transport of (modified) seawater to the site of calcification as reported for some species (Bentov and Erez, 2006; Erez, 2003). These

processes are also likely to affect the concentrations of other elements, such as Mg or Na, at the SOC.

Incorporation of minor and trace elements into the calcite lattice can occur via three different pathways: 1) substitution for Ca^{2+}; 2) at interstitial positions and 3) via (micro-) fluid inclusions. For divalent cations, such as Mg^{2+}, Sr^{2+}, Zn^{2+}, Cd^{2+}, Mn^{2+}, Fe^{2+}, and Co^{2+}, substitution for Ca^{2+} is the main incorporation mechanism, as no charge compensation for Ca^{2+}, also being doubly charged, is needed. However, also ionic radius plays an important role. For example, as the atomic radius of e.g. Mg^{2+} is much smaller than that of Ca^{2+}, incorporation causes stress within the calcite lattice. For monovalent cations, such as Na^{+} or K^{+}, incorporation into the crystal lattice via substitution or at interstitial positions would not only potentially affect the crystal lattice but also require charge compensation, by for example lattice defects in case of interstitial incorporation (Ishikawa and Ichikuni, 1984), or (in case of substitution) by creation of an anion vacancy after replacing two Ca^{2+} by two cations (Yoshimura et al., 2017). Whereas both substitution as well as incorporation at interstitial positions homogeneously distributes elements in the crystal lattice, incorporation via (micro-) fluid inclusions is a less structured process, distributing elements more randomly in the crystal lattice. Next to environmental factors controlling element incorporation, different physical parameters might affect the incorporation mechanisms into the calcite lattice. For example calcite growth rate is found to significantly increase incorporation of Sr and Na (Busenberg and Plummer, 1985; Kısakürek et al., 2008; Nehrke et al., 2007), as well as for many other elements (e.g. Rimstidt et al., 1998; Lorens, 1981).

For proxy development, the relation between (trace) elements and isotopes in foraminiferal shells and environmental parameters can be studied in two ways. First, by collecting living foraminiferal specimens from their natural habitat, for example using core-tops at the sediment surface or plankton tows from the water column, the foraminiferal shell elemental and isotopic composition can be compared directly to in-situ measured environmental conditions. This typically yields empirical calibrations of foraminiferal calcite test compositions to environmental variables. However, environmental parameters such as temperature, alkalinity and salinity often co-vary in the field, complicating individual calibrations of foraminiferal (trace) element to calcium ratios with different environmental parameters, which is problematic in the absence of a mechanistic understanding of calcification. Therefore, controlled foraminiferal and inorganic calcite growth experiments are conducted to independently test the effect of individual environmental parameters and

biology on element incorporation in (foraminiferal) shell carbonate. For at least the last 60 years, the stable isotopic composition of foraminiferal shells (Emiliani, 1955; Epstein et al., 1951; Epstein et al., 1953; Urey et al., 1951), and since the 1990's also foraminiferal (trace) elemental shell chemistry and the combination between both has been used to reconstruct a variety of seawater environmental parameters. For example, Mg/Ca is a well-established proxy for temperature (Elderfield and Ganssen, 2000; Lea et al., 1999; Nürnberg et al., 1996); Mn/Ca is used as a proxy for bottom water (Barras et al., 2018; Groeneveld and Filipsson, 2013) or water column oxygenation (Klinkhammer et al., 2009; Steinhardt et al., 2014; Munsel et al., 2010), as well as to test for diagenetic effects (Boyle, 1983); Ba/Ca for riverine inflow (Hall and Chan, 2004; Lea and Boyle, 1991; Weldeab, 2007) or nutrient proxy (Lea and Boyle, 1991); B/Ca for pH (Yu, 2007); Sr/Ca and S/Ca for seawater carbonate chemistry (Dueñas-Bohórquez et al., 2009; Keul et al., 2017; Russell et al., 2004; van Dijk et al., 2017) and Na/Ca as a potential proxy for salinity and/or calcium concentration of the seawater, depending on the time scale studied (Allen et al., 2016; Bertlich et al., 2018; Geerken et al., 2018; Hauzer et al., 2018; Mezger et al., 2016; Wit et al., 2013) and many more. Furthermore, the oxygen isotopic composition of foraminifera can be used to reconstruct temperature, ice volume and salinity, albeit that all these parameters need corrections for the other parameters (e.g. for salinity reconstructions, $\delta^{18}O$ first has to be corrected for temperature and ice volume), introducing new uncertainties (Epstein et al., 1953; Fairbanks, 1989; Labeyrie et al., 1996; Rohling and Bigg, 1998; Shackleton, 1974, 1987).

1.3 Salinity

Sea water salinity, the amount of salts dissolved in seawater, is considered one of the most important, but challenging parameters to reconstruct in paleoceanography. Together with temperature, salinity controls the density of seawater, driving large scale ocean circulation (the thermo-haline circulation) thereby redistributing oxygen, heat and nutrients worldwide. In the present-day, sea surface salinity has an average value of ~35, but also showing large geographical variations (Fig. 1.1). Salinity is lower in regions where freshwater input is high compared to evaporation, for example close to river mouths, glaciers, and near the equator where rainfall is high, and higher in semi-enclosed basins with evaporation exceeding precipitation (e.g. the Mediterranean Sea and the Red Sea) (Fig. 1.1). On longer (geological) timescales, changes in salinity also reflect waxing and waning of continental ice sheets, sea ice formation and regional and global circulation of water masses.

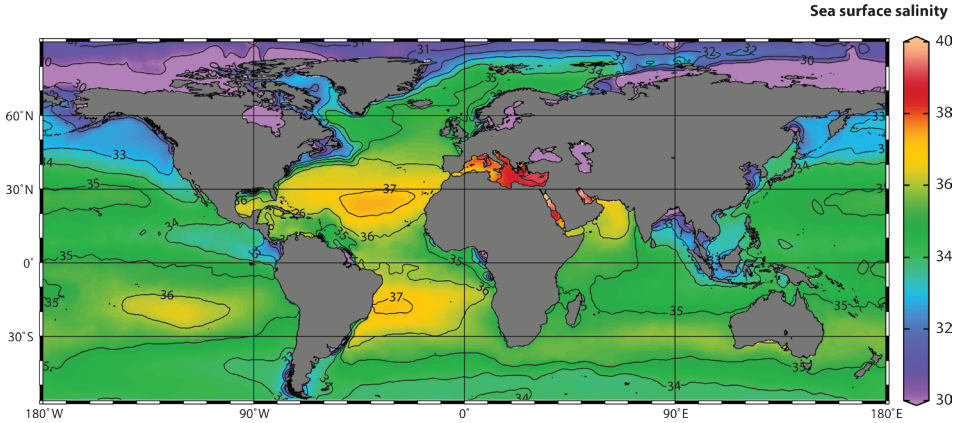

Figure 1.1. Global sea surface salinity map (WOA01 yearly average; Boyer and Levitus, 2002; Schitzer, 2007).

Although salinity varies because of differences in total amounts of dissolved salts, the relative contribution of the major elements is constant (Broecker and Peng, 1982). These elements, such as chloride, potassium, sulfur and sodium display so-called conservative behavior. Most non-conservative elements do not show a one to one relation to salinity, but vary as a consequence of environmental parameters and biological processes. On geological time scales, the major elemental composition of sea salt can, however, vary, depending on the residence time of the elements considered (Broecker and Peng, 1982). Some elements with a relatively short residence time such as Ca vary on a million(s) of years' time scale, whereas other elements, such as Na, have residence times of 100's of millions of years and hence remain a stable component within sea salt over much longer time scales.

1.4 The development of a salinity proxy

Whereas temperature can be reconstructed with reasonable accuracy by various proxies (e.g. molecular $U^{K'}_{37}$: Prahl and Wakeham, 1987, molecular TEX86: Schouten et al., 2002, foraminiferal Mg/Ca: Elderfield and Ganssen, 2000; Lea et al., 1999; Nürnberg et al., 1996, and foraminiferal $\delta^{18}O$: e.g. Zachos et al., 2001), an independent proxy for past salinity remains elusive (e.g. Allen et al., 2016; Bertlich et al., 2018; Mezger et al., 2016; Mezger et al., 2018; Rohling and Bigg, 1998; Schouten et al., 2006; Wit et al., 2013). A proxy for salinity is not only required to reconstruct past hydrological conditions, but also to correct other existing proxies for the effect of salinity, such as foraminiferal Mg/Ca which is commonly used as a temperature proxy, but also affected by salinity (Dueñas-Bohórquez

et al., 2009; Lea et al., 1999). In recent years, progress has been made with the development of Na/Ca as a promising novel tool to reconstruct salinity (Allen et al., 2016; Bertlich et al., 2018; Mezger et al., 2016; Mezger et al., 2018; Wit et al., 2013). Still, currently most salinity reconstructions involve combining (foraminiferal) stable oxygen isotopes with independent (in)organic temperature proxies (e.g. foraminiferal Mg/Ca or molecular $U^{K'}_{37}$; Elderfield and Ganssen, 2000; Rohling and Bigg, 1998; Schouten et al., 2006), but also dinoflagellate cyst morphology (Mertens et al., 2012; Verleye et al., 2012); foraminiferal Ba/Ca (Weldeab, 2007) and δD of long chain ketones and alkenones (e.g. Schouten et al., 2006; Vasiliev et al., 2017) have been proposed. However, preservation issues and uncertainties associated with the indirect controls on these proxy signals result in (large) errors in the reconstructed salinity (Rohling, 2007). Furthermore, such an approach assumes a constant relationship between salinity and stable isotopic composition of seawater, which is known to differ spatially (Zahn and Mix, 1991) and most probably also on geological timescales. Therefore, the relation between salinity and stable isotopes is often modelled and based on assumptions on many hydrological factors (e.g. Rohling and Bigg, 1998), introducing new errors in the reconstructed salinity. These uncertainties can be circumvented by a more direct approach, i.e. a salinity proxy that directly depends on elements defining seawater salinity, such as Na.

Element partitioning is defined as the El/Ca ratio of the foraminifer, divided by that same ratio in seawater. For most conservative elements defining seawater salinity, a constant partitioning has been reported, meaning that no variation in element incorporation occurred with changing salinity (De Nooijer et al., 2007; Evans et al., 2015; Hönisch et al., 2011; Lea and Boyle, 1991; Segev and Erez, 2006). However, for barnacle shells (Gordon et al., 1970), Atlantic oysters (Rucker and Valentine, 1961) and inorganic precipitates (Ishikawa and Ichikuni, 1984; Kitano et al., 1975), Na partitioning increases with increasing salinities. More recently, the positive relation between Na incorporation in foraminiferal shells and salinity was also observed in culturing studies with benthic (Geerken et al., 2018; Wit et al., 2013) and planktonic foraminifera (Allen et al., 2016). This thesis focuses on development and validation of foraminiferal Na/Ca as a proxy for salinity. Existing calibrations for benthic species are complemented by those for planktonic foraminifera, as these are often used in paleoceanography to reconstruct surface water conditions.

1.5 Synopsis of this thesis

This thesis is structured in different chapters, following consecutive steps for the understanding and development of the foraminiferal Na/Ca (salinity) proxy potential (Fig. 1.2). First, the chemical composition (Na/Ca, Mg/Ca and Sr/Ca) of shells of living planktonic foraminiferal specimens (*Globigerinoides ruber* and *Trilobatus sacculifer*) collected from Red Sea surface waters (Fig. 1.2), covering a broad salinity range, is directly compared to in-situ measured salinities and other environmental conditions including temperature and carbonate chemistry. This resulted in the first empirical calibration of planktonic foraminiferal calcite shell Na/Ca to salinity. However, robust application of this Na/Ca-salinity proxy requires studying the transport of the shell Na-signal through the water column up to the sediment surface (core-tops), considering processes potentially changing the Na/Ca shell composition during the life-span of these species (ontogeny) and after death and burial at the seafloor (taphonomy). Therefore, foraminiferal shell Na/Ca compositions, as well as Mg/Ca, are measured from Red Sea plankton tow (also referred to as multi-net) and core-top samples collected at similar locations as the surface water samples (Fig. 1.2). After establishing the importance of taphonomy and ontogeny on Na incorporation, mainly focusing on the presence or absence of Na-enriched spines, the intra-shell Na-distribution is studied to determine how well the Na-salinity signal is captured in the different intra-shell components. This development of Na/Ca as a salinity proxy is complemented by application of this proxy in a multi-proxy study, comparing existing methods with the newly proposed proxy. In this thesis, an application of planktonic foraminiferal Na/Ca as a proxy for salinity is performed in a northeastern Arabian Sea core (PASOM 3), covering the last glacial cycle. Due to glacial sea level low stands, combined with the effect with enhanced evaporation during stronger winter monsoons, major salinity fluctuations are expected in this time interval. Finally, inorganic calcite precipitation experiments were performed to understand how different physico-chemical conditions drive the Na incorporation during calcite precipitation. A proper understanding of the inorganic system allows to evaluate Na/Ca in biogenic carbonates like foraminiferal calcite and to identify the processes responsible for the observed intra-shell variability.

In Chapter 2, the first field calibration of planktonic foraminiferal Na/Ca to salinity is presented. Whereas cultured benthic and planktonic foraminifera already showed that Na incorporation in foraminiferal shell calcite provides a potential independent proxy for salinity, a field calibration was still missing. The Red Sea provides a natural laboratory

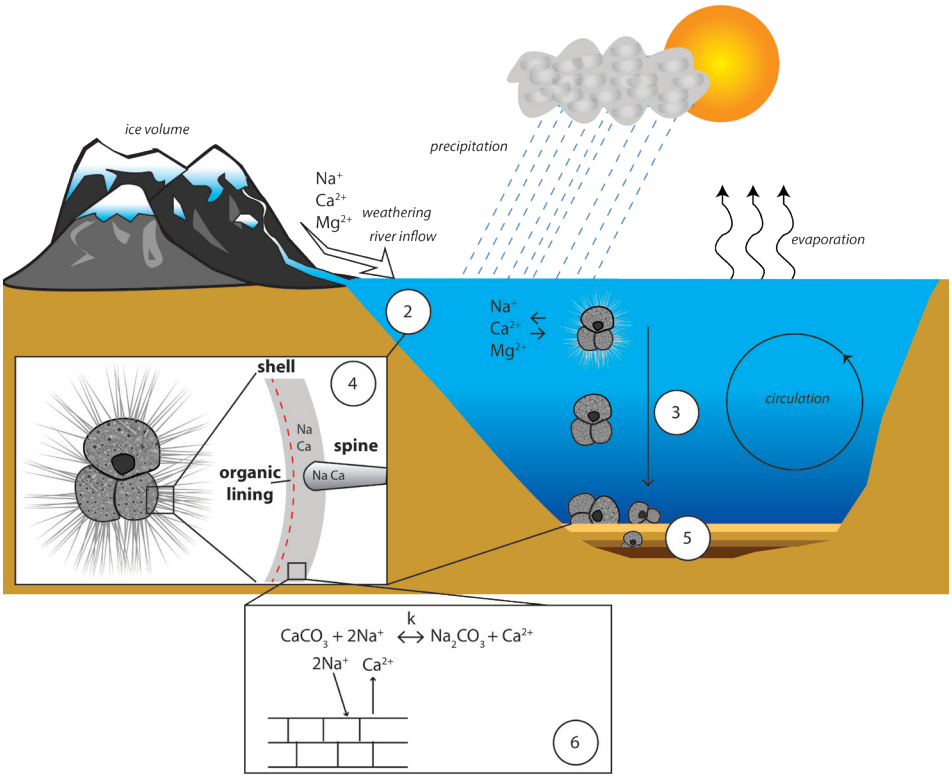

Figure 1.2. Schematic overview of the set-up of this thesis and potential factors influencing sea water salinity (indicated in italic, e.g. evaporation, precipitation, river inflow, ice volume, weathering), with numbers indicating the chapters in which the subject is described. Chapter 2 describes the first surface water collected foraminiferal Na-salinity field calibration, whereas chapter 3 focuses on the transport of this Na-salinity signal through the water column. Chapter 4 describes the intra-shell distribution of Na in planktonic foraminiferal shells. Chapter 5 presents an application of the Na-salinity proxy in a multi-proxy approach, using a northeastern Arabian Sea core covering the last glacial cycle. In chapter 6, underlying mechanisms of Na incorporation are studied in inorganic precipitation experiments.

covering a broad salinity range from ~36 to 40. Living specimens of two planktonic foraminiferal species (*G. ruber and T. sacculifer*) were collected from Red Sea surface water (Fig. 1.3) and analyzed for their Na/Ca content using laser-ablation inductively coupled plasma mass spectrometry (LA-ICP-MS). Both species show increasing Na/Ca values with salinity, however with a relatively large intra- and inter-specimen variability. Absolute Na/Ca values and slopes of the Na/Ca-salinity calibrations are similar for both species, albeit that values for *T. sacculifer* deviate from this trend in the northernmost transect. It is hypothesized that the foraminifera in the northernmost part of the Red Sea are (partly) expatriated and hence should be excluded from the Na/Ca-salinity calibration.

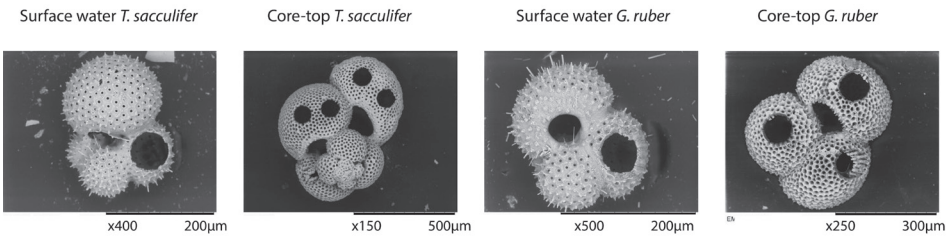

Figure 1.3. Examples of laser-ablated (measured for their chemical composition) planktonic foraminiferal shells of species *Globigerinoides ruber* and *Trilobatus sacculifer,* collected from Red Sea surface water samples and core-tops.

Application of a Na/Ca-based salinity proxy requires calibrations which also include potential effects of how a Na-based salinity signal is transported through the water column and ultimately buried in the sediment. Chapter 3 compares Na/Ca from shells of living specimens collected from Red Sea surface waters (Chapter 2) with shells of specimens collected from 0-500 m water depth and from core-tops from the same locations (Fig. 1.3). This shows that Na/Ca-values in *G. rube*r and *T. sacculifer* shells decrease with increasing water depth until the shells reach the sediment-water interface. This decrease in Na/Ca is probably related to spine loss preceding gametogenesis during settling in the water column, with these spines being enriched in Na. Furthermore, Mg/Ca values have also been measured and were found to increase towards the seafloor in both species, coinciding with deposition of gametogenic calcite, which is enriched in Mg, but has Na/Ca values similar to that in lamellar calcite. Both spine shedding and GAM calcite addition hence affect the average minor/trace element composition of foraminiferal calcite.

Chapter 4 describes the quantification of the intra-shell distribution of Na, considering the relative contributions of shell, spine and spine base calcite and organic linings Na/Ca to the total measured Na/Ca signal. Previous studies showed varying Na concentrations in different parts of foraminiferal shells, with especially spines and regions close to the primary organic sheet being enriched in Na. In this study, Electron Probe Microanalysis (EPMA) and solution-ICP-MS were used to unravel the Na composition of different components of the planktonic foraminiferal shell wall and their potential dependence on salinity. The relative contribution of shell calcite, organic linings, spines and spine bases to whole shell Na chemistry is considered quantitatively and shows that whereas the high Na areas, such as spines and spine bases, may be susceptible to taphonomy, the Na chemistry of the shell itself appears relatively robust. Comparing both shell and spine Na/Ca values with salinity shows that shell chemistry records salinity, albeit with a very modest slope.

The first application of the newly developed proxy is described in Chapter 5, in conjunction with other existing proxies, on a northeastern Arabian Sea core covering the last glacial cycle. Sediment geochemistry, foraminiferal shell stable isotopes, foraminiferal (trace) element incorporation and organic geochemical proxies are combined in a multi-proxy approach to reconstruct past changes in monsoon intensity related sea surface temperatures, salinities and oxygen minimum zone (OMZ) intensity. The Na-salinity proxy is compared to other, more traditional methods such as $\delta^{18}O$ corrected for sea surface temperature and Ba/Ca as a proxy for river outflow. It is found that measured *G. ruber* shell Na/Ca values are heavily impacted by (spine) preservation, albeit that general patterns still follow the expected trends. Reconstructing sea surface salinities is most robust by combining proxies ($\delta^{18}O$ and independent sea surface temperature reconstructions). Reconstructed sea surface temperatures (SST) show a strong dependency on the method used, with foraminiferal Mg/Ca SST reconstructions recording annual averages, whereas reconstructed $U^{K'}_{37}$ based SST's are also recording seasonal differences in productivity. Patterns of the suggested proxy for oxygenation via $[Mn^{2+}]$ of the water-column, planktonic foraminiferal Mn/Ca values, correlate well with independent proxies for OMZ intensity and are higher during warmer time intervals. This correlation could be caused by either synchronous enhanced dust input or the stronger OMZ intensity itself.

In Chapter 6, inorganic calcite precipitation experiments were performed to test the proxy potential of foraminiferal shell Na/Ca, as well as explain intra-shell variability in Na/Ca. The effects of salinity, calcite saturation state (Ω), $[Ca^{2+}]/[CO_3^{2-}]$ stoichiometry and $[Na^+]/[Ca^{2+}]$ of the growth solution on Na incorporation were tested independently using two different experimental set-ups. Sodium partitioning in inorganically precipitated calcites was lower and stayed constant over a range of salinities in contrast to the earlier established increase in foraminiferal shell Na partitioning with increasing salinities. Therefore, foraminifera are suggested to exert a strong biological control on Na incorporation in response to salinity. Furthermore, growth rate, here varied by changing Ω of the solution, as well as $[Na^+]/[Ca^{2+}]$ of the growth solution all affect Na/Ca of inorganically precipitated calcites substantially. Therefore, these parameters are combined in a general model, which can be used as a baseline to evaluate variations in Na/Ca in biogenic calcite. Implications for future proxy use of foraminiferal Na/Ca as a salinity proxy are that the effect of growth rate on Na partitioning, potentially coupled to sea water Ca concentrations, cannot be neglected. Also, this is relevant for the recently suggested paleo-application of Na/Ca in reconstructing past variations in seawater $[Ca^{2+}]$ on timescales longer than 1 million years, as changes in seawater $[Ca^{2+}]$ might also affect growth rate.

2

Chapter 2

Salinity controls on Na incorporation in Red Sea planktonic foraminifera

Eveline M. Mezger

Lennart J. de Nooijer

Wim Boer

Geert-Jan A. Brummer

Gert-Jan Reichart

Published in Paleoceanography (2016)

Abstract

Whereas several well-established proxies are available for reconstructing past temperatures, salinity remains challenging to assess. Reconstructions based on the combination of (in-)organic temperature proxies and foraminiferal stable oxygen isotopes result in relatively large uncertainties, which may be reduced by application of a direct salinity proxy. Cultured benthic and planktonic foraminifera showed that Na incorporation in foraminiferal shell calcite provides a potential independent proxy for salinity. Here we present the first field calibration of such a potential proxy. Living planktonic foraminiferal specimens from the Red Sea surface waters were collected and analyzed for their Na/Ca content using laser ablation quadrupole inductively coupled plasma mass spectrometry (LA-Q-ICP-MS). Using the Red Sea as a natural laboratory, the calibration covers a broad range of salinities over a steep gradient within the same water mass. For both *Globigerinoides ruber* and *Trilobatus sacculifer* calcite Na/Ca increases with salinity, albeit with a relatively large intra- and inter-specimen variability. The field-based calibration is similar for both species from a salinity of ~36.8 up to ~39.6, while values for *T. sacculifer* deviate from this trend in the northernmost transect. It is hypothesized that the foraminifera in the northernmost part of the Red Sea are (partly) expatriated and hence should be excluded from the Na/Ca-salinity calibration. Incorporation of Na in foraminiferal calcite therefore provides a potential proxy for salinity, although species specific calibrations are still required and more research on the effect of temperature is needed.

2.1 Introduction

Seawater salinity is set by several processes, including river discharge, waxing and waning of continental ice sheets, sea ice formation and the balance between evaporation and precipitation. Salinity, together with temperature, plays a major role in setting sea water density, determining seawater circulation patterns both on a global and regional scale. This makes salinity one of the key parameters for reconstructing past ocean functioning and its relation to past climate. At the same time, a proxy for salinity is necessary to correct for the impact of salinity on other proxies, for example temperature reconstructions based on foraminiferal shell $\delta^{18}O$ (Rohling, 2007) and Mg/Ca (e.g. Dissard et al., 2010). Current reconstructions of past salinity are mostly based on combining stable isotopes (e.g. δD of long chained ketones or foraminiferal $\delta^{18}O$) with independent reconstructions for seawater temperature (e.g. foraminiferal Mg/Ca or $U^{k'}_{37}$) (Elderfield and Ganssen, 2000; Schouten et al., 2006). The uncertainty in these calibrations and the independent controls on these proxy signals, leads to error propagation which effectively makes most of these approaches hard to apply (Rohling, 2007). One of the uncertainties is based on the assumption that the relation between seawater stable isotopes and salinity remained constant over the time interval studied. On geological timescales, however, this relation likely varied, as it does spatially (e.g. Gat, 1996; Zahn and Mix, 1991). To circumvent this problem, the relation between salinity and stable isotopes is often modelled (e.g. Rohling and Bigg, 1998), using assumptions on several hydrological factors and thereby increasing the uncertainty in reconstructed salinity.

Ideally, a proxy for salinity directly depends on the elements that determine ocean salinity, e.g. Na, Cl and K, or is co-varying strongly with salinity. For several elements, a direct relation was found between the element/Ca ratio in foraminiferal calcite and that in the ambient seawater (e.g. Mg/Ca: Segev and Erez, 2006, Evans et al., 2015, Ba/Ca: Hönisch et al., 2011, Cu/Ca: De Nooijer et al., 2007, Ba/Ca: Lea and Boyle, 1991). For some (e.g. conservative) elements, their incorporation is generally not (only) dependent on the concentration of these elements in seawater, but (also) on other environmental factors, such as temperature (Mg/Ca: e.g. Anand et al., 2003; Nürnberg et al., 1996) or pH (B/Ca: Yu et al., 2007 and references therein). Na incorporation was found to be correlated to salinity in the carbonate of Atlantic oysters (Rucker and Valentine, 1961) and barnacle shells (Gordon et al., 1970). For inorganically precipitated calcite and aragonite this relation was shown to be dependent on Na concentration rather than the medium's Na/Ca ratio (Kitano et al., 1975; Ishikawa and Ichikuni, 1984). Recently, it was

found that the [Na+] composition of calcite of cultured benthic and planktonic species of foraminifera also positively correlates with salinity (Wit et al., 2013 and Allen et al., 2016, respectively), which was explained by a relative increase in activity of free [Na^+] compared to [Ca^{2+}] activity with increasing salinity (Wit et al., 2013). Robust application of this proxy would, however, require finding this relationship in other cultured species (planktonic and benthic) and in the natural environment. For this purpose, we investigate Na/Ca of living planktonic foraminifera collected across a steep salinity gradient in the Red Sea. The Red Sea provides a natural laboratory with a broad salinity range (36 to 40), from which living specimens of the planktonic foraminifera *Globigerinoides ruber* (white) and *Trilobatus sacculifer* were analyzed for their Na/Ca composition.

2.2 Methodology

2.2.1 Study area and sample collection

The Red Sea, with a total length of approximately 2100 km is enclosed by deserts (Fig. 2.1). The only connection to the open ocean is through the shallow and narrow straits of Bab el Mandeb, connecting the Red Sea with the Gulf of Aden and ultimately the Indian Ocean. Due to the very high evaporation rates in this basin (up to ~2 m/yr) (Sofianos et al., 2002; Morcos, 1970), low mean annual rainfall from 3 mm/yr (N) to 150 mm/yr (S) (Zahran, 2010) and no significant rivers flowing into the basin, the basin is characterized by a pronounced anti-estuarine circulation (Rohling, 1994, and references therein). Surface waters flow northward while evaporating, resulting in a strong south-north gradient in salinity. Monsoonal winds cause seasonal contrasts, also influencing exchange through Bab el Mandeb. During the summer monsoon, circulation becomes three-layered due to a wind-driven upper surface layer flowing into the Gulf of Aden (Siccha et al., 2009, and references therein). This change in monsoonal strength between summer and winter does not affect salinities noticeably (World Ocean Atlas (WOA) 2001: Boyer et al., 2005). However, maximum temperatures become ~2°C lower at the southernmost position (Boyer et al., 2005). The temperature gradient opposes the salinity gradient, with temperatures increasing from north to south. Still, to avoid as much as possible offsets in calibration due to such minor variations in salinity, we here calibrate to seasonal salinity data (April-June 2001). The carbonate ion content (CO_3^{2-}) and pH were calculated from measured dissolved inorganic carbon (DIC) and alkalinity (TA) values recorded during the cruise, using CO2SYS software (Lewis and Wallace, 1998).

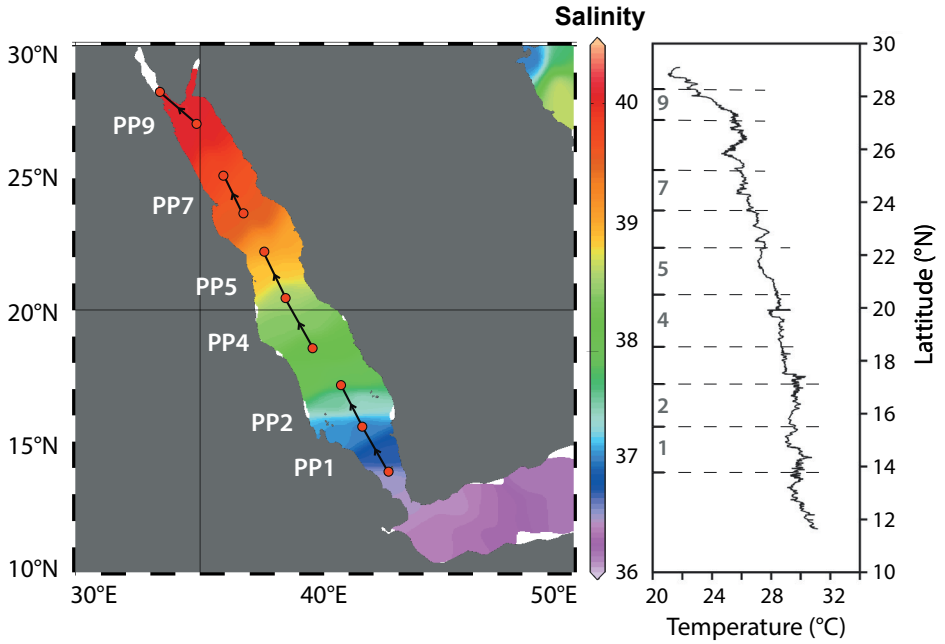

Figure 2.1. Salinity map (WOA 2001, average April-June) with annual average salinities of the Red Sea (a) and aquaflow temperatures (b) for the used plankton pump (PP) transects of RV Pelagia cruise 64PE158. To the left of the temperature graph, the PP samples are also indicated.

Nine plankton pump (PP) samples were collected in May 2000 (RV Pelagia cruise 64PE158), with each sampling interval covering ~225 km on the S to N transect (Fig. 2.1). Aquaflow sea surface temperatures were continuously recorded during the cruise, whereas salinity data were retrieved from average values from April to June from the World Ocean Atlas 2001 (WOA01; Table 2.1) (Boyer et al., 2005). Salinity measurements from CTD casts at five stations were available, with salinity values in close agreement with those obtained from the WOA01 database. Upon collection samples were sieved over a 75 µm mesh, shortly rinsed with ultra-pure water to remove the salts and stored at -40°C. Subsequently, samples were freeze dried and a Low-Temperature-Asher was used to concentrate the foraminiferal specimens and remove organic matter (for samples PP2, PP4 and PP7) (Fallet et al., 2009). After ashing, samples were treated with a few drops of ethanol and ultrapure water to disaggregate the residue, wet-sieved over a 63 µm mesh and dried. Samples PP1, PP5 and PP9 were processed earlier and treated differently: after defrosting the samples, organic matter was removed using hot alkaline H_2O_2 for several hours based on the protocol of Fallet et al. (2009), after which they were rinsed three times with ultrapure water, ultrasonicated with each rinse and dried. Fallet et al. (2009) showed that both methods successfully remove all organic material from foraminiferal

Table 2.1. Details per transect[a]

Transect	Lat. begin-end (°N)	Lon. begin-end (°E)	Avg. SSS	Avg. SST	TA	DIC	CO_3^{2-}	pH
PP1	14.16 - 15.66	42.36 - 41.46	36.8	29.5	2333.6	2043.3	208.0	7.93
PP2	15.66 - 17.12	41.46 - 40.47	37.3	29.4	2354.6	2051.6	216.3	7.94
PP4	19.06 - 20.57	39.10 - 38.21	38.4	28.5	2370.6	2061.9	219.3	7.95
PP5	20.57 - 22.29	38.21 - 37.46	38.8	28.0	2376.5	2065.4	220.4	7.95
PP7	23.70 - 25.40	37.78 - 35.68	39.6	26.3	2409.2	2084.1	229.1	7.99
PP9	27.03 - 28.49	34.67 - 33.14	40.1	24.2	2425.7	2107.6	224.1	8.00

[a]Temperatures (SST), alkalinities (TA) and dissolved inorganic carbon (DIC) were measured during RV Pelagia cruise 64PE158. Sea surface salinities (SSS) were obtained from the world ocean atlas (WOA_2001_ average April-June: Boyer et al., 2005). Carbonate ion content (CO_3^{2-}) and pH values were calculated from the measured DIC and TA values using CO2SYS (Lewis and Wallace, 1998).

shells and yield equal isotope and Mg/Ca values. No offsets in averages for the measured elements were observed between the different methods and scanning electron microscopy (Hitachi High-Tech TM3000 TableTop scanning electron microscope) pictures showed a clean foraminiferal surface with no organic films remaining (Fig. 2.2). Foraminifera were hand-picked and species identified using the species concept of Brummer et al. (1987) for *Globigerinoides sacculifer* (Brady), later assigned to as *Trilobus sacculifer* (Spezzaferri et al., 2015), and *Globigerinoides ruber* (d'Orbigny). Foraminiferal sizes were determined by measuring the diameter, from the top of the final chamber (F) to the bottom. Calculating chamber number in the size fraction employed here (100-460 μm) is very challenging: only a small change in diameter may offset the chamber number appreciably (Brummer et al., 1987). This is due to the exponential increase in size with chamber number (e.g. Hemleben and Bijma, 1994; Brummer et al., 1987). Based on measured sizes, the chamber number was determined for *T. sacculifer* using the study of Hemleben and Bijma (1994). For *G. ruber,* there is unfortunately no such study to base the chamber number over the measured size range. Therefore, we used an extrapolation of the ontogenetic measurements given by Brummer et al. (1987) to estimate the chamber number.

2.2.2 LA-Q-ICP-MS analyses

Prior to analysis, the foraminifera isolated from the plankton pump samples were cleaned with ultrapure water (>18.2 MΩ) and mounted on a stub with double-sided tape. Elemental composition of their calcite was measured by laser ablation quadrupole inductively coupled plasma mass spectrometry (LA-Q-ICP-MS) at the Royal NIOZ (Fig. 2.2). This setup consists of a NWR193UC (New Wave Research) laser, containing an ArF Excimer

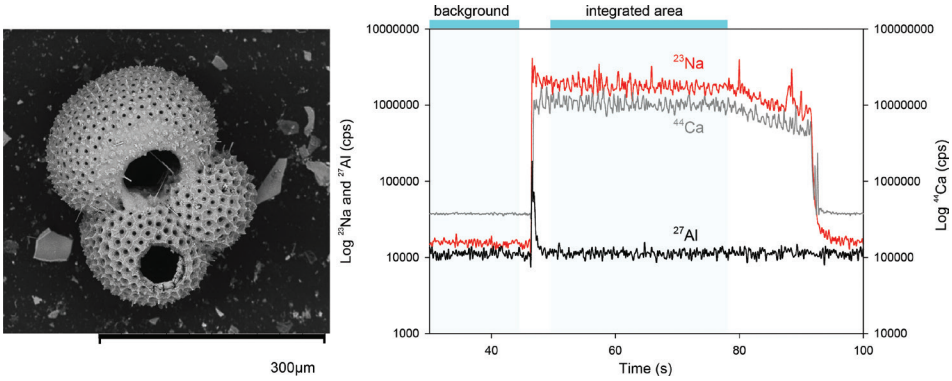

Figure 2.2. Example of a laser ablated specimen of *G. ruber* (a) and the corresponding laser ablation profile (b) with values for Na, Al and Ca in counts per second.

laser (Existar) with deep UV 193 nm wavelength and <4 ns pulse duration, coupled to a quadrupole ICP-MS (iCAP-Q, Thermo Scientific). Laser ablation of calcite was performed with a circular spot size of 60 µm and a fluence of 1 J/cm^2 at a repetition rate of 6 Hz. A fluence higher than 1 J/cm^2 increases the ablation rate and hence, limits the run time length. For the glass NIST-610 and NIST-612 standards, the ablation threshold is at a fluence of 1 J/cm^2 (Brokmann et al., 2002; Hülsenberg et al., 2008). However, since ablation just above this threshold potentially causes fractionation and the fractionation index of Na and Ca remains constant over the range 5-19 J/m^2 (Li et al., 2015), a fluence of 5 J/cm^2 is used. This difference in fluence is shown not to influence the results (Dueñas-Bohórquez et al., 2011; Hathorne et al., 2008). All samples were ablated for between 40 to 60 seconds, depending on the chamber thickness and size of the shell. The laser ablation system was equipped with a dual-volume cell, using helium as a carrier gas with a flow rate of 0.7 L/min. The optimum He flow was determined by several tests, focusing on stability of the signal, intensity, peak shape and wash-out time. Between the ablation cell and mass spectrometer, a smoother was placed to avoid interferences between ablation pulses and cycle time of the MS (Fehrenbacher et al., 2015). From the laser chamber to the ICP-MS, the He flow was mixed with ~0.4 L/min Ar make-up gas and 0.003 mL/min N_2. Before measuring the samples, the make-up gas, extraction lens, focus lens and torch position were automatically tuned for the highest sensitivity of ^{238}U, ^{139}La, ^{59}Co and low ThO/Th ratios (<0.5%) by laser ablating -NIST-610 glass. The masses measured by the ICP-MS were ^{11}B, ^{23}Na, ^{24}Mg, ^{25}Mg, ^{27}Al, ^{39}K, ^{43}Ca, ^{44}Ca, ^{55}Mn, ^{57}Fe, ^{88}Sr, ^{138}Ba, ^{238}U. The duration of one cycle of these 13 isotopes was 0.13 seconds. Every sample run lasted approximately 100 seconds, of which the first 20 seconds consisted of a gas blank. Intensity data were

integrated, background subtracted, standardized internally to ^{43}Ca and calibrated against the NIST-610 signal using Thermo Qtegra software version 2.2.1465.44 and reference values from Jochum et al. (2011). Since ablation of the NIST-610 and NIST-612 standards could increase the sodium background, they were only ablated and analyzed at the end of every sequence and cones were cleaned before the next sequence. The powders JCp-1, the synthetic CaCO3 MACS-3 and an in-house (foraminiferal) calcite standard (NFHS-1, Supporting Information Text 2.1) were pressed to a tablet and used for monitoring drift and quality control and measured every 10 foraminiferal samples (Okai et al., 2002; Wilson et al., 2008). The NFHS-1 standard was made primarily to create a powdered standard as close as possible in composition to foraminiferal calcium carbonate (Na/Ca: ~3-12 mmol/mol).

Relative precision of the Na/Ca analyses was better than 9%, based on the three different calcium carbonate standards (two international, one in-house) used (MACS-3: 27.5±0.8 mmol/mol Na/Ca; JCp-1: 19.5±1.4 mmol/mol Na/Ca; NFHS-1: 5.8±0.5 mmol/mol Na/Ca). Accuracy of the analyses, based on comparing the carbonate standards with internationally reported values (Okai et al., 2002; Wilson et al., 2008), was 101±3% and 97±7% for MACS-3 and JCp-1 respectively. The measurements of Mg and Na per standard were also normally distributed, except for Mg for the NFHS-1 (Supporting information Fig. S2.1, Table S2.1). The fact that the NFHS-1 is not normally distributed is somewhat puzzling. It does suggest multiple phases of carbonate present (i.e. low and high Mg carbonates), but is here irrelevant due to the very small grain size (<1µm) the standard was ground to (Supporting information Text S2.1).

A comparison of our data with solution sector field inductively coupled plasma mass spectrometry (SF-ICP-MS, Thermo Scientific, Element-2) shows no offsets caused by laser ablation (Supporting information Text S2.2, Fig. S2.2, Tables S2.2 and S2.3). We compared these two methods on standard material and artificial pressed pellets with a Na addition series. The linearity (r^2=0.99) of the plot and the slope of 0.98 indicates that LA-Q-ICP-MS delivers accurate Na/Ca data. Although the very low Na/Ca values for the lower part of the inter-comparison are somewhat off, these values are much lower than the range found for foraminifera (3-12 mmol/mol). With concentrations similar to those found for foraminiferal carbonate, Na/Ca values are very close to the reference and solution analyses-based values.

2.2.3 Data processing

Foraminiferal signals were screened for surface contamination and parts of the outside or inside of the shell with elevated Mg, often accompanied by a small peak in Na and Al, were eliminated from the area selected for integration. Since shells were collected from living specimens and have never been in contact with the sediment, surface contaminations must be caused during the sample processing. Measurements were discarded in cases when the shell (test) wall was very thin and the analytical sequence was too short (<5 seconds). Only the last 3 shell chambers were analyzed to minimize potential impacts of migration of the collected specimens. Outliers are identified routinely by the average –2SD and average +2SD per transect. In total 153 specimens of *G. ruber* (white) were analyzed, varying between 5 and 50 per transect. For *G. ruber* a total of 171 analyses, including duplicates and outliers, provided the data for calculating the average foraminiferal shell chemical composition per transect (Figs. 2.3-2.5, Supporting information Figs. S2.3-S2.8). For *T. sacculifer*, in total 46 specimens were analyzed, varying between 2 and 19 specimens per transect, to a total of 70 single spot analyses including outliers and duplicates. No significant differences were found between the analyzed chambers' position (respectively F and F-1). Values deviating from the average by more than twice the standard deviation of the whole population of a species per transect were considered outliers and excluded from further calculations. Even though the internal variability expressed as relative standard deviation (RSD (%) = average/SD*100) per single spot analysis for Mg/Ca was relatively high with an average below 40% for both species, the standard error of the mean (= RSD/√n) per single spot measurement was ~2.5%. For Sr/Ca, the variability per measurement was below 30% on average for both species with a standard error of ~1.8%. The variability per single-spot measurement for Na/Ca was always less than 35% for both species with a standard error of ~2.1%.

Ratios for Mg/Ca, Sr/Ca and Na/Ca per sampled transect are either normally or randomly distributed for both *T. sacculifer* and *G. ruber* (Supporting information Figs. S2.3-S2.8, Table S2.4). Relative standard deviations for these elements per group of single spot analyses per transect vary around 10%, which is close to the analytical error. Due to the large number of replicates, standard errors are considerably lower (Table 2.2). Before calculating correlations or applying statistics, elemental ratios for both species per transect were first tested for normality with the Shapiro-Wilk test.

Table 2.2. Mg/Ca, Sr/Ca and Na/Ca values for *G. ruber* and *T. sacculifer*[a]

		Mg/Ca				Sr/Ca				Na/Ca			
Species	**Salinity**	**mmol/mol**	**n**	**2*SD**	**SE**	**mmol/mol**	**n**	**2*SD**	**SE**	**mmol/mol**	**n**	**2*SD**	**SE**
G. ruber	36.8	4.09	7	0.93	0.35	1.75	7	0.47	0.18	8.10	7	2.06	0.39
T. sacculifer		3.93	6	0.71	0.27	1.90	6	0.28	0.11	8.67	5	0.76	0.17
G. ruber	37.3	5.11	45	1.84	0.69	1.64	43	0.17	0.03	9.07	43	1.42	0.11
T. sacculifer		4.37	7	1.21	0.46	1.67	7	0.35	0.13	9.08	7	1.51	0.29
G. ruber	38.4	4.67	49	1.38	0.52	1.61	50	0.22	0.03	9.57	51	2.87	0.20
T. sacculifer		3.97	13	1.24	0.47	1.51	13	0.12	0.03	9.66	10	2.13	0.34
G. ruber	38.8	3.85	8	0.85	0.32	1.53	9	0.14	0.05	9.33	8	1.85	0.33
G. ruber	39.6	4.65	39	1.74	0.66	1.50	37	0.15	0.02	10.30	39	3.49	0.28
T. sacculifer		3.84	18	1.10	0.42	1.47	20	0.16	0.04	10.45	18	2.84	0.33
G. ruber	40.1	3.73	11	1.58	0.60	1.72	13	0.37	0.10	11.34	11	3.74	0.56
T. sacculifer		3.03	21	1.01	0.38	1.69	22	0.44	0.09	9.23	20	2.48	0.28

[a]Standard deviations (SD), standard errors (SE = $\sigma/\sqrt{n}$) and number of specimens per transect (n).

2.3 Results

2.3.1 Na/Ca

Values for single-chamber Na/Ca for *G. ruber* are either normally distributed within transects (PP1, PP2, PP5, PP9), slightly skewed (PP7) or randomly (PP4) distributed (Supporting information Fig. S2.3, Table S2.4). However, despite the positive results for PP9 Na/Ca values in the Shapiro-Wilk test, the distribution appears randomly instead of normally distributed. Standard deviations within transects vary from 8 to 17% (Table 2.2). For *T. sacculifer*, Na/Ca values are normally distributed for all transects except for PP7, with standard deviations varying between 4 to 14% (Table 2.2, Supporting information Fig. S2.6 and Table S2.5).

A significant positive correlation is found between salinity and average Na/Ca values for *G. ruber*, while for *T. sacculifer* only a positive trend is observed (Fig. 2.3). Linear regressions equal: Na/Ca = 0.66 * S – 15.75 (r^2=0.88, p<0.001) for *G. ruber* and the non-significant Na/Ca = 0.229 * S + 0.67 (r^2=0.19, p=0.11) for *T. sacculifer*. Na/Ca of both species follow the same positive trend up to a salinity of 39.6, while values for the northernmost transect PP9 for *T. sacculifer* deviate strongly from this trend. When excluding the northernmost transect (Discussion, section 4.1.2), linear regressions equal Na/Ca = 0.57 * S – 12.38 (r^2=0.91, p<0.001) for *G. ruber* and Na/Ca = 0.60 * S - 13.49 (r^2=0.999, p<0.001) for *T. sacculifer*.

Since salinity and temperature are anti-correlated in our dataset, increasing Na/Ca towards the North of the Red Sea may also be interpreted as a negative correlation between Na/Ca and temperature. When including the northernmost transect, the correlation between Na/Ca and temperature has an r^2 of 0.90 for *G. ruber*, p<0.001, and r^2=0.02 and p=0.56 for *T. sacculifer*. The relationship between Na/Ca and temperature, when excluding the northernmost transect (Fig. 2.3), has r^2 values of 0.84 and p<0.001 for *G. ruber* and r^2=0.95 and p<0.001 for *T. sacculifer*. For the correlation between Na/Ca and CO_3^{2-}, r^2=0.71 and p<0.001 for *G. ruber*, and r^2=0.64 and p=0.003 for *T. sacculifer*. When excluding PP9, r^2=0.92 and p<0.001 for *G. ruber* and r^2=0.97 with a p<0.001 for *T. sacculifer*.

2.3.2 Mg/Ca and Sr/Ca

For *G. ruber*, values for Mg/Ca are normally distributed (Supporting information Fig. S2.4, Table S2.4). Standard deviations for Mg/Ca for each transect vary between 11 and 21% (Supporting information Fig. S2.4, Table 2.2). The Sr/Ca results are also normally

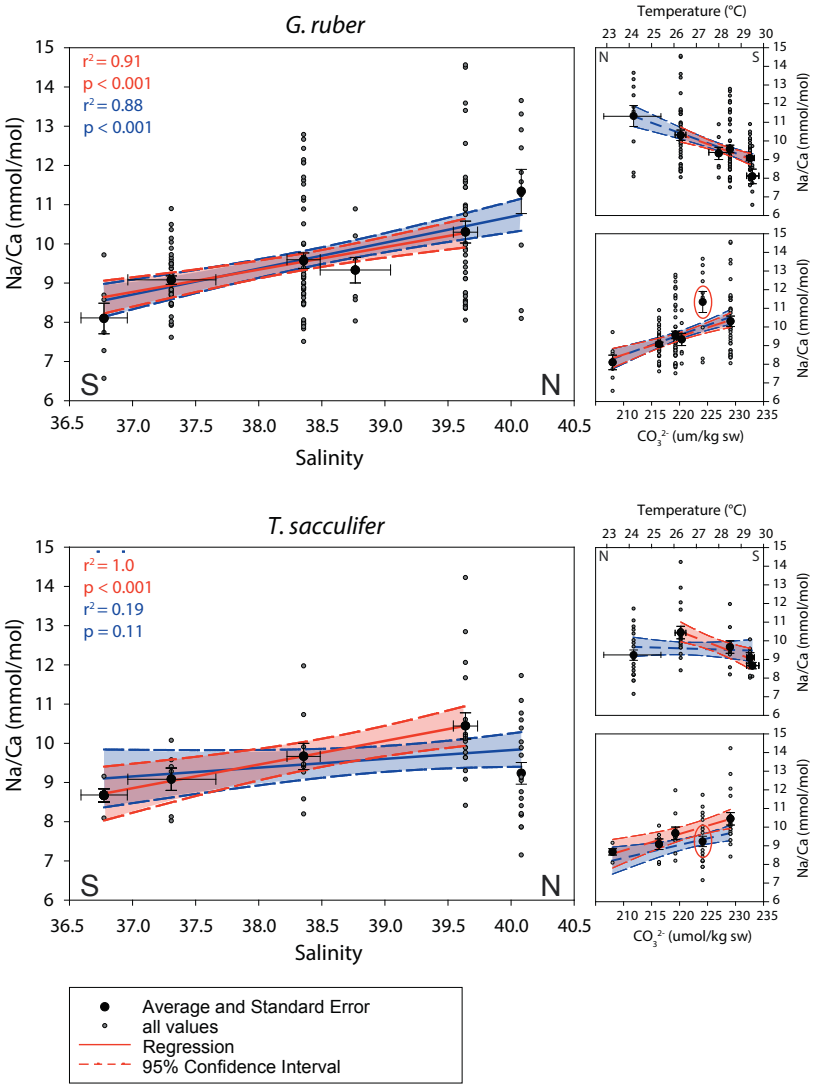

Figure 2.3. *G. ruber* and *T. sacculifer* Na/Ca values, plotted against salinity (WOA01, average April-June), measured temperatures and calculated CO32-. For reasons further explained in the discussion (section 4.1.2), all calibrations are given with (blue) and without (red) the northernmost transect. The r2 value was calculated using weighted averages and shaded areas around the calibrations indicate the 95% confidence interval of the regressions. Horizontal error bars for salinity and temperature indicate values recorded at the start and end of each transect. Vertical error bars are the standard errors of the mean. Note that the south (S) to north (N) scales are reversed for the two temperature plots (right panels). For the Na/Ca – temperature relationship, excluding the northernmost transect results in r2 values of 0.84 and p<0.001 for *G. ruber* and r2=0.95 and p<0.001 for *T. sacculifer.* When including the northernmost transect, the Na/Ca – temperature relationship has an r2 of 0.90 for *G. ruber,* p<0.001, and r2=0.02 and p=0.56 for *T. sacculifer.* For the Na/Ca – CO32- correlation, r2=0.92 and p<0.001 for *G. ruber* and r2=0.97 with p<0.001 for *T. sacculifer.* When including the northernmost transect, the Na/Ca – CO32- relationship has an r2 of 0.71 for *G. ruber,* p<0.001, and r2=0.64 and p=0.003 for *T. sacculifer.*

distributed for all transects and standard deviations vary between 4.5 and 13.5% (Supporting information Fig. S2.5, Tables 2.2 and S2.4). Single spot measurements for *T. sacculifer* showed that Mg/Ca values are normally distributed for all transects with standard deviations varying from 9 to 17% (Supporting Information Fig. S2.7, Tables S2.5 and 2.2). Values for Sr/Ca are normally distributed as well, with standard deviations varying between 4 and 13% (Supporting information Fig. S2.8, Tables 2.2 and S2.5). Despite the positive results for PP9 Sr/Ca values for the Shapiro-Wilk test, the distribution looks randomly instead of normally distributed.

The correlation between temperature and Mg/Ca is not significant for either species when excluding the northernmost transect (r^2=0.12 and p=0.1 for *G. ruber* and r^2=0.80 and p=0.15 for *T. sacculifer*) (Figs. 2.4 and 2.5). However, this correlation is significant for both species when including the northernmost transect (r^2=0.38 and p<0.001 for *G. ruber* and r^2=0.84 and p<0.001 for *T. sacculifer*) due to the considerably lower Mg/Ca for specimens from the northernmost section of the Red Sea, especially for *T. sacculifer.* Also the correlation between salinity and Mg/Ca is not significant for either species when excluding PP9 (r^2=0.15, p=0.07 for *G. ruber* and r^2=0.54, p = 0.15 for *T. sacculifer*) and significant when including this transect (r^2=0.29 and p=0.02 for *G. ruber* and r^2=0.59 and p<0.001 for *T. sacculifer*). A significant negative correlation with salinity was found for Sr/Ca, again with deviating values for the northernmost station (r^2=0.90, p<0.001 for *G. ruber* and r^2=0.53, p<0.001 for *T. sacculifer* excluding PP9, and r^2=0.25 and p<0.001 for *G. ruber* and r^2=0.53 and p<0.001 for *T. sacculifer* including PP9 (Figs. 2.4 and 2.5). With increasing temperatures, Sr/Ca values increase, except for the northernmost transect (r^2=0.86, pp<0.001 for *G. ruber* and r^2=0.34, p<0.001 for *T. sacculifer* without PP9, and r^2=0.06 and p=0.09 for *G. ruber* and r^2=0.02 and p=0.93 for *T. sacculifer* including PP9). The correlation between carbonate ion content (CO_3^{2-}) and Mg/Ca is not significant for either species, whether the northernmost transect is in- or excluded (r^2=0.02 and p=0.54 for *G. ruber* and r^2=0.25 and p=0.006 for *T. sacculifer* excluding PP9 and r^2=0.04 and p=0.24 for *G. ruber* and r^2=0.13 and p=0.06 for *T. sacculifer* including PP9). A significant negative correlation is observed between Sr/Ca and CO_3^{2-} for both scenarios and both species (r^2=0.94, p<0.001 for *G. ruber* and r^2=0.64, p<0.001 for *T. sacculifer* without PP9, and r^2=0.55 and p<0.001 for *G. ruber* and r^2=0.34 and p<0.001 for *T. sacculifer* including PP9).

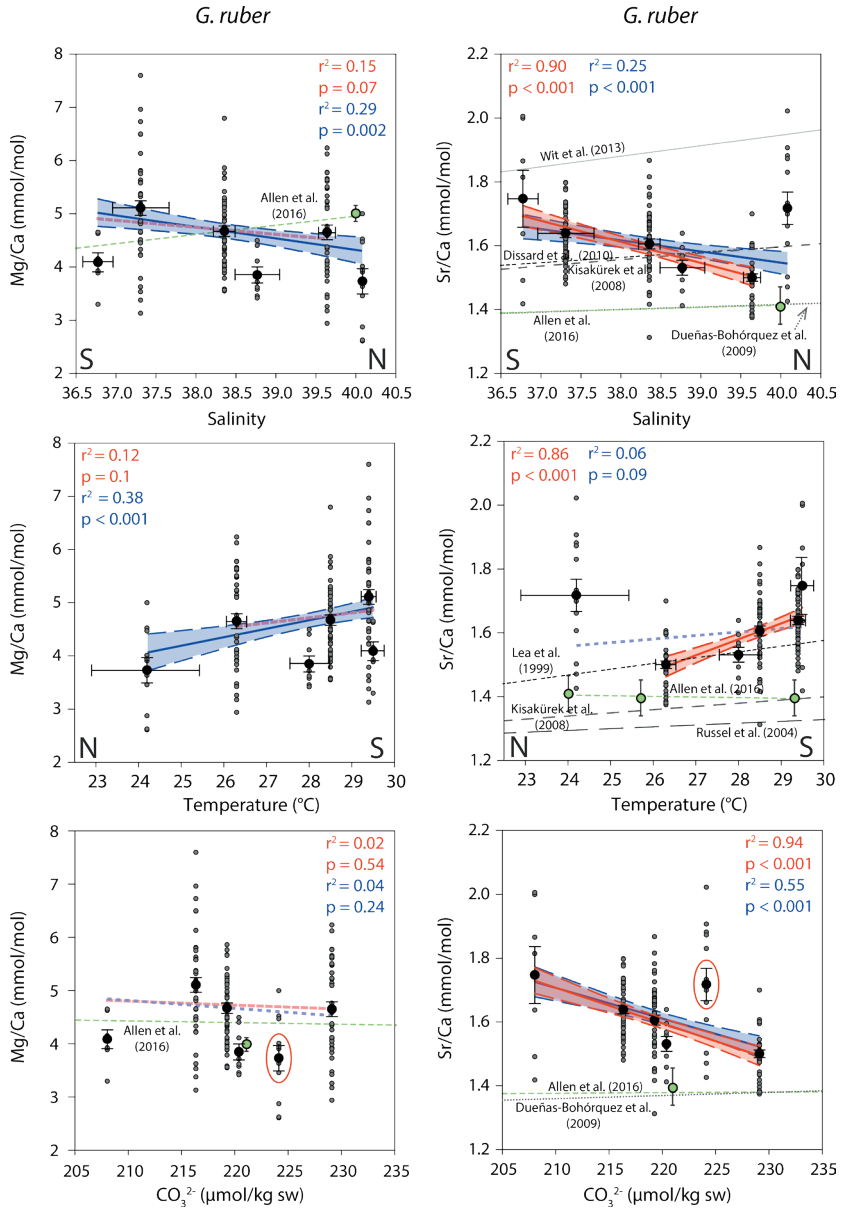

Figure 2.4. Sr/Ca and Mg/Ca values for *G. ruber,* plotted against salinity (WOA01, average April-June), measured temperatures and calculated CO32-. Non-significant calibrations from this study are indicated in light-blue (including northernmost transect) and light pink (excluding the northernmost transect) dotted trend lines. Other Sr/Ca – temperature and salinity correlations are from Wit et al. (2013) and Dissard et al. (2010) for *A. tepida,* Kısakürek et al. (2008) for *G. ruber,* Dueñas-Bohórquez et al. (2009) for *T. sacculifer, G. ruber* and *O. universa* combined and Russel et al. (2004) for *O. universa*. The red ovals indicate the northernmost transect in the CO32- plots. The green dots with analytical errors and green dotted lines give the data of Allen et al. (2016) for *T. sacculifer* and *G. ruber.* For further explanations, see caption of Figure 2.3.

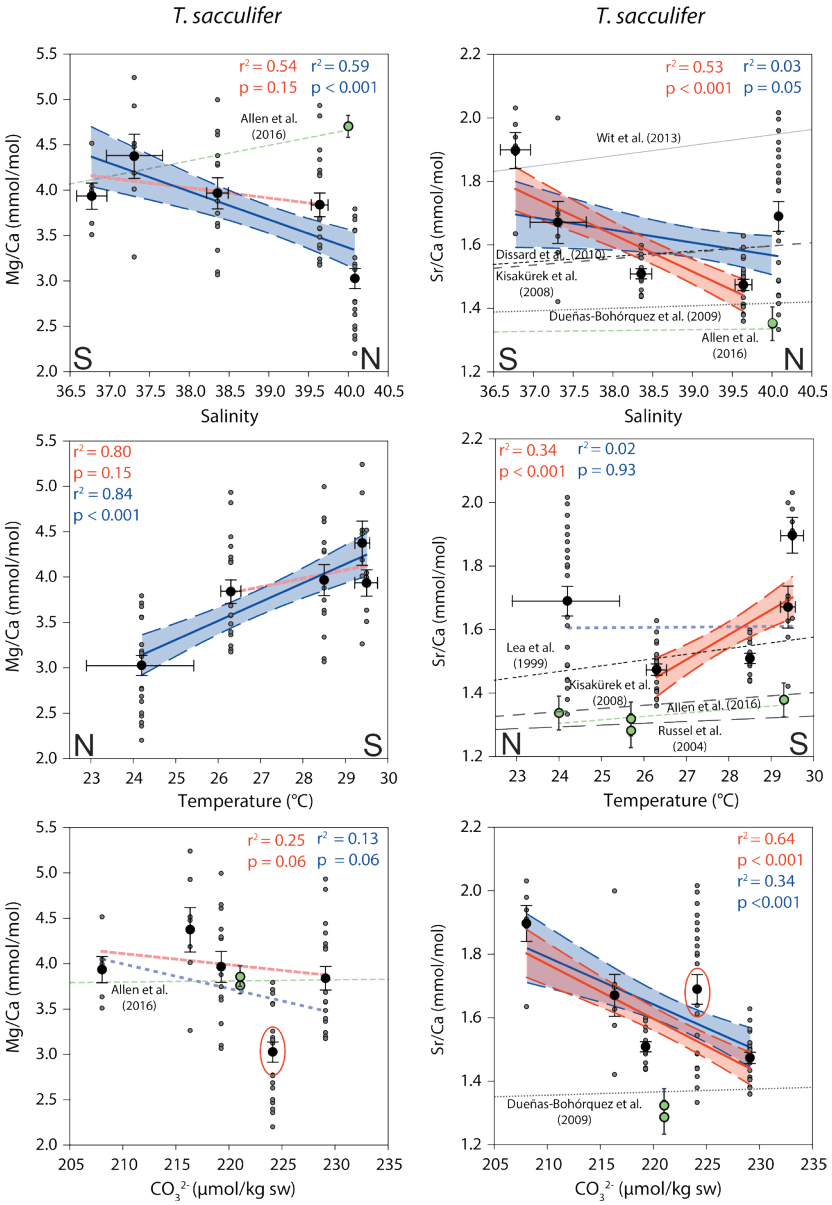

Figure 2.5. Sr/Ca and Mg/Ca values for *T. sacculifer,* plotted against salinity (WOA01, average April-June), measured temperatures and calculated CO32-. For further explanations, see caption of Figure 2.3 and 2.4.

2.3.3 Foraminiferal shell diameter

Only Na/Ca, Mg/Ca and Sr/Ca in specimens from the size fraction >75 µm were analyzed, but those from the larger end of the size spectrum were more often selected for LA-Q-ICP-MS analyses. The diameter of these specimens varies from 129 to 353 µm for *G. ruber* and from 126 to 486 µm for *T. sacculifer*. Within transects, there is no correlation between size and Na/Ca. The number of chambers for *T. sacculifer* ranges from n=14 to n=17 (Hemleben and Bijma, 1994) and for *G. ruber* between n=14 and n=22 (Brummer et al., 1987). When comparing chamber numbers to the measured Na/Ca values, a negative correlation is found for *T. sacculifer* (Fig. 2.6, r^2=0.88, p=0.005) and no correlation is present in Na/Ca versus chamber number in *G. ruber*. For the northernmost station (PP9), diameters are considerably larger for both species when compared to those of the other transects (Fig. 2.7). Combining all transects except the northernmost transect, a negative and significant correlation between salinity and size was observed (r^2=0.61, p<0.001 for *G. ruber* and r^2=0.99, p<0.001 for *T. sacculifer*). Including the northernmost transects does not result in a significant correlation between size and salinity (r^2=0.06, p=0.8 for *G. ruber* and r^2=0.0003, p=0.92 for *T. sacculifer*).

2.4 Discussion

Currently, few Na/Ca values are reported for planktonic foraminifera to compare our data to, but overall values correspond well to those reported before for *T. sacculifer* (Delaney et al., 1985, Allen et al., 2016), *G. ruber* (pink) (Allen et al., 2016) and the benthic foraminiferal species *A. tepida* (Wit et al., 2013), albeit with an offset towards higher absolute values. Both planktonic foraminifera and *A. tepida* are known to build shells relatively low in minor and trace elements compared to the composition of large benthic foraminifera (Lea et al., 1999; Munsel et al., 2010). Measured Mg/Ca and Sr/Ca are similar to values reported previously for *G. ruber* and *T. sacculifer* (e.g. from a sediment trap study reporting values for 10 planktonic species in Anand et al., 2003; Fallet et al., 2010; Hönisch et al., 2013; Kısakürek et al., 2008; Steinhardt et al., 2014).

2.4.1 Na/Ca

Comparison to previous calibrations

The Na/Ca values of calcite of living planktonic G. ruber specimens from the Red Sea show a clear positive and significant linear correlation with salinity (Na/Ca = 0.66 * S – 15.75, r^2=0.88, p<0.001), which is insignificant for T. sacculifer (Na/Ca = 0.229 * S + 0.67, r^2=0.19, p=0.11) (Fig. 2.3). Laser ablation analyses, although also adding to the number of analyses

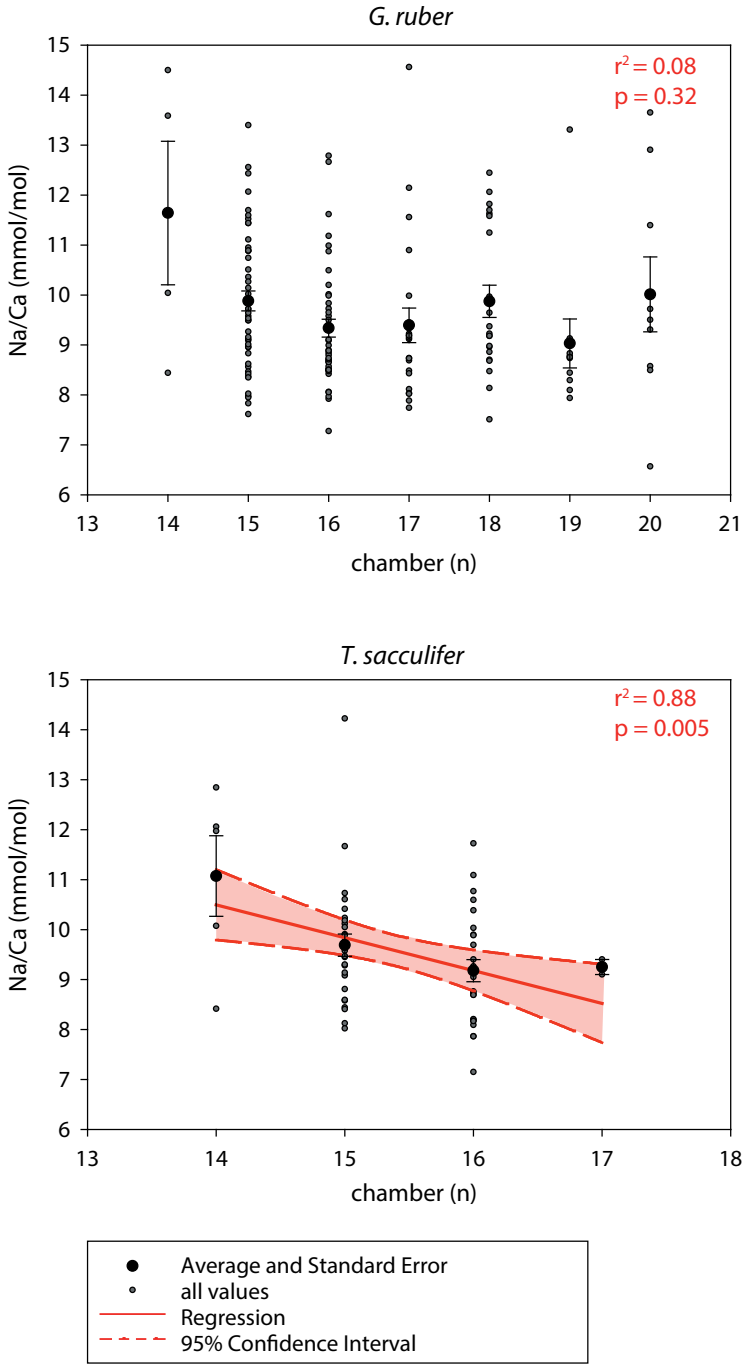

Figure 2.6. Na/Ca values for *G. ruber* and *T. sacculifer,* plotted against chamber number, with 95% confidence interval. The chamber number is calculated based on the measured shell diameter (Hemleben and Bijma, 1994; Brummer et al., 1987).

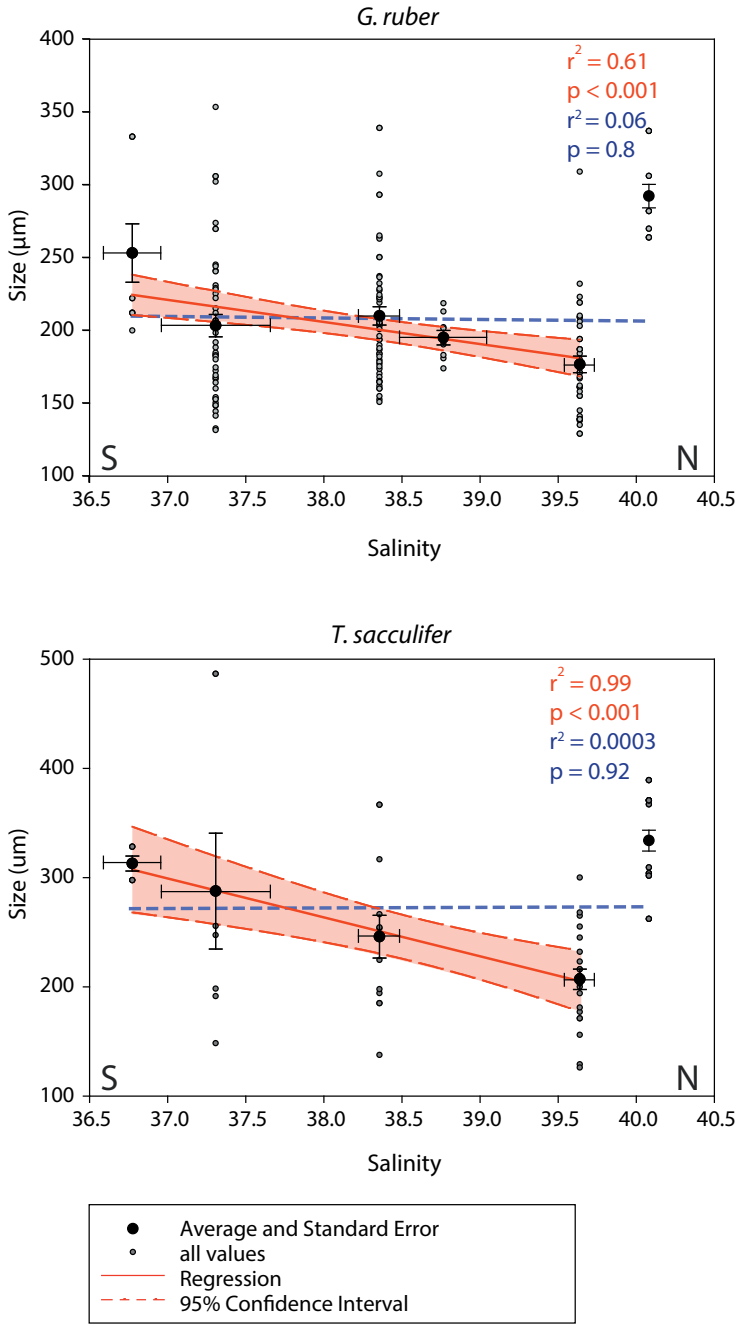

Figure 2.7. Salinity (transects) versus size for *G. ruber* and *T. sacculifer*; r2 was calculated using weighted average size values per salinity. Horizontal error bars for salinity indicate values at the start and end of each transect. The dotted (light blue) trend lines show the non-significant correlations between salinity and size, when including the northernmost transect.

needed per transect, allows identifying intra- and inter-specimen variability. In contrast to solution SF-ICP-MS, measurements can be performed on individual specimens and chambers, allowing investigating natural variability. In case Na would be ad- or absorbed to the calcite shell surface, this is also obvious from ablation profiles. In such cases, part of the profile with elevated trace or minor element/Ca ratios were discarded and therefore do not bias the analysis. However, only minor surface contamination was observed, in conjunction with Al in some specimens. Hence, Na contamination can be ruled out as a factor causing variability in Na/Ca within and between specimens and species. Due to the small shell size of these foraminifera, we were not able to perform sufficient duplicate measurements on single chambers to allow robust statistical testing of intra chamber variability. However, variability in Na/Ca values between chambers was up to 14%, which is comparable to or smaller than that observed for Mg/Ca in other studies using LA-Q-ICP-MS (e.g. Dueñas-Bohórquez et al., 2009; De Nooijer et al., 2014a). So far, there is no consensus on the cause of this small-scale variability in composition for other elements. Environmental variability cannot account for (all) element variability between single-chamber analyses. Possibly, the same process responsible for small-scale heterogeneity (i.e. banding) in Mg/Ca (e.g. Eggins et al., 2004), could also partially explain the observed scatter in Na. Since the calcite precipitated during each chamber addition also envelops the rest of the foraminiferal shell, higher Na concentrations associated with earlier stages of chamber addition could offset element/Ca ratios between chambers. In this case small changes in thickness of these bands could affect elemental ratios measured at a single spot or between chambers due to the nature of foraminifera to add chambers. However, within the ablation profiles no evidence for such banding was observed and studies specifically addressing the micro-scale distribution in a smaller scale than laser ablation of Na in a calcite foraminifer shell are necessary to understand the potential role of the observed small scale variability in element/Ca ratios.

Foraminiferal sizes do not correlate with measured Na/Ca ratios in this study. However, for *T. sacculifer* calculated chamber numbers do show a correlation with Na/Ca ratios (Fig. 2.6). The apparent correlation between Na/Ca ratios and chamber position suggests that chamber position, rather than absolute size, might influence Na incorporation. However, even though a significant negative trend is observed between chamber number and Na/Ca, many other factors co-vary as well along the Red Sea (e.g. salinity, temperature and CO_3^{2-}). Also although Wit et al. (2013) did show a correlation between size and Na/Ca for *A. tepida*, they argued that this correlation is spurious. Since final size of the cultured foraminifera changed with salinity, it was argued that this was an indirect relation, with

salinity being the main contributor to the observed trend in size versus Na/Ca. This observation may also explain the trend in Na/Ca with chamber number in our dataset. As all our specimens were collected from surface waters using a plankton pump, we can exclude such trends related to gradual changes with water depth during foraminiferal life (ontogenetic vertical migration).

Comparing the Na/Ca-salinity relationship of both planktonic species with the previously reported benthic species *Ammonia tepida* (Wit et al., 2013) shows a positive response of Na incorporation for all species with salinity (Fig. 2.8), albeit that the sensitivity reported here is higher for the planktonic than for the benthic species. For the culture study with *G. ruber* (pink) and *T. sacculifer* of Allen et al. (2016), as well as the benthic *A. tepida* (Wit et al., 2013), the correlations of this study show a slight offset towards higher absolute values and a significantly steeper slope (one-way ANCOVA, $p<0.5$) (Fig. 2.8). Also, Allen et al. (2016) found that only the relation between salinity and Na/Ca for *G. ruber* is significant although different absolute values for *G. ruber* and *T. sacculifer* were measured. Potential explanations for the observed offset between these studies include 1) the limited overlap of salinity intervals studied in these studies and with the benthic *A. tepida*, 2) different biomineralization controls or life stage, or 3) an effect of carbonate chemistry and temperature in the field-collected specimens.

First, there is only limited overlap in salinity intervals between this study (from 36.8 to 40.1 in this study and from 30.0 to 38.6 in Wit et al., 2013). This complicates comparing responses to salinity (Fig. 2.8). However, recent culture results on the same species suggest that this proxy for *G. ruber* can be extended to a salinity of 33 (Allen et al., 2016), albeit with a less steep slope.

Second, partition coefficients ($D_{Na}=(Na/Ca)_{foraminifer}/(Na/Ca)_{seawater}$ in mmol/mol) of this study ($D_{Na}=0.18\text{-}0.25*10^{-3}$) are slightly higher than for Wit et al. (2013) ($D_{Na}=0.12\text{-}0.16*10^{-3}$) and Allen et al. (2016) ($D_{Na}=0.1*10^{-3}$), but comparable to inorganic precipitation experiments ($0.07–0.20\times10^{-3}$; Kitano et al., 1975; Ishikawa and Ichikuni, 1984, Okumura and Kitano, 1986), suggesting no major impact of biology. However, although the two planktonic species here are comparable in their calibration (up to a salinity of ~39.6, Fig. 2.3), we do observe a difference with results presented by Allen et al. (2016). This difference between our field-collected *G. ruber* and *T. sacculifer* and their cultured specimens, may be caused by additional controls in the field environment (e.g. the effect of a particular combination of salinity, temperature and carbonate chemistry in the Red Sea),

which is discussed later in this section, or a difference in size/lifestage (e.g. Anand et al., 2003). At different foraminiferal developmental stages, also the partitioning of elements from seawater to calcite could change (e.g. Dueñas-Bohórquez et al., 2011). Furthermore, terminal calcification features (e.g. cortex or crust) for many planktonic species are found to have a different structure and thickness and differ in Mg and probably also other elements (e.g. Nürnberg et al., 1996, Steinhardt et al., 2015). Also, when applying a linear correlation for the combined planktonic species of this study, the extrapolated calibration intersects the Y-axis (i.e. at a foraminiferal Na/Ca of 0 mmol/mol) at a salinity of 20.7,

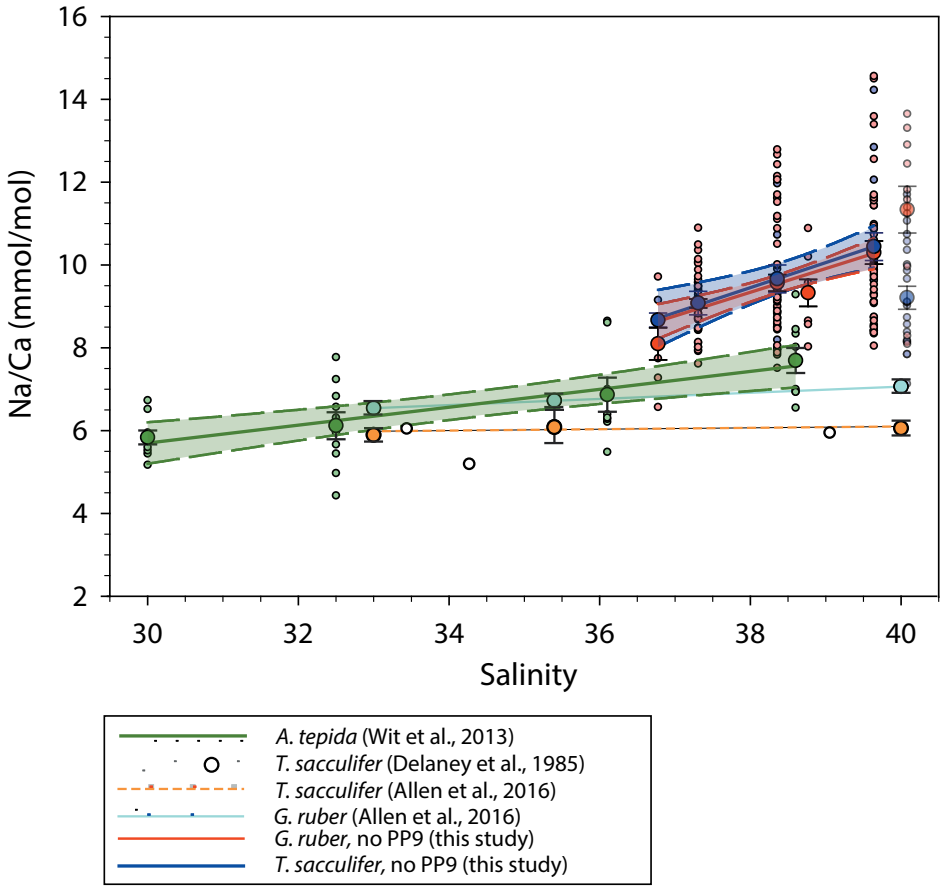

Figure 2.8. Our Na/Ca data for *T. sacculifer* and *G. ruber*, compared to the benthic species *Ammonia tepida* from culturing (Na/Ca = 0.22*S – 0.75, Wit et al., 2013), values from culture experiments for *T. sacculifer* from Delaney et al. (1985) and culture study results for *G. ruber* (pink) and *T. sacculifer* from Allen et al. (2016). Averages (large dots), standard errors, linear regressions (straight lines) and the 95% confidence interval (shaded areas) are also indicated. The error bars of Allen et al. (2016) are based on the largest % difference among three consistency standards, or the 1σ replicate of replicate measurements.

implying that Na/Ca decreases more strongly with salinity below ~36.5. Extrapolating the correlation from the benthic foraminiferal culturing study (Wit et al., 2013), results in a zero Y-axis intercept at a salinity approximating zero, suggesting that incorporation of Na as a function of salinity follows a linear trend over a large salinity range and, moreover, is consistent with inorganic precipitation experiments (Kitano et al., 1975; Ishikawa and Ichikuni, 1984). The observed offset between species and between benthic and planktonic foraminifera from this study might be caused by differences in biomineralization controls. Possibly, Na-incorporation in benthic foraminifera resembles inorganic partitioning, whereas biomineralization in planktonic species is offset by a process responsible for a slight enrichment in Na during chamber formation. However, this contradicts with the study by Allen et al. (2016) for the same planktonic species, in which the absolute values are similar to *A. tepida* (Wit et al., 2013). Also the presence of symbionts in the studied planktonic species, in contrast to the benthic *A. tepida* studied by Wit et al. (2013) might affect Na partitioning. Photosynthesis by foraminiferal symbionts influences uptake of inorganic carbonate species, thereby potentially enhancing calcification and affecting element incorporation (Rink et al., 1998; Köhler-Rink and Kühl, 2005; De Nooijer et al., 2014b). This does not, however, explain the difference between our results and those of Allen et al. (2016).

The most probable explanation for the different Na/Ca calibrations between our results and those from previous studies is that the Red Sea has many co-varying factors and an unusual environmental setting compared to those applied in culturing studies. Also several parameters from the sea water carbonate system (calcite saturation state (Ω), DIC and alkalinity) from the Red Sea differ markedly from the open ocean, since these factors increase with increasing salinities (e.g. Sarmiento and Gruber, 2006), favoring calcium carbonate shell precipitation and possibly enhance incorporation of Na and other elements as a result of enhanced growth rates. Although observed trends in Na incorporation can be fully explained using changes in Na and Ca activities (Wit et al., 2013), a (minor) role of carbonate chemistry cannot be fully excluded. Recent culture results suggest a positive trend in Na/Ca values with increasing (CO_3^{2-}) (Allen et al., 2016), which is opposite of the trend observed here. Still, the range in carbonate ion concentrations sampled here is relatively limited. Comparing the carbonate ion content in the study of Wit et al. (2013), on average 246.5 µmol/kg seawater, which is much higher than that of the Red Sea (219.5 µmol/kg seawater), would imply a stronger impact on the benthic foraminiferal values, which is not observed here. Temperature may also have an effect on Na incorporation. Recent culture results using the same two planktonic species cultured in different

temperatures, carbonate chemistry and salinities suggest that temperature has a negative effect on Na/Ca values (Allen et al., 2016). The negative trend suggested by Allen et al. (2016) between temperature and Na/Ca might have resulted in a slightly steeper slope compared to the Wit et al. (2013) data and Allen et al. (2016), but this offset is not enough to explain the overall observed difference. Moreover, the only significant correlation between environmental variables and Na/Ca in cultured planktonic foraminifera (Allen et al., 2016) was with salinity, which is in line with Wit et al. (2013).

Still, because of the many co-varying factors compared to culture experiments, it remains challenging to fully compensate for all potential additional effects in a natural environment like the Red Sea. The correlations suggested between Na/Ca values, temperature and carbonate ion content are more likely the consequence of environmentally co-varying factors (e.g. carbonate chemistry and salinity) (Fig. 2.5).

Na/Ca in G. ruber *versus* T. sacculifer

Results show a significant positive correlation between Na/Ca and salinities for *G. ruber*, but not for *T. sacculifer* (Fig. 2.3). This is similar to the results found by Allen et al. (2016), also showing that only Na/Ca in *G. ruber* has a significant positive correlation with salinity. The observed difference between these two species could be due to Na/Ca for *T. sacculifer* simply not being correlated to salinity or to a larger uncertainty in the regression in the Allen et al. (2016) study. Also clearly visible is the fact that average Na/Ca values in foraminifera from the northernmost transect for *T. sacculifer* strongly deviate from the observed overall trend and from the trend observed for *G. ruber*. This offset in the northernmost location is not only observed for Na/Ca, but also for Mg/Ca and Sr/Ca, as well as shell size for both species studied. In addition, at this transect the distribution of element concentrations also displays slightly more variability and/or clustering into two groups, especially for the Na/Ca in *G. ruber* and Sr/Ca in *T. sacculifer* (Figs. 2.3, 2.4, 2.5, 2.7, Supporting Information Figs. S2.3, S2.8). The overall difference of the last transect suggests that the foraminifera sampled are somehow not representative for the environment they were collected from. Possible explanations for these deviating values and distribution of element concentrations in the northernmost transect are: 1) post-mortem inorganic overgrowths (Hoogakker et al., 2009) and/or, 2) advection of an expatriate population/ specimens (Auras-Schudnagies et al., 1989) and/or, 3) prevalence of specimens with a different life stage in this area and/or, 4) high temporal or spatial environmental variability in this part of the Red Sea.

Inorganic overgrowths are known to affect elemental ratios measured on foraminifera from core top material (Hoogakker et al., 2009). However, since all foraminifera were collected from surface waters using plankton pumping, diagenesis can be ruled out as a potential source for the observed offset. Upon collection samples were directly washed and stored to minimize potential impacts on the foraminiferal calcite elemental composition after sample collection (see methods). Hence the reported Na/Ca, Mg/Ca and Sr/Ca represent the primary signal as precipitated by the foraminifera while still living.

Second, the difference in (monsoonal) intensity, source and distribution of surface water currents, as already found by Auras-Schudnagies et al. (1989), or exchange with another water mass might explain the distribution of species in an area. Using stable oxygen isotopes, Auras-Schudnagies et al. (1989) discovered that the species *Globorotalia menardii* survives transport from the south to the north of the Red Sea, but stops calcifying during this journey. If this were also true for *G. ruber* and *T. sacculifer*, this would also explain the larger sizes in the northernmost transect, corresponding to the larger sized foraminifera in the southernmost transect. Also the lower Na/Ca values and Mg/Ca values in the northernmost transect would respectively indicate lower salinities and colder temperatures from the southern Red Sea. The change in monsoonal strength between summer and winter does not affect salinities noticeably (world ocean atlas (WOA) 2001: Boyer et al., 2005) and maximum temperatures only become ~2°C lower at the southernmost position (Boyer et al., 2005). Therefore, the deviating values could not be fully explained by a change in monsoonal strength. Moreover, one would expect similar effects in all of the transects in between, which is not observed.

Another, and to our opinion more probable source for expatriates, involves inflow from the less saline Mediterranean, which would introduce an anti-Lessepsian population into this area. Such a population would be influenced by geochemical signals recorded in the Suez Canal (with salinities of to 45) and/or the eastern Mediterranean (S=~20.8, T=~38.9, WOA01: Boyer et al., 2005). Even though transport through the Suez Canal is found to be mostly from south to north (e.g. Por, 2012), the flow through the Bitter Lakes does change its' flow direction from July to September (Biton, 2015). This is confirmed using ocean modelling and environmental observations (e.g. Golani, 1998). The presence of two living *G. ruber* (pink) specimens in our northernmost sample also suggests inflow from north to south. This species has not been observed in the Red Sea area since 120,000 years BP (Thompson et al., 1979), but is still common in the Mediterranean. Being expatriated from the Mediterranean these foraminifera would also (partially) be affected by lower

salinities and temperatures, which is in line with the observed lower Na/Ca and Mg/Ca values (Figs. 2.3, 2.4, 2.5). Furthermore, temperatures decrease very sharply northward of the last sampled transect, compared to the rest of the Red Sea (Fig. 2.1b), potentially indicating inflow from colder Mediterranean Sea water. The overall larger shell sizes found in the northernmost transect also suggest a later moment in ontogeny compared to the specimens sampled on the other transects (Fig. 2.7), which is in line with a population largely being made up of expatriates.

Third, even though the specimens analyzed here were selected based on shell size, with the larger ones being more suitable for analyses and a size fraction <75 µm not taken into account, this does not explain the overall differences in element uptake. Although the 'larger' sized foraminiferal assemblage could explain part of the offset (Figs. 2.7 and 2.8), the observed difference is much larger. Moreover, not all elements showing contrasting elemental ratios are also correlated to shell size. Hence shell size alone cannot explain the observed offset for the northernmost transect.

Fourth, it is unlikely that all specimens collected at the northernmost transect derive from a specific event such as upwelling or a local rainfall and freshwater event, since upwelling typically occurs in the southern Red Sea and rainfall is extremely low in this area (3mm/yr) (Zahran, 2010). Still, since the population of analyzed foraminifera for each transect was collected over a distance of approximately 225 kilometers and foraminiferal densities (specimens per liter seawater) were not necessarily evenly distributed along these transects, element ratios might be biased towards specific intervals. Short lived events and or local phenomena might hence be disproportionally represented. A detailed temperature record obtained during the cruise (Fig. 2.1b) shows that at least temperature increased gradually over the transect (Fig. 2.1). Salinities within this transect vary no more than 0.02 units, which would only explain an offset of 0.01 mmol/mol in Na/Ca, based on the calibration in Fig. 2.3.

The deviating sizes, Mg/Ca, Sr/Ca and Na/Ca values of the foraminifera at the northernmost transect, in conjunction with the observation of living *G. ruber* (pink) specimens, indicating inflow from the colder, less saline Mediterranean, argues for excluding the northernmost transect from the calibrations. This results in similar, positive and significant correlations for both planktonic species, respectively Na/Ca (mmol/mol) = 0.57 * S – 12.38 (r^2=0.91, p<0.001) for *G. ruber* and Na/Ca = 0.60 * S - 13.49 (r^2=0.999, p<0.001) for *T. sacculifer*.

2.4.2 Mg/Ca and Sr/Ca

Values for Mg/Ca of *G. ruber* closely correspond to those given by Kısakürek et al. (2008) and are somewhat lower than in the sediment trap study (for ten planktonic species) by Anand et al. (2003). For the reported salinities, *G. ruber* Mg/Ca values are comparable to Hönisch et al. (2013) and Kısakürek et al. (2008). *Trilobatus sacculifer* shows somewhat lower Mg/Ca values compared to *G. ruber*, which is in line with previous observations (Anand et al., 2003; Nürnberg et al., 1996). For the measured temperatures and salinities, Mg/Ca values of *T. sacculifer* are somewhat lower than measured by Nürnberg et al. (1996), Anand et al. (2003), Hönisch et al. (2013) and Dueñas-Bohórquez et al. (2009). In our dataset, Mg/Ca values for both species are significantly positive correlated to temperature and negative to salinity. For reasons mentioned in section 4.1,2, we think that specimens collected at the northernmost transect might not be representative for the environment they were collected in. When excluding this transect from the regressions, this results in non-significant correlations between Mg/Ca and temperature as well salinity for both species. As salinity and temperature both positively affect foraminiferal Mg/Ca (e.g. Dueñas-Bohórquez et al., 2009; Anand et al., 2003; Wit et al., 2013) and are inversely correlated in the Red Sea, their influence on the specimens measured here, counteract the incorporation of Mg. Even though the relative impact of salinity on Mg/Ca is small (respectively 0.11 mmol/mol per salinity unit: Dueñas-Bohórquez et al., 2009 and references therein, 0.15 mmol/mol per salinity unit: Hönisch et al., 2013 and 0.16 mmol/mol per salinity unit: Kısakürek et al., 2008), this could explain the absence of a significant correlation between temperature and Mg/Ca in our dataset when excluding PP9. Accordingly, when applying species-specific salinity corrections for a salinity of 35 on the Mg/Ca ratios, the calibrations between temperature and Mg/Ca ratios become steeper and also (more) significant, also when including the northernmost transect (respectively r^2=0.51 and p<0.001 for *G. ruber* and r^2=0.88 and p<0.001 for *T. sacculifer* without PP9 and r^2=0.69 and p<0.001 for *G. ruber* and r^2=0.96 and p<0.001 for *T. sacculifer* with PP9) (Kısakürek et al., 2008; Hönisch et al., 2013) (Fig. 2.9). In total, Mg/Ca values after the salinity corrections decreased by 9% (south) to 31% (north) for *G. ruber* and by 8.5% (south) to 34.5% (north) for *T. sacculifer*. This implies that although Mg/Ca values in the sediment are not well connected to temperature (Hoogakker et al., 2009), surface water temperatures are well registered by foraminiferal Mg/Ca values.

Also size could have an effect on the Mg/Ca, as well as on the Sr/Ca ratio. It was found by Elderfield et al. (2002) that Mg/Ca increases with size whereas Sr/Ca decreases with size for both *G. ruber* and *T. sacculifer*. However, this would only account for a maximum

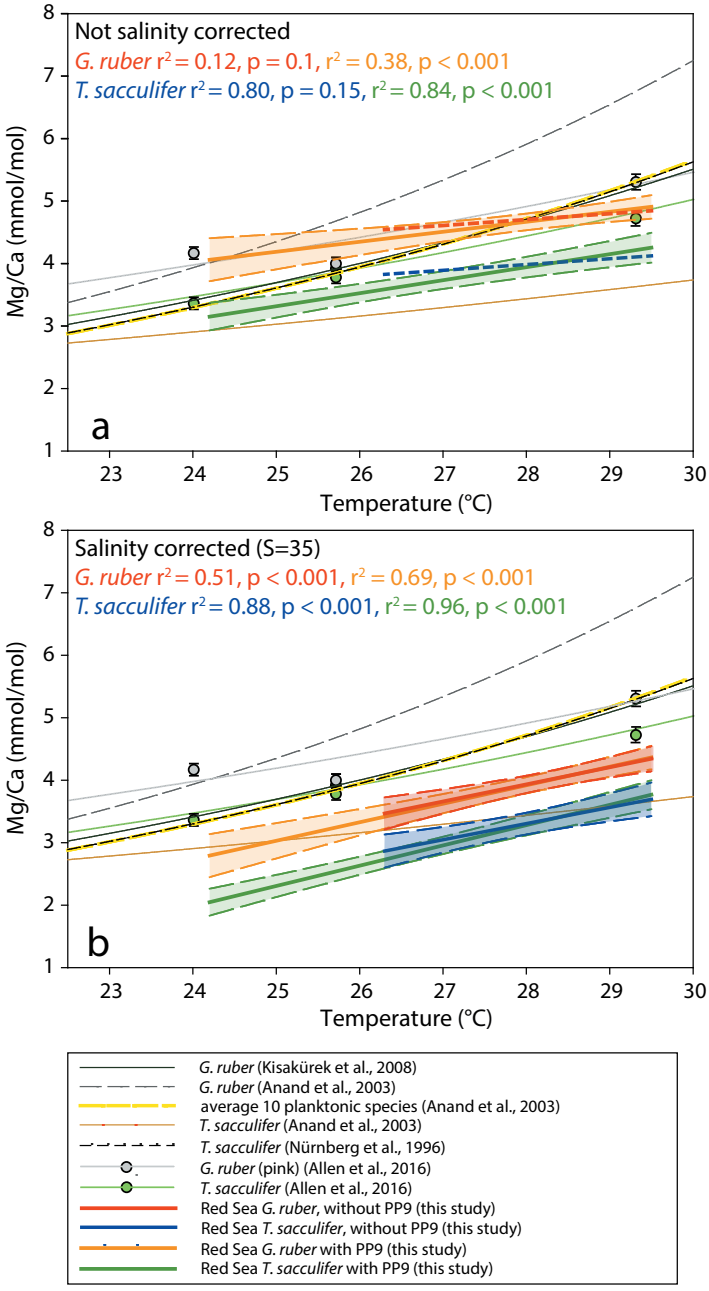

Figure 2.9. Calibrations of (a) non salinity-corrected Mg/Ca values and (b) salinity-corrected Mg/Ca for a salinity of 35, based on the calibrations of Kısakürek et al. (2008) for *G. ruber* and Hönisch et al. (2013) with their 95% confidence intervals. Horizontal error bars indicate temperatures recorded at the start and end of each transect. The vertical error bars are the standard errors of the mean, except for the Allen et al. (2016) data, where they represent the long-term relative standard deviation. Calibrations from other studies are also added (Kısakürek et al., 2008; Anand et al., 2003; Nürnberg et al., 1996; Allen et al., 2016).

Mg/Ca difference of 0.49 mmol/mol for *G. ruber* and 0.16 mmol/mol for *T. sacculifer* in the size ranges measured in this study. Since sizes decrease towards the north as well as temperatures and Mg/Ca values, one would expect the size effect to result in a steeper relation adding to the correlation with temperature, which is not the case. Hence we refrained from correcting for size here.

According to Steinke et al. (2005), morphotypes could influence the Mg/Ca composition with ~0.37 mmol/mol difference between the *G. ruber* sensu stricto (s.s.) and sensu lato (s.l.) morphotype. We were not able to distinguish between morphotypes among *G. ruber* in our samples as distinctive morphological traits are restricted to terminal (reproductive) stages typically found in sediments, whilst our samples are from a growing population of late neanic to late adult (non-reproductive) stages (Brummer et al., 1987). However, as also suggested by Steinke et al. (2005), either depth habitat or seasonality plays a role in the distribution of these subspecies. The *G. ruber* s.s. morphotype records higher temperatures (Mg/Ca and $\delta^{18}O$) than *G. ruber* s.l.. Since the sensu stricto morphotype is identified to dwell in the upper 30 m of the water column and the sensu lato morphotype at greater depths (Wang, 2000), our surface water specimens most likely mainly consists of the *G. ruber* s.s. morphotype. Therefore, it is very unlikely that different morphotypes influenced our data.

Obtained Sr/Ca values are similar or somewhat higher compared to those reported in previous studies (Lea et al., 1999; Dissard et al., 2010; Wit et al., 2013; Dueñas-Bohórquez et al., 2009; Kısakürek et al., 2008; Russel et al., 2004). However, the observed negative trend with salinity, both with and without the northernmost transect, differs remarkably from other studies, previously suggesting a (sometimes slightly) positive correlation (Dissard et al., 2010; Wit et al., 2013; Dueñas-Bohórquez et al., 2009; Lea et al., 1999; Kısakürek et al., 2008). This implies that other factors along the Red Sea from south to north must somehow override an impact of salinity on Sr incorporation. Other potential known impacts for Sr incorporation are 1) sea water carbonate chemistry, 2) temperature, salinity and size, 3) sea water Sr/Ca values, and 4) sea water Ca to carbonate ion stoichiometry.

First, carbonate chemistry (dissolved inorganic carbon (DIC), total alkalinity (TA)) is found in controlled growth experiments to affect Sr incorporation positively with higher TA or DIC values (Dissard et al., 2010; Dueñas-Bohórquez et al.; 2009). In general, with increasing salinities, DIC and seawater alkalinity also increase (Sarmiento and Gruber, 2006) and thus higher DIC, alkalinity and related carbonate ion values are found in the

north (Table 2.1). This would therefore result in increased Sr incorporation towards the north, which is opposite to the observed negative correlation.

Second, temperature has been suggested to impact foraminiferal Sr/Ca values as well (Kısakürek et al., 2008; Lea et al., 1999). The incorporation of Sr was shown to increase with increasing temperatures, with a slope for *G. ruber* of Δ(Sr/Ca)/ΔT=0.01 mmol/mol/°C (Kısakürek et al., 2008). The difference in temperature from south to north is 5.3°C, which would result in a decrease of 0.053 mmol/mol Sr/Ca (and without northernmost transect 4.2°C, resulting in a difference of 0.042 mmol/mol). The difference in temperature across the Red Sea could hence account for not more than 10% of the observed decrease in Sr values towards the northern Red Sea. Also salinity has been suggested to have a small impact on Sr/Ca ratios, with an increase of 0.008 mmol/mol Sr per °C (Dueñas-Bohórquez et al. and references therein, 2009). However, an opposite trend is observed between salinity and Sr/Ca in these samples, suggesting an overriding effect of another variable on the incorporation of Sr. The difference in salinity between south and north is 3.3, which would only account for an increase of 0.03 mmol/mol Sr/Ca from south to north. The effect of size on Sr/Ca is negligible: within the size range measured in this study, the Sr/Ca ratio could differ 0.02 mmol/mol for *G. ruber* and 0.03 mmol/mol for *T. sacculifer* (Elderfield et al., 2002).

Third, even though Sr is considered to be a conservative element in seawater (residence time 4.9 * 10^6 yr), changes in Sr/Ca values are observed in both depth profiles as well as in aging surface waters. Acantharians, abundant marine planktonic protists, incorporate Sr into their skeletons and cysts in the form of celestite ($SrSO_4$), thereby transporting Sr from the sea surface towards deeper layers of the ocean and/or seas where Sr is enriched through the subsequent remineralization/dissolution of these frustules (Bernstein et al., 1987; North, 1974, Odum, 1951; Hurd and Spencer, 1991). The Sr concentration in the Red Sea surface seawaters could thus gradually deplete in Sr as it slowly flows from Bab el Mandeb towards the north. De Deckker (2004) calculated that with a hypothetical 10 specimens per liter, up to 7.6 μg of Sr would be taken up in one generation of acantharids. For the Red Sea, assuming 2 generations per year and a residence time of Red Sea water of 36 years, this would remove up to ~547 μg per liter (Cember, 1988; De Deckker, 2004) and hence result in an ~7% offset in Sr concentrations. With a constant D_{Sr} this would result in gradually lower foraminiferal Sr/Ca values, with similar amplitude as observed. A potential temperature effect could thus be enhanced by a gradual Sr depletion towards

the north. Still, no actual proof exists for such offsets being present in Red Sea surface water and a role of acantharians therein.

Fourth, also the calcium to bicarbonate ratio is known to affect Sr incorporation (Nehrke et al., 2007). The $[Ca^{2+}]/[CO_3^{2-}]$ stoichiometry is known to affect growth rate of calcite (Nehrke et al., 2007), with highest growth rates for a $[Ca^{2+}]/[CO_3^{2-}]$ ratio close to 1. Growth rates, on the other hand, influence the partition coefficient of Sr into calcite positively. However, one would not expect this ratio to change significantly in sea water as both Ca and carbonate ion concentration are intimately tied through carbonate production. Either way, the negative correlation between salinity and foraminiferal Sr/Ca is sufficiently significant in the Red Sea to warrant further investigation.

2.4.3 Sodium as a direct proxy for salinity and future application

Even though Na/Ca values of calcite of living planktonic species from the Red Sea show a promising significant linear correlation with salinity for either both species (*T. sacculifer* and *G. ruber*) or only *G. ruber*, several issues need further research. Since the plankton pump samples are collected over intervals of approximately 225 km along which foraminiferal densities most likely varied, specimens analyzed might not have produced their shells at the average recorded salinity of that transect (Fig. 2.1). An offset from the average salinity towards the minimum or maximum salinity of a transect could account for at most a 0.62 mmol/mol offset in Na/Ca within a transect (PP2: difference minimum and maximum salinity is 1.15). Most transects cover much less change in salinity, varying from 0.02 to 0.5 between the minimum and maximum salinity, and could account for at most 0.27 mmol/mol of the observed Na/Ca ranges. Additional controlled growth experiments isolating individual parameters are necessary to reduce uncertainties in planktonic Na/Ca, and potentially reconcile observed differences between cultured and field-derived calibrations. Furthermore, for the wider applicability of this proxy, it is necessary to test whether the correlation, and offset with the earlier reported calibration, is specific to the Red Sea area. Bijma et al. (1990a) showed that *T. sacculifer* grows between salinities of 19-48 and *G. ruber* between 19-50, making an extension of the salinity range for this Na/Ca salinity proxy theoretically possible. Recent results from a culture study for the same species (Allen et al., 2016), shows that a relationship to salinity for *G. ruber* holds down to salinities of 33. Extrapolation to the natural environment would need to be verified using samples from outside the Red Sea.

The large intra- and inter-specimen variability is currently limiting the precision of Na-based salinity reconstructions. The observed variability in Na/Ca between individuals and/or foraminiferal shell chambers might be considerable, but is in line with previous studies using single spot foraminiferal shell analyses (e.g. Reichart et al., 2003; Wit et al., 2013; Dueñas-Bohórquez et al., 2009; Dissard et al., 2010; De Nooijer et al., 2014a; Sadekov et al., 2008). The uncertainty in reconstructed salinities associated with the here established Na/Ca to salinity calibration is still considerable at ~0.8 and ~1.2 for *G. ruber* and *T. sacculifer*, respectively (95% confidence intervals of calibration in central part of the calibration). This uncertainty does not affect reconstructed relative changes, which would mainly suffer from uncertainties in Na/Ca values at a specific interval. The standard errors of the averages are relatively low due to the number of specimens measured in this study. By increasing the number of specimens analyzed, the precision (not accuracy) of these reconstructions improves considerably. Based on the measured SD, the number of specimens needed for estimating past salinity better than 0.1 unit (SE=~0.05 mmol/mol), is between 14 and 37 for *G. ruber* and between 7 and 28 for *T. sacculifer* (Supporting information Fig. S2.9). Within the open ocean salinity variations are, however, small and other analytical approaches and or calibrations would be necessary. However, application of Na/Ca to areas experiencing large salinity changes, such as more marginal settings and estuaries is with the existing calibrations now within reach.

2.5 Conclusions

This study represents the first field calibration on incorporation of Na in foraminiferal calcite as a potential proxy for salinity. The Red Sea area is particularly suitable for this purpose, since it covers a broad salinity range in a steep gradient within the same water mass. Values for Na/Ca of the planktonic foraminifera *G. ruber* (white) and *T. sacculifer* collected alive from Red Sea surface waters, correlate positively and significantly with salinity. Furthermore, absolute values and slopes are similar for both species. Based on (1) the deviating Na/Ca, Mg/Ca, Sr/Ca, (2) the larger size of the specimens and (3) the occurrence of *G. ruber* (pink), it is hypothesized that specimens in the northernmost transect are likely expatriated (i.e. from the Eastern Mediterranean), and should therefore be excluded from the Na/Ca-salinity calibration. However, Na/Ca values differ significantly from previously reported values for a cultured benthic species and for the planktonic species *T. sacculifer* and *G. ruber* (pink), which may be due to differences in biomineralization controls between these groups or the additional effects of co-varying environmental variables in the Red Sea. Due to the opposing gradients in salinity and

temperature in the Red Sea, the absence of a correlation between Mg/Ca values and temperature is an indication of the dampening effect of salinity over temperature on the incorporation of Mg into planktonic foraminiferal calcite. As was already found for other elements in previous studies, intra- and inter- specimen variability in Na/Ca (as for other elements) is considerable even though the average is very accurate, which could result in relatively large uncertainties in salinity reconstructions when not measuring sufficient specimens. Future research should therefore focus on the cause(s) for the observed variability between chambers, should quantify the impact of other environmental variables on Na incorporation, include other species and investigate Na incorporation across planktonic foraminiferal life stages. Based on this study, incorporation of Na in foraminiferal calcite appears a valuable proxy for salinity, although species specific calibrations seem necessary.

Acknowledgments

All data supporting the conclusions in this manuscript can be obtained from the different tables in the manuscript and supporting information. We thank Bärbel Hönisch for the DIC and alkalinity data from the RV Pelagia cruise 64PE158 and her constructive comments. We acknowledge Katherine Allen for sharing her culture study results at an early stage. We also thank the two anonymous reviewers for their critical reading of the manuscript and comments, which substantially improved this manuscript. We are also grateful to all technical staff on board of the RV Pelagia cruise 64PE158 as well as Inge van Dijk and Rineke Gieles for help in producing the NIOZ house standard for foraminiferal calcite. This work is supported by the Gravitation grant NESSC from the Dutch Ministry of Education, Culture and Science.

Supporting information to Chapter 2

This supporting information provides additional text, tables and graphs about the settings of the solution sector field inductively coupled plasma mass spectrometry (SF-ICP-MS) measurements and the comparison of these analyses with laser ablation quadrupole inductively coupled plasma mass spectrometry (LA-Q-ICP-MS) (Text S2.2, Fig. S2.2, Tables S2.2 and S2.3). The preparation of the NIOZ in-house standard (NFHS-1) is explained in Text S2.1. Distribution plots and tables of the standards and measured foraminiferal specimens are shown in Figures S2.1, S2.3-S2.8 and Tables S2.1, S2.4 and S2.5. Figure S2.9 shows the standard errors in Na/Ca and salinity related to the number of specimens measured.

S2.1 Preparation of the NIOZ Foraminiferal in-House Standard (NFHS-1)

The NFHS-1 standard was made primarily to create a powder standard as close as possible in composition to foraminiferal carbonate (~3-12 mmol/mol). Foraminifera were collected from a calcareous ooze using a gravity core at the Walvis ridge and sieved over three sieves with a 63, 180 and 355 µm mesh size, using reversed osmosis water for the final step. After drying the samples, the 180-355 µm size fraction was cleaned according to an adjusted Barker protocol because of the weight of the material (~300 grams instead of milligrams) (Barker et al., 2003). The cleaned foraminifera were checked on eventual contamination such as coccolithophorids with a scanning electron microscopy (Hitachi, SEM3000), after which they were dried. The remaining ~100 gram of dried material was finely grained and homogenized with a Retsch Planetary Ball Mill PM 100 with cleaned zirconoxide beakers to <1µm particle size. Eventually, a tablet was pressed using a homemade pellet holder and press with a diameter of 5 mm by weighing 80 mg of standard and pressing with 1000 kg during 1 minute.

S2.2 Solution SF-ICP-MS

To verify our laser-ablation Na/Ca, Mg/Ca and Sr/Ca data, we compared laser ablation-Q-ICP-MS to solution SF-ICP-MS (Thermo Scientific, Element-2) measured on the same reference material (Tables S2.2 and S2.3, Fig. S2.2). To check the accuracy (and linearity) in the lower Na/Ca range, we prepared 5 spiked Na standards. Approximately 100 mg of JCp-1, NFHS-1 and the five Na spiked $CaCO_3$ standards were dissolved in 10 ml 1M ultrapure nitric acid (HNO_3). To obtain a matrix of 50 ppm calcium, the standards were further diluted (~100 times) with 0.1M ultrapure nitric acid (HNO_3). The instrument sensitivity and stability were optimized by changing Ar nebulizer gas, torch position

and lenses using a Finnegan tune solution and 50 ppm calcium NFHS-1 tune solution. A double spray chamber was used to obtain a stable signal. The isotopes ^{23}Na, ^{43}Ca and ^{88}Sr were analyzed in low resolution, while ^{25}Mg was analyzed in medium resolution. Elemental ratios were quantified using an intensity ratio calibration method of Villiers et al. (2002). An interlaboratory study using our SF-ICPMS data proved that our Mg/Ca and Sr/Ca data obtains high accuracy and precision (Hathorne, 2013). The same is found for Na/Ca in JCp-1 (Table S2.2). Therefore, the solution SF-ICP-MS data can be regarded as 'reference values' (Fig. S2.2, Table S2.2). Analyzing NFHS-1 gave 'reference' values of 2.9±0.07 (2% RSD, n=44), 5.3±0.06 (1% RSD, n=44) and 1.4±0.01 (0.2% RSD, n=44) for Mg/Ca, Na/Ca and Sr/Ca respectively.

The linearity (r^2 = 0.99) of the plot and the slope of 0.98 indicates that LA-Q-ICP-MS delivers accurate Na/Ca data. In the range of foraminiferal Na/Ca values (~3-12 mmol), accuracies range from 97 to 108%. For Mg/Ca and Sr/Ca measured on JCp-1, values for laser ablation are within 9% difference from the solution data for Mg and within 1% for Sr (Table S2.3). For the NFHS-1, values for laser ablation for Mg/Ca differ within 8% from solution data and Sr/Ca values differ within 1% from the solution data (Table S2.3).

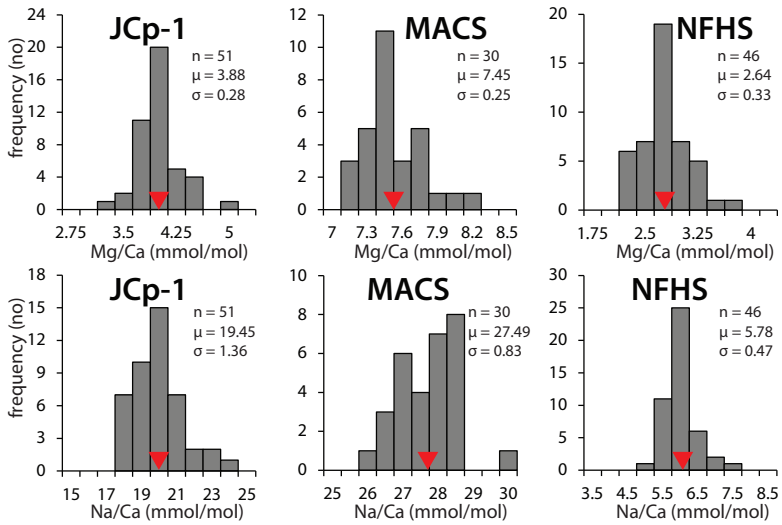

Figure S2.1. Distribution plots of Mg/Ca and Na/Ca values of the calcite standards measured, with bin sizes of 0.5. The red triangles indicate the average value (μ), n is the number of specimens analyzed and σ is the standard deviation.

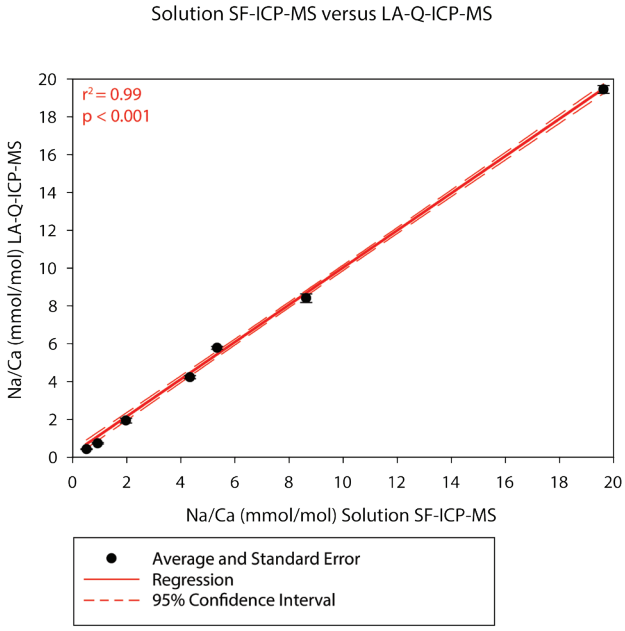

Figure S2.2. Comparison of laser-ablation-ICP-MS data and solution SF-ICP-MS for the same reference material.

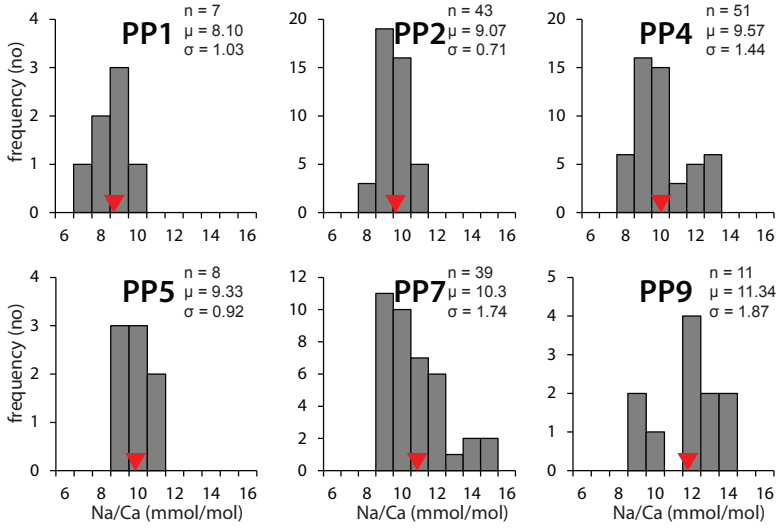

Figure S2.3. Distribution plots of *G. ruber* Na/Ca values from single spot analysis (n), bin sizes of 1 mmol/mol and averages (μ) indicated with the red triangle and standard deviations (σ).

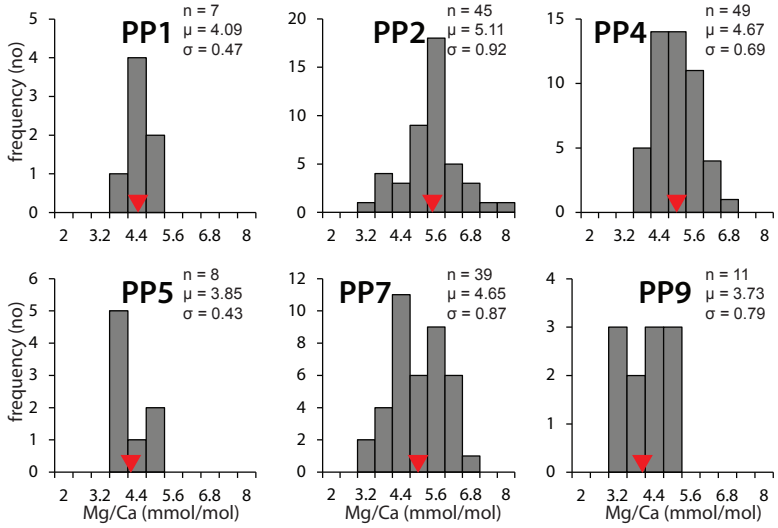

Figure S2.4. Distribution plots of *G. ruber* Mg/Ca values from single spot analysis (n), bin sizes 0.6 mmol/mol and averages (μ) indicated with the red triangle and standard deviations (σ).

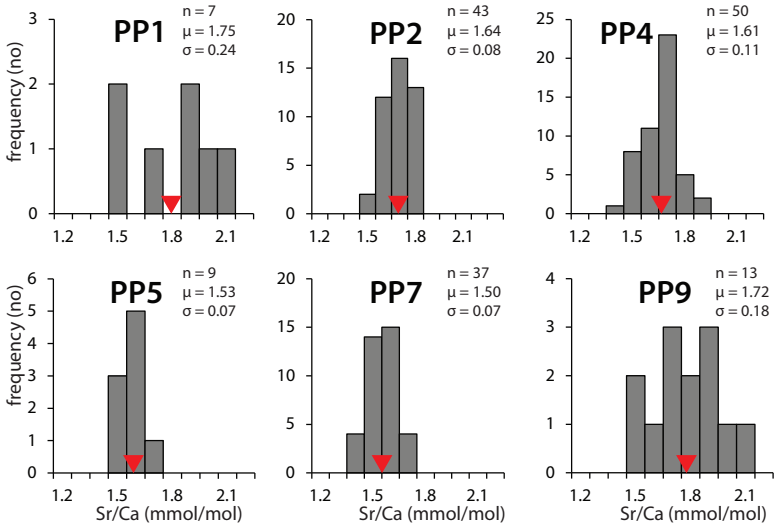

Figure S2.5. Distribution plots of *G. ruber* Sr/Ca values from single spot analysis (n), bin sizes of 0.1 mmol/mol and averages (μ) indicated with the red triangle and standard deviations (σ).

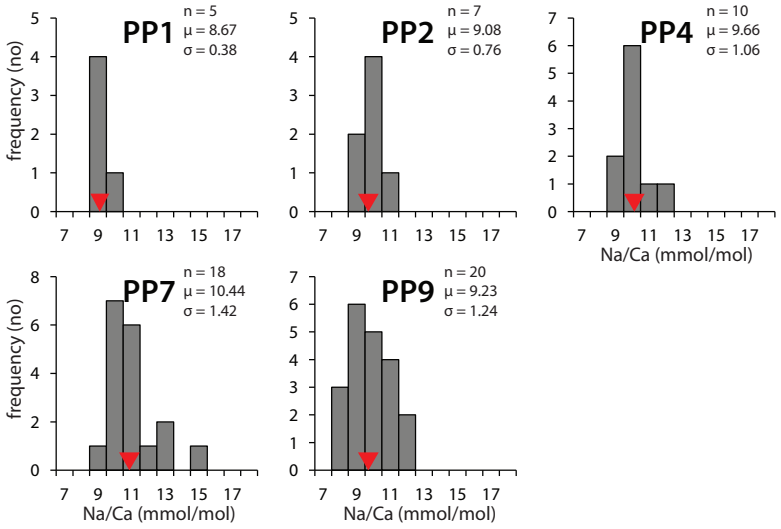

Figure S2.6. Distribution plots of *T. sacculifer* Na/Ca values from single spot analysis (n), bin sizes of 1 mmol/mol and averages (μ) indicated with the red triangle and standard deviations (σ).

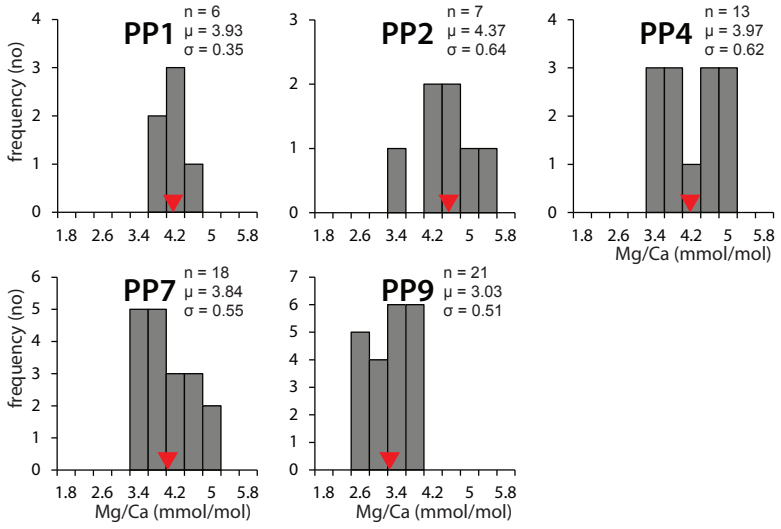

Figure S2.7. Distribution plots of *T. sacculifer* Mg/Ca values from single spot analysis (n), bin sizes of 0.4 mmol/mol and averages (μ) indicated with the red triangle and standard deviations (σ).

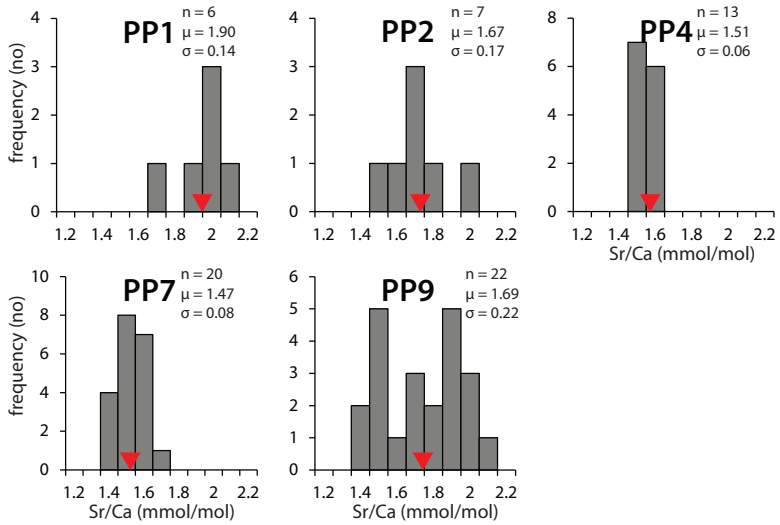

Figure S2.8. Distribution plots of *T. sacculifer* Sr/Ca values from single spot analysis (n), bin sizes of 0.1 mmol/mol and averages (μ) indicated with the red triangle and standard deviations (σ).

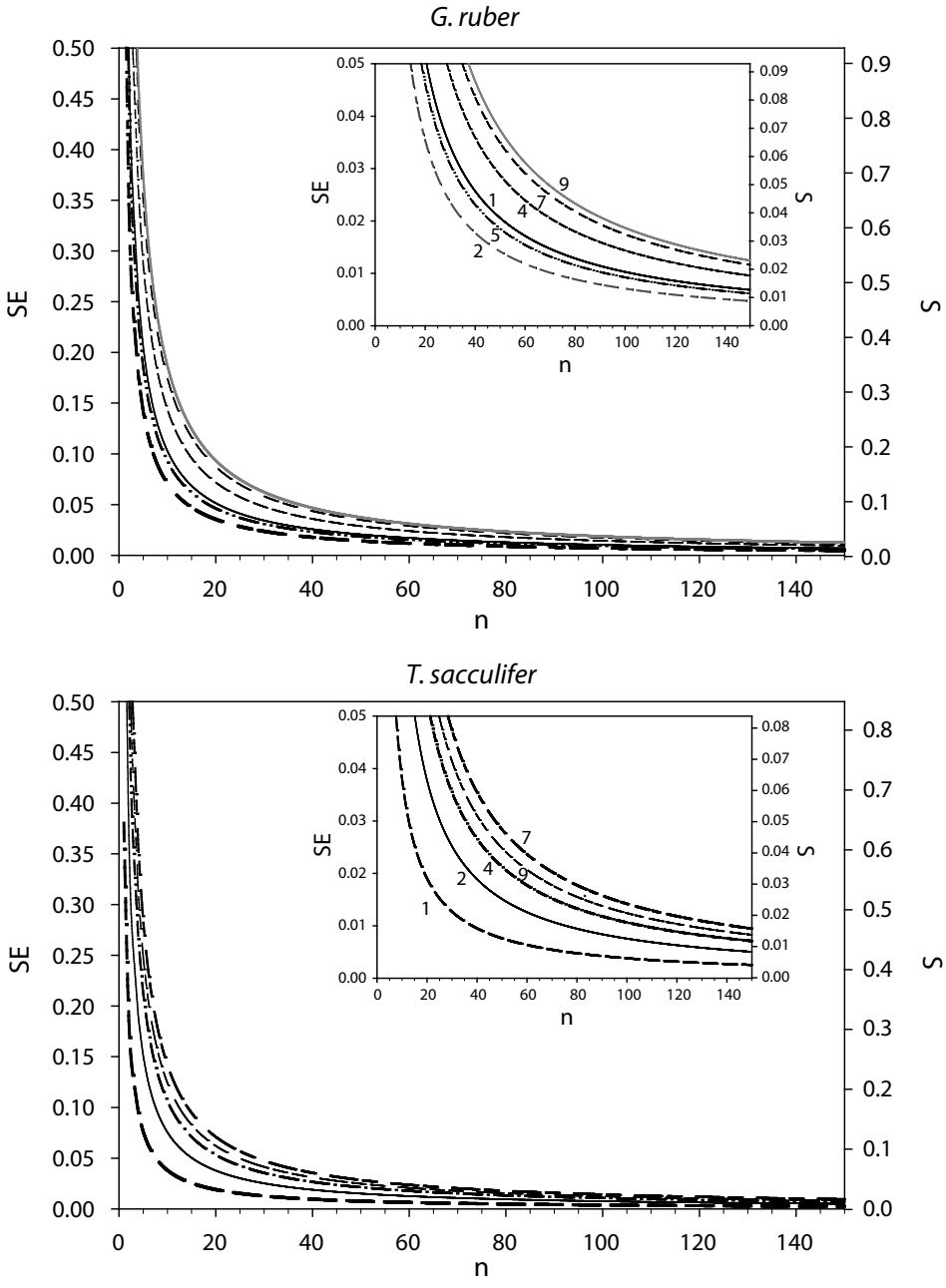

Figure S2.9. Standard errors (SE = SD/√n) in mmol/mol Na/Ca, the respective salinity accuracies (S) and the number of measurements or specimens (n) needed to achieve a certain standard error for both *G. ruber* and *T. sacculifer*. In the zoomed-in graphs, numbers of the plankton pumps are indicated, which are represented by the different lines in the graph.

Table S2.1. Shapiro-Wilk W-test for normality and p-values for the calcium carbonate reference material[a]

Standard	Element	W	p	normal?
JCp-1	Mg	0.952	0.066	yes
	Na	0.953	0.07	yes
MACS-3	Mg	0.974	0.657	yes
	Na	0.942	0.101	yes
NFHS-1	Mg	0.944	0.028	no
	Na	0.965	0.184	yes

[a]with $p<0.05$, the data differ significantly from the pattern expected for a normally distributed data series.

Table S2.2. Comparison of laser-ablation-ICP-Q-MS Na/Ca data and solution SF-ICP-MS for the same reference material

	LA-Q_ICP-MS		Solution	Reference	Accuracy	
Standard	Na/Ca (mmol/mol)	SD	Na/Ca (mmol/mol)	Na/Ca (mmol/mol)	LA/SF (%)	Ref/LA (%)
Na spiking 1	0.42	0.06	0.51	-	82%	-
Na spiking 2	0.73	0.12	0.92	-	79%	-
Na spiking 3	1.93	0.41	1.96	-	98%	-
Na spiking 4	4.23	0.27	4.34	-	97%	-
Na spiking 5	8.41	0.72	8.63	-	97%	-
NFHS-1	5.78	0.47	5.34	-	108%	-
JCp-1	19.45	1.36	19.63	20.03	99%	103%

Table S2.3. Comparison of Mg/Ca and Sr/Ca values for laser-ablation-Q-ICP-MS and solution SF-ICP-MS

Standard	Mg/Ca (mmol/mol)	Sr/Ca (mmol/mol)
NFHS-1 (LA-Q-ICP-MS)	2.64±0.33	1.45±0.06
NFHS-1 (SF-ICPMS)	2.91±0.07	1.43±0.01
Accuracy (LA/solution)	**91%**	**101%**
JCp-1 (LA-Q-ICP-MS)	3.88±0.28	8.93±0.26
JCp-1 (SF-ICPMS)	4.22±0.01	8.81±0.01
JCp-1 reference values	4.20±0.07	8.84±0.09
Accuracy (LA/solution)	**92%**	**101%**
Accuracy (solution/REF)	**103%**	**100%**

Table S2.4. Shapiro-Wilk W-test for normality and p-values for *G. ruber* collected at the different transects[a]

Transect	Element	W	p	normal?
PP1	Mg	0.928	0.538	yes
	Sr	0.911	0.403	yes
	Na	0.992	>0.99	yes
PP2	Mg	0.928	0.538	yes
	Sr	0.911	0.403	yes
	Na	0.983	0.826	yes
PP4	Mg	0.970	0.248	yes
	Sr	0.983	0.691	yes
	Na	0.895	<0.001	no
PP5	Mg	0.864	0.130	yes
	Sr	0.990	0.996	yes
	Na	0.972	0.912	yes
PP7	Mg	0.970	0.386	yes
	Sr	0.958	0.178	yes
	Na	0.913	0.005	no
PP9	Mg	0.946	0.598	yes
	Sr	0.965	0.827	yes
	Na	0.912	0.256	yes

[a]with $p<0.05$, the data differ significantly from the pattern expected for a normally distributed data series.

Table S2.5. Shapiro-Wilk W-test for normality and p values for *T. sacculifer* collected at the different transects

Transect	Element	W	p	normal?
PP1	Mg	0.948	0.725	yes
	Sr	0.838	0.126	yes
	Na	0.896	0.387	yes
PP2	Mg	0.973	0.919	yes
	Sr	0.915	0.434	yes
	Na	0.909	0.390	yes
PP4	Mg	0.956	0.687	yes
	Sr	0.922	0.269	yes
	Na	0.914	0.308	yes
PP7	Mg	0.915	0.105	yes
	Sr	0.954	0.425	yes
	Na	0.870	0.018	no
PP9	Mg	0.939	0.204	yes
	Sr	0.931	0.128	yes
	Na	0.966	0.659	yes

[a]with $p<0.05$, the data differ significantly from the pattern expected for a normally distributed data series.

3

Chapter 3

Taphonomic and ontogenetic effects on Na/Ca and Mg/Ca in spinose planktonic foraminifera from the Red Sea

Eveline M. Mezger

Lennart J. de Nooijer

Michael Siccha

Geert-Jan A. Brummer

Michal Kucera

Gert-Jan Reichart

Published in Geochemistry, Geophysics, Geosystems (2018)

Abstract

As a recorder of the hydrological cycle and ocean circulation, salinity is one of the most wanted parameters in paleoceanography. Current paleo-salinity reconstructions mostly rely on the interpretation of stable oxygen isotope signals combined with an independent paleo-temperature proxy. Due to error propagation, this indirect approach is associated with large uncertainties. Recent culture studies and a Red Sea field study have shown that incorporation of Na in foraminiferal shell calcite depends on salinity, providing a potential direct proxy for salinity. However, application of a Na/Ca-based salinity proxy requires further calibration, which should also consider settling of foraminifera through the water column and burial in the sediment. Here we compare Na/Ca in living specimens from Red Sea surface waters with specimens collected from 0-500 m water depth and sedimentary specimens from core-tops. This shows that Na/Ca in *Globigerinoides ruber* and *Trilobatus sacculifer* shells decreases with increasing water depth and until the sediment surface. For both species, laser-ablation-Q-ICP-MS measurements combined with Electron Probe microanalysis show that Na is enriched in the spines. Loss of spines during settling of foraminifera through the water column hence provides a mechanistic explanation for the observed Na decrease in bulk specimens with water depth. In contrast, average Mg/Ca values increase towards the seafloor in both species, coinciding with deposition of GAM calcite, which is enriched in Mg, but has Na/Ca values similar to that in lamellar calcite. Both spine shedding and GAM calcite addition hence affect the average minor/trace element composition of foraminiferal calcite.

3.1 Introduction

Seawater salinity drives, together with temperature, the global thermohaline circulation and therefore it is a highly desired parameter in paleoceanographic reconstructions. Changes in salinity reflect important hydrological processes including river runoff, evaporation/precipitation and sea ice formation and, on geological timescales, also the waxing and waning of continental ice sheets. Whereas many temperature proxies have been developed and are widely applied (e.g. $U^{k'}_{37,}$ Prahl and Wakeham, 1987; TEX86, Schouten et al., 2002; Mg/Ca, Elderfield and Ganssen, 2000; Lea et al., 1999; Nürnberg et al., 1996; and foraminiferal $\delta^{18}O$, e.g. Zachos et al., 2001), proxies for past salinity remain, however, rather scarce (e.g. Allen et al., 2016; Mezger et al., 2016; Rohling and Bigg, 1998; Schouten et al., 2006; Wit et al., 2013).

Paleo-salinity reconstructions mostly involve combining independent (in-)organic temperature proxies with (foraminiferal) stable oxygen isotopes (Elderfield and Ganssen, 2000; Rohling and Bigg, 1998; Schouten et al., 2006; Vasiliev et al., 2017). Such an approach assumes a strong and constant relationship between salinity and stable isotopic composition of seawater. Since it is known that this relationship differs spatially (Zahn and Mix, 1991) and most probably also on geological timescales, a more sophisticated approach is required, involving modelling of the hydrosphere and its isotopes (Rohling and Bigg, 1998). Error propagation from calibrations and model assumptions on the hydrological regime, result in relatively large uncertainties in reconstructed salinity (Rohling, 2007). These uncertainties can be circumvented by a more direct approach, i.e. a salinity proxy that directly depends on elements defining seawater salinity (e.g. Na, Cl).

Salinity is defined as the total mass in grams of all dissolved substances in one kilogram of seawater. Although salinity varies because of differences in total amounts of dissolved salts, the relative contribution of the major constituents is constant. These elements, such as chloride, potassium, sulfur and sodium display a so-called conservative behavior. Most other elements do not show a one to one relation to salinity, but vary as a consequence of many environmental parameters.

For most conservative elements, element incorporation does not vary with salinity, and a constant partitioning has been reported (De Nooijer et al., 2007; Evans et al., 2015; Hönisch et al., 2011; Lea and Boyle, 1991; Segev and Erez, 2006). However, for barnacle shells (Gordon et al., 1970), Atlantic oysters (Rucker and Valentine, 1961) and inorganic

precipitates (Ishikawa and Ichikuni, 1984; Kitano et al., 1975), a correlation has been reported between salinity of the growth medium and carbonate bound Na/Ca. This implies that although Na is a conservative element in sea water, its incorporation in calcium carbonate is not conservative. More recently, a significant positive relation between Na incorporation in foraminiferal shells and salinity was observed in culturing studies with benthic (Geerken et al., 2018; Wit et al., 2013) and planktonic foraminifera (Allen et al., 2016). A field-study with living planktonic species (*Globigerinoides ruber* and *Trilobatus sacculifer*) from surface waters (plankton pump) collected from a transect spanning the largest part of the Red Sea (Mezger et al., 2016), confirmed the impact of salinity on foraminiferal Na incorporation, although absolute Na/Ca values are higher than those found in culturing studies. For applicability of a Na/Ca-based salinity proxy and to understand this offset between studies, further calibration studies are needed. Ideally, such studies should also consider settling of foraminifera through the water column and their subsequent burial in the sediment.

To what extent primary signals are preserved in the sedimentary record is still unknown. Primary trace metal signals may be altered both during changes in habitat depth of living foraminifera in the water column (ontogenetic vertical migration) as well as during settling of the empty shells and upon burial in the sediment (taphonomic effects). These effects need to be quantified before such a potential proxy can be applied to sediment cores for paleoceanographic reconstructions. Therefore, we studied the alteration of the primary signal by comparing Na/Ca in specimens of *G. ruber* and *T. sacculifer* from surface waters with those collected by depth-stratified plankton tows to 500 m depth and from core-tops (0-1 cm) in the Red Sea. Comparing primary and potentially altered signals allows unraveling the influence of life stages as well as the export flux of post-gametogenic empty shells and early diagenesis from the impact on the shell chemical composition. Several processes, including the formation of gametogenic (GAM) calcite (Nürnberg et al., 1996; Sadekov et al., 2005), crust formation (Steinhardt et al., 2015), inorganic overgrowths in high salinity environments (Hoogakker et al., 2009), or other diagenetic processes (e.g. etching due to partial dissolution, Brown and Elderfield, 1996; or Na leakage due to ageing, Yoshimura et al., 2017) might affect the original Na/Ca-salinity relationship. These ontogenetic (Nürnberg et al., 1996; Steinhardt et al., 2015) and diagenetic (Brown and Elderfield, 1996; Hoogakker et al., 2009) processes are known to influence the Mg/Ca composition of the shell, occasionally to such a degree that these can no longer be used for reliable temperature reconstructions. Because these processes impacting Mg/Ca are related to for instance a change in calcification strategy or early diagenesis, they

could potentially also affect Na/Ca. To test this hypothesis, we perform Electron Probe microanalyses (EPMA) of individual shells to investigate potential effects of ontogeny and depositional processes on the within-shell micro-distribution of Mg and Na.

3.2 Materials and Methods

3.2.1 Study area and sample collection

For the present study, we sampled shells of planktonic foraminifera from sediments and the water column of the Red Sea to investigate the salinity dependency of foraminiferal Na/Ca along a strong natural salinity gradient. The Red Sea is characterized by a pronounced anti-estuarine circulation (Rohling, 1994, and references therein)), resulting in a strong south-north gradient in surface salinity. In contrast, annual mean temperature shows the opposite trend, with highest values in the middle to South. Red Sea and Gulf of Aden surface sediment samples were collected during three different cruises (for details see Siccha et al., 2009) from south to north (Table 3.1, Fig. 3.1).

After collection, core-top samples were washed over a 63 µm sieve, air dried and dry-sieved over a 150 µm mesh. The isolated specimens of *G. ruber* and *T. sacculifer* were cleaned according to the protocol described in (Barker et al., 2003), with the exception of the reductive step. Foraminiferal diameters were determined by measuring the distance from the top of the final chamber (F) to the bottom between the F-1 and F-2 chamber. Based on their size, specimens were divided into 4 size categories corresponding to the mesh sizes used for the plankton tows (later this section). We targeted the symbiont-bearing planktonic foraminiferal species *G. ruber* and *T. sacculifer* as these species were most abundant and commonly used as proxy signal carriers globally. Average mean annual surface water temperature and salinity were taken from the world ocean atlas (WOA09: Antonov et al., 2010; Locarnini et al., 2010).

Depth-stratified plankton tows were taken using a modified Hydro Bios Multinet in May 2000 (RV Pelagia cruise 64PE158), covering the upper 10-500 m of the water column in eight discrete depth intervals at ~23.7°N and 36.8°E (which is close to core-top sample M5/2 MC-71, Fig. 3.1, Tables 3.1, 3.2). Salinity and temperature profiles are based on the in-situ measurement by a CTD cast deployed immediately prior to the Multinets (Table 3.2, Fig. 3.2). Upon collection, samples were drained on a 75 µm mesh sieve, shortly washed with ultrapure water to remove the salts, frozen and stored at -40 °C. Sample processing was performed at the Royal Netherlands Institute for Sea Research (Royal NIOZ), located

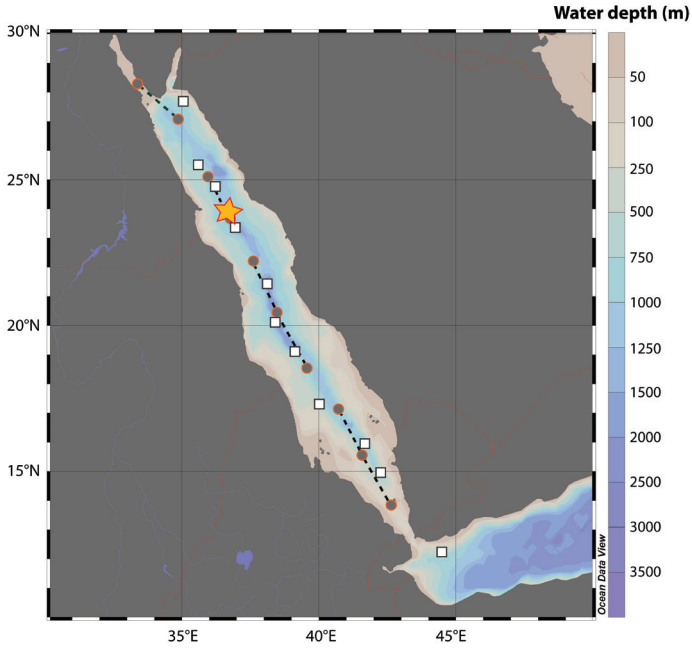

Figure 3.1. Map of sampling locations in the Red Sea. The star represents the location of plankton tows, the squares represent the core-top locations and the surface water sample transects (published in Mezger et al., 2016) are indicated with the dots (start and end of transect) and dashed lines (transect).

Table 3.1 Overview cruises and location of the Red Sea core-top samples [a]

Cruise	Name	type	Lat [°N]	Long [°E]	depth [m]	SSS	SST [°C]
M 44/3	MC-601	MC	27.71	35.05	863	40.3	25.3
M 31/2	MC363	MC	25.52	35.61	941	40.0	25.8
M 31/2	MC364	MC	24.76	36.23	1185	39.8	26.7
M 5/2	MC-71	MC	23.39	36.98	1387	39.6	26.8
VA 29	707KG	BC	21.43	38.10	1985	39.1	28.0
M 5/2	MC-101	MC	20.11	38.42	2309	38.7	28.7
M 5/2	MC-107	MC	19.13	39.12	1161	38.3	29.1
M 31/2	MC366	MC	17.36	40.02	475	38.0	29.3
SO 121	SO-98	MC	15.94	41.68	959	37.3	29.0
SO 121	SO-100	MC	15.00	42.21	826	37.1	28.7
SO 121	SO-110	MC	12.25	44.47	740	36.3	28.0

[a] sea surface salinities (SSS) and sea surface temperatures (SST) are retrieved from the WOA09_annual average. The grey bar coincides with the plankton tow location. MC: multicore, BC: box core

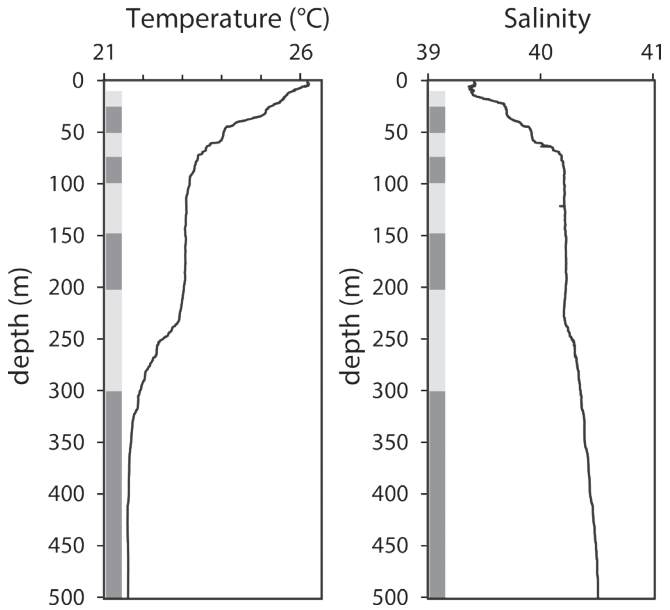

Figure 3.2. In situ depth profiles of the water column at the site where the plankton tow samples were collected. Depth intervals of the plankton tows are indicated at the left side of the graphs.

Table 3.2 Position, depth, salinity and temperature during plankton tows, derived from CTD profiles (RV Pelagia cruise 64PE158).

Net	Lat [°N]	Long [°E]	depth range [m]	average Salinity	average Temperature [^{0}C]
05c-net4	23.70	36.78	10-25	39.5	25.6
05c-net3	23.70	36.78	25-50	39.8	24.7
05c-net2	23.70	36.78	50-75	40.0	23.7
05c-net1	23.70	36.78	75-100	40.2	23.3
05a-net4	23.64	36.82	100-150	40.2	23.1
05a-net3	23.64	36.82	150-200	40.2	23.1
05a-net2	23.64	36.82	200-300	40.3	22.5
05a-net1	23.64	36.82	300-500	40.4	21.7

on the island of Texel, the Netherlands. Samples were freeze dried and a Low-Temperature-Asher (LTA) was used to remove organic matter and thereby concentrate foraminiferal specimens (Fallet et al., 2009). A few drops of ethanol and ultrapure water were added to disperse the ashed residue, wet-sieved over a 63 µm mesh and dried at 50 °C. According to Fallet et al. (2009), both methods (Barker protocol, Barker et al., 2003, and LTA) remove all organic material from foraminiferal shells and yield the same stable oxygen and carbon isotope and Mg/Ca values. To divide foraminiferal shells into several size categories, different mesh sizes were used for dry sieving (150 µm, 250 µm, 355 µm and 500 µm, respectively). Identification of species was performed using the ontogenetic species concept of Brummer et al. (1987) for *Globigerinoides sacculifer* (Brady), later assigned to as *Trilobus sacculifer* (Spezzaferri et al., 2015), and *Globigerinoides ruber* (d'Orbigny). Surface water (plankton pump) samples collected during the same cruise at the same location (respectively plankton pump 7) were described and analyzed in Mezger et al. (2016).

3.2.2 LA-Q-ICP-MS analyses

For the core-top samples, a total of 286 specimens with 37-11 specimens per location for *G. ruber* and 288 specimens with between 45-7 specimens per location for *T. sacculifer* were analyzed. For each plankton tow sample, at least 30 specimens were selected when available, measured and grouped into one of four size classes to allow for testing the relation between size/life stage and element composition of the shells. In total, 238 specimens were measured for *G. ruber* and 133 specimens for *T. sacculifer*. Multiple measurements per specimens for subsequent chamber stages and duplicates on the same chamber were often performed and outliers removed by -2SD and +2SD.

After the cleaning, foraminifera were mounted on a stub with double-sided sticky tape with a non-detectable amount of the measured elements, ensuring that the tape does not affect the measurements. Laser ablation quadrupole inductively coupled plasma mass spectrometry (LA-Q-ICP-MS) was used to measure the elemental composition of the shells at the Royal NIOZ. The set-up consisted of a NWR193UC (New Wave Research) laser, containing an ArF Excimer laser (ExciStar) with deep UV 193 nm wavelength and <4 ns pulse duration, coupled to a quadrupole ICP-MS (iCAP-Q, Thermo Fisher Scientific). Due to different ablation thresholds, laser ablation for calcite was performed with a fluence of 1 J/cm^2 at a repetition rate of 6 Hz, while the glass NIST-610 and NIST-612 standards were ablated with a fluence of 5 J/m^2. This difference in fluence was found previously not to influence results for Mg and Sr (Dueñas-Bohórquez et al., 2011; Hathorne et al., 2008). Specimens were ablated between 40 to 60 seconds, depending on the thickness of the wall

and size of the chamber. Using a dual-volume cell, helium was used as a carrier gas with a flow rate of 0.5 L/min, which is mixed between the ablation cell and mass spectrometer with Argon (Ar) make-up gas and 0.003 mL/min N_2. The Ar make-up gas was adjusted using the normalized Ar index (NAI) (Fietzke and Frische, 2016). Torch position, collision cell technology (CCT) focus and extraction lens were optimized daily. The ThO/Th ratio, a measure for oxide formation, was always <0.5%. The masses monitored by the ICP-MS were ^{7}Li, ^{11}B, ^{23}Na, ^{24}Mg, ^{25}Mg, ^{27}Al, ^{43}Ca, ^{44}Ca, ^{57}Fe, ^{88}Sr, ^{138}Ba, ^{238}U, with a duration of 0.12 seconds for one cycle through these 12 masses. In between the laser and ICP-MS, a smoother is used optimizing the signal. Every run started and ended with a 20 s gas blank. A spot size of 80 µm was used to ablate the shells. Elemental ratios of the shells and standards were calibrated and calculated following the method described in Van Dijk et al. (2017). The calcium carbonate standard MACS-3 (Wilson et al., 2008) was used for a linear correction for potential drift during each run and therefore ablated after every 10 samples. Relative analytical precision (in RSD) of all MACS-3 measurements is 3.9% for ^{23}Na, 3.3% for ^{24}Mg and 3.1% for ^{25}Mg, with accuracies of 100.2% for Na/Ca (based on ^{23}Na) and 100.1% for Mg/Ca (averaged ^{24}Mg and ^{25}Mg) compared to the reference values. Results from our in-house foraminiferal standard (NFHS-1, Mezger et al., 2016) indicated a relative analytical precision of 5.8% for ^{23}Na, 11.3% for ^{24}Mg and 11.6% for ^{25}Mg, with accuracies of 96.7% for Na/Ca and 90.3% for Mg/Ca. At the start and end of each measurement series, the glass NIST-610 and NIST-612 standards were measured and compared to elemental values reported earlier (Jochum et al., 2011). For NIST-610, a relative precision of 4.4% for ^{23}Na, 4.6% for ^{24}Mg and 3.9% for ^{25}Mg was observed, with accuracies of 106.7% for Na/Ca and 110% for Mg/Ca compared to reference values. For NIST-612, a precision of 3.5% for ^{23}Na, 2.9% for ^{24}Mg and 3.2% for ^{25}Mg was observed, with accuracies of 107.8% for Na/Ca and 94% for Mg/Ca compared to reference values.

For LA-Q-ICP-MS of the foraminiferal spines, settings used were similar to the shell carbonate analyses, but with a rectangular (40 x 80 µm) shaped 'spot' and a delay of only 1 second after switching on the laser. In total, 31 measurements on foraminiferal spines of both *G. ruber* and *T. sacculifer* were performed, focusing on clusters of spines outside of different shells (example measured specimens: Fig. 3.3). Aliasing was avoided by using very short cycle times, with every cycle, measuring ^{23}Na, ^{24}Mg and ^{43}Ca, costing only 0.03s, whereas the laser ablated every 0.17s (6Hz).

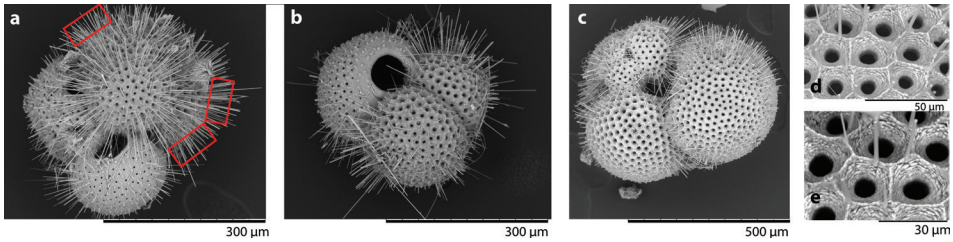

Figure 3.3. SEM pictures of foraminifera from plankton tow 05c-net4, with a) and b) *G. ruber* with spines and examples of LA-spots, and c) *T. sacculifer* with spines (and zoomed-in, d and e).

For some ablations Mg was excluded from the analytical matrix (in which case a cycle lasted only 0.02s), as we used the first series of analyses to test our set-up for Na/Ca only. Due to the low quantity of calcium carbonate when ablating spines, laser ablation profiles were relatively short. Using only the data with at least a modest Ca signal, data acquisition lasted between 2 and 16 seconds for the individual analyses (Table 3.5, 3.6). Such short profiles are generally disregarded (e.g. Mezger et al., 2016), however, for our purposes and due to the very short cycle times used, still suitable. During spine measurements, for MACS-3, a relative precision of 8.88% is observed for Na/Ca based on ^{23}Na and 6.76% for ^{24}Mg, with accuracies of 100.6% and 99.97% compared to reference values.

3.2.3 Electron Probe Micro Analyses (EPMA) and Scanning Electron Microscopy

Surface structures of the laser-ablated foraminifera were studied using scanning electron microscopy (SEM3000, Hitachi). For this, magnifications between 150 and 2.5*10^3 were used.

Directly upon low-temperature ashing, multi-net specimens (RV Pelagia cruise 64PE158) were isolated for spine analysis and transferred without sieving to preserve the spines. After addition of ethanol and a few drops of ultrapure water, to disaggregate the sample, a saturated $CaCO_3$ solution was added to avoid any dissolution of spines. *G. ruber* and *T. sacculifer* specimens were transferred with a glass pipette into a clean Petri dish, in which they were rinsed with ultrapure water three times. Multiple specimens with abundant spines (which were most specimens isolated this way) were embedded in resin (Araldite 20/20) in a vacuum chamber to avoid air bubbles being trapped in the samples. After 48 hours in an oven at approximately 50 °C, the resin was fully hardened and specimens were polished and carbon coated.

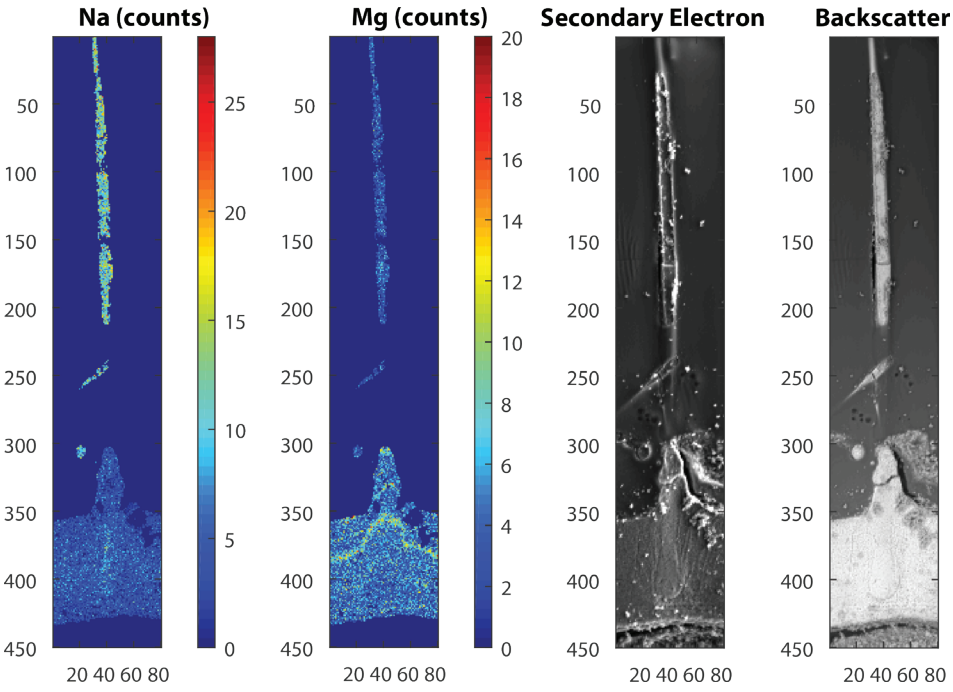

Figure 3.4. Example of the identification of a (in this case) *T. sacculifer* spine still attached to the shell by secondary electron and backscatter electron imaging, with its corresponding electron probe micro analysis Na (counts) and Mg (counts) map. The number of pixels (1pixel: 0.2 µm) is indicated at the left side and bottom of the images.

Whole shell and spine element mapping for Na, Mg and Ca was performed with an electron microprobe at Utrecht University (JEOL JXA-8530F Field emission Electron Probe Micro Analyzer). Maps were generated with a focused electron beam with a beam current of 10nA and an accelerating voltage of 7kV. The dwell time was set at 300 ms and a step/pixel size of 0.2 µm (Fig. 3.4). Counts, representing current strength, were converted to elemental ratios using analyses on standard material. We used Jadeite for Na, foraminiferal calcite for Ca and Forsterite for Mg, assuming a linear dependency of concentration (in mass %) on the signal and a constant background. Background intensities, measured for the same (foraminiferal) samples with similar settings as the measurements, were first subtracted from the total element intensities before converting to mass %. Pixel-based quantifications were eliminated from further analyses when the Ca mass percentage was below 30%. Identification of spines and spine related structures was based on backscatter and secondary electron imaging (Fig. 3.4).

3.3 Results

3.3.1 Depth-stratified plankton tows

Na/Ca

For *G. ruber*, average Na/Ca values from the plankton tows (per depth interval) vary between 10.30±0.24 and 6.93±0.05 mmol/mol, and for *T. sacculifer* between 9.28±0.11 and 6.69±0.11 mmol/mol (Table 3.3; Fig. 3.5). Very few specimens of *T. sacculifer* were found at depths between 200 to 500 m, thereby limiting observations of Na/Ca change at larger depth. Still, for both species a significant negative trend is observed between Na/Ca and depth (m) (Na/Ca=-0.027*depth (m) + 9.14, r^2=0.53 and p<0.001 for *G. ruber*, and Na/Ca=-0.032*depth (m) + 9.93, r^2=0.77 and p<0.001 for *T. sacculifer*) in the upper 100 m of the water column, when combined with surface water plankton samples (Mezger et al., 2016) (Fig. 3.5). This trend reverses below 100 meters, as Na/Ca in both species increases slightly from 100 to 200 m depth (Fig. 3.5). In general, lower Na/Ca values are observed for larger sized foraminiferal shells of *T. sacculifer* (Fig. S3.1, Table S3.2-3.3). For *G. ruber* no clear trend is observed with shell size within the water column, albeit that Na/Ca values of size class 2 (250-355 μm) lower than or similar to size class 1 (150-250 μm) (Fig. S3.1). For further details on shell size and relative distributions, see Supporting information 3.1.1.

Mg/Ca

Average Mg/Ca values per depth interval for *G. ruber* vary between 4.65±0.16 and 6.85±0.12 mmol/mol, and for *T. sacculifer* between 3.92±0.10 and 6.62±0.32 mmol/mol (Table 3.3, Fig. 3.5), with almost consistently higher Mg/Ca for *G. ruber* compared to *T. sacculifer*. From 0-150 meter depth (including surface water specimens), Mg/Ca values for both species increase significantly with water depth (*G. ruber*: y=0.013x + 5.5, r^2=0.50, p<0.001, *T. sacculifer*: y=0.016x + 3.94, r^2=0.64, p<0.001). In the upper 150 meter, average Mg/Ca values decrease again and subsequently remain similar with increasing water depth. No clear trend of Mg/Ca with size is observed for *G. ruber* nor *T. sacculifer* from the plankton tows, even though in some depth intervals differences between size classes are observed (Fig. S3.2, Tables S3.4-3.5).

3.3.2 Core-tops

Na/Ca

The final chamber (F), F-1 and F-2 were measured where possible, depending on size and preservation, while avoiding the sac-chamber for *T. sacculifer*. Average Na/Ca values per core-top location vary from 6.34 (±0.07) mmol/mol to 8.00 (±0.22) mmol/mol for *G. ruber*

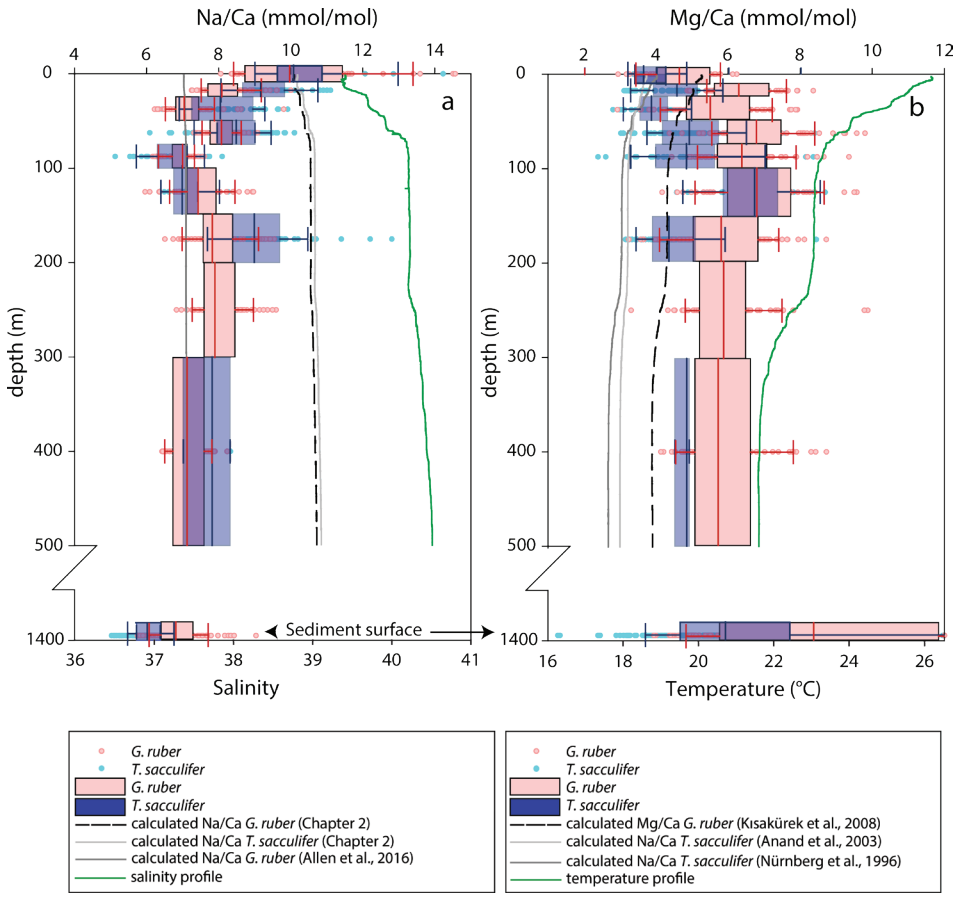

Figure 3.5. Plankton tows Na/Ca (a) and Mg/Ca (b) Box-Whisker plots, indicating median, 1st and 3rd quartile and maxima and minima. Dots that fall outside this plot indicate individual single-chamber Na/Ca and Mg/Ca. For clarity, the highest Mg/Ca values of the sediment surface fall partly outside the plotted range (Table 3.4; Figure 3.6). For comparison, examples of expected Na/Ca and Mg/Ca values are also indicated, based on salinity and temperature depth profiles and existing Na/Ca-salinity calibrations (Allen et al., 2016; Mezger et al., 2016: Chapter 2), Mg/Ca-temperature calibrations (Anand et al., 2003; Nürnberg et al., 1996) and a Mg/Ca-temperature and salinity calibration (Kısakürek et al., 2008).

and between 5.36 (±0.04) and 6.76 (±0.07) for *T. sacculifer* (Table 3.4). For *G. ruber*, relative standard deviations are between 5 and 9.9% per location, whereas the RSE's are much smaller (between 0.8 and 1.3%) because of the relatively large number of measurements performed (Table 3.4). For *T. sacculifer*, relative standard deviations are between 7 and 13.2% percent per location, whereas the RSE's are between 0.5 and 2.1% (Table 3.4).

With salinity (WOA09:Antonov et al., 2010; Locarnini et al., 2010), *T. sacculifer* Na/Ca shows a significant correlation ($y = 0.14x + 0.41$, $R^2 = 0.15$, $p<0.0001$), whereas for *G. ruber*, salinity and Na/Ca are not correlated ($y = 0.005x + 6.52$, $R^2 = 0.0004$, $p=0.8$) (Fig. 3.6). Shell size does not have a significant effect on the Na/Ca ratio with depth for either species (for further details: Supporting information 3.2.1).

Table 3.3 Overview of sampling depth and elemental ratios (*mmol/mol) of specimens from Red Sea plankton tows, with n=number of specimens, nm=number of measurements performed, including duplicates of specimens excluding outliers (a)

Net	depth range [m]	Species	n	Na/Ca *				Mg/Ca *				avg S	avg T
				nm	avg.	SD	SE	nm	avg.	SD	SE		
05c-net4	10-25	*G. ruber*	*30*	52	**10.3**	1.74	0.24	54	**4.65**	0.87	0.12	39.5	25.6
		T. sacculifer	*30*	61	**9.28**	0.86	0.11	62	**4.58**	0.90	0.11		
05c-net3	25-50	*G. ruber*	*34*	65	**8.22**	0.63	0.08	65	**6.38**	0.89	0.11	39.8	24.7
		T. sacculifer	*30*	40	**8.06**	0.93	0.15	40	**3.92**	0.62	0.10		
05c-net2	50-75	*G. ruber*	*34*	62	**7.16**	0.61	0.08	65	**5.68**	1.19	0.15	40.0	23.7
		T. sacculifer	*30*	82	**8.44**	0.82	0.09	86	**5.00**	1.11	0.12		
05c-net1	75-100	*G. ruber*	*30*	54	**8.08**	0.42	0.06	56	**6.85**	1.17	0.16	40.2	23.3
		T. sacculifer	*20*	33	**6.69**	0.66	0.11	33	**4.95**	1.41	0.24		
05a-net4	100-150	*G. ruber*	*25*	46	**6.93**	0.35	0.05	46	**6.43**	1.02	0.15	40.2	23.1
		T. sacculifer	*4*	13	**7.11**	0.52	0.14	14	**6.62**	1.18	0.32		
05a-net3	150-200	*G. ruber*	*30*	78	**7.48**	0.68	0.08	76	**6.85**	1.34	0.15	40.2	23.1
		T. sacculifer	*16*	62	**9.12**	1.10	0.14	62	**4.54**	1.00	0.13		
05a-net2	200-300	*G. ruber*	*25*	62	**7.94**	0.71	0.09	62	**5.86**	1.19	0.15	40.3	22.5
		T. sacculifer	*1*	-	-	-	-	-	-	-	-		
05a-net1	300-500	*G. ruber*	*30*	48	**7.17**	0.49	0.07	49	**5.92**	1.17	0.17	40.4	21.7
		T. sacculifer	*2*	3	**7.46**	0.74	0.43	3	**4.74**	0.22	0.12		

a) salinity (S) and temperatures (T) are derived from CTD profiles during RV Pelagia cruise 64PE158, n:n° specimens

Table 3.4 Overview measured elemental ratios (*mmol/mol) Red Sea core-top samples, with n=number of specimens, nm=number of measurements performed, including duplicates of specimens excluding outliers (a)

Cruise	Name	W		Na/Ca *				Mg/Ca *					
			n	nm	avg.	SD	SE	nm	avg.	SD	SE	SSS	SST[°C]
M 44/3	MC-601	*G. ruber*	31	58	**6.64**	0.45	0.06	59	**7.70**	2.16	0.28	40.3	25.3
		T. sacculifer	37	64	**5.86**	0.65	0.08	63	**6.47**	2.71	0.34		
M 31/2	MC363	*G. ruber*	11	12	**8.02**	0.75	0.22	12	**9.77**	3.15	0.91	40.0	25.8
		T. sacculifer	38	69	**6.76**	0.60	0.07	68	**7.47**	3.39	0.41		
M 31/2	MC364	*G. ruber*	30	62	**6.39**	0.39	0.05	63	**9.35**	3.22	0.41	39.8	26.7
		T. sacculifer	30	62	**5.72**	0.76	0.10	60	**6.86**	3.29	0.42		
M 5/2	MC-71	*G. ruber*	22	76	**6.89**	0.68	0.08	76	**9.29**	4.17	0.48	39.6	26.8
		T. sacculifer	36	242	**6.08**	0.49	0.03	242	**7.44**	4.67	0.30		
VA 29	707KG	*G. ruber*	30	59	**6.37**	0.42	0.05	57	**6.09**	1.32	0.17	39.1	28.0
		T. sacculifer	28	154	**5.79**	0.41	0.03	156	**5.31**	1.40	0.11		
M 5/2	MC-101	*G. ruber*	37	55	**6.93**	0.53	0.07	53	**8.25**	2.39	0.33	38.7	28.7
		T. sacculifer	45	93	**6.05**	0.55	0.06	93	**5.66**	2.19	0.23		
M 5/2	MC-107	*G. ruber*	30	28	**6.86**	0.48	0.09	30	**8.02**	2.18	0.40	38.3	29.1
		T. sacculifer	16	41	**6.02**	0.43	0.07	41	**6.09**	2.22	0.35		
M 31/2	MC366	*G. ruber*	30	53	**6.63**	0.50	0.07	54	**7.15**	1.92	0.26	38.0	29.3
		T. sacculifer	32	113	**5.36**	0.46	0.04	111	**4.79**	1.37	0.13		
SO 121	SO-98	*G. ruber*	20	43	**7.02**	0.35	0.05	43	**7.72**	1.65	0.25	37.3	29.0
		T. sacculifer	12	42	**6.17**	0.67	0.10	42	**5.37**	2.25	0.35		
SO 121	SO-100	*G. ruber*	17	39	**7.01**	0.34	0.05	40	**6.67**	1.66	0.26	37.1	28.7
		T. sacculifer	7	22	**5.98**	0.59	0.13	22	**6.67**	1.79	0.38		
SO 121	SO-110	*G. ruber*	28	47	**6.34**	0.49	0.07	46	**5.01**	1.17	0.17	36.3	28.0
		T. sacculifer	7	14	**5.82**	0.63	0.17	12	**4.10**	0.98	0.28		

a) sea surface salinities (SSS) and sea surface temperatures (SST) are retrieved from the WOA09_annual average

Mg/Ca

For *G. ruber* and *T. sacculifer* (Fig. 3.6), Mg/Ca changes significantly with SST from north to south along the investigated transect ($p<0.001$ for both species, $y=-0.41x+19.03$ and $r^2=0.16$ for *G. ruber*, $y=-0.62x+23.46$, $r^2=0.58$ for weighted averaged *T. sacculifer*). Highest values are observed in the northern part of the transect, which is characterized by the lowest temperatures and highest salinities. A slight significant positive correlation between shell size and Mg/Ca is observed for *T. sacculifer,* albeit that r^2 is very low (Supporting information: $y=5.6x+636.9$, $r^2=0.013$, $p=0.001$). This is in line with the high variability observed in the data (Fig. S3.4, Supporting information 3.2.2). For *T. sacculifer*, highest Mg/Ca values are found in specimens larger than 500 µm in size, a size class that was not observed in the water column plankton samples.

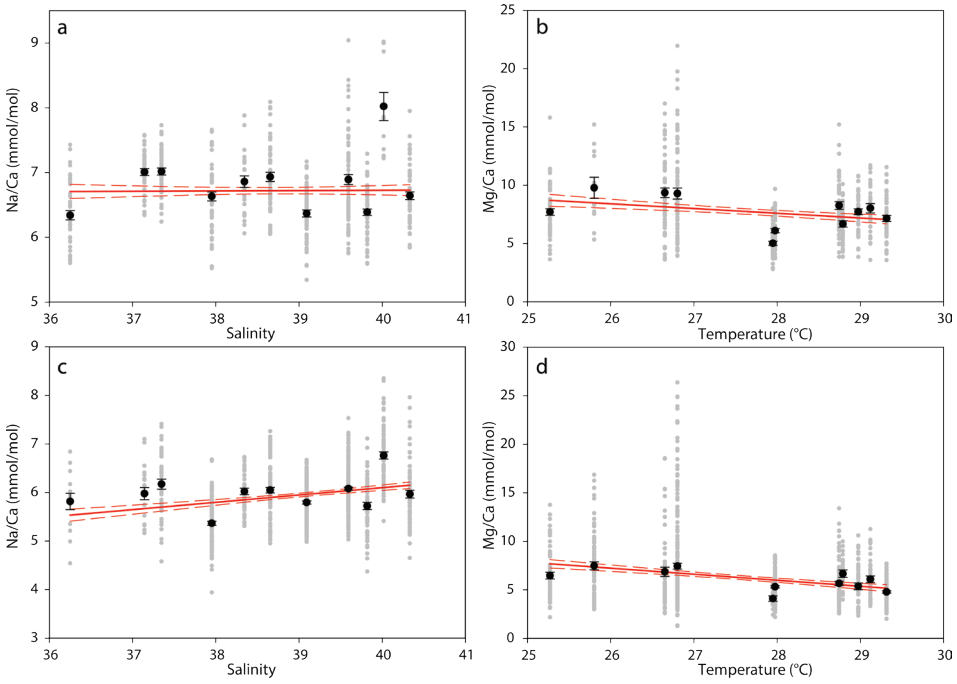

Figure 3.6. Core-top Na/Ca (a,c) and Mg/Ca (b,d) values, plotted against SSS (Na, WOA09) and latitude (Mg, WOA09) with: a) *G. ruber* Na/Ca, averages and SE are indicated, as well as the linear regression and 95% confidence interval; b) *G. ruber* Mg/Ca, and; c) *T. sacculifer* Na/Ca; d) *T. sacculifer* Mg/Ca.

3.3.3 Spines

Laser ablation

Since spine laser ablation profiles are relatively short, outliers potentially have a major effect on average Element/Ca (El/Ca) ratios. Therefore, raw data were first evaluated and ^{43}Ca intensities below 6000 counts per second (with an average ^{43}Ca background of approximately 1000 counts per second) were eliminated from further calculations. Subsequently, averages were calculated based on 2 different approaches: first the molar ratio was calculated using the integrated profile (i.e. the average of the El/Ca ratios throughout the profiles) and second by averaging single scan ratios. The last approach allows distinguishing mean (average Na/average Ca) and median for all spine measurements per species combined (Fig. 3.7). Calculating the median minimizes the effect of tailing, or outliers compared to the mean. When combining Na/Ca ratios from all individual scans (Fig. 3.7), average *G. ruber* spine Na/Ca values vary from 27.5 (median) to 28.0 mmol/mol (mean), and average Na/Ca values for *T. sacculifer* spines vary from 28.5 (mean) to 28.8 mmol/mol (median) (Fig. 3.7). For Mg/Ca, average *G. ruber* spine values vary from 7.8 (median) to 9.1 mmol/mol (mean), whereas *T. sacculifer* spine values vary from 5.8 (median) to 6.6 (mean). Because the ablations of the spines were more or less of similar duration, the data from the individual scans (average of individual scans) and from combined ablations (combining raw data from all measurements) compare well. Average spine Na/Ca and Mg/Ca (mmol/mol) values of the separate measurements are hence similar to the average of the combined raw data (Tables 3.5 and 3.6, Fig. 3.7). For *G. ruber*, average spine Na/Ca values from separate profiles (Table 3.5) vary from 26.7 (median) to 27.4 mmol/mol (mean), while for *T. sacculifer* averages vary from 29.3 (median) to 30.6 mmol/mol (mean) (Table 3.6). Values for Mg/Ca vary on average from 7.4 (median) to 11.0 (mean) for *G. ruber* and from 5.1 (median) to 6.9 (mean) for *T. sacculifer* (Tables 3.5, 3.6). The standard deviation per ablation is less than the average standard deviation for the grouped analyses (Tables 3.5, 3.6).

Table 3.5 Overview of spine measurements with elemental ratios in mmol/mol, with s: duration spine integration interval (s) and n: number of measurements during s.

Net	Depth range (m)	species	s	n (~)	mean				median			
					Na/Ca	±	Mg/Ca	±	Na/Ca	±	Mg/Ca	±
net 4	10_25	*G. ruber*	*14*	*538*	34.1	1.6	17.8	0.9	32.1	1.5	9.2	0.4
net 4	10_25	*G. ruber*	*2*	*77*	27.7	0.8	7.7	0.2	27.3	0.8	7.1	0.2
net 4	10_25	*G. ruber*	*4*	*121*	28.8	1.1			27.7	1.1		
net 4	10_25	*G. ruber*	*4*	*154*	23.7	1.0	8.9	0.4	23.2	0.9	7.4	0.3
net 4	10_25	*G. ruber*	*9*	*346*	22.3	0.7	5.9	0.2	21.9	0.7	5.2	0.2
net 4	10_25	*G. ruber*	*10*	*385*	37.3	1.5	14.5	0.6	35.4	1.5	9.5	0.4
net 4	10_25	*G. ruber*	*5*	*192*	27.2	1.3	5.3	0.3	27.2	1.3	4.9	0.2
net 4	10_25	*G. ruber*	*2*	*77*	26.7	1.1	7.6	0.3	25.9	1.1	5.6	0.2
net 4	10_25	*G. ruber*	*4*	*154*	20.3	0.8	14.4	0.6	19.9	0.8	9.6	0.4
net 4	10_25	*G. ruber*	*3*	*115*	26.4	1.1	17.2	0.7	26.4	1.1	8.6	0.4
total number of measurements				*2159*								
average (mmol/mol)					**27.4**		**11.0**		**26.7**		**7.4**	
(average) SD					**5.1**	**1.1**	**4.9**	**0.5**	**4.6**	**1.1**	**1.9**	**0.3**
(average) SE					**1.6**		**1.6**		**1.5**		**0.6**	

Table 3.6 Overview of spine measurements with elemental ratios in mmol/mol, with s: duration spine integration interval (s) and n: number of measurements during s.

Net	Depth range (m)	species	s	n (~)	mean				median			
					Na/Ca	±	Mg/Ca	±	Na/Ca	±	Mg/Ca	±
net 4	10_25	*T. sacculifer*	*5*	*130*	32.0	4.9	7.3	0.3	31.7	4.8	4.0	0.2
net 4	10_25	*T. sacculifer*	*5*	*130*	28.7	3.5	8.2	0.5	28.5	3.5	5.9	0.3
net 4	10_25	*T. sacculifer*	*3*	*78*	26.9	3.5	6.4	0.2	26.8	3.5	3.8	0.1
net 4	10_25	*T. sacculifer*	*10*	*261*	23.7	1.7	5.8	0.3	23.5	1.7	5.2	0.2
net 4	10_25	*T. sacculifer*	*7*	*183*	23.0	2.0	4.2	0.2	22.9	2.0	3.3	0.1
net 4	10_25	*T. sacculifer*	*5*	*130*	19.1	2.2	4.9	0.2	18.9	2.2	3.5	0.2
net 4	10_25	*T. sacculifer*	*8*	*209*	32.2	3.5	7.6	0.3	31.2	3.4	6.2	0.3
net 4	10_25	*T. sacculifer*	*3*	*78*	29.2	5.2	6.9	0.3	28.8	5.2	3.1	0.1
net 4	10_25	*T. sacculifer*	*13*	*339*	33.7	3.2	7.6	0.4	32.6	3.1	6.2	0.3
net 4	10_25	*T. sacculifer*	*16*	*417*	28.9	2.5	10.4	0.5	29.1	2.5	9.4	0.5
net 4	10_25	*T. sacculifer*	*2*	*98*	33.7	1.0			32.4	1.0		
net 4	10_25	*T. sacculifer*	*6*	*294*	34.1	1.1			29.3	0.9		
net 4	10_25	*T. sacculifer*	*5*	*245*	29.0	1.0			28.4	1.0		

Table 3.6 *(continued)* Overview of spine measurements with elemental ratios in mmol/mol, with s: duration spine integration interval (s) and n: number of measurements during s.

Net	Depth range (m)	species	s	n (~)	mean				median			
					Na/Ca	±	Mg/Ca	±	Na/Ca	±	Mg/Ca	±
net 4	10_25	*T. sacculifer*	*6*	*294*	27.3	0.9			27.2	0.9		
net 4	10_25	*T. sacculifer*	*6*	*294*	27.1	0.9			26.6	0.9		
net 4	10_25	*T. sacculifer*	*7*	*343*	27.6	0.9			27.2	0.9		
net 4	10_25	*T. sacculifer*	*2*	*98*	48.7	2.0			37.0	1.6		
net 4	10_25	*T. sacculifer*	*2*	*98*	41.5	1.0			39.9	1.0		
net 4	10_25	*T. sacculifer*	*5*	*245*	34.2	0.9			32.3	0.9		
net 4	10_25	*T. sacculifer*	*3*	*147*	31.8	0.7			31.1	0.7		
total number of measurements				*4115*								
average (mmol/mol)					**30.6**		**6.9**		**29.3**		**5.1**	
(average) SD					**6.5**	**2.1**	**1.8**	**0.3**	**4.7**	**2.1**	**1.9**	**0.2**
(average) SE					**1.4**		**0.6**		**1.1**		**0.6**	

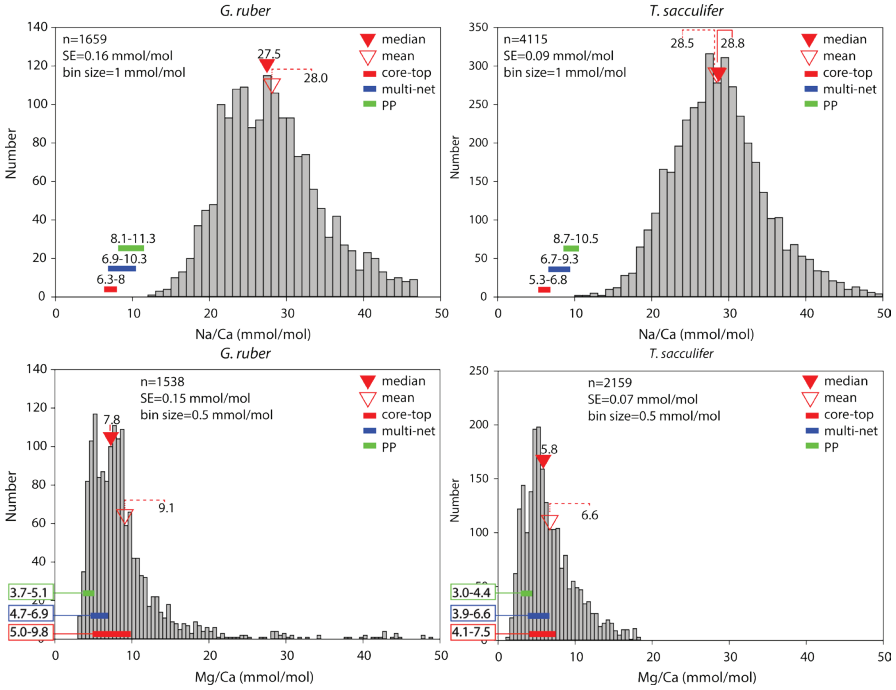

Figure 3.7. Spine distribution plots for all Na/Ca and Mg/Ca (mmol/mol) measurements for *G. ruber* and *T. sacculifer*, including average Na/Ca and Mg/Ca ranges (entire Red Sea) for specimens from core-tops, plankton tows (multi-net) and plankton pump (PP) specimens.

EPMA

For both species, EPMA analyses shows that Na is not homogeneously distributed within the shell wall (Figs. 3.4, 3.8, 3.9). However, unlike Mg, the distribution of Na does not show clear banding, but a more patchy distribution with clear zones of higher concentrations in the spine region. Measurements on spines of both species show Na/Ca-values similar to those established by LA-Q-ICP-MS (Section 3.3.1), which are much higher than the average shell Na/Ca values (Figs. 3.4, 3.8, 3.9). However, it was more challenging to measure *G. ruber* spines than *T. sacculifer* spines, as these were much thinner and more easily lost in the polishing process. Spine Mg/Ca values are similar to or lower than shell Mg/Ca values (Figs. 3.7 and 3.4), based on both LA-ICP-MS and EPMA analyses.

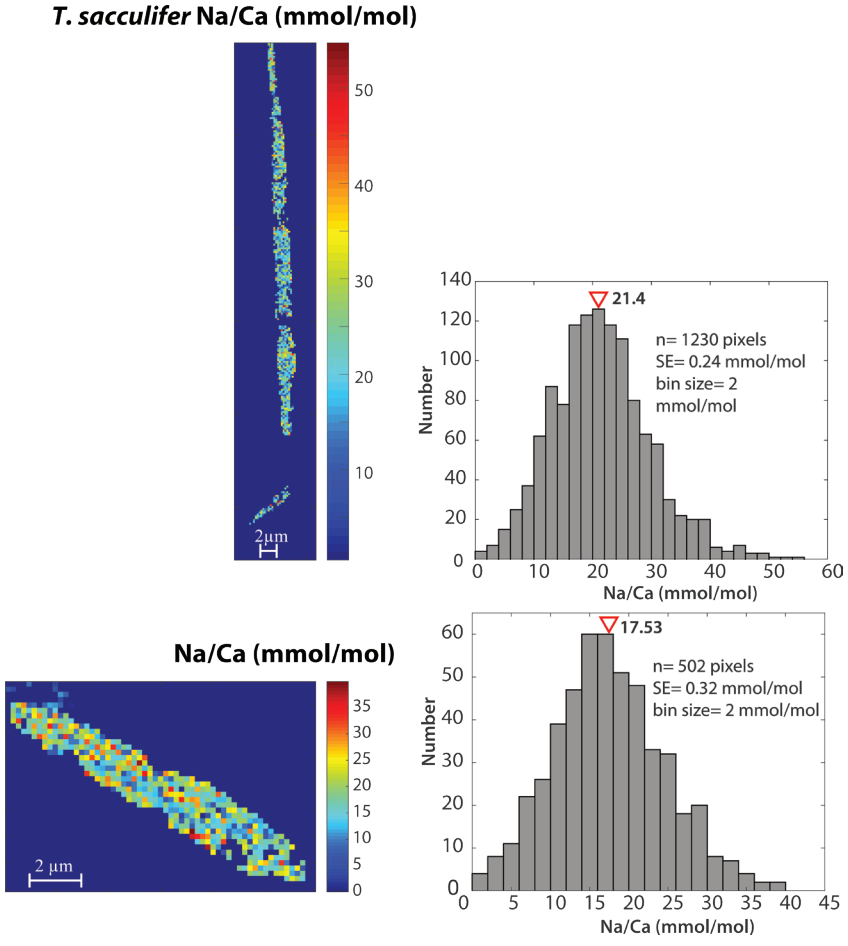

Figure 3.8. *Trilobatus sacculifer* EPMA spine measurements and accompanying histograms.

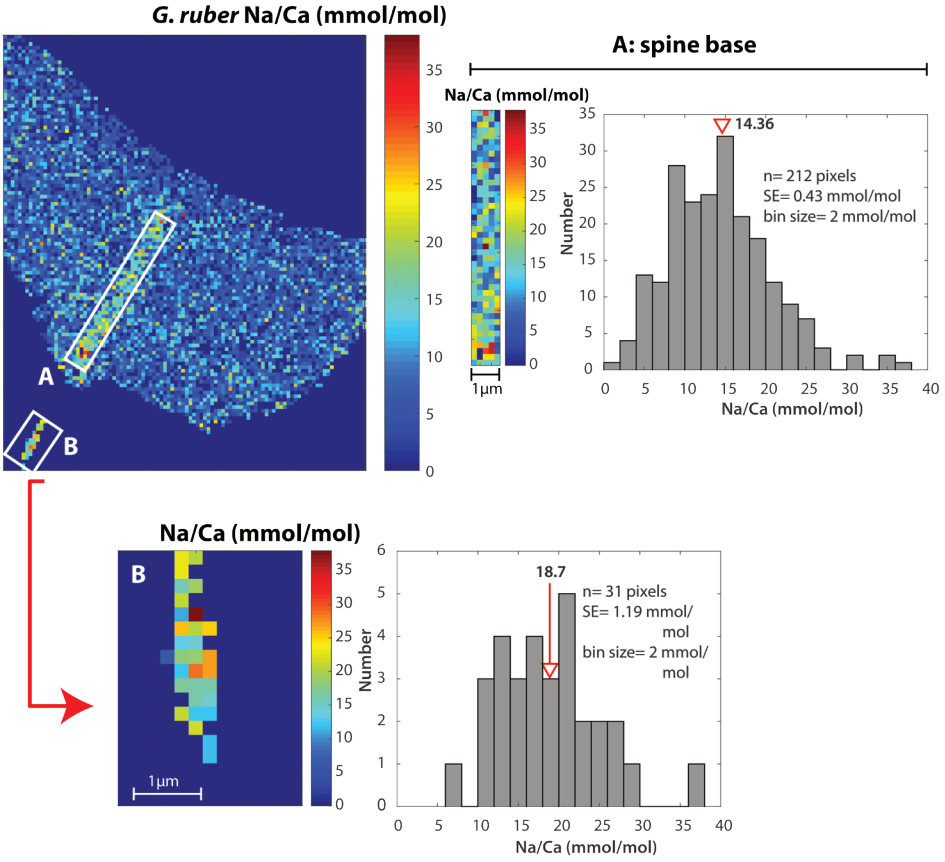

Figure 3.9. *Globigerinoides ruber* EPMA spine measurements and accompanying histograms.

3.3.4 Shell wall surface structure

Scanning Electron microscope pictures reveal that the shells of specimens collected from core-tops differ from those of the same species collected from the water column (~17.5 m, Fig. 3.4) in terms of wall thickness, average test size (within the plankton pump samples specimens never reached the size observed in the core-tops) and surface texture (Figs. 3.4, 3.10 and 3.11). In general, surface water specimens are smaller (~125-500 µm for *T. sacculifer* and ~125-350 µm for *G. ruber*), have spines and are thin-walled. The outer surface of the final chamber is often smoother than the other chambers, particularly for pre-adult or young adult specimens (Brummer et al., 1987). Coarse surface textures with spines growing from or near the corners is commonly observed in living *T. sacculifer*, but is less pronounced in *G. ruber* (Figs. 3.4 and 3.10). Such topography arising from the

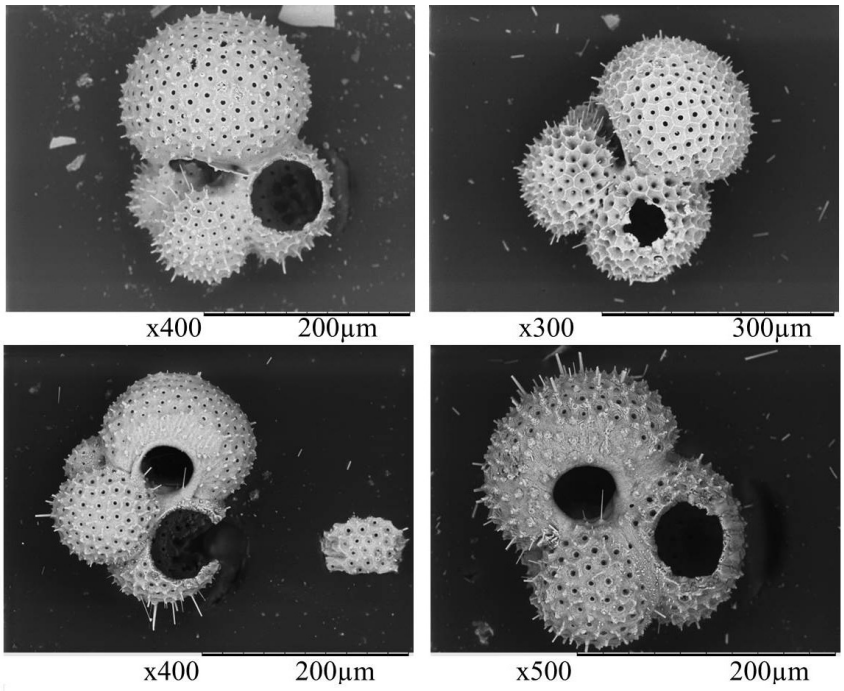

Figure 3.10. Specimens of *T. sacculifer* (upper panels) and *G. ruber* (lower panels) from surface water (plankton pump samples 4 and 7), showing an incipient cancellate surface with elevated spines bases.

spine-shell interface is usually more pronounced in larger specimens, where the build-up of calcite plaques around the spine bases (Bé, 1980; Hemleben, 1975) results in terraced structures. Unfortunately, spines partially broke off in specimens collected from surface water due to the plankton pump sampling and sample processing. In the depth-stratified plankton tows (~17.5 m depth, Fig. 3.4), specimens have thicker and longer spines and shell walls appear also somewhat thicker compared to those from surface waters. The former also show a better developed cancellate surface texture in *T. sacculifer,* as well as a thicker build-up of calcite plaques around the base of the spines in *G. ruber.*

Compared to specimens collected from the water column, those from core-tops are larger (184-516 µm for *G. ruber and* 229-1284 µm for *T. sacculifer*), do not have spines and have much thicker shell walls, which also appears to be reflected in generally longer laser ablation profiles. Both species show surface textures with indications for processes preceding gamete release, e.g. 'smoother' surfaces caused by deposition of GAM calcite, spine holes, thicker shell walls and terminal ontogenetic features like the sac-like chamber

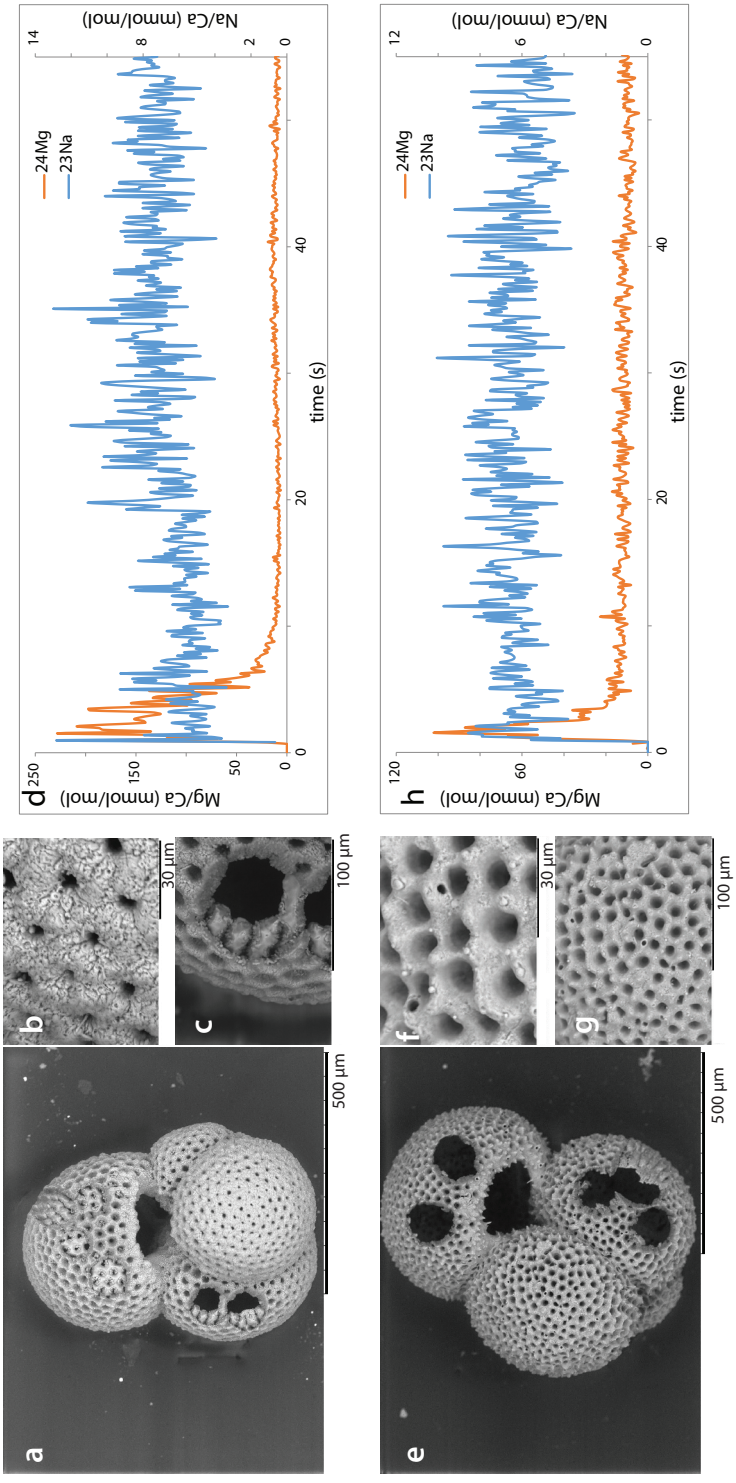

Figure 3.11. a) Etched and thick GAM of a *T. sacculifer* from the northern Red Sea (core-top MC71, M5/2) with a close-up of the surface structure (b), and LA crater with a visible thick GAM calcite layer (c) as indicated by elevated Mg/Ca in the laser ablation profile (d). e) Thick-walled *G. ruber* specimen from the same core-top with GAM calcite and overgrown spine holes (f,g). Also slight signs of dissolution are visible (f,g)) and accompanying laser ablation profile showing a high Mg layer (GAM) at the outside of the shell.

in *T. sacculifer* (Bé, 1980; Bijma and Hemleben, 1994; Brummer et al., 1987) (Fig. 3.11). Often, specimens with (abnormally) high Mg/Ca values in the northernmost part of the Red Sea also display signs of dissolution of the shell's surface in combination with a thick shell wall that no longer displays clear ridges and/or hexagonal patterns (Fig. 3.11). The high-Mg phase of these specimens is often visible in the laser ablation profiles as elevated Mg/Ca at the outer surface (Fig. 3.11), while inorganic overgrowth crystals appear absent. Depending on the thickness and absolute Mg/Ca of this layer, the average Mg/Ca may be elevated.

3.4 Discussion

Average shell Na/Ca values of *G. ruber* and *T. sacculifer* collected from Red Sea core-tops (Fig. 3.12) correspond well to values reported in previous culture and field studies of the same species (Allen et al., 2016; Delaney et al., 1985) and to those of cultured benthic foraminifer *Ammonia tepida* (Wit et al., 2013), but are significantly lower than those of the same species collected from surface waters of the Red Sea (Mezger et al., 2016). In addition, the correlation between Na/Ca and salinity of surface water planktonic species collected in situ (Mezger et al., 2016) is absent in the specimens from the core-tops.

In the southern Red Sea Mg/Ca values are similar to those reported earlier (Allen et al., 2016; Anand et al., 2003; Kısakürek et al., 2008), but in the northern Red Sea we find values higher compared to earlier work (Allen et al., 2016; Anand et al., 2003; Kısakürek et al., 2008) and also higher than in the same species collected from surface waters of the Red Sea (Mezger et al., 2016). Mg/Ca values in the northern Red Sea are too high to be explained by known temperature and salinity dependencies and reach values comparable to those from earlier Mediterranean studies (Ferguson et al., 2008), a sea which is also a known for its overall high salinity. Still, other studies in the Mediterranean looking at Mg/Ca values suggest calibrations rather similar to that for the open ocean (Wit et al., 2010). Values measured are considerably lower compared to paleo Red Sea studies exhibiting inorganic overgrowth (Hoogakker et al., 2009). Still, average values are also similar to those observed for specimens of *T. sacculifer* that underwent GAM calcification (Nürnberg et al., 1996) (Fig. 3.13).

For foraminiferal specimens collected by plankton tows in the Red Sea (Fig. 3.5) between 10 and 500 meters of water depth, Na/Ca values are similar to those reported in previous studies (Allen et al., 2016; Delaney et al., 1985; Wit et al., 2013). However, Na/Ca and

Mg/Ca in our specimens do not show a clear relationship to changes in salinity and/or temperature with depth. Whereas Na/Ca decreases with increasing water depth, Mg/Ca increases over the same depth interval (Fig. 3.5). Given an approximate sinking speed between 198 and 838 meter per day (*G. ruber*) and between 200 and 1396 meter per day (*T. sacculifer*) for post-mortem planktonic foraminifera (Fok-Pun and Komar, 1983; Takahashi and Be, 1984; Van Sebille et al., 2015), only a very small fraction of specimens collected in each sample were sinking post-mortem. Assuming that this has no appreciable effect on the results presented here, these trends in elemental compositions through the water column may reflect a combination of (1) ongoing calcification with depth-related

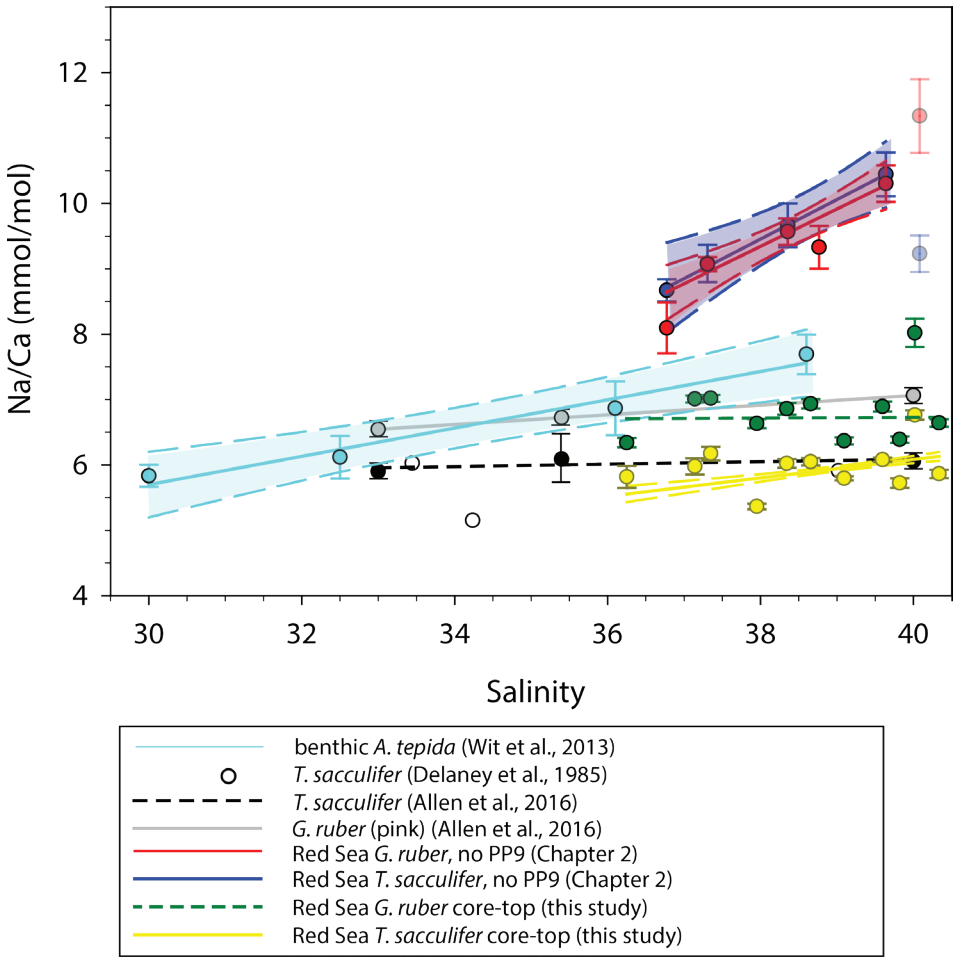

Figure 3.12. Core-top Na/Ca values versus sea surface salinity, compared to published relationships. Plankton pump 9 (PP) is excluded from the calibration, as described in Mezger et al. (2016).

environmental changes (e.g. salinity and temperature), (2) changes related to different life stages and (3) chemical alteration of the shell within the water column.

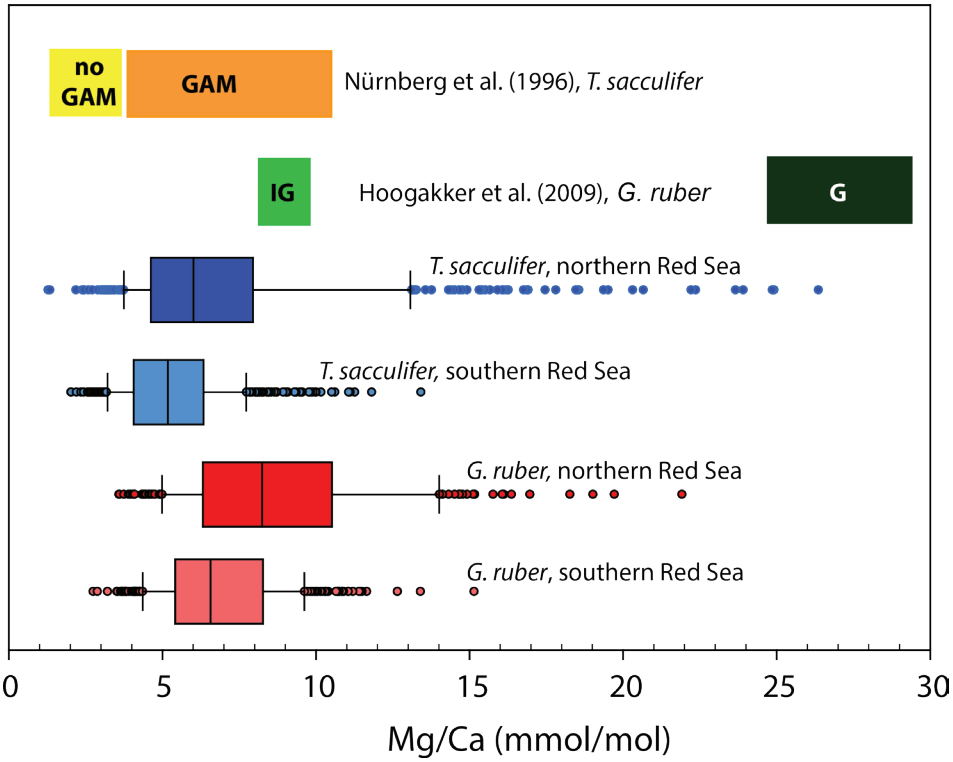

Figure 3.13. All core-top Mg/Ca values, compared to interglacial (IG) and glacial (G) Mg/Ca values for *G. ruber* specimens (whole-batch measurements FT-TRA-ICP-MS) including overgrowths (Hoogakker et al., 2009), and cultivated *T. sacculifer* specimens under different salinities and temperatures that underwent gametogenesis (GAM) and did not undergo gametogenesis (no-GAM) (Nürnberg et al., 1996). The distinction between the northern and southern Red Sea is at 22.4 °N and longitude of 37.5 °E. Data from the Red Sea is based on single-chamber Mg/Ca (one dot is one laser ablation measurement), whereas variability in the other two datasets represents maximum and minimum values, resulting from inter-specimen variability.

3.4.1 Environmental changes

Water column Na/Ca and Mg/Ca

For both species, Na/Ca values decrease with increasing water depth within the upper 10-100 m of the water column and are consistent with the Na/Ca values observed in the surface water specimens (Mezger et al., 2016; Fig. 3.12). Since it is known that Na/Ca in cultured benthic as well as cultured and field collected planktonic foraminiferal shells increases with salinity (Allen et al., 2016; Mezger et al., 2016; Wit et al., 2013) and salinity

increases with depth in the Red Sea, it is unlikely that the observed decrease in Na/Ca is due to ongoing calcification with depth. In addition, temperature also decreases with depth, which would have an additional, albeit small, positive effect on Na/Ca (Allen et al., 2016).

The depth-resolved pattern in Mg/Ca is opposite to that in Na/Ca (Fig. 3.5), as Mg/Ca increases with depth. Similar to Na/Ca, ongoing calcification with depth and the lower sub-surface temperatures would result in lowering Mg/Ca rather than increasing it. Although salinity is known to affect Mg/Ca, the observed change of ~1 salinity unit (Fig. 3.2) over the studied depth range is insufficient to fully explain the observed difference in Mg/Ca between living surface water specimens and plankton-tow specimens, as Mg-incorporation depends only to a limited extent on salinity compared to temperature (between 0.11 and 0.21 mmol/mol per salinity unit for an environmental relevant salinity range (Dueñas-Bohórquez et al., 2009; Gray et al., 2018; Hönisch et al., 2013; Kısakürek et al., 2008). Moreover, the difference in Na/Ca between *G. ruber* and *T. sacculifer* is not correlated with the difference in Mg/Ca between these species from the same depth interval.

These observations and the resulting opposing trends in Na/Ca and Mg/Ca compared to the sea water temperature and salinity profiles imply that continued calcification with depth cannot explain the observed trends. Consequently, the shell chemistry must have been altered by precipitation of chemically distinct calcite during changes in habitat and/or life-stage changes of the foraminifer.

Core top Na/Ca and Mg/Ca

A small difference was observed between the deepest (300-500 m) water column samples and core-tops, with the core-top specimens being slightly lower in Na/Ca and slightly higher in Mg/Ca. A decrease in Na/Ca in fossil specimens has been observed before, but was associated with ageing over a time scale of several millions of years (Yoshimura et al., 2017). It was observed that Na/Ca values decrease in a Quaternary core in the planktonic species *Globorotalia tumida*, which was attributed to ongoing leaching of Na from the crystal lattice. However, such an effect unlikely plays a role in foraminifera from core-tops as the time scale involved is much shorter.

Values reported for Mg/Ca here are also higher than those previously published for Mg/Ca in *G. ruber* and *T. sacculifer* species from culture studies and field calibrations (e.g.

Allen et al., 2016; Anand et al., 2003; Kısakürek et al., 2008; Nürnberg et al., 1996). Since sea surface temperatures decrease towards the north of the Red Sea, Mg/Ca in specimens from the core-top samples show an apparent negative correlation to temperature and a positive correlation to salinity.

While *T. sacculifer* and *G. ruber* show similar Mg/Ca values at the sea surface (Mezger et al., 2016), both water column and core-top *T. sacculifer* show lower Mg/Ca values compared to *G. ruber*. Such an offset is consistent with results from several other studies (e.g. Anand et al., 2003; Nürnberg et al., 1996). In many culturing studies (e.g. Kısakürek et al., 2008) and field studies (e.g. Anand et al., 2003), it was found that Mg incorporation is positively correlated to temperature. Assuming continued calcification in the colder sub-surface water, lower Mg/Ca values are expected for the plankton tow and core-top collected shells compared to specimens from surface waters (Allen et al., 2016; Anand et al., 2003; Kısakürek et al., 2008; Nürnberg et al., 1996). Even if salinity would have a much larger effect on Mg incorporation (Ferguson et al., 2008) than explained in section 4.1.1, the large changes in Mg/Ca with water depth observed here cannot be explained solely by continued calcification in deeper water, which is merely one salinity unit higher.

3.4.2 The role of spines on shell chemistry

One clue to explain the changes in Na/Ca of the shells comes from changes in shell preservation. The EPMA-based element distribution shows that Na is enriched in the spines and at the spine bases (Figs. 3.4, 3.8, 3.9). This is in contrast to the Mg/Ca distribution, showing a banding of the lamellar wall calcite similar to that observed earlier (e.g. Erez, 2003). The inhomogeneity in Na/Ca, related to the foraminiferal spines, offers an alternative explanation for the depth related changes observed in Na/Ca. Loss of the spines during a foraminifer's life cycle would clearly result in an overall lowering of Na/Ca values (see mass balance calculation below). Foraminifera are known to shed their spines deeper in the water column before gamete release and also when under stress (e.g. Bé, 1980; Caron et al., 1990; Hemleben, 1975). Additionally, crystal growth rates for spines versus those for the shell calcite may explain differences in Na/Ca, as was shown in synthetically grown calcites (Busenberg and Plummer, 1985). As early stage foraminifera have a faster growth rate (Hemleben and Bijma, 1994), this could potentially also result in enhanced Na incorporation, whereas adult specimens with lower calcification rates might incorporate less Na. The combined effect of spine loss and decreasing growth rates with life stage and hence depth could therefore contribute to the observed decrease in Na/Ca values with

depth. Since foraminifera do not secrete their shell at the same conditions throughout their life cycle it remains, however, difficult to deconvolve such potential effects.

Spine related Na/Ca change with depth

Already the pioneering foraminiferal culture studies of (Bé, 1980; Caron et al., 1990; Hemleben, 1975) showed that foraminifera lose their spines at the end of their life cycle preceding gamete release or due to stress. For both species studied here spines protrude from the POS (primary organic sheet) through the entire chamber wall (Hemleben, 1975). During successive episodes of calcification, on the outer surface of the shell wall calcite plaques build up around the spine bases, giving the surface a terraced structure (Bé, 1980; Hemleben, 1975; Spero, 1988) (e.g. Fig. 3.10). At the same time, a polygonal pattern of inter-pore ridges is deposited by the same process in *T. sacculifer* (Bé, 1980) (e.g. Fig. 3.10). In preparation for gametogenesis, these spines are possibly partially resorbed and subsequently shed by rhizopodial activity, resulting in the appearance of spine holes (Bé, 1980) similar to those observed here (Fig. 3.11). Because of the high Na/Ca values of the spines, this results in shell Na/Ca values to decrease in fossil specimens as the relative contribution of the spines decreases. Often, only spine bases remain when specimens are deposited at the sediment. Confirming this hypothesis, all specimens collected from the surface water contain spines (Fig. 3.4), whereas spines were no longer present for the specimens collected from the sediment surface (Fig. 3.11).

For both species, lowest Na/Ca values are observed for the smallest size class in the water column (Supporting information 3.1.1). Potentially, shell size could have an effect on the elemental ratios measured. For example for Mg/Ca, (Elderfield et al., 2002) found that with increasing shell size Mg/Ca values increase. For Na/Ca, values increase with decreasing shell size in culture experiments with the benthic *A. tepida* (Wit et al., 2013) or chamber number (Mezger et al., 2016). However, it is argued that this relation is indirect, with salinity being the primary factor affecting shell size and thereby also Na incorporation (Mezger et al., 2016; Wit et al., 2013). In this study, no correlation is found between shell size and single-specimen Na/Ca for the core-top specimens, confirming that for spinose planktonic foraminifera, life stage (spines) rather than shell size determines the average Na/Ca measured. For *T. sacculifer,* highest core-top Mg/Ca values are observed for the largest specimens, albeit that this is also most probably associated with life stage (section 4.2.2) rather than shell size.

Measured spine LA-Q-ICP-MS Na/Ca values, confirmed by EPMA spine measurements, were up to 3 times higher compared to average foraminiferal shell Na/Ca values (Tables 3.3-3.6). A simple mass balance, based on measured spine Na/Ca values and the difference between core-top and surface water specimen Na/Ca values, shows that the difference between living and core-top specimens would require a relative spine contribution of 18.9% in *T. sacculifer* and 16.7% in *G. ruber* respectively (Tables 3.5, 3.6). These percentages represent the lower limit, as spines are often partly broken during sample collection and preparation. Bé (1980) and Erez and Honjo (1981) previously showed that GAM deposition potentially adds up to 28% or even 50% weight to the pre-GAM shell. Assuming that this calcite is possibly derived from resorbed spines (Bé, 1980), such a contribution of spines to the overall shell carbonate is not unrealistic. The loss of spines with depth hence likely explains the significant decrease of Na/Ca with depth in the upper 100 meters of the water column, as reproduction in the Red Sea mostly occurs before 80 meters depth (Bijma and Hemleben, 1994). Moreover, as spines have similar Mg/Ca-values as the shells (Tables 3.5, 3.6), loss of spines unlikely affects the Mg/Ca signal.

Since the previously published Na/Ca to salinity relationships were based on chamber-specific spot analysis of the whole shell of specimens collected from the Red Sea surface water, a major part of this correlation must be due to spine chemistry. Such an (additional) impact of spine chemistry is in line with results obtained from a culturing study with the benthic foraminifer *A. tepida* (Wit et al., 2013), which is non-spinose, having much lower overall Na/Ca values and also a lower sensitivity towards salinity. Similarly the cultured planktonic species used by Allen et al. (2016) likely lost part of their spines due to stress in a culture setting, explaining concentrations and sensitivity corresponding to the benthic species.

Spine related morphological changes: Mg/Ca change with depth

As the Mg/Ca value of spines is similar compared to the shell Mg/Ca, higher Mg/Ca in the core-tops specimens cannot be explained by spine loss. However, also other morphological/terminal changes in many planktonic species may occur, potentially associated with spine loss (Fig. 3.14).

After shedding of spines, ridged/terraced surface structures are replaced by a relatively smooth outer layer (GAM calcite) produced before gametogenesis (Bé, 1980; Bijma et al., 1990a; Brummer et al., 1987). Resorption of spines precedes precipitation of this GAM calcite (Bé, 1980), reducing the average Na/Ca. Gametogenic calcite, as well as

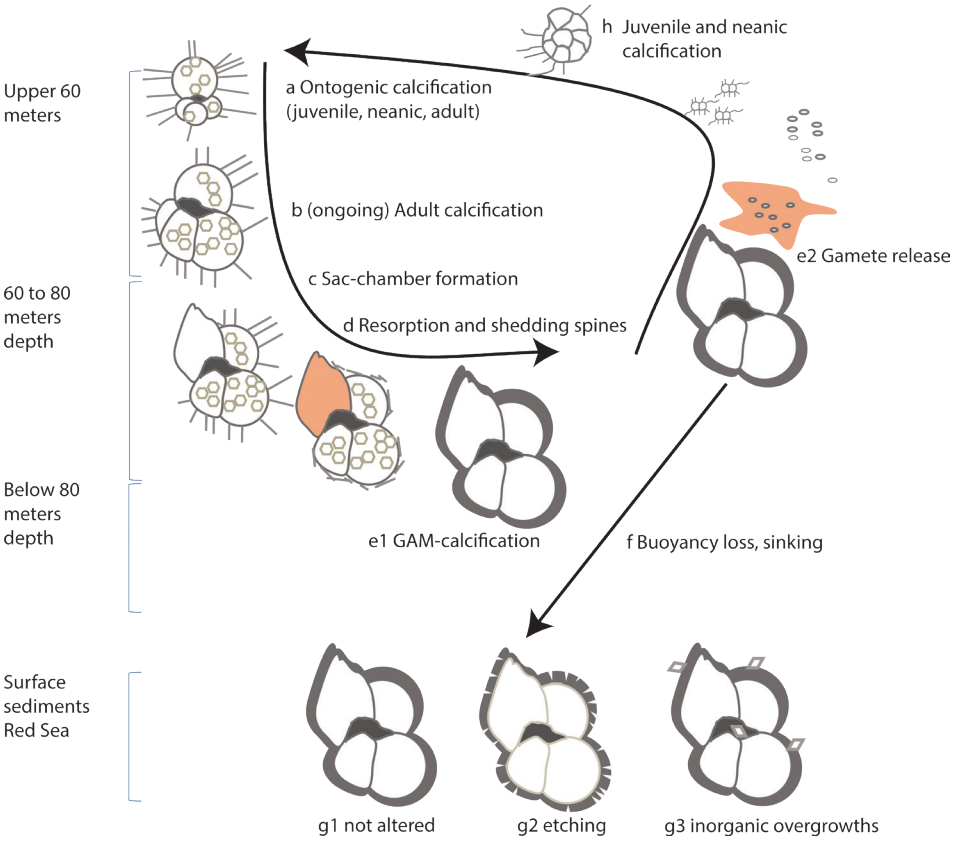

Figure 3.14. Morphology of *T. sacculifer* with depth and potential different life stages, based on Red Sea assemblage and depth studies of Bijma and Hemleben (1994); Hemleben and Bijma (1994); Bé (1980); Brummer et al. (1986); 1987), Brown and Elderfield (1996) and Hoogakker et al. (2009). We assume the processes to be alike for *G. ruber*, but reproduction depths might be somewhat shallower.

formation of another terminal feature like crust calcite, is known to change the elemental composition of the whole shell (Bijma et al., 1990b; Steinhardt et al., 2015). Because under natural conditions deposition of GAM calcite often occurs in a deeper temperature and salinity environment compared to lamellar calcite precipitation, the impact of GAM and/or crust carbonate is difficult to quantify. (Nürnberg et al., 1996) showed that *T. sacculifer* specimens that underwent GAM in culture under constant temperature conditions had much higher (up to 276% in GAM) Mg/Ca values compared to no-GAM specimens.

Values for Mg/Ca measured in planktonic foraminiferal shells collected in the northern Red Sea are similar to values reported by Hoogakker et al. (2009) for inter-glacial

specimens of *T. sacculifer* collected down-core (Fig. 3.13). With the exception of a few single tests, values are considerably lower than those of the glacial specimens, which according to (Hoogakker et al., 2009) are related to the abnormally high salinities at those times causing secondary high Mg-rich overgrowths. Such inorganic overgrowths were not observed in SEM- or EPMA images of the specimens studied here. Van Raden et al. (2011) also found a layer of elevated (diagenetic) Mg/Ca values outside of the shell of *G. inflata* with laser ablation analysis, which was not visible in SEM images. We also observed a thin layer of high Mg/Ca on the outside of the shell of both species with laser ablation. The layer thickness seems to correspond to what morphologically seems GAM calcite adhered to the outside of the shell. The very high Mg/Ca values of this layer suggest that either the GAM calcite was precipitated strongly offset from pre-GAM carbonate or subsequently altered chemically without changing the morphology. The relatively high Mg/Ca of the GAM calcite make this layer more prone to post-mortem dissolution, causing the etched features on the outside of the shell (Fig. 3.11).

For the Red Sea core-top specimens, a GAM layer is not only observed for *T. sacculifer*, but also in *G. ruber* (Fig. 3.11). The (increase in) average Mg/Ca and high variability in Mg/Ca for specimens >500 μm in *T. sacculifer* likely reflects differences in thickness of the GAM layer (Fig. 3.11). After reproduction/gamete release (below 80 meters depth), spinose foraminifera lose their buoyancy (Bijma and Hemleben, 1994). In the sediment, specimens containing a thick GAM layer are dominant over thin ontogenetic (only, or pre-GAM) shells (Bé, 1980). The relative contribution and thickness of GAM shells (Fig. 3.11) and associated processes (spine loss) hence explains the increase in Mg/Ca with depth (increased contribution GAM shells), as well as the observed decrease in Na/Ca. Especially in the northern Red Sea core-tops, thick GAM shells are found (Fig. 3.11), possibly explaining the observed extreme Mg/Ca values in the north and the apparent anti-correlation with temperature.

Spine ontogeny

Assuming that the loss or relative contribution of spines is responsible for observed differences in Na/Ca values between surface water, subsurface water column and core-top specimens, this still does not explain the observed differences in slope for Na/Ca to salinity relationships (Allen et al., 2016; Mezger et al., 2016; Wit et al., 2013). Whereas the Na/Ca of specimens collected alive in surface waters show a high sensitivity to changes in salinity (Mezger et al., 2016), the response to salinity is more dampened in foraminiferal culture studies (Allen et al., 2016) and benthic species (Wit et al., 2013). Since we argue that

spine chemistry may explain the observed difference between surface water and core-top specimens, this suggests that either spine Na/Ca or foraminiferal spine density (spines per chamber and/or spine length) increases with increasing salinity (Fig. S3.5). Based on the measured Na/Ca values of the spines at a salinity of 39.6, this implies that for the Red Sea salinity range from 36 to 41 either *G. ruber* spine densities have to increase about three times (from 6.9 to 20.5%) and for *T. sacculifer* about two times (from 11.3 to 21.9%), or Na/Ca values increase approximately two times within the spines. These values have been calculated with two simple mass balances, assuming that the difference in Na/Ca between core-top and surface water calibrations for both species can be fully explained by an increase in spine density (assuming a constant spine Na/Ca) or spine Na/Ca values (assuming constant spine density). Although it is not possible to fully exclude a change in spine length, a shift in spine density high enough to explain the shift in Na/Ca values was not observed. Still, also the shell chemistry itself will respond to salinity as observed for the benthic species *A. tepida* (Wit et al., 2013) and cultured planktonic ones (Allen et al., 2016), albeit with a much reduced sensitivity.

The relatively high Na/Ca in foraminiferal spines and spine bases may be associated with a difference in growth mechanism between spines and the rest of the shell. Assuming that the formation of foraminiferal spines is comparable to that of some other biogenic calcium carbonate structures (e.g. the spines of sea urchins), they consist of a single calcite crystal (Beniash et al., 1997; Hemleben, 1975; Rodriguez-Blanco et al., 2011). Such a single crystal-structure might result from an initial deposition of nanoparticles consisting of amorphous calcium carbonate (ACC) that spontaneously form a single calcite crystal (Rodriguez-Blanco et al., 2011). Since the fluid-ACC transition is relatively fast compared to rates observed in non-biogenic step-wise growth described from laboratory studies (Morse et al., 2007), the fractionation against e.g. Na is less strong and hence, the spines may have a higher Na/Ca than the rest of the shell. Also this would imply a more direct, one to one, uptake of Na in spine carbonate in relation to salinity.

Conclusions

In this study, we tested the applicability of the foraminiferal Na/Ca-based salinity proxy by comparing the chemical composition of core-top and plankton tow collected planktonic foraminifera from the Red Sea to those living in surface waters. Results show that Na/Ca of both *G. ruber* and *T. sacculifer* decreases with increasing water depth, thereby dampening the initial Na/Ca to salinity signal. In contrast, Mg/Ca values increase for both species

towards the seafloor. Laser-ablation-Q-ICP-MS measurements combined with Electron Probe microanalysis (EPMA) show that for both species, Na is concentrated at the spines. Loss of spines in the water column provides a mechanistic explanation for the observed Na/Ca decrease with depth. Additionally, SEM pictures and LA profiles show that the deposition of GAM calcite - high in Mg, but with Na/Ca values similar to lamellar calcite – or (diagenetic) recrystallization of GAM calcite explains the increasing Mg/Ca values. Na/Ca values of the core-top specimens coincide with the earlier established correlation with salinity for benthic and planktonic foraminifera from controlled growth experiments. This study revealed the unexpected role of spine calcite on foraminiferal Na/Ca and found that Mg/Ca is elevated beyond known salinity and temperature calibrations, requiring an additional process enriching Mg in shells. The origin of the Na/Ca signal is better understood now, but still requires more research to serve as a robust proxy for salinity.

Acknowledgements

This research is funded by the NIOZ – Royal Netherlands Institute for Sea Research and supported by the Gravitation grant NESSC from the Dutch Ministry of Education, Culture and Science. We thank W. Boer (NIOZ) and T. Bouten (Utrecht University) for their analytical assistance. We are also grateful to all technical staff on board of RV Pelagia cruise 64PE158 and the other cruises.

Supporting information to Chapter 3

This supporting information consists of all data, figures and calculations referred to in the manuscript, including normality calculations for core-tops and multi-nets and comparisons between shell sizes and the chemical composition of the shells. Furthermore, an illustration is added of the mass balance calculations mentioned in the discussion of the manuscript.

S 3.1 Plankton tows

S 3.1.1 Na/Ca

For *G. ruber*, Na/Ca values are only normally distributed in the 50-75 and 100-150 m sampled depth intervals. In contrast, most Na/Ca values for *T. sacculifer* are normally distributed except for 150-200 m and 300-500 m depth intervals (Table S3.1).

Within the different plankton tows, sizes for both species range from 150 to 500 μm, which are divided into three (*G. ruber*) or four (*T. sacculifer*) size classes, based on the mesh sizes of the sieves used (Figure S3.1, Table S3.2). Per depth interval, the number of specimens per size class very between 27 and 5 specimens of *G. ruber* and between 19 and 1 specimen(s) for *T. sacculifer* (Figure S3.1, Tables S3.2-3.5). The low number of specimens available clearly limits the statistical power of our analyses. In general, lower Na/Ca values are observed for larger sized foraminiferal shells for *T. sacculifer* (Figure S3.1, Table S3.3 on sizes). No clear trend in Na/Ca values with shell size is observed within the water column for *G. ruber,* albeit that size class 2 (250-355 μm) often displays similar or lower Na/Ca ratios compared to size class 1 (150-250 μm) (Figure S3.1). For *T. sacculifer*, lowest Na/Ca values are measured for the largest size class (355-500 μm), as well as the highest variability. For both species, all size classes have a similar trend in Na/Ca with water depth.

S 3.1.2 Mg/Ca

Almost all Mg/Ca values are normally distributed at each depth interval and for both species (Table S3.4, S3.5), except for *G. ruber* from 200-300 m and 300-500 m, and *T. sacculifer* from 150-200 m. No clear trend of Mg/Ca with size is observed for *G. ruber* and *T. sacculifer* specimens in the plankton tow samples, even though at some depths size related differences are observed (Figure S3.2).

S 3.2 Core-tops and box-core

S 3.2.1 Na/Ca

For *G. ruber,* all Na/Ca values are normally distributed (Shapiro-Wilk) per group of measurements per location, except for northern Red Sea positions M5/2 MC71 and M31/2 MC363 (Table S3.6). For *T. sacculifer*, distributions per location are either normal (all southern positions until the middle Red Sea), or not normal (a few northern positions, Table S3.7).

Shell sizes vary between 184 and 515 µm for *G. ruber* and between 229 and 1284 µm for *T. sacculifer.* A significant correlation between size and Na/Ca is observed for *G. ruber*, albeit that reconstructed change and r^2 is very low (y=0.0008x + 6.4, p=0.007, r^2=0.015) (Figure S3.3). The relation between size and Na/Ca for *T. sacculifer* is not significant (r^2=0.008 and p=0.011, Figure S3.3). Dividing all Na/Ca data from both species in different size classes (Figure S3.3), none of the regressions per size class for *G. ruber* are significant (Figure S3.3). For *T. sacculifer*, only size class 4 (500-355 µm) is significant (y=0.23x-2.90, r^2=0.11, p<0.0001).

S 3.2.2 Mg/Ca

For *G. ruber,* almost all Mg/Ca values per location are normally distributed, except for the northern locations M44/3 MC601 and M5/2 MC71 (Table S3.6). For *T. sacculifer*, only three southern Red Sea locations are normally distributed (Table S3.7).

No significant correlation between size and Mg/Ca is observed for *G. ruber* (p=0.48) and a slight significant positive relation for *T. sacculifer* (y=5.6x+636.9, r^2=0.013, p=0.001), which is in line with the high amount of scatter observed in the data (Figure S3.4). For *T. sacculifer*, most variability and highest Mg/Ca values are measured in specimens larger than 500 µm in size, a size class not sampled by plankton nets or –pumps. Dividing all Mg/Ca values from both species in different size classes (Figure S3.4), only the relation between SST for *G. ruber* size classes 2 and 3 are significant (250-355 µm: r^2=0.07, p=0.0001, 355-500um: r^2=0.14, p<0.0001). However, these two calibrations are not significantly different (one-way ANCOVA, p=0.008). For *T. sacculifer*, only a correlation between size class 4 Mg/Ca and SST (>500 µm) is found (r^2=0.07, p<0.001), albeit with a small r^2.

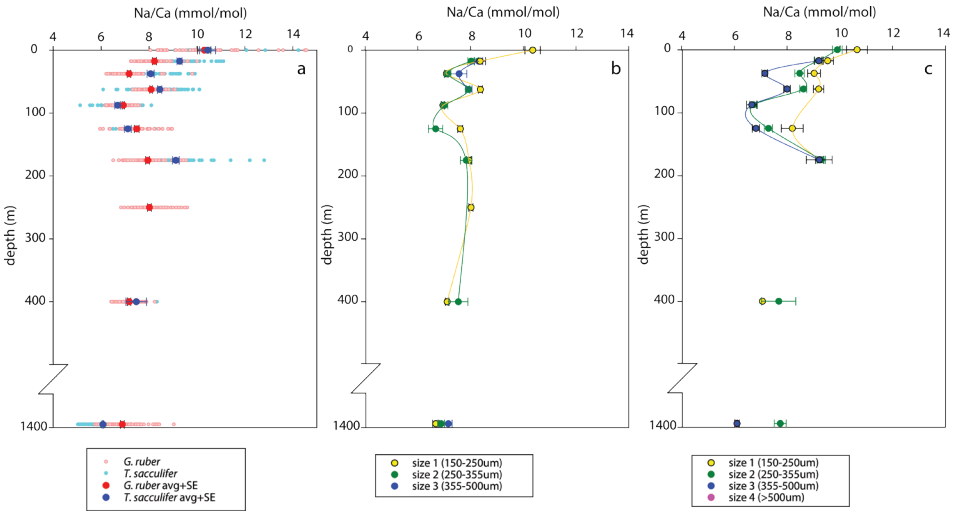

Figure S3.1 Na/Ca changes for *G. ruber* (red) and *T. sacculifer* (blue) plotted with average depth (Table S4-7), with a) Average Na/Ca for both species, averages and standard errors indicated, b) *G. ruber* size classes and c) *T. sacculifer* size classes. The surface water sample is from the plankton pumps (Mezger et al., 2016) and the surface sediment sample is from core-tops.

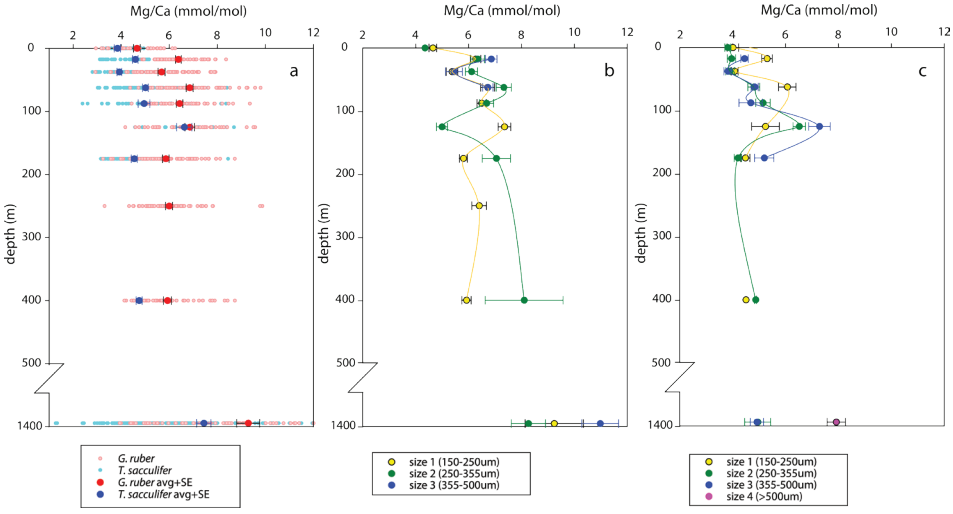

Figure S3.2 Mg/Ca changes for *G. ruber* (red) and *T. sacculifer* (blue) plotted with average depth (Table S4-7), with a) Average Mg/Ca for both species, averages and standard errors indicated, b) *G. ruber* size classes and c) *T. sacculifer* size classes. The surface water sample is from the plankton pumps (Mezger et al., 2016) and the surface sediment sample is from core-tops.

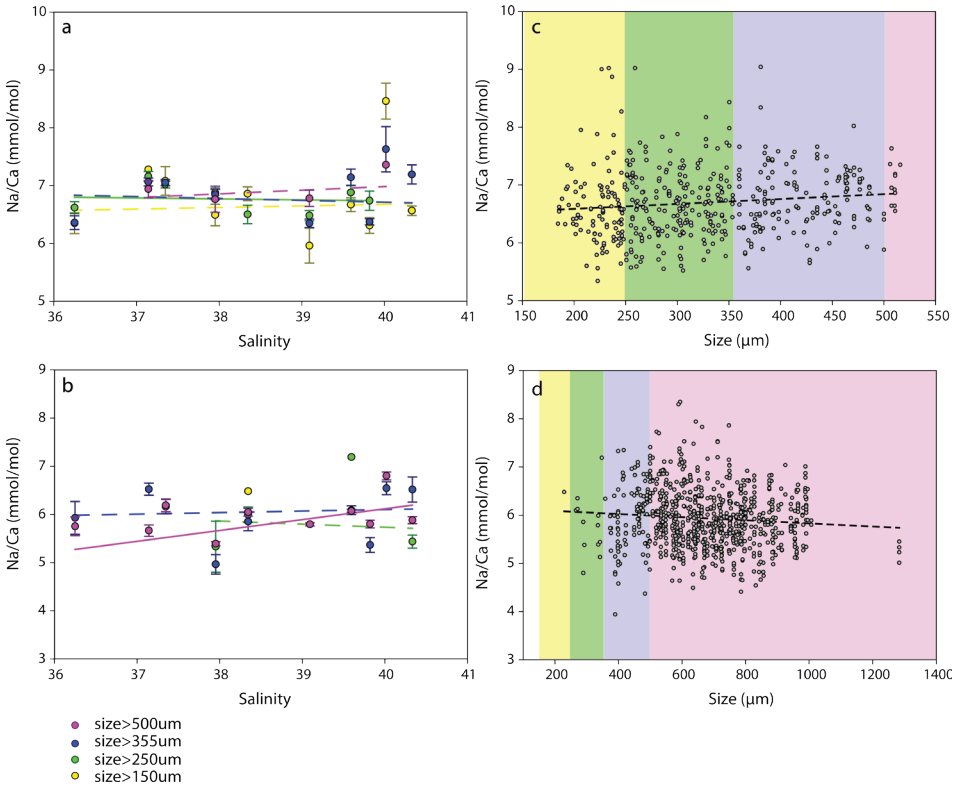

Figure S3.3 Core-top Red Sea Na/Ca values (mmol/mol), with a) *G. ruber* size groups 1-4 and their Na/Ca, b) *T. sacculifer* size groups 1-4 and their Na/Ca, c) *G. ruber* sizes, plotted against all measured Na/Ca values, and d) *T. sacculifer* sizes, plotted against all measured Na/Ca values.

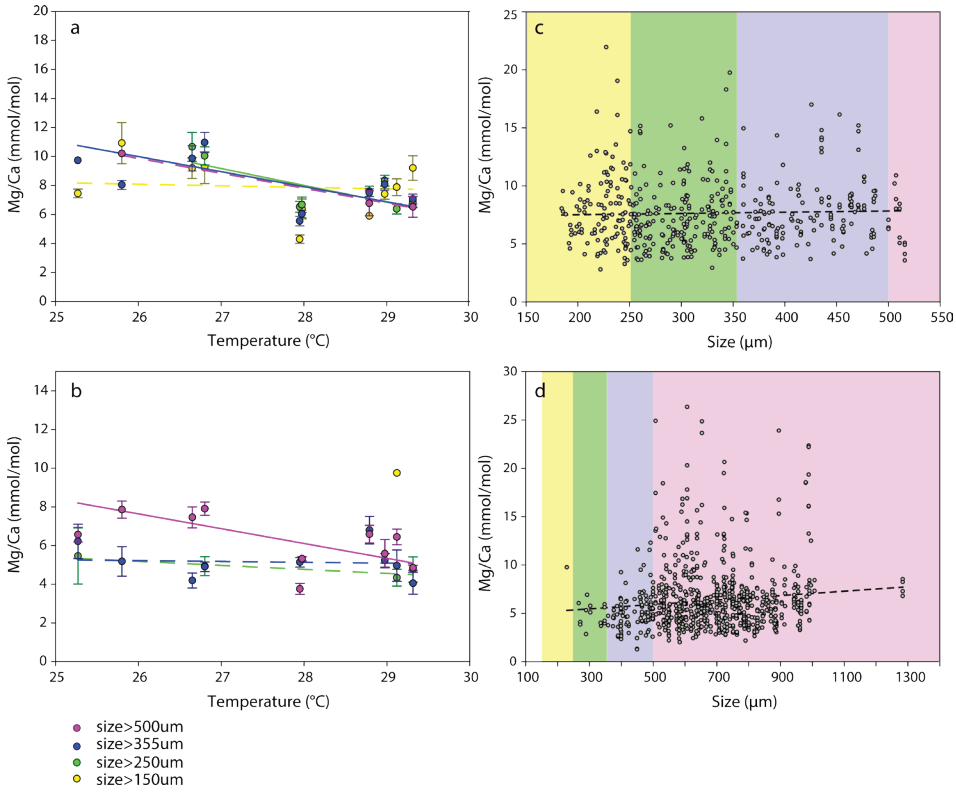

Figure S3.4 Core-top Red Sea Mg/Ca values (mmol/mol), with a) *G. ruber* size groups 1-4 and their Mg/Ca, b) *T. sacculifer* size groups 1-4 and their Mg/Ca, c) *G. ruber* sizes, plotted against all measured Mg/Ca values, and d) *T. sacculifer* sizes, plotted against all measured Mg/Ca values.

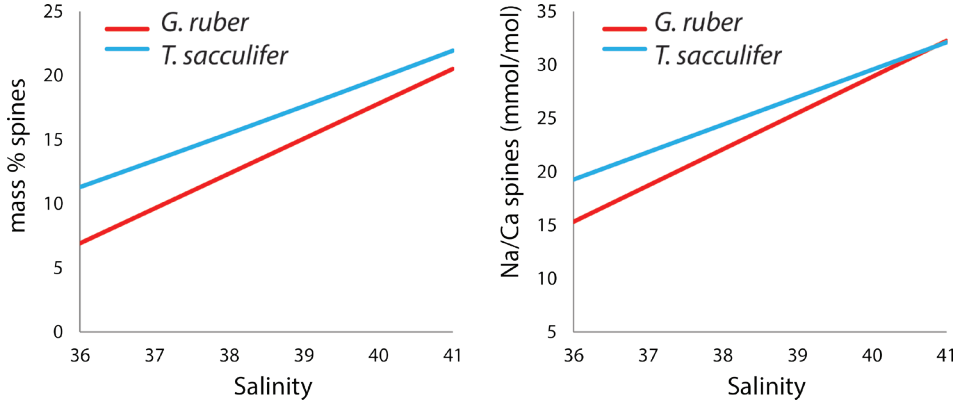

Figure S3.5 Differences in Na/Ca (mmol/mol) between core-top and plankton pump specimens as a function of spine density (a) or Na/Ca concentration of the spines (b).

Table S3.1 Overview depth and normality of the Red Sea plankton tows(a)

				Na/Ca				Mg/Ca			
Net	**depth range [m]**	**species**	**n**	**nm**	**W**	**p**	**normal?**	**nm**	**W**	**p**	**normal?**
05c-net4	10-25	*G. ruber*	*30*	52	0.95	0.02	no	54	0.96	0.06	yes
		T. sacculifer	*30*	61	0.97	0.18	yes	62	0.97	0.12	yes
05c-net3	25-50	*G. ruber*	*34*	65	0.90	<0.001	no	65	0.99	0.61	yes
		T. sacculifer	*30*	40	0.97	0.35	yes	40	0.97	0.34	yes
05c-net2	50-75	*G. ruber*	*34*	62	0.98	0.47	yes	65	0.98	0.27	yes
		T. sacculifer	*30*	82	0.99	0.71	yes	86	0.98	0.18	yes
05c-net1	75-100	*G. ruber*	*30*	54	0.96	0.05	no	56	0.98	0.46	yes
		T. sacculifer	*20*	33	0.99	0.96	yes	33	0.96	0.33	yes
05a-net4	100-150	*G. ruber*	*25*	46	0.98	0.50	yes	46	0.98	0.60	yes
		T. sacculifer	*4*	13	0.96	0.71	yes	14	0.97	0.89	yes
05a-net3	150-200	*G. ruber*	*30*	78	0.96	0.02	no	76	0.99	0.86	yes
		T. sacculifer	*16*	62	0.95	0.02	no	62	0.91	<0.001	no
05a-net2	200-300	*G. ruber*	*25*	62	0.96	0.03	no	62	0.93	0.00	no
		T. sacculifer	*1*	-				-			
05a-net1	300-500	*G. ruber*	*30*	48	0.95	0.03	no	49	0.94	0.02	no
		T. sacculifer	*2*	3	0.77	0.04	no	3	0.88	0.31	yes

a) salinity (S) and temperatures (T) are derived from CTD profiles during RV Pelagia cruise 64PE158

Table S3.2 Overview depth and Na/Ca per size ratios of *G. ruber* of the Red Sea plankton tows(a)

			Na/Ca (mmol/mol)														
		Size (µm): ->	(1) 150-250					(2) 250-355					(3) 355-500				
Net	**depth range [m]**	**species**	**n**	**nm**	**mmol/ mol**	**SD**	**SE**	**n**	**nm**	**mmol/ mol**	**SD**	**SE**	**n**	**nm**	**mmol/ mol**	**SD**	**SE**
05c-net4	10-25	*G. ruber*	10	18	8.36	0.93	0.22	10	17	8.01	0.49	0.12	10	16	8.30	0.62	0.16
05c-net3	25-50	*G. ruber*	15	26	7.07	0.36	0.07	15	29	7.13	0.66	0.12	4	8	7.56	0.85	0.30
05c-net2	50-75	*G. ruber*	15	26	8.37	0.40	0.08	15	30	7.91	0.36	0.07	4	7	7.93	0.33	0.13
05c-net1	75-100	*G. ruber*	25	47	6.95	0.39	0.06	5	9	7.01	0.39	0.13					
05a-net4	100-150	*G. ruber*	22	40	7.61	0.60	0.10	3	6	6.67	0.67	0.27					
05a-net3	150-200	*G. ruber*	27	68	7.93	0.70	0.08	3	9	7.83	0.66	0.22					
05a-net2	200-300	*G. ruber*	25	62	8.01	0.62	0.08										
05a-net1	300-500	*G. ruber*	25	42	7.11	0.47	0.07	5	7	7.53	0.97	0.37					
core-top	1387	*G. ruber*	9	22	6.67	0.56	0.12	8	32	6.87	0.72	0.13	5	22	7.14	0.67	0.14

Table S3.3 Overview depth and Na/Ca per size ratios of *T. sacculifer* of the Red Sea plankton tows(a)

			Na/Ca (mmol/mol)																		
		Size (µm): ->	(1) 150-250					(2) 250-355					(3) 355-500					(4) >500				
Net	**depth range [m]**	**species**	**n**	**nm**	**mmol/mol**	**SD**	**SE**	**n**	**nm**	**mmol/mol**	**SD**	**SE**	**n**	**nm**	**mmol/mol**	**SD**	**SE**	**n**	**nm**	**mmol/mol**	**SD**	**SE**
05c-net4	10-25	*T. sacculifer*	10	16	9.53	0.89	0.22	9	14	9.18	0.53	0.14	10	31	9.19	0.95	0.17					
05c-net3	25-50	*T. sacculifer*	9	11	9.01	0.80	0.24	9	14	8.46	0.66	0.18	10	15	7.14	0.42	0.11					
05c-net2	50-75	*T. sacculifer*	9	13	9.18	0.71	0.20	10	22	8.61	0.62	0.13	19	49	7.99	0.88	0.13					
05c-net1	75-100	*T. sacculifer*						10	19	6.72	0.63	0.14	10	14	6.65	0.72	0.19					
05a-net4	100-150	*T. sacculifer*	2	3	8.18	0.72	0.42	1	4	7.28	1.01	0.50	1	7	6.81	0.36	0.14					
05a-net3	150-200	*T. sacculifer*	10	27	9.22	0.82	0.16	3	17	9.29	0.66	0.16	3	18	9.21	2.09	0.49					
05a-net2	200-300	*T. sacculifer*																				
05a-net1	300-500	*T. sacculifer*	1	1				1	2	7.67	0.92	0.65										
core-top	1387	*T. sacculifer*						3	4	7.73	1.36	0.68	6	34	6.09	0.53	0.09	29	194	6.08	0.48	

a) size 1: 150-250um, size 2: 250-355um, size3: 355-500um

Table S3.4 Overview depth and Mg/Ca per size ratios of *G. ruber* of the Red Sea plankton tows(a)

			Mg/Ca (mmol/mol)														
		Size (µm): ->	(1) 150-250					(2) 250-355					(3) 355-500				
Net	**depth range [m]**	**species**	**n**	**nm**	**mmol/mol**	**SD**	**SE**	**n**	**nm**	**mmol/mol**	**SD**	**SE**	**n**	**nm**	**mmol/mol**	**SD**	**SE**
05c-net4	10-25	*G. ruber*	10	20	6.26	0.90	0.20	10	19	6.34	1.12	0.26	10	17	6.86	0.91	0.22
05c-net3	25-50	*G. ruber*	15	29	5.37	1.15	0.21	15	30	6.11	1.27	0.23	4	8	5.44	0.90	0.32
05c-net2	50-75	*G. ruber*	15	29	6.72	1.40	0.26	15	30	7.33	1.57	0.29	4	8	6.73	0.55	0.19
05c-net1	75-100	*G. ruber*	25	48	6.49	1.19	0.17	5	10	6.68	0.85	0.27					
05a-net4	100-150	*G. ruber*	22	42	7.36	1.55	0.24	3	6	4.99	0.51	0.21					
05a-net3	150-200	*G. ruber*	27	70	5.80	1.26	0.15	3	10	7.05	1.69	0.54					
05a-net2	200-300	*G. ruber*	25	65	6.40	2.23	0.28										
05a-net1	300-500	*G. ruber*	25	44	5.92	1.16	0.17	5	7	8.10	3.90	1.47					
core-top	1387	*G. ruber*	9	22	9.23	5.15	1.10	8	33	8.25	3.73	0.65	5	21	10.97	3.20	0.70

Table S3.5 Overview depth and Mg/Ca per size ratios of *T. sacculifer* of the Red Sea plankton tows(a)

			Mg/Ca (mmol/mol)																			
		Size (µm): ->	(1) 150-250					(2) 250-355					(3) 355-500					(4) >500				
Net	**depth range [m]**	**species**	**n**	**nm**	**mmol/mol**	**SD**	**SE**	**n**	**nm**	**mmol/mol**	**SD**	**SE**	**n**	**nm**	**mmol/mol**	**SD**	**SE**	**n**	**nm**	**mmol/mol**	**SD**	**SE**
05c-net4	10-25	*T. sacculifer*	10	16	5.29	0.80	0.20	9	14	3.95	0.60	0.16	10	31	4.44	0.77	0.14					
05c-net3	25-50	*T. sacculifer*	9	10	4.07	0.43	0.13	9	13	3.90	0.59	0.16	10	15	3.81	0.58	0.15					
05c-net2	50-75	*T. sacculifer*	9	13	6.06	1.19	0.33	10	23	4.80	1.09	0.23	19	50	4.83	0.96	0.14					
05c-net1	75-100	*T. sacculifer*						10	19	5.14	1.20	0.27	10	14	4.68	1.66	0.44					
05a-net4	100-150	*T. sacculifer*	2	3	5.24	0.91	0.52	1	4	6.52	0.47	0.24	1	7	7.28	1.08	0.41					
05a-net3	150-200	*T. sacculifer*	10	27	4.47	0.91	0.18	3	17	4.19	0.57	0.14	3	18	5.19	1.53	0.36					
05a-net2	200-300	*T. sacculifer*																				
05a-net1	300-500	*T. sacculifer*	1	1				1	2	4.87	0.05	0.04										
core-top	1387	*T. sacculifer*						3	4	4.94	0.98	0.49	6	34	4.90	1.46	0.25	29	204	7.91	4.91	0.34

a) size 1: 150-250um, size 2: 250-355um, size3: 355-500um

Table S3.6 Overview normality Red Sea core-top samples, *G. ruber*

				Na/Ca				Mg/Ca			
Cruise	**Name**	**species**	**n**	**nm**	**W**	**p**	**normal?**	**nm**	**W**	**p**	**normal?**
M 44/3	MC-601	*G. ruber*	31	58	0.966	0.106	yes	59	0.954	0.025	no
M 31/2	MC363	*G. ruber*	11	12	0.828	0.02	no	12	0.949	0.622	yes
M 31/2	MC364	*G. ruber*	30	62	0.983	0.542	yes	63	0.978	0.314	yes
M 5/2	MC-71	*G. ruber*	22	76	0.965	0.036	no	76	0.916	<0.001	no
VA 29	707KG	*G. ruber*	30	59	0.987	0.765	yes	57	0.978	0.369	yes
M 5/2	MC-101	*G. ruber*	37	55	0.974	0.275	yes	53	0.968	0.165	yes
M 5/2	MC-107	*G. ruber*	30	28	0.953	0.239	yes	30	0.975	0.675	yes
M 31/2	MC366	*G. ruber*	30	53	0.979	0.474	yes	54	0.975	0.303	yes
SO 121	SO-98	*G. ruber*	20	43	0.99	0.96	yes	43	0.98	0.633	yes
SO 121	SO-100	*G. ruber*	17	39	0.962	0.204	yes	40	0.972	0.408	yes
SO 121	SO-110	*G. ruber*	28	47	0.957	0.08	yes	46	0.98	0.599	yes

Table S3.7 Overview normality Red Sea core-top samples, *T. sacculifer*

				Na/Ca				Mg/Ca			
Cruise	**Name**	**species**	**n**	**nm**	**W**	**p**	**normal?**	**nm**	**W**	**p**	**normal?**
M 44/3	MC-601	*T. sacculifer*	37	64	0.94	0.003	no	63	0.907	<0.001	no
M 31/2	MC363	*T. sacculifer*	38	69	0.978	0.278	yes	68	0.92	<0.001	no
M 31/2	MC364	*T. sacculifer*	30	62	0.988	0.813	yes	60	0.806	<0.001	no
M 5/2	MC-71	*T. sacculifer*	36	242	0.985	0.013	no	242	0.767	<0.001	no
VA 29	707KG	*T. sacculifer*	28	154	0.982	0.038	no	156	0.985	0.098	no
M 5/2	MC-101	*T. sacculifer*	45	93	0.976	0.081	yes	93	0.904	<0.001	no
M 5/2	MC-107	*T. sacculifer*	16	41	0.956	0.119	yes	41	0.919	0.006	no
M 31/2	MC366	*T. sacculifer*	32	113	0.989	0.46	yes	111	0.978	0.065	yes
SO 121	SO-98	*T. sacculifer*	12	42	0.983	0.773	yes	42	0.932	0.016	no
SO 121	SO-100	*T. sacculifer*	7	22	0.93	0.121	yes	22	0.953	0.361	yes
SO 121	SO-110	*T. sacculifer*	7	14	0.973	0.918	yes	12	0.952	0.662	yes

4

Chapter 4

Planktonic foraminiferal spine versus shell carbonate Na incorporation in relation to salinity

Eveline M. Mezger

Lennart J. de Nooijer

Jacqueline Bertlich

Jelle Bijma

Dirk Nürnberg

Gert-Jan Reichart

Published in Biogeosciences (2019)

Abstract

Sea surface salinity is one of the most important parameters to reconstruct in paleoclimatology, reflecting amongst others the hydrological cycle, paleo-density, ice volume, and regional and global circulation of water masses. Recent culture studies and a Red Sea field study revealed a significant positive relation between salinity and Na incorporation within benthic and planktonic foraminiferal shells. However, these studies reported varying partitioning of Na between and within the same species. The latter could be associated with ontogenetic variations, most likely spine loss. Varying Na concentrations were observed in different parts of foraminiferal shells, with especially spines and regions close to the primary organic sheet being enriched in Na. In this study, we unravel the Na composition of different components of the planktonic foraminiferal shell wall using Electron Probe microanalysis (EPMA) and solution-ICP-MS. A model is presented to interpret EPMA data for spines and spine bases to quantitatively assess differences in composition and contribution to whole shell Na/Ca signals. The same model can also be applied to other spatial inhomogeneities observed in foraminiferal shell chemistry, like elemental (e.g. Mg, Na, S) banding and/or hotspots. The relative contribution of shell carbonate, organic linings, spines and spine bases to whole shell Na chemistry is considered quantitatively. This study shows that whereas the high Na areas may be susceptible to taphonomic alterations, the Na chemistry of the shell itself seems relatively robust. Comparing both shell and spine Na/Ca values with salinity shows that shell chemistry records salinity, albeit with a very modest slope.

4.1 Introduction

Salinity is one of the most wanted parameters to reconstruct in paleoceanography, driving together with temperature, the thermohaline circulation as well as reflecting regional hydrological cycling. Whereas temperature can be reconstructed by a variety of proxies (e.g. $U^{k'}_{37}$: Prahl and Wakeham, 1987; foraminiferal Mg/Ca: Elderfield and Ganssen, 2000;Lea et al., 1999;Nürnberg et al., 1996; foraminiferal $\delta^{18}O$: e.g. Zachos et al., 2001;Elderfield and Ganssen, 2000 and TEX_{86}: Schouten et al., 2002), equally reliable proxies for salinity are still under development (Wit et al., 2013;Mezger et al., 2016;Allen et al., 2016;Rohling and Bigg, 1998;Schouten et al., 2006). A number of approaches have been proposed to reconstruct salinity, including a combination of stable isotopes ($\delta^{18}O$ from foraminiferal shells or δD of long chain ketones) with independent reconstructions of sea surface temperature (e.g. Mg/Ca or $U^{k'}_{37}$, Elderfield and Ganssen, 2000;Schouten et al., 2006); foraminiferal Ba/Ca (Weldeab, 2007), dinoflagellate cyst morphology (e.g. Verleye et al., 2012;Mertens et al., 2012) and δD of long chain ketones and alkenones (e.g. Vasiliev et al., 2017). However, uncertainties associated with the indirect controls on these proxy signals or preservation issues result in (large) errors in the reconstructed salinity (Rohling, 2007). This can be circumvented by a more direct approach, related to elements determining seawater salinity (e.g. Cl, Na). Even though Na is considered as a conservative element in seawater, recent culture studies and a Red Sea field study reveal a significant positive relation between salinity and Na incorporation within benthic (Wit et al., 2013;Geerken et al., 2018) and planktonic (Allen et al., 2016;Mezger et al., 2016;Bertlich et al., 2018) foraminiferal shells. This relation between salinity and Na incorporation, potentially related to an increase of the Na^+/Ca^{2+} activity ratio with salinity, is not only observed for foraminiferal calcite (Allen et al., 2016;Mezger et al., 2016;Wit et al., 2013), but also for barnacles and Atlantic oyster shells (Rucker and Valentine, 1961;Gordon et al., 1970) and inorganically precipitated calcium carbonate (Kitano et al., 1975;Ishikawa and Ichikuni, 1984).

Previous studies on the incorporation of Na into biogenic and inorganic calcite varied in reported partition coefficients, despite similar conditions (White, 1978;Ishikawa and Ichikuni, 1984;Kitano et al., 1975). These differences are not only observed between inorganic and biogenic studies, but also between and within the same foraminiferal species, either growing in culture or the natural environment (Mezger et al., 2016;Allen et al., 2016;Wit et al., 2013;Bertlich et al., 2018). Recently, Mezger et al. (2018) studied the preservation of the Na-salinity signal of the *G. ruber* and *T. sacculifer* species through the

water column, comparing sedimentary and water-column collected specimens (0-500 m) of the Red Sea. It was found that Na/Ca values decrease with water depth, thereby aligning the lower Na/Ca from the surface sediment samples with those observed in culture studies (Allen et al., 2016;Wit et al., 2013;Mezger et al., 2018;Bertlich et al., 2018). The loss of spines, highly enriched in Na (Branson et al., 2016;Mezger et al., 2016), during settling in the water column is hypothesized to be the controlling factor of the decreasing Na/Ca values, as foraminifera shed their spines before gametogenesis (Bé, 1980). Furthermore, it has been suggested that calcite growth rate (Busenberg and Plummer, 1985), temperature (Allen et al., 2016), environmental differences between field and controlled growth experiments (Wit et al., 2013;Allen et al., 2016;Mezger et al., 2016), life stages (Mezger et al., 2018) ageing/leakage (Yoshimura et al., 2017), or organic linings (Yoshimura et al., 2017;Branson et al., 2016) affect Na incorporation. The inhomogeneous inter-shell distribution of sodium, partially due to life stage, could influence measured Na values (Geerken et al., 2018;Branson et al., 2016;Mezger et al., 2018), and potentially explain part of the observed differences. Similar to reports for other inter-shell element distributions (e.g. Mg: Sadekov et al., 2005;Hathorne et al., 2009;Kunioka, 2006), Na appears to occur in bands of alternating high- and low concentrations (Geerken et al., 2018). However, the thickness and intensity of these bands is not similar between species (Geerken et al., 2018). For the planktonic species *Globigerinoides ruber* and *Trilobatus sacculifer*, elevated concentrations of Na are also observed in regions where the spines meet the rest of the shell wall (Branson et al., 2016;Mezger et al., 2018), close to the Primary Organic Sheet (POS). This may indicate that different species vary in their calcification mechanisms: i.e. spines and gametogenic (GAM) calcite in planktonic species may be precipitated by different biomineralization pathways and hence, may have various element compositions (Steinhardt et al., 2015;Nürnberg et al., 1996;Sadekov et al., 2005). Clearly, the internal Na distribution influences measured Na/Ca values and is hence important for the potential application of foraminiferal shell Na/Ca for salinity reconstructions. In this study, different parts of planktonic foraminiferal shells are distinguished geochemically to quantify the relative contribution of shell calcite, spine calcite and organic linings on the total foraminiferal Na/Ca. We use high resolution quantitative Electron Probe Microanalyses (EPMA) to distinguish differences in element composition between different parts of the shell and Scanning Electron Microscopy (SEM) to determine the relative contribution of spines (thickness, density) of surface water specimens. Not only field collected surface water specimens (Mezger et al., 2016), but also cultured *T. sacculifer* (Bertlich et al., 2018), Red Sea water column and surface sediment *T. sacculifer* and *G. ruber* specimens (Mezger et al., 2018) are measured for comparison. Furthermore, we assess the impact

on the foraminiferal shell chemistry of the organic linings by isolating these linings and analyzing their Na/Ca. These data are subsequently evaluated along a (surface water) salinity gradient, considering the potential impact of taphonomic alterations to evaluate the proxy potential of foraminiferal shell Na/Ca values.

4.2 Methodology

Living Red Sea field-collected *T. sacculifer* and *G. ruber* specimens were collected in May 2000 during RV Pelagia cruise 64PE158 (Mezger et al., 2016). Core-top and box-core (upper 0-1 cm) specimens from similar locations were collected during different cruises as described in Siccha et al. (2009). Cultured *T. sacculifer* specimens were collected at 3–8 m water depth 1–2 miles off the south coast of Curacao and off the west coast of Barbados, after which they were grown in filtered seawater with salinities ranging from 26 to 45 (Nürnberg et al., 1996;Bijma et al., 1990;Bertlich et al., 2018). To study the relative contribution of Na in different parts of the shell to the total Na/Ca composition, high resolution quantitative Electron Probe microanalyses was performed at Utrecht University (section 4.2.1). Spine thickness and densities (number of spines per surface area) were derived by Scanning Electron Microscopy (section 4.2.2). For the chemical analyses of organic linings (section 4.2.3), foraminifera within the size fraction of 250-355 µm for *T. sacculifer* and 100-355 µm for *G. ruber* were collected from calcareous ooze, retrieved by a gravity core at the Walvis ridge (similar to the material used for the NFHS-1, Mezger et al., 2016).

4.2.1 Electron Probe Micro Analyses (EPMA)

The Na/Ca composition of the spines and shells collected from the Red Sea water column, and core-tops were measured at a high spatial resolution using EPMA (Table 4.1). Several specimens of both species were selected and embedded in resin (Araldite 20/20) in a vacuum chamber. Multi-net collected specimens were isolated directly upon low temperature ashing for spine analysis and transferred without sieving to preserve the spines and embedded in resin as well (Mezger et al., 2018). After drying for at least 48 hours in an oven at approximately 50°C, the specimens embedded in resin were polished. This polishing was performed until reaching the center of the shell, as potential differences in element incorporation related to the 3D structure of foraminiferal shells are still not well known. Upon polishing samples were cleaned by rinsing three times with double de-ionized water and coated with carbon after drying. Element mapping for Na and Ca of cultured specimens of *T. sacculifer* (Bertlich et al., 2018) as well as Red Sea-derived

Table 4.1. List of characteristics of the EPMA measurements, excluding the multi-nets. The phrase 'in-situ' indicates that the measured chambers were not grown in culture, but formed in the natural environment 1-2 miles off the south coast of Curaçao (S=~35.9) before sampling. 'PP' refers to Red Sea plankton pump samples, 'CT' to Red Sea core-tops samples and 'exp' to experiments.

Position	species	PP/CT/ exp	Magni-fication	HFW (total picture pixel width in µm)	pixel size (µm)	T (°C)	S
31Jan_1	*G. ruber*	PP	2500	48	0.24	29.4	37.3
31Jan_2	*G. ruber*	PP	2500	48	0.24	29.4	37.3
31Jan_3	*T. sacculifer*	PP	2500	48	0.24	29.4	37.3
31Jan_4	*T. sacculifer*	PP	2500	48	0.27	29.4	37.3
31Jan_5	*T. sacculifer*	PP	2500	48	0.24	29.4	37.3
31Jan_6	*T. sacculifer*	PP	2500	48	0.27	26.3	39.6
31Jan_7	*G. ruber*	CT	2500	48	0.24	26.7	39.8
31Jan_8	*T. sacculifer*	CT	1600	75	0.38	26.7	39.8
31Jan_9	*T. sacculifer*	CT	2300	52	0.26	26.7	39.8
2Feb_1	*G. ruber*	CT	1700	48	0.24	26.7	39.8
2Feb_2	*G. ruber*	PP	2000	54	0.27	26.3	39.6
1Feb_1	*T. sacculifer*	T-exp	1400	86	0.43	23.5	36
1Feb_2	*T. sacculifer*	T-exp	2000	60	0.30	19.5	33
1Feb_3	*T. sacculifer*	T-exp	2500	48	0.24	19.5	33
1Feb_4	*T. sacculifer*	T-exp	1700	71	0.35	in-situ	in-situ
1Feb_5	*T. sacculifer*	T-exp	1400	86	0.34	26.5	33
2Feb_1	*T. sacculifer*	S-exp	1700	71	0.35	in-situ	in-situ
2Feb_2	*T. sacculifer*	S-exp	2222	54	0.30	in-situ	in-situ
2Feb_3	*T. sacculifer*	S-exp	2500	48	0.24	in-situ	in-situ
2Feb_4	*T. sacculifer*	S-exp	2222	54	0.30	26.5	45
2Feb_5	*T. sacculifer*	S-exp	1800	67	0.33	in-situ	in-situ
2Feb_6	*T. sacculifer*	S-exp	2200	55	0.27	in-situ	in-situ
3Feb_1	*G. ruber*	CT	1700	48	0.24	26.7	39.8
3Feb_2	*G. ruber*	PP	2000	54	0.27	26.3	39.6

specimens of *G. ruber* and *T. sacculifer* was performed with an electron microprobe at Utrecht University (JEOL JXA-8530F Field emission Electron Probe Micro Analyzer). Maps were generated with a focused electron beam, a beam current of 10 nA and an accelerating voltage of 7 kV. The dwell time was set at 300 ms and pixel sizes ranged between 0.2 and 0.43 µm. Counts, representing current strength, were converted to elemental ratios using analyses on standard material. We used Jadeite for Na, foraminiferal calcite for Ca and Forsterite for Mg, assuming a linear dependency of concentration (in mass %) on the signal and a constant background. Background intensities, measured for the same (foraminiferal) samples with similar settings, were subtracted from total element intensities before converting to mass %. Single points were eliminated from further analyses when the Ca mass percentage of that spot was below 30%. Unfortunately, this (EPMA) method did not allow for chlorine (Cl) measurements, being present in seawater in similar concentrations as Na and therefore potentially also a suitable proxy for salinity, since their concentrations in calcite are much lower (~40 times) than those of Na (Kitano et al., 1975).

In this article, we refer to 'whole shell' for total shell measurements including high Na regions such as spines (e.g. laser ablation measurements in Mezger et al., 2016), and 'shell-only' when spine (base) regions are excluded from analysis. For the elemental analyses of the foraminiferal shell, regions of the shell not containing spines (shell-only) were selected including potential banding, but excluding Na hotspots, which were observed near spine bases (e.g. Fig. 4.1 and Fig. S4.1). Deconvolving the "true" maximum Na values within the mixed spine signal is challenging, as the EPMA Na/Ca signal has a limited resolution. Values hence consist of shell calcite values, as well as pixel averaged mixed signals and the real spine signal. Because of the limited size of the spines and spine bases only a few of the analyses will capture spine carbonate, while more analyses capture a mixture of both spine and ontogenetic carbonate and most analyses will show ontogenetic carbonate only. In the discussion, we suggest how the limited data of the spine chemistry can still be interpreted (section 4.4.2).

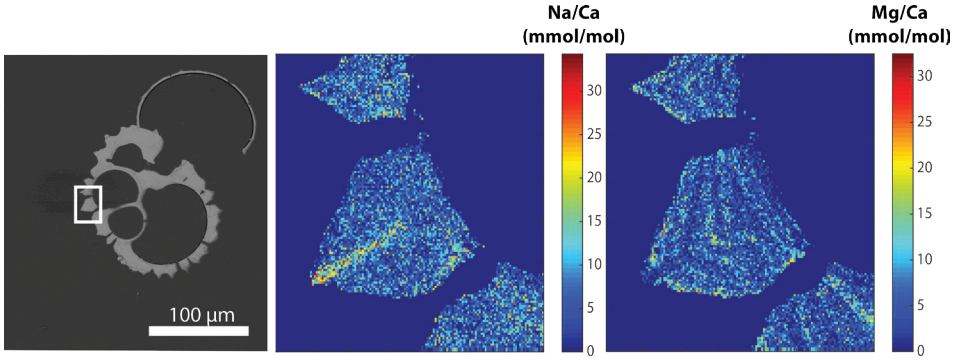

Figure 4.1. Example of a backscattered electron overview image of an embedded and polished *G. ruber* plankton tow specimen with the white square indicating the zoom-in region (left), and the Na/Ca (middle) and Mg/Ca (right) EPMA images of this zoom-in, showing the relative distribution of both elements within the shell. Whereas Na appears to be mainly concentrated in the spine (base), Mg mainly occurs in clear bands sloping upwards towards the spine and somewhat lower in the spine region (Mezger et al., 2018).

The similarity between Na/Ca EPMA measurements of the same cultured *T. sacculifer* specimens performed at GEOMAR in Kiel, grown at different salinity and temperature conditions (for standards and measurements: Bertlich et al., 2018) and Utrecht University was used to assess consistency of the measurements, which was between 101.8% and 106.4% for the line scans and between 101 and 122% for the maps (concentrations Utrecht/Kiel). These values are a conservative estimate, as the selection of the lines and regions to compare are never identical to previous measurements on the same shell (Fig. S4.2). Details for these cultured specimens can be found in (Bijma et al., 1990). Elemental analysis on JCP-1 powder (n=6) (Okai et al., 2002) were included, with similar settings as the sample measurements, to assess accuracy (sample/reference) of Sr (99.3%), Mg (106.3%), S (103.4%) and Na (85%). Although the error on the Na quantification is considerable, offsets are minor compared to the ranges studied here.

4.2.2 Scanning Electron Microscopy

Surface structures of foraminifera, including spine density, length and width, were quantified using scanning electron microscopy (Hitachi High-Tech TM3000 TableTop scanning electron microscope). However, as a consequence of sampling (plankton pump, sieving) and sample preparation (low temperature ashing – LTA Mezger et al., 2016;Fallet et al., 2010), many of the spines (partially) broke off and the total spine lengths could not be determined and not used for further calculations. Spine density was calculated from pictures of a 50 µm x 50 µm square, focusing on the F-2 and if not available, the final or penultimate chamber. We used the surface water collected specimens for two

species (*G. ruber* and *T. sacculifer*), which were measured previously for their Na/Ca composition with laser ablation-Q-ICP-MS (Mezger et al., 2016). Previously ablated areas were avoided, but using these exact specimens allows comparing the earlier published whole shell data (respectively shells including spine(s) (bases)) with the here presented spine distributions. The number of spines was determined by counting the number of pores, as these morphological features are more robust. This quantification is based on the assumption that a spine is/was present at every corner of the cancellated (hexagonal) shell structure around each pore for these species (Bé, 1980). The thickness of the round spines was measured at the base of the spine. This effectively avoids potential pitfalls of the method associated with tapering of spines (Fig. 4.2). Foraminiferal size was measured as described by Mezger et al. (2016).

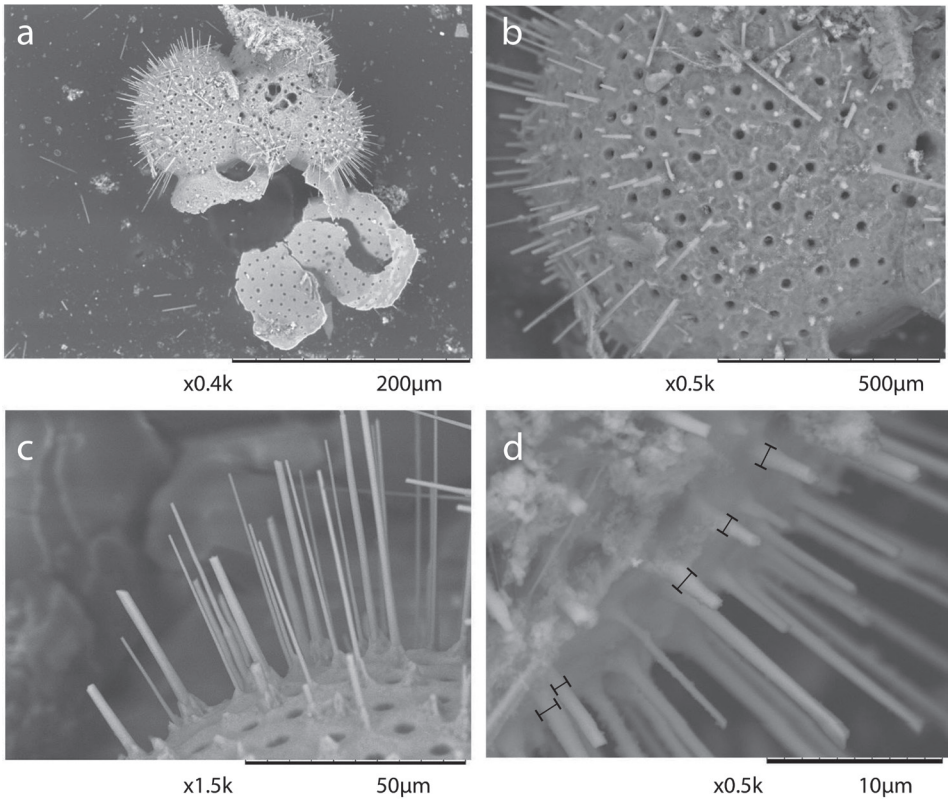

Figure 4.2. Example of SEM-images of the foraminiferal specimens studied here: a) example of a laser-ablated *T. sacculifer* specimen, b) spine count area in the F-2 chamber, c) zoom-in of spines, showing the tapering shape of spines and d) spine width measurements at the base of the spines.

4.2.3 Organic linings

For isolation of organic linings, 257 *G. ruber* specimens and 150 *T. sacculifer* specimens were selected from a calcareous ooze isolated from a gravity core recovered from the Walvis ridge (similar to the material used for the NFHS-1: Mezger et al., 2016). After isolation of the specimens, samples were treated to remove organic matter on the outside of the shell with buffered 1% hydrogen peroxide in a heated water bath at 90°C. Thereafter, samples were crushed lightly to enable clay particle removal from the inside of the shell by ultra-sonication. The calcite shells were subsequently dissolved in a glass beaker filled with 0.1M ultrapure weak acetic acid, leaving these overnight to dissolve. After visual inspection of the dissolution of the shells, organic linings (OL) were isolated, centrifuged and rinsed three times with ultrapure water. Weights were determined after drying the isolated linings in a laminar cabinet at room temperature. In total, 0.04 mg OL was isolated from 5.66 mg *T. sacculifer* shells (0.7%), and 0.02 mg OL from 4.95 mg *G. ruber* (0.4%). After drying and weighing, the isolated OL was destructed in a PTFE tube overnight in an oxidative acid mixture (0.09 mL ultrapure HNO_3 and 0.01 mL ultrapure perchloric acid) in a 70°C water bath. The sample was brought to near dryness before being transferred to a PTFE digestion tube with 0.075 mL ultrapure HNO_3 and kept at 150°C for 12 hours. After cooling down another aliquot of 0.05 mL ultrapure perchloric acid was added and left to react at 180°C on a thermostatic block. After the samples were inspected for total destruction the sample was diluted to 2.5 mL with ultrapure water and small amounts of ultrapure HNO_3. The elemental composition was subsequently measured with a Thermo Fisher Scientific iCAP-Q. Elements were quantified using their relevant isotopes (respectively ^{23}Na, ^{24}Mg, ^{43}Ca and ^{88}Sr). Calibration standards used were taken up in a similar matrix (1M HNO_3). OL quantifications were based on back calculating original shell and OL weights.

4.3 Results

4.3.1 EPMA

Shell Na/Ca

Generally, Na is rather homogeneously distributed throughout the shell, although Na hotspots are observed in spines and near the spine bases (Fig. 4.1, Fig. S4.1). For none of the specimens from plankton pumps, core-tops or multi-nets, banding is observed, except for one specimen of *T. sacculifer* (specimen 31-4). Several areas from shell cross-sections were selected in such a way to avoid areas enriched in Na ('shell-only'). This basically excludes areas with spines and spine bases. Plankton pump shell-only *G. ruber* Na/Ca values range

from 5.6 ±0.18 to 7.7 ±0.25 mmol/mol (averages and standard errors) for a Red Sea surface water salinity of 37.3 and between 5.91 ±0.21 and 6.39 ±0.29 for a Red Sea surface water salinity of 39.6 (Table 4.2). For plankton pump collected *T. sacculifer*, shell-only Na/Ca values range between 6.12 ±0.20 and 6.83 ±0.13 mmol/mol for a Red Sea surface water salinity of 37.3 and between 6.12 ±0.15 and 6.75 ±0.31 for a Red Sea surface water salinity of 39.6 (Table 4.2). Shells collected from the 0 to 100 m water depth interval show Na/Ca values for *T. sacculifer* ranging from 5.6 ±0.12 mmol/mol to 7.1 ±0.10 mmol/mol and for *G. ruber* between 5.95 ±0.13 and 8.42 ±0.18 (Table 4.3). Core-top shell-only Na/Ca values range from 5.41 ±0.17 to 6.84 ±0.25 mmol/mol for *G. ruber* and from 5.52±0.14 to 6.22±0.23 mmol/mol for *T. sacculifer* (Table 4.2).

Table 4.2. Overview EPMA shell measurements of different parts of the shell for core-tops and plankton pumps.

Position	Species	PP/CT	Salinity	#Pixels	Na/Ca mean (mmol/mol)	Na/Ca median (mmol/mol)	SD	SE
31Jan_7	*G. ruber*	CT	39.8	1512	5.45	4.28	3.55	0.10
31Jan_7	*G. ruber*	CT	39.8	810	5.45	5.32	3.42	0.13
31Jan_7	*G. ruber*	CT	39.8	549	5.41	4.05	3.75	0.17
31Jan_7	*G. ruber*	CT	39.8	630	5.76	4.48	3.70	0.16
31Jan_8	*T. sacculifer*	CT	39.8	310	6.02	5.63	3.91	0.23
31Jan_8	*T. sacculifer*	CT	39.8	368	6.18	5.83	3.97	0.21
31Jan_8	*T. sacculifer*	CT	39.8	180	5.69	4.10	4.14	0.31
31Jan_8	*T. sacculifer*	CT	39.8	405	6.22	5.91	3.98	0.23
31Jan_8	*T. sacculifer*	CT	39.8	288	5.98	5.90	3.76	0.24
31Jan_9	*T. sacculifer*	CT	39.8	864	5.52	4.25	3.74	0.14
31Jan_9	*T. sacculifer*	CT	39.8	851	5.78	4.37	3.89	0.14
3Feb_1	*G. ruber*	CT	39.8	288	6.84	6.34	4.16	0.25
3Feb_1	*G. ruber*	CT	39.8	350	6.72	6.27	4.22	0.23
3Feb_1	*G. ruber*	CT	39.8	774	6.36	5.96	3.95	0.15
3Feb_1	*G. ruber*	CT	39.8	644	6.39	6.00	4.03	0.17
31Jan_1	*G. ruber*	PP2	37.3	420	5.75	5.40	3.78	0.20
31Jan_1	*G. ruber*	PP2	37.3	444	5.66	4.27	3.84	0.20
31Jan_1	*G. ruber*	PP2	37.3	468	5.89	5.40	4.03	0.20
31Jan_1	*G. ruber*	PP2	37.3	468	5.60	4.31	3.72	0.18
31Jan_1	*G. ruber*	PP2	37.3	546	6.62	5.91	4.38	0.20
31Jan_1	*G. ruber*	PP2	37.3	420	6.61	6.02	4.12	0.20

Table 4.2. *(continued)* Overview EPMA shell measurements of different parts of the shell for core-tops and plankton pumps.

Position	Species	PP/CT	Salinity	#Pixels	Na/Ca mean (mmol/mol)	Na/Ca median (mmol/mol)	SD	SE
31Jan_2	*G. ruber*	PP2	37.3	476	7.73	6.98	5.03	0.25
31Jan_2	*G. ruber*	PP2	37.3	476	7.66	7.27	4.98	0.25
31Jan_3	*T. sacculifer*	PP2	37.3	406	6.77	6.20	4.50	0.14
31Jan_3	*T. sacculifer*	PP2	37.3	338	6.81	6.34	4.22	0.17
31Jan_3	*T. sacculifer*	PP2	37.3	351	6.29	5.97	4.03	0.15
31Jan_3	*T. sacculifer*	PP2	37.3	450	6.86	6.18	4.26	0.17
31Jan_3	*T. sacculifer*	PP2	37.3	540	6.12	5.75	3.90	0.20
31Jan_4	*T. sacculifer*	PP2	37.3	1584	6.37	5.97	4.09	0.23
31Jan_4	*T. sacculifer*	PP2	37.3	858	6.32	5.93	3.82	0.22
31Jan_4	*T. sacculifer*	PP2	37.3	720	6.50	5.99	4.41	0.22
31Jan_4	*T. sacculifer*	PP2	37.3	768	6.36	5.95	4.01	0.18
31Jan_5	*T. sacculifer*	PP2	37.3	858	6.83	6.10	4.48	0.13
31Jan_5	*T. sacculifer*	PP2	37.3	756	6.54	5.98	4.23	0.15
31Jan_5	*T. sacculifer*	PP2	37.3	204	6.48	5.94	4.21	0.16
31Jan_6	*T. sacculifer*	PP7	39.6	357	6.44	5.72	4.44	0.17
31Jan_6	*T. sacculifer*	PP7	39.6	476	6.49	5.97	4.41	0.15
31Jan_6	*T. sacculifer*	PP7	39.6	261	6.12	5.52	4.01	0.15
31Jan_6	*T. sacculifer*	PP7	39.6	208	6.75	6.25	4.51	0.32
3Feb_2	*G. ruber*	PP7	39.6	1053	6.20	5.88	4.08	0.23
3Feb_2	*G. ruber*	PP7	39.6	735	5.91	5.60	3.88	0.20
3Feb_2	*G. ruber*	PP7	39.6	780	6.32	5.93	3.99	0.26
3Feb_2	*G. ruber*	PP7	39.6	6952	6.39	6.05	4.07	0.29

Table 4.3. Overview of multi-net Na/Ca shell values. Similar colors indicate that these are measurements from the same specimen (except for the white color).

Position	Species	#Pixels	Na/Ca mean (mmol/mol	Na/Ca median (mmol/mol)	SD	SE
0001_1	*T. sacculifer*	2898	7.09	6.77	4.58	0.10
0001_1	*T. sacculifer*	1568	6.96	6.33	4.78	0.13
0002_1	*T. sacculifer*	903	6.61	5.67	4.32	0.15
0002_3	*T. sacculifer*	1060	6.76	6.69	4.14	0.13
0002_4	*T. sacculifer*	2652	6.13	5.27	4.06	0.08
0002_8	*T. sacculifer*	609	6.08	5.17	4.25	0.17
0002_8	*T. sacculifer*	587	6.30	5.25	4.79	0.20
0002_11	*T. sacculifer*	1109	6.79	6.54	4.38	0.13
0002_12	*T. sacculifer*	567	5.80	5.09	4.18	0.18
0002_12	*T. sacculifer*	1567	5.73	4.89	4.10	0.10
0002_13	*T. sacculifer*	1150	5.55	4.91	3.93	0.12
0004_24	*T. sacculifer*	966	6.26	5.50	4.18	0.13
0004_7	*G. ruber*	777	8.42	7.43	5.04	0.18
0004_7	*G. ruber*	913	8.07	7.52	4.84	0.16
0004_12	*G. ruber*	1299	6.82	6.65	4.32	0.12
0004_13	*G. ruber*	1195	6.90	6.65	4.37	0.13
0004_14	*G. ruber*	1361	7.12	6.81	4.27	0.12
0004_15	*G. ruber*	1013	5.95	5.18	4.08	0.13
0004_16	*G. ruber*	2479	6.78	6.58	4.47	0.09
0004_17	*G. ruber*	1248	6.88	6.47	4.62	0.13
0004_18	*G. ruber*	1665	5.97	5.04	4.09	0.10
0004_19	*G. ruber*	439	6.29	5.33	4.13	0.20
0004_22	*G. ruber*	850	6.64	6.23	4.55	0.16

Spine Na/Ca

For the multi-net derived samples we were able to directly measure spine Na/Ca values on spines sticking out of the shell. Within the spines a considerable variability in Na/Ca values is observed, but not with a consistent zonation or trend. Spine *G. ruber* Na/Ca values for the multi-nets (S=~39.8) range from 10 ±1.3 mmol/mol to 23.5 ±1.9 mmol/mol, whereas *T. sacculifer* Na/Ca values range from 10.7 ±0.8 mmol/mol to 24.9 ±1.9 mmol/mol. Intra-specimen spine variability is more than 200% for both *G. ruber* and *T. sacculifer* (highest/lowest average spine Na/Ca values, Tables 4.4, 4.5). Spine Na/Ca values are consistently much higher compared to shell Na/Ca values (e.g. Fig. 4.3, Tables 4.2-4.5). Comparing shell-based Na/Ca values with the Na/Ca values measured on spines for the same specimen, for *T. sacculifer* spines are 2 to 4.3 times higher and for *G. ruber* spines are 1.4 to 2.5 times higher (Tables 4.2-4.5). No correlation is observed between spine and shell-based Na/Ca values for neither species.

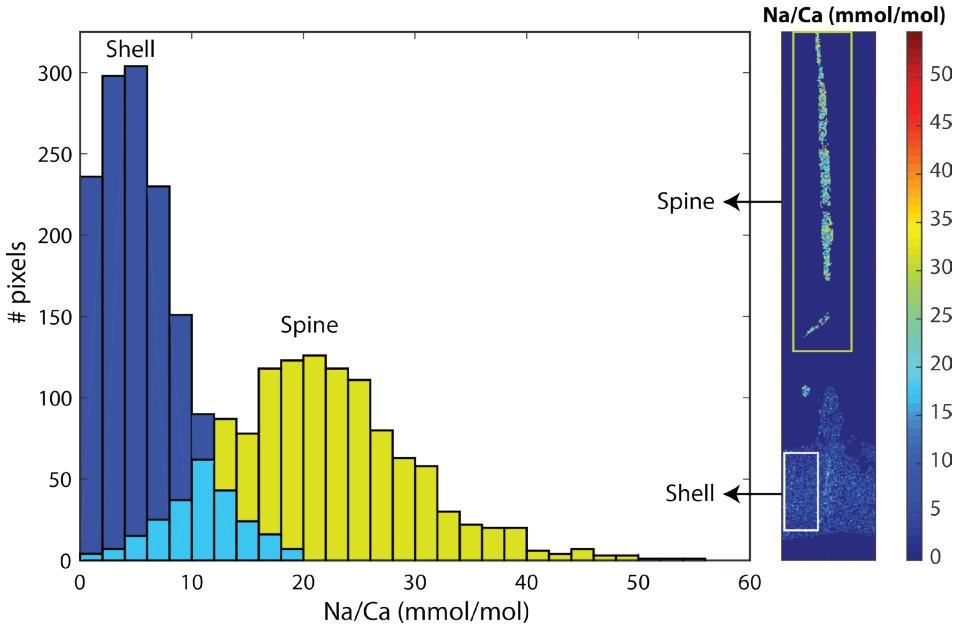

Figure 4.3. Comparison between spine Na/Ca values (green columns) and shell Na/Ca values (blue columns) within the same specimen (specimen 0002_13, *T. sacculifer*, Table 4.3) and EPMA-map indicating the regions represented by the histograms (white box: shell, green box: spine). The turquoise color represents the overlap region of the spine and shell histogram (not the spine base). Clearly, spine Na/Ca values are higher compared to shell Na/Ca values.

For several specimens we were able to measure both spines and spine bases. The EPMA-analyses show a clear difference in Na/Ca values between spines and spine bases. The spine bases show values in between the high spine and low shell Na/Ca values. Still, as the spine bases are surrounded by foraminiferal shell calcite, this possibly results in mixing signals between spine base and shell carbonate due to the resolution of the analyses, which would decrease values for the spine base. Clearly, Na/Ca values will also depend on the selected cross section analyzed with EPMA. The distribution plots for the spine base Na/Ca values show a clear difference from the shell-only areas and generally higher values.

4.3.2 SEM measurements of spine morphology and densities

In total, 125 *G. ruber* and 38 *T. sacculifer* specimens were analyzed for their spine widths and spine density at the shell surfaces. In general, the number of spines is higher for *G. ruber* compared to *T. sacculifer*, whereas spine thickness is lower (Fig. 4.4). Spine density varied from 0.09 to 0.30 spines per μm^2 for *T. sacculifer* and from 0.12 to 0.30 spines per μm^2 for *G. ruber* (Fig. 4.4). Spine widths show a high variability between and within specimens, ranging from 0.89 µm to 3.96 µm for *T. sacculifer* and from 0.56 um to 3.78 µm for *G. ruber*. A weak positive correlation is observed for *G. ruber* and *T. sacculifer* between spine width and the size of the foraminiferal shell (*G. ruber*: R^2=0.04, p<0.0001; *T. sacculifer*: R^2=0.04, p=0.004, based on Shapiro-Wilk test, Fig. 4.4). Spine width correlates negatively with salinity, based on weighted averages of the widths per salinity group for both species (*G. ruber*: R^2 = 0.35, p<0.0001; *T. sacculifer*: R^2 = 0.46, p<0.0001) (Fig. 4.4). Furthermore, a negative correlation is observed between Na/Ca values and spine width (*G. ruber*: R^2 = 0.016, p=0.006; *T. sacculifer* : R^2 = 0.03, p=0.006 for).

A significant negative correlation is observed between foraminiferal shell size and the number of spines for both species (*G. ruber*: R^2 = 0.17, p<0.0001; *T. sacculifer*: R^2 = 0.38, p<0.0001, Fig. 4.4). Between salinity and spine density both species show a negative significant correlation (*G. ruber*: R^2 = 0.24, p<0.0001; *T. sacculifer*: R^2 = 0.18, p = 0.006, Fig. 4.4). However, average spine density values for *G. ruber* are not statistically different for the different salinities and therefore no correlation is observed between salinity and spine density (student t-test between data points, p>0.78 for *G. ruber*). For *T. sacculifer*, in contrast, spine density values differ statistically significant for the highest salinity compared to the other salinities (40.1, p<0.038). The lowest salinity for *T. sacculifer* could not be taken into account for these calculations, because it only consisted of one single data point. No significant correlation is found between Na/Ca and spine density (*G. ruber*: R^2 = 0.02, p=0.1; *T. sacculifer*: R^2 = 0.004, p = 0.7).

Table 4.4. Overview of spine and spine base Na/Ca values *T. sacculifer* multi-nets. Similar colors indicate that these are measurements from the same specimen.

Position	Species	spine/ base	#Pixels	Na/Ca mean (mmol/mol	Na/Ca median (mmol/mol)	SD	SE
0001_1	*T. sacculifer*	base	160	12.57	11.70	6.15	0.49
0002_1	*T. sacculifer*	spine	621	13.10	12.72	6.06	0.24
0002_3	*T. sacculifer*	base	69	13.78	13.97	6.48	0.78
0002_3	*T. sacculifer*	spine	220	15.52	15.42	7.06	0.67
0002_4	*T. sacculifer*	spine 1	91	17.30	17.15	6.79	0.73
0002_4	*T. sacculifer*	base 1	98	13.84	13.04	6.16	0.63
0002_4	*T. sacculifer*	base 2	50	16.54	16.78	6.53	0.92
0002_5	*T. sacculifer*	spine	345	19.89	19.43	7.59	0.41
0002_5	*T. sacculifer*	base	64	16.01	15.89	6.75	1.05
0002_6	*T. sacculifer*	spine	234	19.53	18.74	7.47	0.49
0002_7	*T. sacculifer*	spine	97	21.41	20.27	8.23	0.84
0002_8	*T. sacculifer*	spine 1	98	21.33	21.35	8.29	0.84
0002_8	*T. sacculifer*	spine 2	141	15.97	15.44	7.94	0.67
0002_9	*T. sacculifer*	spine	190	15.69	14.73	7.75	0.56
0002_10	*T. sacculifer*	spine	209	14.68	14.08	6.75	0.47
0002_11	*T. sacculifer*	spine	502	17.53	17.24	7.09	0.32
0002_12	*T. sacculifer*	spine 1	43	20.67	23.73	8.43	1.29
0002_12	*T. sacculifer*	base 1	189	10.35	9.24	5.67	0.42
0002_12	*T. sacculifer*	spine 2	25	24.87	25.90	9.71	1.94
0002_12	*T. sacculifer*	base 2	68	18.35	18.14	7.16	0.91
0002_13	*T. sacculifer*	base	70	10.43	8.98	5.99	0.72
0002_13	*T. sacculifer*	spine	1230	21.40	20.93	8.35	0.24
0004_24	*T. sacculifer*	spine	362	13.45	13.10	6.73	0.35

Table 4.5. Overview of spine and spine base Na/Ca values *G. ruber* multi-nets. Similar colors indicate that these are measurements from the same specimen (except for white).

Position	Species	spine/ base	#Pixels	Na/Ca mean (mmol/mol	Na/Ca median (mmol/mol)	SD	SE
0002_14	*G. ruber*	spine	47	17.34	15.86	1.18	8.11
0004_1	*G. ruber*	spine	28	9.98	8.60	6.95	1.31
0004_4	*G. ruber*	spine	55	13.83	13.24	6.80	0.91
0004_5	*G. ruber*	spine	41	14.12	13.60	7.27	1.14
0004_6	*G. ruber*	spine	36	13.03	11.94	5.41	0.90
0004_7	*G. ruber*	base	42	19.38	18.02	5.72	0.88
0004_10	*G. ruber*	spine	94	11.55	11.30	6.56	0.68
0004_11	*G. ruber*	spine	53	23.50	20.80	14.02	1.92
0004_12	*G. ruber*	base	150	15.15	14.44	6.41	0.53
0004_12	*G. ruber*	spine	31	18.70	18.37	6.63	1.19
0004_13	*G. ruber*	spine	30	19.71	18.98	7.47	1.36
0004_13	*G. ruber*	base	91	16.41	15.97	7.12	0.80
0004_14	*G. ruber*	base	100	15.01	13.70	7.33	0.73
0004_15	*G. ruber*	base	124	14.81	14.60	6.49	0.59
0004_16	*G. ruber*	spine	53	16.72	16.42	5.26	0.72
0004_16	*G. ruber*	base	108	15.57	14.82	7.04	0.73
0004_17	*G. ruber*	spine	64	15.41	15.09	6.92	0.87
0004_17	*G. ruber*	base	108	16.33	15.48	6.36	0.66
0004_18	*G. ruber*	spine	41	16.06	14.38	8.16	1.27
0004_19	*G. ruber*	base	128	15.10	13.66	8.13	0.76
0004_20	*G. ruber*	spine	53	12.01	11.53	5.90	0.81
0004_21	*G. ruber*	spine	21	16.01	15.45	7.28	1.59
0004_22	*G. ruber*	spine	75	13.92	12.72	6.13	0.71

Table 4.6. Overview spine base measurements of cultured and field-collected specimens (Table 4.1)

Position	Species	Salinity	#Pixels	Na/Ca mean (mmol/mol	Na/Ca median (mmol/mol)	SD	SE
1Feb_1	*T. sacculifer*	36.0	59	18.29	17.05	6.97	0.91
1Feb_1	*T. sacculifer*	36.0	90	10.24	9.14	6.06	0.67
1Feb_3	*T. sacculifer*	33.0	50	11.82	11.35	5.56	0.79
1Feb_4	*T. sacculifer*	36.0	160	19.70	18.90	8.64	0.69
1Feb_5	*T. sacculifer*	33.0	174	10.12	10.29	5.31	0.41
2Feb_2	*T. sacculifer*	36.0	98	16.81	16.13	8.26	0.84
2Feb_3	*T. sacculifer*	36.0	70	12.96	12.80	6.77	0.81
2Feb_4	*T. sacculifer*	45.0	84	12.07	11.11	6.63	0.75
2Feb_4_spine2	*T. sacculifer*	45.0	56	13.69	13.71	6.84	0.94
2Feb_5	*T. sacculifer*	36.0	150	12.58	10.56	9.36	0.98
2Feb_6_spine1	*T. sacculifer*	36.0	70	11.19	9.68	6.41	0.80
2Feb_6_spine2	*T. sacculifer*	36.0	117	11.44	9.88	6.10	0.79
31Jan_1	*G. ruber*	37.3	153	10.70	10.72	6.11	0.91
31Jan_2	*G. ruber*	37.3	24	17.90	17.36	6.32	1.29
31Jan_3	*T. sacculifer*	37.3	48	12.64	10.92	6.51	0.94
31Jan_4	*T. sacculifer*	37.3	50	13.10	11.21	6.86	0.97
31Jan_6	*T. sacculifer*	39.6	50	11.44	10.96	6.28	1.11
31Jan_6	*T. sacculifer*	39.6	72	12.36	12.65	5.97	0.71
3Feb_2	*G. ruber*	39.6	42	11.64	11.30	5.32	0.83
31Jan_7	*G. ruber*	39.8	45	13.01	13.43	7.38	1.11
31Jan_7	*G. ruber*	39.8	25	13.19	14.41	7.31	1.46
31Jan_7	*G. ruber*	39.8	36	13.24	11.68	6.92	1.17
31Jan_8	*T. sacculifer*	39.8	20	14.15	14.63	3.81	0.85
31Jan_8	*T. sacculifer*	39.8	30	11.01	8.77	6.69	1.26
31Jan_8	*T. sacculifer*	39.8	36	9.57	7.63	6.76	1.14
31Jan_8	*T. sacculifer*	39.8	36	9.71	8.12	6.00	1.04
31Jan_9	*T. sacculifer*	39.8	70	15.34	13.99	8.79	1.08
31Jan_9	*T. sacculifer*	39.8	44	11.99	11.26	8.24	1.24
3Feb_1	*G. ruber*	39.8	15	10.98	11.73	4.05	1.05

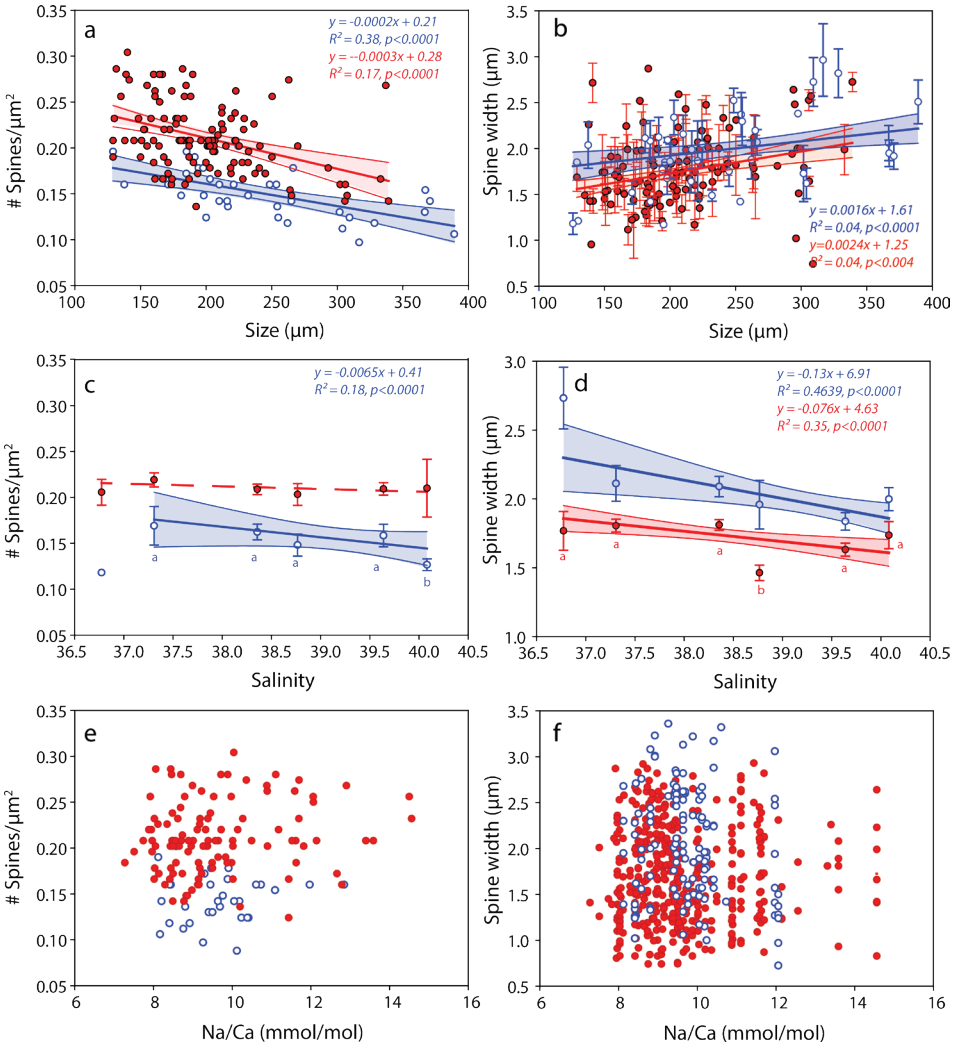

Figure 4.4. Results from the SEM spine density and width counts for *G. ruber* (red closed circles) and *T. sacculifer* (blue open circles) specimens, with standard errors indicated and enveloped into a 95% certainty interval, with: a) number of spines versus the size (µm) of the foraminiferal specimen these were counted on, b) spine width (µm) versus the size (µm) of the specimen these were counted on, c) number of spines versus salinity, d) spine width versus salinity, e) number of spines and the measured whole-shell Na/Ca composition and f) spine width versus the measured whole-shell Na/Ca composition.

4.3.3 Organic linings

The minor and trace elemental composition of the isolated organic linings is similar for *T. sacculifer* and *G. ruber* (Table 4.7). Although concentrations of Na and Mg seem enriched within the isolated organics (Table 4.7), when calculating their contribution to the whole shell elemental composition, Na from the linings contributes only 5.61 ppm, or 0.024 mmol/mol for *G. ruber* and 12.03 ppm, or 0.052 mmol/mol, for *T. sacculifer* to the whole shell Na/Ca. For Mg values the contribution from the isolated linings to the total shell concentration are 37.68 ppm, or 0.16 mmol/mol for *G. ruber* and 69.25 ppm, or 0.28 mmol/mol for *T. sacculifer*. There is no measurable Ca concentration in the organic linings.

Table 4.7. Elemental composition of organic linings calculated for shell weight and estimated elemental composition based on OL weight.

	Na	Mg	Sr
G. ruber			
ppm OL (average + SE)	1389±29	9325±34	84±0.19
average test El/Ca (mmol/mol)*	6.42	4.2	1.63
relative contribution OL Na to total shell Na			
ppm	5.61	37.68	0.34
mmol/mol	0.024	0.16	0.0004
%	0.38	3.69	0.02
T. sacculifer			
ppm OL (average + SE)	1703±11	9798±24	34±0.04
average test El/Ca (mmol/mol)*	6.38	4.1	1.6
relative contribution OL Na to total shell Na			
ppm	12.03	69.25	0.24
mmol/mol	0.052	0.28	0.0003
%	0.82	6.95	0.02

* average shell Sr/Ca and Mg/Ca based on *Mezger et al.*, 2016, shell Na/Ca based on *Mezger et al.*, 2018

4.4 Discussion

Shell-only (i.e. spine-free) Na/Ca values of *G. ruber* and *T. sacculifer*, collected in the Red Sea from surface waters, the water column and the sediment surface, all fall within the range of previously established calibrations (Geerken et al., 2018;Allen et al., 2016;Wit et al., 2013) (Fig. 4.5). Average values reported here are, however, somewhat higher than results from Bertlich et al. (2018). Red Sea sediment surface Na/Ca values measured by laser ablation (LA)-ICP-MS and EPMA from the same specimens compare well (Mezger et al., 2018, Fig. 4.5). However, for the specimens collected from the sea surface, the EPMA-derived shell-only Na/Ca values are much lower than those from the LA-ICP-MS analyses (Fig. 4.5). When measuring whole-shell chemistry using LA-ICP-MS, all different shell components contribute to the signal including the Na-rich spines and spine bases. It is therefore hypothesized that spine loss is responsible for the observed offset in absolute Na/Ca between specimens from surface water and those from deeper in the water column (Mezger et al., 2018). The fact that the shell-only Na/Ca values between core-top and surface water specimens are similar confirms this hypothesis (Fig. 4.5).

Several recent studies showed foraminiferal Na/Ca values to vary with salinity (Geerken et al., 2018;Wit et al., 2013;Allen et al., 2016;Mezger et al., 2016;Mezger et al., 2018;Bertlich et al., 2018) (Fig. 4.5). The slopes of these calibrations and absolute Na/Ca values, however, differ between studies (Geerken et al., 2018;Allen et al., 2016;Wit et al., 2013;Delaney et al., 1985;Mezger et al., 2016;Mezger et al., 2018;Bertlich et al., 2018). Whereas some offsets may be due to inter-species differences, potentially also caused by variability of morphospecies and genotypes (e.g. Schiebel and Hemleben, 2017; Steinke et al., 2005), other offsets reflect variability within one species. Whereas potential differences in Na incorporation between different morpho- and genotypes require further study, studies focusing on intra-shell variability in Na/Ca have shown that there are also large differences in Na/Ca within single shells (Branson et al., 2016;Geerken et al., 2018;Yoshimura et al., 2017;Mezger et al., 2018). Therefore, part of all this variability may be explained by uneven contributions of various parts of the foraminiferal shell, which means that the Na/Ca composition of these parts needs to be determined independently. This allows calculating relative contributions of different parts of the shell to the whole-shell Na/Ca composition from previous studies. Based on suggestions made before, we here focus on the contribution of organic linings, spines and spine bases to the overall Na-composition of the foraminiferal shell.

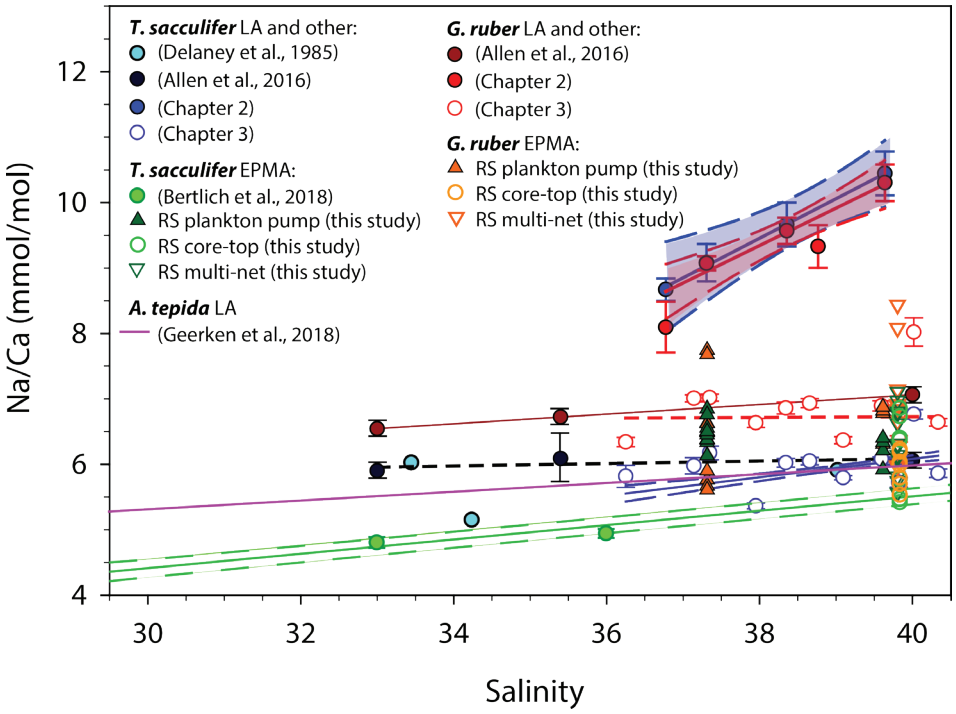

Figure 4.5. Comparison of most existing planktonic foraminifer Na/Ca-salinity studies, including different culture studies (Allen et al., 2016, Bertlich et al., 2018, Wit et al., 2013, Delaney et al., 1985), a field survey (Mezger et al., 2016: Chapter 2, Mezger et al., 2018: Chapter 3), and a benthic culture study (Geerken et al., 2018) compared to new electron microprobe shell Na/Ca values of Red Sea plankton pumps, core-tops and multi-nets (this study). Distinction had been made between EPMA and laser ablation measurements (LA), where EPMA measurements refer to shell-only measurements. The shown regressions are associated with the datapoints in the same color.

4.4.1 Organic Linings

Using TOF-SIMS and an atom-probe, Branson et al. (2016) found Na concentrations to be enriched at foraminiferal spine bases and in (the proximity of) the organic linings. Values in the enriched areas appear approximately 1.3 times higher compared to the shell in *Orbulina universa* (Branson et al., 2016). Geerken et al. (2018 discovered Na to preferentially occur in bands with concentrations 1.1-1.75 times higher compared to the surrounding layers with lower Na/Ca values. These bands seem to coincide with Mg-rich bands, which have previously been linked to the proximity of organic linings (Branson et al., 2016;Geerken et al., 2018). Although this coincidence suggests that high Na is indeed linked to the organic calcifying matrix, the values measured on the isolated linings also indicate that their relative contribution to the overall shell Na/Ca is negligible (Table 4.7). Still, the higher concentrations of these linings might explain (part of the) observed

banding pattern, as the absolute concentration within the linings is similar to or higher than that of the shell carbonate. One potential pitfall of the method used here for isolating the organic linings is that minor and trace metals adsorbed and/or loosely bound to the organic linings could have been removed during the rinsing phases of the isolation.

When not directly related to the organic layers, zones of high Mg and high Na may be indirectly coupled via processes responsible for the banding. For planktonic species, chamber formation (usually at night) may be responsible for the observed banding (Fehrenbacher et al., 2017;Spero et al., 2015). Here banding in Na is only reported in one EPMA image, but not conclusive in other maps (e.g. Fig. 4.1). Furthermore, the visual absence of organic linings in the EPMA images from this study is most likely due to the relatively low contribution (0.4-0.7%) of the organic linings for these species to the total shell weight. Potentially the expression of banding is also related to the absolute Na concentrations of the shell, as banding in *Ammonia tepida* (lower in Na) was less pronounced than in *Amphistegina lessonnii* (Geerken et al., 2018). Accordingly, the banding in planktonic foraminifera may also be less pronounced and hence not detectable within our approach. Irrespective, the relative contribution of these bands can be considered minor in comparison with the other zones of high Na/Ca values such as the spines and spine bases, which are clear also within the limited resolution of our analytical approach.

4.4.2 Unravelling spines and spine base Na/Ca

Several studies showed that Na/Ca in foraminiferal shells is not homogeneously distributed but is present at higher concentrations in bands and also at the (bases of) spine(s) (Branson et al., 2016;Mezger et al., 2018). Accordingly, Na-hotspots at spines and spine bases were selected to quantify Na/Ca values and compare these values with Na/Ca measured on shell-only areas. Furthermore, the preservation state of spine bases were studied, as these might still partially remain after spine shedding processes (Bé, 1980).

Spines sticking out of the shell showed Na/Ca to be consistently much higher than shell Na/Ca values from the same specimens. Spine base regions were selected based on backscattered and secondary electron images. Analyses from spine base areas, however, are likely influenced by mixing with lower Na/Ca values from adjacent regions. During EPMA analyses, the electron beam excites both areas/volumes in the region close to the interface between spine base and surrounding low-Na shell calcite. Moreover, EPMA analyses target a 2-D surface, whereas the spine is not necessarily oriented parallel to the sampling surface. Hence, also in three dimensions variable amounts of spine-base related

carbonate is analyzed during EPMA. Furthermore, due to its conic shape, spine thickness decreases towards the edges of the spine, also within the spine base. The sampling volume and pixel size together determines the obtained spine and spine-base Na/Ca signal. Therefore, the center of the spine - being the thickest and probably least affected by the polishing process - most likely reflects true spine base Na/Ca values. To estimate these signals, a mathematical approach was used in which we narrow the area perpendicular to the center of the spine base for determining the Na/Ca (Fig. 4.6, Fig. S4.3). Narrowing the width of the spine base sampling area results in increasing Na/Ca values until they approach a plateau, which is assumed to reflect the true spine base Na/Ca value (Fig. 4.6a,b, Fig. S4.3). When no plateau is observed, e.g. the analyzed cross section is too small, true Na/Ca may remain unknown (Fig. 4.6a). Conversely, when increasing the width of the region used for calculating average values, values converge towards the shell values signal (Fig. 4.6a,b). As a result of decreasing the area used for calculating the average Na/Ca, standard errors increase (Fig. 4.6a,b).

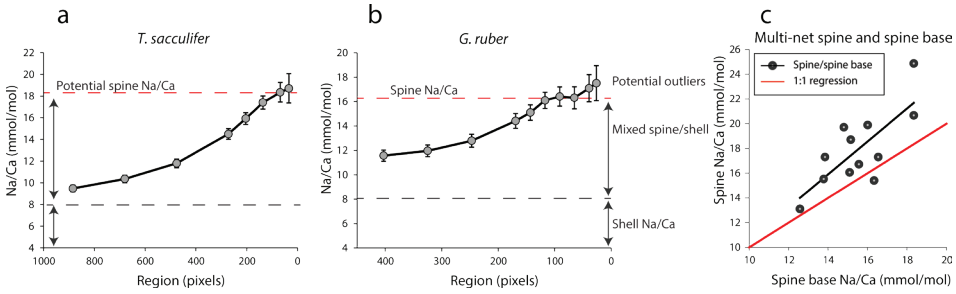

Figure 4.6. Examples of results of our spine-base quantification method, with: a): example of the quantification of a spine base (*T. sacculifer*, 2_12_multinet, Table 4.3), b) similar for *G. ruber*, (4_13_multinet, Table 4.4). The smaller/narrower the selected region, the higher the Na/Ca values, resulting from confining the analysis to the core of the spine. Due to the decreasing sampling volume, standard errors also increase. Panel c) shows the spine Na/Ca values measured, versus the spine base Na/Ca obtained with the method described in Figure S4.3 and discussion section 4.4.2. For panel 4.6a, the word 'potential' is used, as no plateau Na/Ca value is reached.

Based on our quantification approach, spine base Na/Ca values for the water column collected specimens range from 12.6 to 18.4 mmol/mol for *T. sacculifer* and from 15.0 to 16.1 mmol/mol for *G. ruber* (Table 4.6). Part of the variability in spine base Na/Ca values might be explained by differences in spine morphotypes (Schiebel and Hemleben, 2017), although by far most spines seem to have a rounded cross section. Still, more research would be needed to investigate a potential effect of spine morphotype on Na incorporation. Compared to Na/Ca values of the spines from the same specimens, spine base values are 4 to 35% lower (Fig. 4.6c). Although this offset is consistent and considerable, it cannot

be excluded that it is primarily caused by the fundamental complication of estimating Na/Ca values in the spine bases. Whereas the spine bases are surrounded by low Na/Ca carbonate, spines are surrounded by the embedding material only, which does not affect the analyses. For the spine bases of specimens of the Red Sea surface water, sediment surface and cultured *T. sacculifer* specimens, Na/Ca values vary from 9.6 to 20 mmol/mol, with averages being consistently lower compared to laser ablation measured spines (Mezger et al., 2018) and parts of the spines still sticking out after embedding, measured here with EPMA (Fig. 4.6c, Table 4.6).

The relatively high concentration of Na in spines and spine bases may be attributed to relatively fast growth rates compared to shell carbonate. Inorganic precipitation experiments suggest that growth rate enhances incorporation of most minor and trace metals, including Na (Busenberg and Plummer, 1985). Moreover, analogous to spine formation in sea urchins, an amorphous precursor may be responsible for the prismatic shape of the foraminiferal spines, which rapidly transforms into calcite (Beniash et al., 1997). Such a precursor phase has also been shown by Jacob et al. (2017) to occur during foraminiferal shell calcification, with formation of vaterite. They also suggest that an amorphous precursor may have been present in two planktonic foraminiferal species (Jacob et al., 2017). Such an amorphous calcium carbonate likely contains much more minor and trace elements, although a subsequent phase transformation from amorphous calcium carbonate (ACC) to calcite (potentially via vaterite) would still affect element incorporation (Littlewood et al., 2017). Interestingly, this would not only influence Na incorporation, but also most other minor and trace metals. Application of foraminiferal trace metals for proxy reconstructions should, therefore, also address the potential effect of differences in spine chemistry.

Foraminiferal shell, spine (base) and organic linings differ in Na composition, potentially due to leakage (Yoshimura et al., 2017), banding (Branson et al., 2016;Geerken et al., 2018), diffusion or adhesion and may vary as a function of salinity (Allen et al., 2016;Geerken et al., 2018;Mezger et al. 2016, 2018; Wit et al., 2013) or calcium concentration of the seawater (Hauzer et al., 2018) (Figure 4.7). The consistently lower Na concentration of the spine base compared to the actual spines suggests a gradual transition from low-Na/Ca of the shell calcite to the high-Na/Ca of the spine (Fig. 4.6c, Fig. 4.7). Although our approach does not allow to fully exclude an analytical bias, alternatively leakage or diffusion of Na from the high-Na spine base to the low-Na shell through time (Yoshimura et al., 2017) could also explain (part of) the observed intermediate values (Fig. 4.7). The spine would

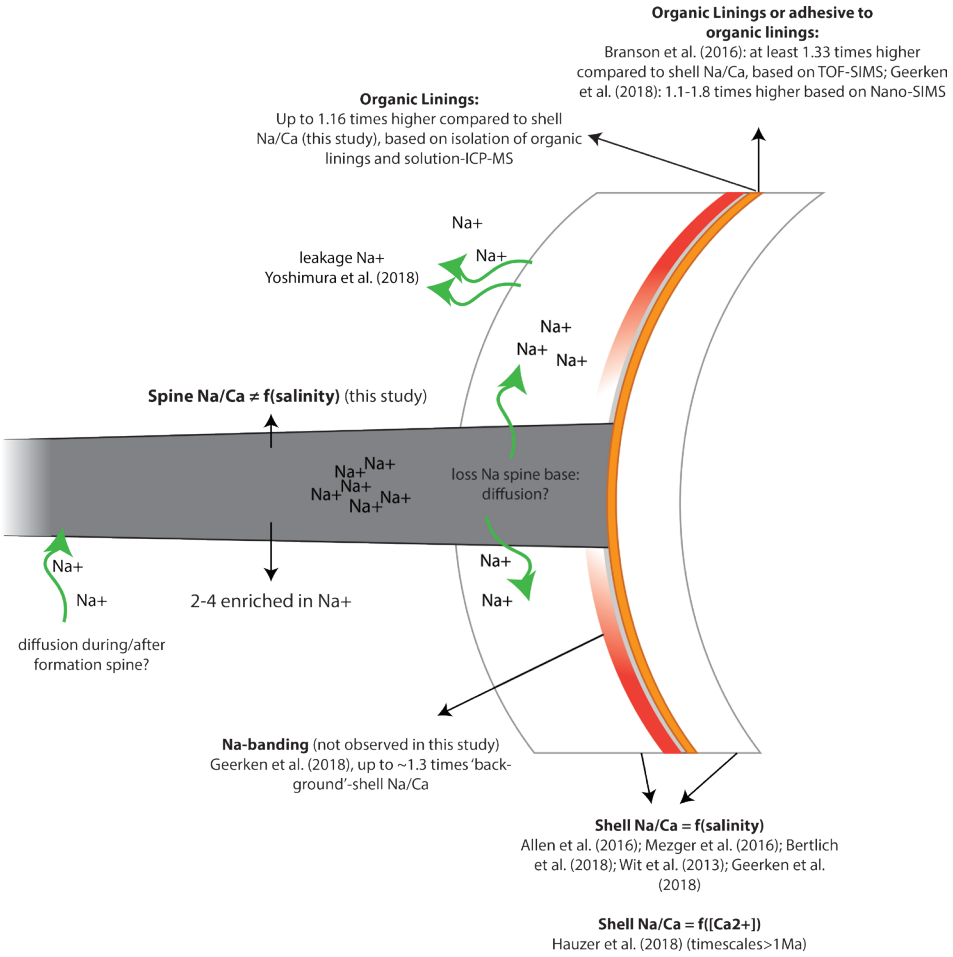

Figure 4.7. Potential processes influencing the Na/Ca composition of the shell, spines and organic linings. Na from spines may be transported to the surrounding seawater or into the adjacent calcite with a relatively low Na/Ca. The latter may be difficult to distinguish from mixing of material from the spine and that of the low-Na/Ca calcite.

not be affected, or even has higher Na concentrations, as Na diffusion from seawater into the spine after or during spine formation could increase the Na content of the spine. This would increase the observed shell, spine-base to spine concentration gradient, but not influence the average whole-shell Na composition. Using synchrotron X-ray spectroscopy, Yoshimura et al. (2017) found that Na incorporation is associated with substitution for Ca in the calcite lattice. This is in contrast to what was proposed earlier by e.g. Ishikawa and Ichikuni (1984) and with the charge difference between Na^{+} and Ca^{2+} being compensated

by the creation of CO_3^{2-} vacancies (Yoshimura et al., 2017). These vacancies in the crystal lattice result in weaker calcite lattice spots at the locations of Na incorporation, facilitating leaching of Na from the calcite crystal on geological timescales (Yoshimura et al., 2017). However, in this study the Na/Ca composition of the foraminiferal shells (shell-only) of the same species (Red Sea water column and core-tops, as well as cultured specimens) were here found to remain similar (Fig. 4.5), implying no appreciable Na exchange on these relatively short time scales (thousands of years). Still, it is not clear whether the spines, with relatively high Na concentrations and hence weak calcite lattice spots and a large surface to volume ratio, have been affected.

4.4.3 Consequences of differences in spine and shell chemistry

The differences in Na/Ca between spine, spine base and shell-only carbonate can potentially explain differences observed between calibrations (Mezger et al., 2018; Fig. 4.5). Differences between calibrations are observed in absolute Na/Ca concentrations and also between the slopes as a function of salinity (Mezger et al., 2016;Mezger et al., 2018;Bertlich et al., 2018;Allen et al., 2016). When spines fully account for the observed difference in both slopes and absolute Na/Ca values between e.g. the cultured *T. sacculifer*, measured shell-only with EPMA (Bertlich et al., 2018), and planktonic foraminifera with spines (Fig. 4.5, Mezger et al., 2018), this implies that either Na/Ca_{spines} must increase with increasing salinities and/or the relative contribution of spine carbonate to the integrated whole test signal must increase with increasing salinity (Fig. 4.8). In case of the latter explanation this can be due to relative changes in spine-density, -thickness and/or -length compared to the thickness of the shell wall (Fig. 4.8).

Average Na/Ca calcite compositions of whole foraminiferal specimens reflect the relative contributions of Na/Ca in shell calcite (ρ) plus the contribution of Na/Ca in spine calcite (1-ρ) (Fig. 4.8). To determine the contribution of spines to the total $Na/Ca_{calcite}$ ('whole shell' Na/Ca) (Fig. 4.6), chamber-specific laser ablation-Q-ICP-MS Na/Ca values from Red Sea surface water collected *T. sacculifer* and *G. ruber* specimens (Mezger et al., 2016) are compared to the Na/Ca composition of shell-only EPMA-measured cultured *T. sacculifer* (Bertlich et al., 2018). Because the spines of surface-dwelling foraminifera are still largely intact, the difference in absolute values and the slope between these calibrations allows calculating the relative contribution of spine bound Na to whole shell Na/Ca values (Figs. 4.5 and 4.8). To compare the exponential calibrations of *G. ruber* and *T. sacculifer*, the calibration of Bertlich et al. (2018), was extrapolated with an exponential calibration. The relative contribution of spines to the total Na/Ca, based on LA-ICP-MS measured spine

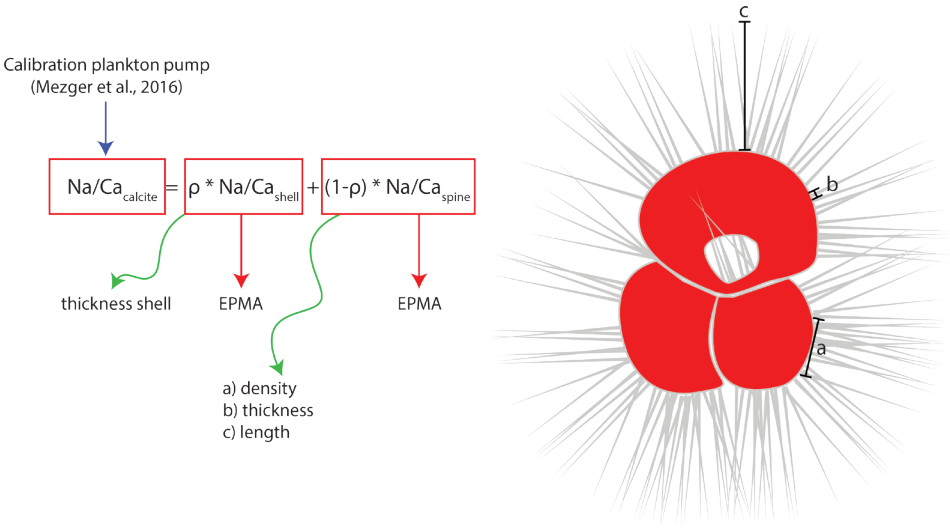

Figure 4.8. General mass balance model combining relative contribution (ρ) of spine (Na/Ca_{spine}) and shell calcite (Na/Ca_{shell}) Na/Ca values to explain the whole shell ($Na/Ca_{calcite}$) Na/Ca values measured. The relative contribution of shell calcite depends on the shell thickness relative to the number of spines, whereas the relative contribution of spines depends on spine density, thickness and length. The Na composition of the individual shell parts was measured with EPMA, and the total shell Na/Ca values are derived from laser ablation measurements on specimens still containing shell and spines (Mezger et al., 2016). Spines could be up to 2-3 mm long and are therefore not shown in their true scale in this image.

Na/Ca at a salinity of 39.6 (27.5 mmol/mol Na/Ca for *G. ruber* and 28.5 mmol/mol for *T. sacculifer*,Mezger et al., 2018) as well as EPMA-based spine Na/Ca at a salinity of 39.8 (on average 15.6 mmol/mol Na/Ca for *G. ruber* and 16.9 mmol/mol for *T. sacculifer*, was calculated based on the following equations:

$$Na/Ca_{Mezger\ et\ al.\ 2016} = \rho * Na/Ca_{Bertlich\ et\ al.\ 2018} + (1-\rho) * Na/Ca_{spine} \quad (1)$$

$$Na/Ca_{Mezger\ et\ al.\ 2016} - Na/Ca_{spine} = \rho * (Na/Ca_{Bertlich\ et\ al.\ 2018} - Na/Ca_{spine}) \quad (2)$$

$$\rho = (Na/Ca_{Mezger\ et\ al.\ 2016} - Na/Ca_{spine}) / (Na/Ca_{Bertlich\ et\ al.\ 2018} - Na/Ca_{spine}) \quad (3)$$

This suggests a relative spine and spine base contribution from 20.8% (exp) to 19.75% (lin) for *G. ruber* and from 20.63% (exp) to 19.82% (lin) for *T. sacculifer*. However, when calculating the relative spine contribution from EPMA-based spine Na/Ca values, the relative spine contribution ranges from 46.7% (exp) to 43.3% (lin) for *G. ruber* and from 42.83% (exp) to 42.93% (lin) for *T. sacculifer*, which seem unrealistically high. To calculate

the Na/Ca_{spine} based on a constant ρ for different salinities (Fig. 4.8), the following equation is used:

$$(Na/Ca_{Mezger\ et\ al.\ 2016} - (\rho * Na/Ca_{Bertlich\ et\ al.\ 2018}))/\ (1-\rho) = Na/Ca_{spine} \quad (4)$$

Based on these calculations, LA-based spine Na/Ca values should increase 1.4 to 2.1 times (lin-exp *G. ruber*), and for *T. sacculifer* 1.4 to 2.2 times (lin-exp) within a natural salinity range from 30 to 40 to account for the difference in absolute values between studies (Fig. 4.9). Alternatively, the Na concentration of spines (1-ρ) changes with increasing salinities (equation 3), from 8.6 to 21.6% or 19.9 to 27.8% for *G. ruber* (exp-lin) and from 7.9 to 21.4% or 13.4 to 20.1% for *T. sacculifer* (exp-lin).

No appreciable change in number of spines (e.g. spine density) with increasing salinity has been observed and also the width of the spines appears to decrease rather than increase with increasing salinity (Fig. 4.4). Spine length could vary with salinity, but we were unable to quantify spine length as spines easily break off during sampling and sample processing. Spines are connected to the planktonic foraminiferal shell through a thin organic lining, which is easily removed during cleaning. The slight offset in absolute values between the cultured *T. sacculifer* and core-tops can be explained by spine bases, still partially present in the shell wall after gametogenesis or burial.

Combining all spine and spine base Na/Ca values compared to ambient salinity, would suggest a trend towards higher Na incorporation with higher salinities which is, however, not significant. Compared to shell Na/Ca composition of the same specimens, spine Na/Ca values are 2-4 times higher. For Red Sea core-tops, no spines are observed (Mezger et al., 2018), and SEM images often show spine holes, probably associated with life-stage related (gametogenesis) spine loss. Some spine bases remain present, allowing quantification of core-top spine base Na/Ca. Comparing the EPMA measured spine and spine base Na/Ca values with values calculated using a mass balance (see above, Figs. 4.8-4.10) shows that measured absolute Na/Ca values are lower and not in line with the calculated difference in slopes. This suggests that either 1) spine base Na/Ca does not vary with salinity, 2) EPMA measured values for spine-base and spine Na/Ca underestimate true spine values (Fig. 4.10) or 3) spine base Na/Ca values are significantly lower compared to the actual spine values. Furthermore, in this study, we analyzed a limited number of individuals and more specimens and measurements would be needed to identify a potential relationship between spine Na and salinity. Although we here show a major impact of spines and spine bases

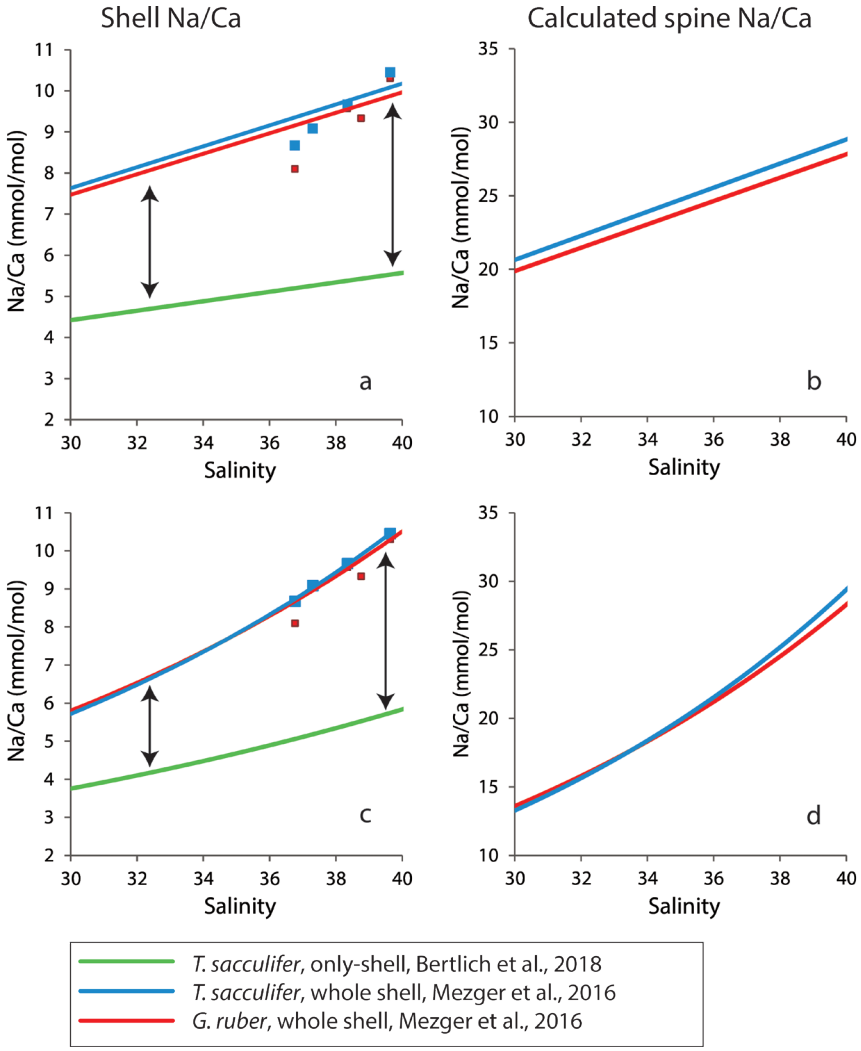

Figure 4.9 Comparison of Na/Ca-salinity calibrations between surface water collected spinose planktonic specimens still containing spines (whole shell) (Mezger et al., 2016) and extrapolated cultured only-shell *T. sacculifer* (Bertlich et al., 2018). The difference in absolute values is assumed to be caused by spines (arrow) (a). b) Theoretically calculated Na/Ca values of the spines, in case of a). (c) Difference in absolute values by exponential calibrations. d) Theoretical calculated Na/Ca values of the spines, in case of c).

on Na/Ca, the Na/Ca values of the shell itself seem relatively robust (Figs. 4.7 and 4.10). Comparing both shell and spine Na/Ca values with salinity shows that shell chemistry records salinity, albeit with a very modest slope (Figs. 4.5 and 4.10).

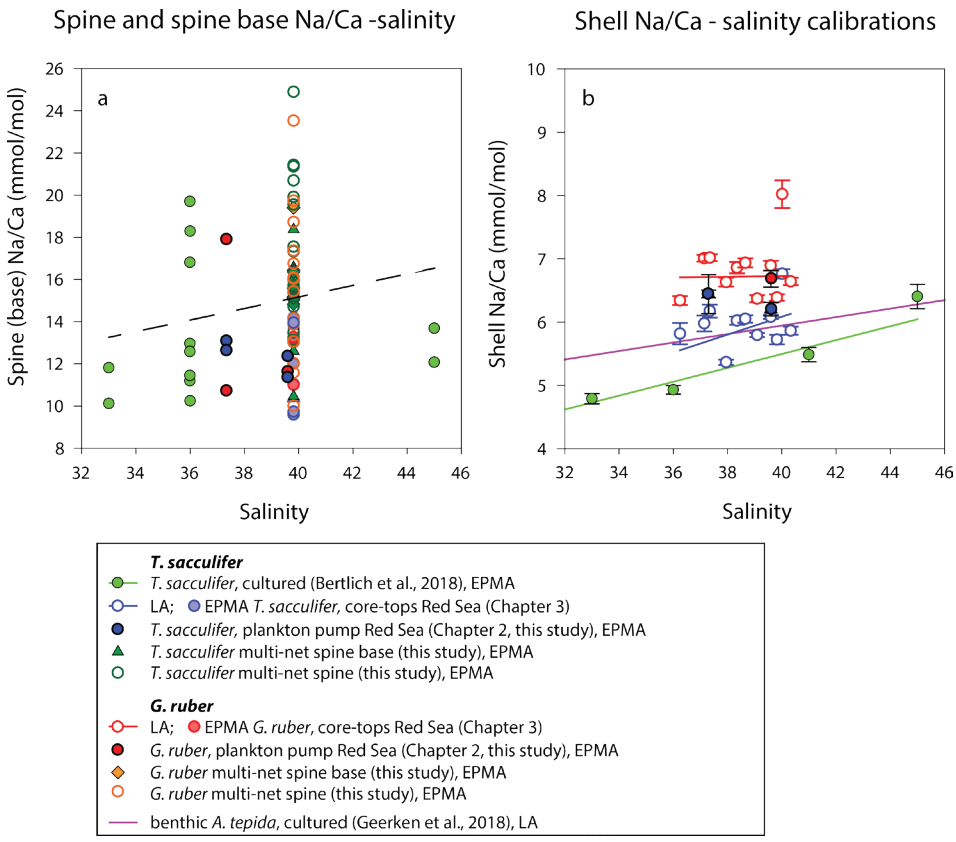

Figure 4.10 a) Changes of Na/Ca spine bases and spines (multi-net only) with salinity, with the trend of all data indicated with the dashed line and b) comparison of different existing Na/Ca shell – salinity calibrations with indicated standard errors. The regression lines refer to the samples in the same color (also indicated in the legend). We have also separated data based on the analytical technique used, which were EPMA and laser ablation measurements (LA), respectively.

Conclusions

Whole shell Na/Ca values, including spines and spine bases, show an offset to shell-only values due to the (variable) contribution of spine and spine base related carbonate, enriched in Na. Both absolute values and its relation to salinity show an offset between specimens with and without spines. Whereas the high Na areas may be susceptible to taphonomic or ontogenetic alteration, the chemistry of the shell itself appears relatively robust. The Na composition of foraminiferal organic linings is, although higher than shell Na/Ca, not sufficient to significantly influence the overall Na/Ca values measured. Spine Na/Ca values, nor their width or density appears to respond to changes in salinity.

However, potential effects of diffusion or sampling volume errors related to EPMA could also have resulted in somewhat lower spine base compared to spine Na/Ca values. Comparing both shell and spine Na/Ca values with salinity shows that shell-only values still record salinity, albeit with a low sensitivity. This is relevant for the paleo-application of Na/Ca in reconstructing salinity since spines may not always preserve well.

Acknowledgements

This research is funded by the NIOZ – Royal Netherlands Institute for Sea Research and supported by the Gravitation grant NESSC from the Dutch Ministry of Education, Culture and Science. We thank W. Boer, P. Laan, B. van der Wagt (NIOZ), S. Matveev and T. Bouten (Utrecht University) for their analytical assistance. Furthermore, we would like to thank L. Dämmer and S. de Goeyse (NIOZ) for their help with picking foraminiferal specimens for spine analyses, and E. Geerken for her assistance with EPMA data processing. We would also like to thank the editor and two reviewers, T. Toyofuku and R. Schiebel, for the constructive comments. We are also grateful to all technical staff on board of RV Pelagia cruise 64PE158 and the other cruises.

Supporting information to Chapter 4

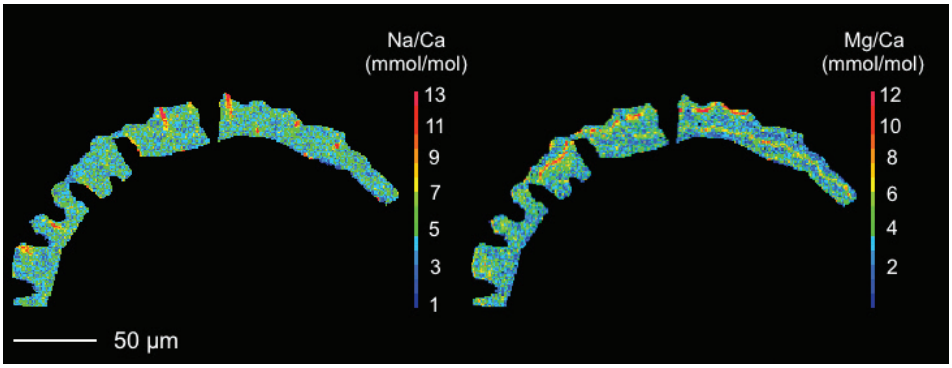

Figure S4.1. Overview of a cross-section of a *T. sacculifer* shell, measured at the GEOMAR in Kiel. Clearly, Mg is distributed in bands, whereas Na is more concentrated in the spine base regions.

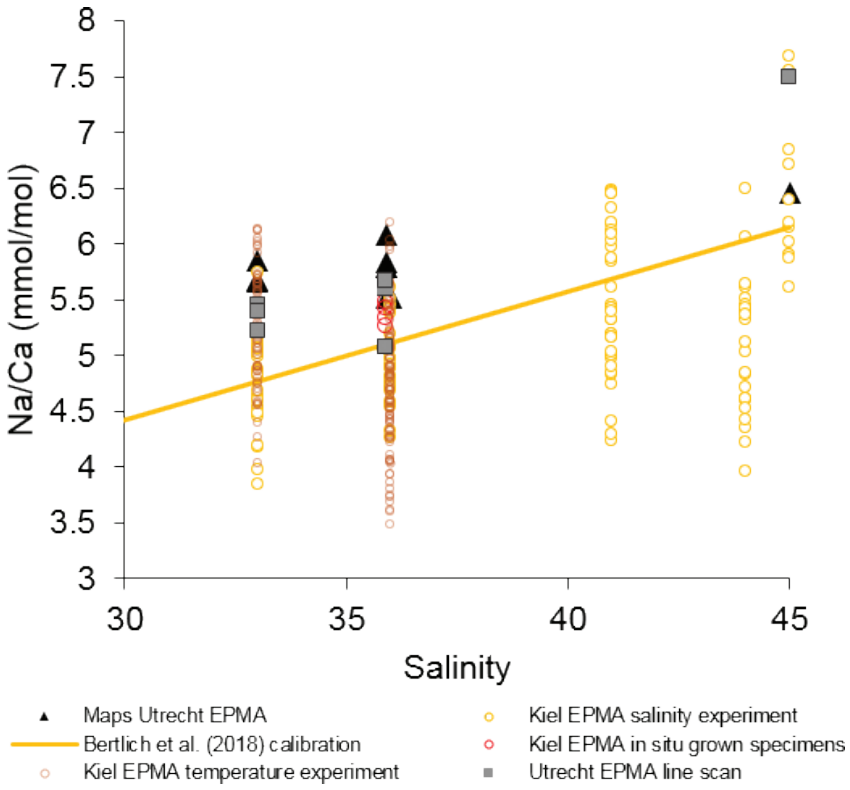

Figure S4.2. Comparison between Na/Ca map-values for the same embedded *T. sacculifer* specimens measured with EPMA at the GEOMAR in Kiel (Bertlich et al., 2018), and line-scan and map values measured in Utrecht.

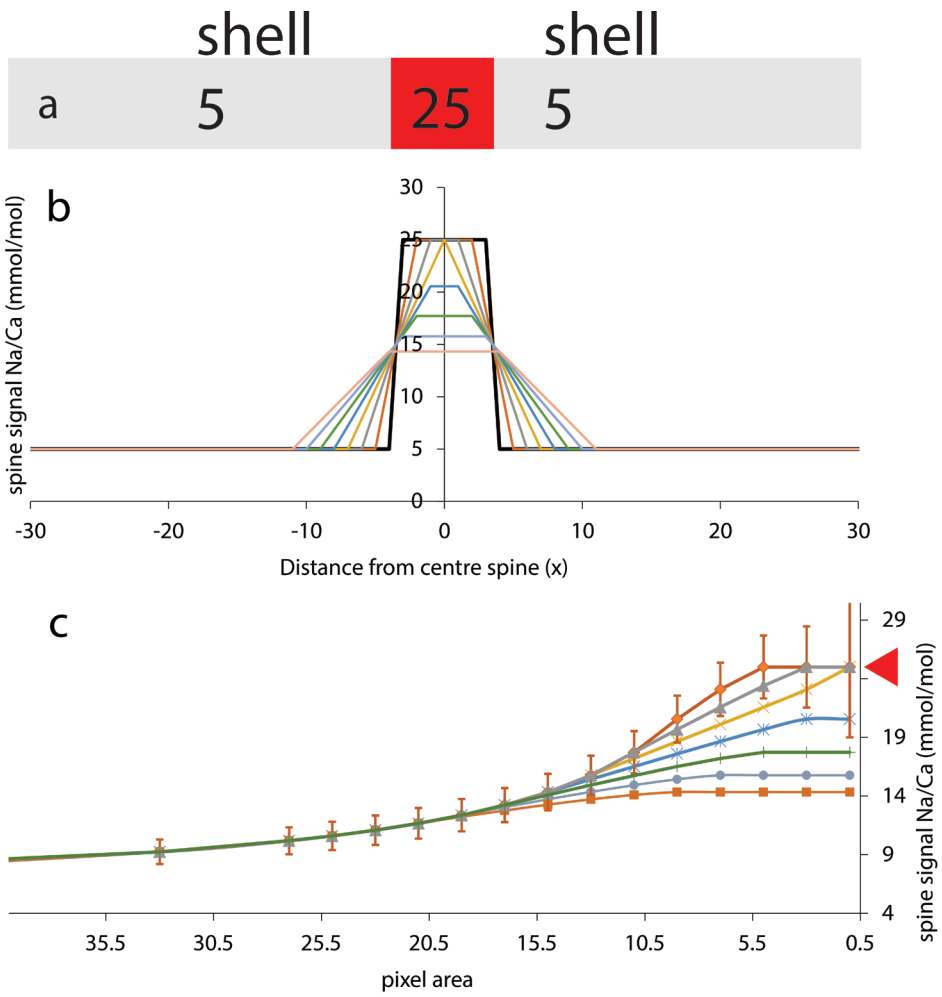

Figure S4.3. Spine base quantification model, showing: a) a schematic representation of a spinose planktonic foraminiferal shell cross section, including Na/Ca values of a spine (in red: 25 mmol/mol) sandwiched by two layers (in grey: 5 mmol/mol) of calcite with lower Na/Ca; b) the effect of differences in sampling volume on Na/Ca values measured (the 'EPMA-image'), obtained for hypothetical cross section 'a)'. Clearly, when increasing the sampling volume with a step-size of one at the time, the original signal can only be preserved at the center of the spine. However, when the sampling width is too large, the original spine base Na/Ca signal is no longer preserved (Y-axis). The different colors represent different sampling widths and the resulting Na/Ca values measured on the Y-axis, c) the effort to obtain the original spine base (red triangle) value by narrowing the surface area around the center of the spine base in a spine base map, with the same colors indicating the same scenarios described in 'b)'.

5

Chapter 5

Arabian Sea salinity and temperature changes over the last glacial cycle and impact on the oxygen minimum zone

Eveline M. Mezger

Zeynep Erdem

Julie Lattaud

Marit R. van Erk

Stefan Schouten

Gert-Jan Reichart

(under review in Palaeogeography, Palaeoclimatology, Palaeoecology)

Abstract

Arabian Sea climate is characterized by the monsoon, caused by the bi-annual shift in the pressure gradient between the Asian landmass and the South Indian Ocean. Intensity of the monsoons and relative impact of the Southwest summer monsoon (SWM) versus the Northeast winter monsoon (NEM) varies on glacial – interglacial, as well as millennial and centennial time scales. Changes in monsoon intensity profoundly affect local hydrography, biology and particle fluxes. High biological productivity is mainly associated with SWM-driven upwelling, which together with the restricted circulation result in the very intense local oxygen minimum zone (OMZ). Changes in monsoon intensity are often assessed by reconstructing biological productivity, whereas the NEM has been linked to the depth of convective overturning. However, both monsoons also impact local sea surface salinity (SSS) and temperature (SST), with an intensified summer monsoon being characterized by low salinities and an intensified winter monsoon by high salinities and low temperatures. Whereas past SST can be reconstructed with reasonable accuracy, changes in SSS are less well constrained. Here we compare two records from the northeastern Arabian Sea, one offshore Pakistan and the other more central in the northern Arabian Sea, to reconstruct changes in sea surface hydrology. Sediment geochemistry, foraminiferal shell stable isotopes, foraminiferal (trace) element incorporation and organic geochemical proxies are combined in a multi-proxy approach covering the last glacial cycle. Reconstructing SSS seems most reliable based on proxy approaches combining $\delta^{18}O$ and independent SST reconstructions. Convective overturning is stronger near the coast, related to intensified NEM's, indicated by higher SSS. During interstadials and during the Holocene, SST's are similar at both locations, in line with a modest impact of NEM and limited convective turnover. At those times also lower salinities are recorded, probably due to increased Indus River input. The intensity of the OMZ co-varies with the SWM, enhanced during interstadials, and is negatively correlated with the NEM.

5.1 Introduction

Arabian Sea climate is characterized by a bi-annual change in wind direction, the so-called monsoons. The intensity of these monsoons is known to vary considerably on multi-annual, millennial and orbital time scales (e.g. Altabet et al., 2002; Clemens et al., 1991; Dansgaard et al., 1993; Deplazes et al., 2013; Deplazes et al., 2014; Gupta et al., 2003; Haake et al., 1993; Naqvi et al., 1990; Reichart et al., 1998; Schulz et al., 1998; Ziegler et al., 2010). The strength and direction of monsoonal winds is governed by a pressure gradient between the Tibetan Plateau and the South Indian Ocean (Rixen et al., 2000; Webster et al., 1998; Wyrtki, 1973). During boreal winters (December-March), snow cover over central Asia creates a high pressure zone, forcing dry and cold north easterlies over the Arabian Sea towards the low pressure intertropical Convergence Zone (ITCZ) causing the Northeast monsoon (NEM). These winds cool the Arabian Sea surface water, resulting in turbulent mixing of the upper water column, which brings nutrients to the surface resulting in a (modest) productivity maximum (Madhupratap et al., 1996). During boreal summers (June-September), a reversal of the atmospheric pressure gradient results in the intense Southwest monsoon (SWM) (Reichart et al., 1997). These winds are much more intense than the winter monsoon as the transport of latent heat to the Tibetan Plateau intensifies the pressure gradient (e.g. Clemens et al., 1991). The associated humid and warm southwesterly winds result in both coastal and open ocean Ekman pumping, which brings up cold, nutrient-rich water (e.g. Haake et al., 1993; Wakeham et al., 2002, Figure 5.1). This upwelling results in high primary productivity and the associated high fluxes of organic matter settling through the water column, which enhances oxygen consumption at intermediate depths. Because of poor ventilation of the water column at mid-depth, an intense oxygen minimum zone (OMZ) is present (Swallow, 1984; Wyrtki, 1973; Wyrtki et al., 1971). Oxygen Minimum Zones are regions with extremely low oxygen conditions at intermediate depths, associated with high primary productivity and reduced deep water ventilation (Böning and Bard, 2009; Schenau et al., 2002; Schulte et al., 1999; Schulz et al., 1996). On millennial time scales, stadials enhance the cold and dry winds of the NEM, which intensifies convective overturning, whereas interstadials are associated with a stronger, warm and more humid SWM and hence more upwelling (Dansgaard et al., 1993; Reichart et al., 2004). On these longer (geological) time scales, the thickness and intensity of the northern Arabian Sea OMZ might have varied as a result of stratification, ventilation and primary productivity (Reichart et al., 2002; Schulz et al., 1998), related to relative impact of the monsoons.

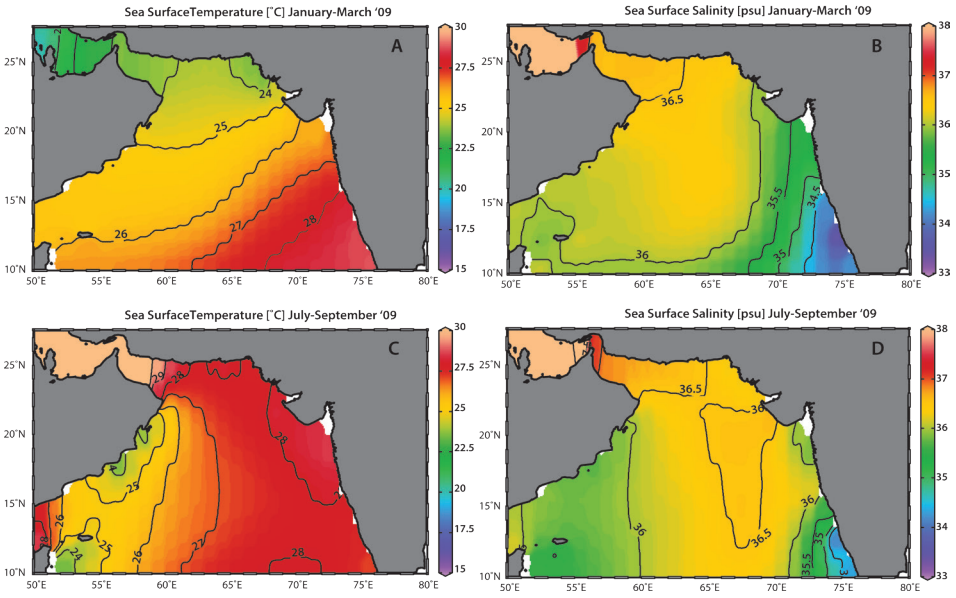

Figure 5.1. Present day changes in local hydrography (sea surface temperature and salinity) of the northern Arabian Sea between Southwest summer monsoon (SWM) and Northeast winter monsoon (NEM) conditions (World Ocean Atlas 2009, DIVA gridded: Antonov et al., 2010; Locarnini et al., 2010). Clearly, during SWM conditions (C,D), upwelling brings cooler water to the surface, mainly at the coast of Oman. However, cold winds from the northeast during NEM conditions (A,B) also cool the water column and cause a high evaporation rate, especially in the northern Arabia Sea. Saline Arabian Sea surface water flows into the Persian Gulf (top left of the map), as well as the Red Sea (beyond the scale of this figure). The West India Coastal Current (WICC) carries lower salinity waters from the Bay of Bengal into the northeast Arabian Sea, changing seasonally (Gupta et al., 2016).

Sediments from the Arabian Sea provide a potential archive to reconstruct past changes in monsoon intensity (e.g. Deplazes et al., 2013; Reichart et al., 1998; Schulz et al., 1998). Previous studies showed that strong SWM periods can be recognized by darker sediments with a high total organic carbon (TOC) content, caused by high productivity at times of intense upwelling (Reichart et al., 1998; Schulz et al., 1998). In contrast, at times dominated by an intensified NEM, sediments are lighter coloured with a lower TOC content (Deplazes et al., 2013; Reichart et al., 1998; Schulz et al., 1998; Von Rad et al., 1999). Also sea surface temperatures (SST's) are lower at times of enhanced NEM activity, when cold and dry winds cool the water surface. During stronger SWM's, SST's are higher due to warm winds coming from the south west, albeit that upwelling near the coast of Oman also locally brings colder water to the surface. Many records for past monsoon intensity are hence based on sea surface temperature and productivity proxies ((Barber et al., 2001; Gupta et al., 2003; Gupta et al., 2016; Palmer et al., 2010; Reichart et al., 1997; Reichart et al., 1998;

Rostek et al., 1997; Schulz et al., 2002; Wakeham et al., 2002; Weldeab, 2007; Wyrtki, 1973; Ziegler et al., 2008; Ziegler et al., 2010).

Sea surface salinity (SSS) is also assumed to have varied appreciably over time in the Arabia Sea but is much less well understood (e.g. Gupta and Naqvi, 1984; Reichart et al., 2004; Reichart et al, 2002; Weldeab, 2007; Wyrtki, 1973). Today, the Arabian Sea is characterized by a negative precipitation over evaporation balance, and connected with the highly evaporative Red Sea and Persian Gulf via 125 and 50 m deep sills (Gupta and Naqvi, 1984). As a result of these high evaporation rates, present-day surface salinities of the Arabian Sea reach maxima of 37 (Wyrtki, 1973). High salinity surface waters from the Arabian Sea water flow into the Persian Gulf, reaching even higher values before returning at depth (150-300 m). For the Red Sea, outflow waters return at even greater depths between 700 and 800 m (Reichart et al., 2002; Wyrtki, 1973; Wyrtki et al., 1971). Both marginal basins thereby provide a pathway for excess salinity from the surface to larger depths. In contrast to the Arabian Sea, the Bay of Bengal has a positive fresh water balance. Water from the Bay of Bengal flows as the low saline West India Coastal Current (WICC) into the Arabian Sea during the NEM, which makes the southeastern Arabian Sea somewhat less saline (Gupta and Naqvi, 1984; Wyrtki, 1973).

On geological time scales, Northern Hemispheric glaciations increased global salinity, as fresh water was stored in continental ice sheets (Fairbanks, 1989; Reichart et al., 2004). In the Arabian Sea, changes in the relative intensity of the summer and winter monsoons also contributed to changes in sea surface salinity (Reichart et al., 2002). Added to that, during glacials export of saline waters at depth to the Red Sea and into the Persian Gulf was hampered, potentially resulting in even more saline surface water conditions (Reichart et al., 2002). Reconstructions of Arabian Sea salinity were, however, limited to one single record from the Pakistan Margin and on one single proxy approach, foraminiferal $\delta^{18}O$, only (Reichart et al., 2004; Reichart et al., 2002).

In this study we applied traditional and novel approaches for the reconstruction of SSS and SST to a record in the central northern Arabian Sea to unravel the impact of summer and winter monsoons on local hydrography and OMZ intensity on a millennial time scale. First aim is to test consistency of the different proxies available and, second, to evaluate changes in sea surface salinity and temperature in the context of past changes in summer and winter monsoon intensity in the northern Arabian Sea. High resolution core scanning XRF and reflectance data is used for constructing an age model (Reichart et al., 1998;

Richter et al., 2006; Weltje and Tjallingii, 2008; Ziegler et al., 2008). Changes in sediment geochemistry are subsequently used to reconstruct past changes in productivity and OMZ intensity. Sea surface temperatures are investigated through Mg/Ca values measured on *G. ruber* shells and the organic geochemical $U^{K'}_{37}$ proxy (Prahl and Wakeham, 1987; Müller et al., 1998). We applied the recently new suggested salinity proxy based on Na incorporation in foraminiferal calcite (Allen et al., 2016; Bertlich et al., 2018; Geerken et al., 2018; Mezger et al., 2016; Wit et al., 2013) together with more traditional approaches based on combining stable isotopes (foraminiferal $\delta^{18}O$) corrected for ice volume (Labeyrie et al., 1996; Reichart et al., 2002) and SST (from both Mg/Ca and $U^{K'}_{37}$, Elderfield and Ganssen, 2000). Foraminiferal Ba/Ca has been suggested as a potential proxy for river inputs, and hence salinity, and is tested here as well (Edmond et al., 1978; Hall and Chan, 2004; Lea and Boyle, 1991; Weldeab, 2007). Results are compared to Mn/Ca values measured on foraminifera, which was recently suggested as a proxy for bottom water oxygenation (Barras et al., 2018; Groeneveld and Filipsson, 2013) and oxygenation of the water column (Klinkhammer et al., 2009; Munsel et al., 2010).

5.2 Methodology

5.2.1 Core collection and sampling

The PASOM 3 sediment core was retrieved from the Murray ridge in January 2009, from 1172 meter below the sea surface (mbss) (22°19.9'N and 63°36.0'E) during PASOM expedition 64PE301, with the RV Pelagia (Figure 5.2). At this depth, measured oxygen concentrations of 5.0 μM indicate it is located at the lower boundary of the present-day OMZ, between 150-1250 mbss (Reichart et al., 2002; Von Rad et al., 1999). PASOM 3 total core-length of 5.37 meter was divided into 6 sections and sampled every 5 cm for the upper 470 cm with a syringe of 1.6 cm in diameter, whereas from 470-530 cm the sampling interval increased to 10 cm. For this study, we compared the more proximal NIOP 478 record with our more distal PASOM 3 record, to investigate differences between both locations. Therefore, we improved the NIOP478 age model of Reichart et al. (1998) to the similar resolution as PASOM 3, using reflectance (L*) data.

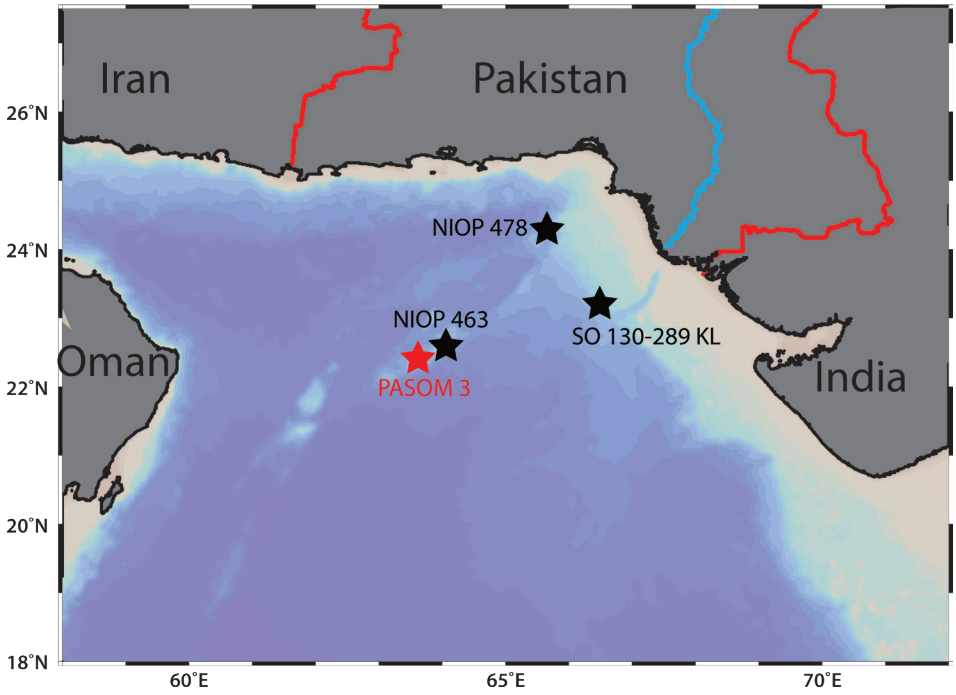

Figure 5.2. Location of PASOM 3 and reference cores used for this study (WOA09, Antonov et al., 2010; Locarnini et al., 2010). Depths of the cores are 1172 mbss (PASOM 3); 920 mbss (NIOP 463, Ziegler et al., 2010); 565 mbss (NIOP 478, Reichart et al., 2004) and 571 mbss (SO 130-289 KL, Deplazes et al., 2013).

5.2.2 Age model PASOM 3

The age model of the PASOM 3 core is based on tuning of PASOM 3 reflectance (L*) data with a resolution of 0.009 cm to the NGRIP and the nearby northeastern Arabian Sea SO-130-289KL record, as described by Deplazes et al. (2013), by focusing on the Greenland Stadial (GS) and Interstadial (GI) alternations (Figure 5.3; Andersen et al., 2004; Rasmussen et al., 2014). This method relies on previous observations that showed that cold GS's are associated with lighter sediments and a high reflectance (low organic carbon, higher calcium carbonate), whereas warmer GI's are associated with a higher organic content and hence lower reflectance. As the age model is primarily based on tuning the reflectance data, three accelerator mass spectrometry (AMS) Carbon-14 dates (Beta Analytic Inc., Florida, USA), measured on mixed planktonic foraminiferal species (predominantly *Orbulina*), are used as a final check for age model consistency. Calendar ages were calculated assuming a constant regional reservoir age (ΔR=232 ± 26 years) and Marine13 calibration curve (Reimer et al., 2013) as input for the CALIB 7.1 software

(Stuiver et al., 2017). The age model is based on linear interpolations between 41 control points (Table 5.1). The abundances of deep dwelling planktonic foraminifera (*Globorotalia truncatulinoides* and *Globorotalia crassaformis*) responsible for so-called *Globorotalia* events (Reichart et al., 1998; Ziegler et al., 2010), were compared to their independently dated occurrences (Ziegler et al., 2010). Because of the significantly different methods used and the much lower temporal resolution in NIOP 463, these age models differ somewhat. However, to enable visual comparisons between these records we added several lines connecting them. Sedimentation rates vary between 1.0 and 19.8 cm/ka, with an average sedimentation rate of 7.6 cm/ka.

Table 5.1 Tie points for the age model of PASOM 3

Tie points P3			Tie points II P3		
Depth (cm)	**Age (ka)**	**Sedimentation rate (cm/kyr)**	**Depth (cm)**	**Age (ka)**	**Sedimentation rate (cm/kyr)**
0.0	3.1	3.9	320.7	47.3	7.4
19.8	8.2	4.0	331.1	48.7	6.0
29.0	10.5	3.5	335.9	49.5	4.4
31.6	11.2	5.1	337.0	49.7	6.1
38.3	12.5	10.6	338.5	50.0	1.6
58.3	14.4	8.4	342.4	52.4	4.7
68.4	15.6	2.9	343.4	52.6	10.9
75.7	18.1	1.6	369.6	55.0	4.0
77.3	19.1	12.0	372.6	55.8	10.2
120.0	22.7	12.4	383.3	56.8	12.2
178.1	27.4	12.0	392.5	57.6	19.4
200.3	29.2	13.4	420.7	59.0	19.6
240.4	32.2	9.8	429.5	59.5	19.8
253.2	33.5	10.0	436.4	59.8	5.4
270.7	35.3	5.1	438.0	60.1	4.6
285.9	38.3	9.3	458.9	64.6	8.2
294.7	39.2	4.2	520.7	72.2	3.7
299.0	40.3	1.0	528.5	74.2	14.2
299.8	41.0	2.9	529.4	74.3	1.6
301.7	41.6	3.5	533.9	77.1	
314.0	45.1	3.1			

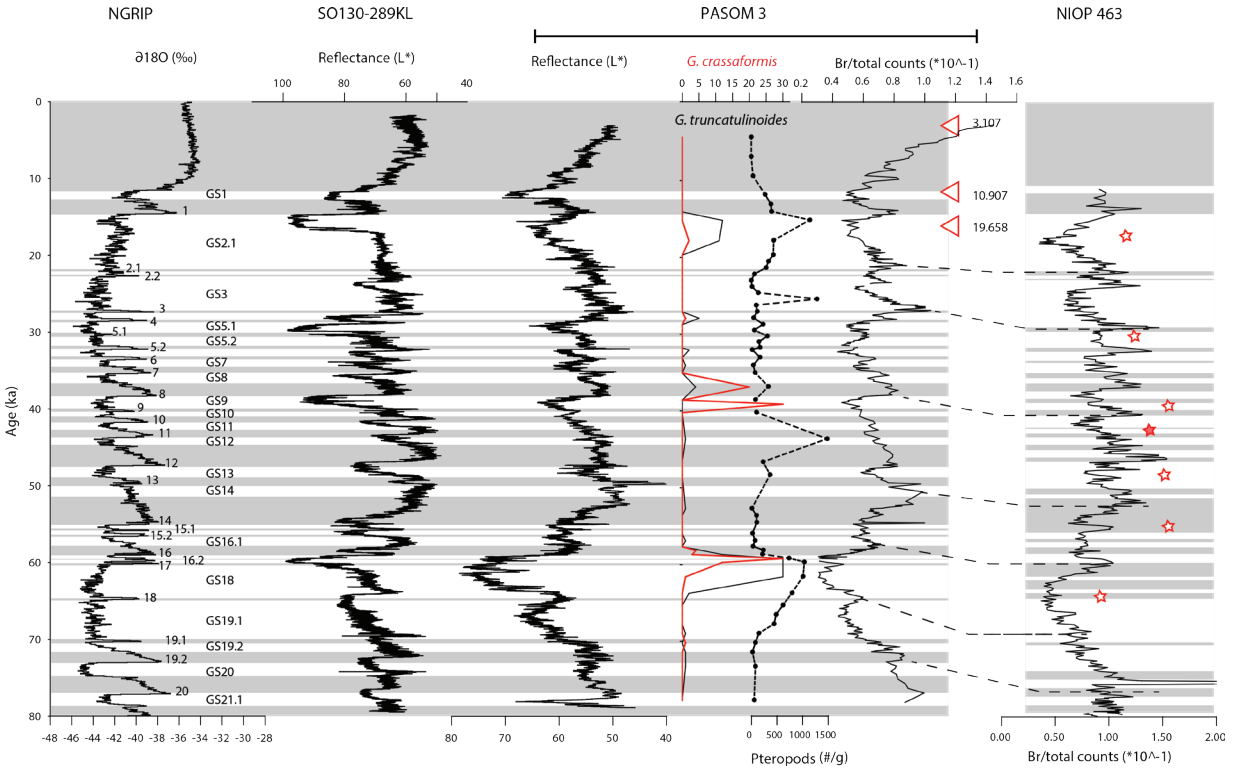

Figure 5.3. Age model of PASOM 3, based on tuning the reflectance (L*) data to that of the nearby SO130-289KL reflectance record (Deplazes et al., 2013) and NGRIP (Andersen et al., 2004). *Globorotalia* events are indicated by red stars (highlighting *G. crassaformis* and *G. truncatulinoides*) (Reichart et al., 1998; Ziegler et al., 2010), ^{14}C ages are indicated by triangles. Greenland Stadials (GS) are indicated in white and numbered (Rasmussen et al., 2014), Interstadials are indicated in grey and also numbered (without GS). A comparison with the Br record of nearby NIOP 463 core shows some discrepancies, probably related to the lower tuning resolution used in (Ziegler et al., 2010), based on *Globorotalia* events only. For clarification, extra lines are added between the same events. Tie points with the NGRIP and SO130-289KL are listed in Table 5.1.

5.2.3 Age model NIOP 478

A new age model was constructed for Pakistan Margin core NIOP 478 using 20 tie-points (Table 5.2), based on correlation of (new) reflectance data for NIOP478 to NGRIP, SO130-289KL and PASOM 3. Three accelerator mass spectrometry (AMS) Carbon-14 (^{14}C) dates already available (Reichart et al., 2004) and occurrences of deep dwelling planktonic foraminifera (*G. truncatulinoides* and *G. crassaformis*) (Reichart et al., 1998; Ziegler et al., 2010) are in line with this new age model (Figure 5.4). The average sedimentation rate of NIOP 478 is 23.5 cm/kyr, which is high compared to PASOM 3.

Table 5.2. Tie points for the age model of NIOP 478

Tie points NIOP 478			Tie points II NIOP 478		
Depth (cm)	**Age (ka)**	**Sedimentation rate (cm/kyr)**	**Depth (cm)**	**Age (ka)**	**Sedimentation rate (cm/kyr)**
0.0	0.0	17.0	918.4	43.4	16.5
246.3	14.5	19.5	983.6	47.3	11.9
498.4	27.4	20.9	1095.0	56.7	29.3
559.9	30.4	50.3	1186.1	59.8	4.4
652.9	32.2	31.5	1207.8	64.7	17.6
694.0	33.5	29.1	1294.5	69.6	72.3
747.8	35.4	24.9	1336.4	70.2	6.9
818.7	38.2	19.0	1354.3	72.8	16.0
859.5	40.4	10.5	1422.5	77.1	22.1
874.1	41.8	27.7	1428.4	77.3	

5.2.4 Oxygen isotopes

After wet-sieving and drying, 50 *G. ruber* specimens per sample from the 250-355 µm and ~15 *Neogloboquadrina dutertrei* specimens from the 212-400 µm dry-sieved fraction were hand-picked for elemental and isotopic analyses. Only specimens showing no signs of partial dissolution or contamination were selected. Before cleaning, all foraminiferal specimens were crushed lightly between two glass plates and transferred into two micro centrifuge ('Eppendorf') tubes. Approximately one third of the sample was used for isotopic analyses and two third was used for dissolution inductively coupled plasma mass spectrometry (dissolution-ICP-MS). Before analysis, the crushed specimens were cleaned according to an adapted Barker protocol (Barker et al., 2003), without the reductive

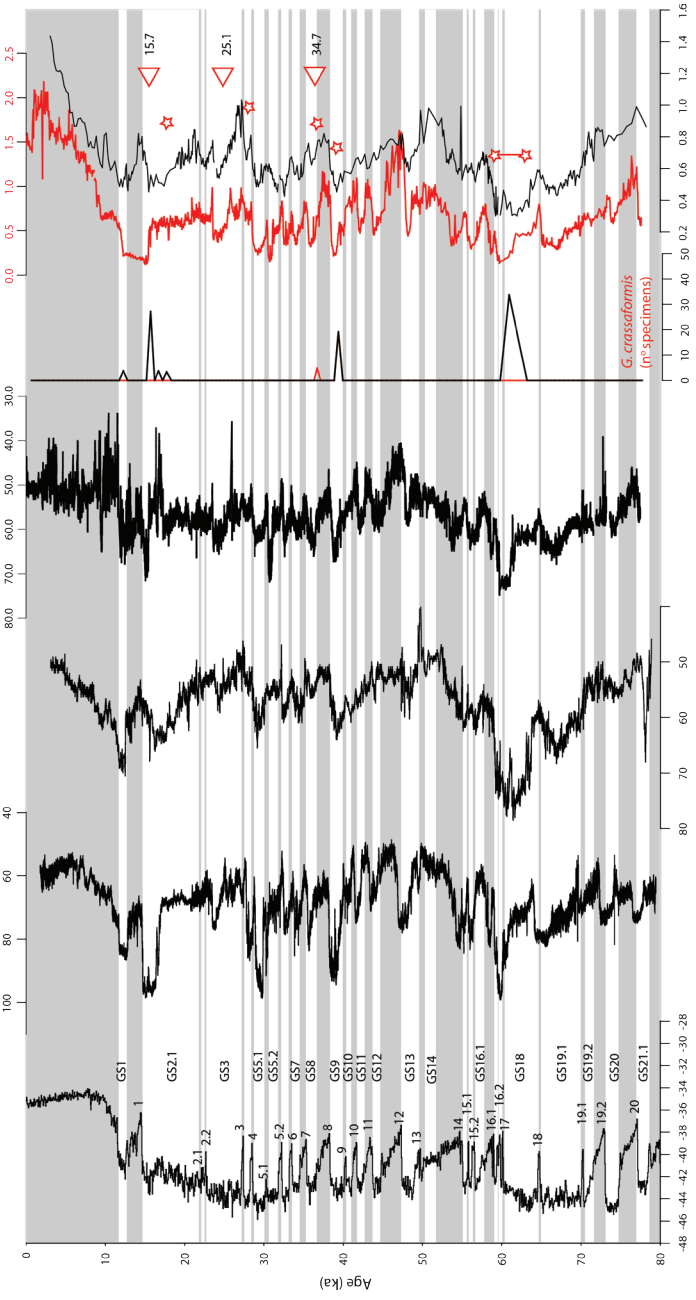

Figure 5.4. Age model of NIOP 478, based on reflectance (L*) tuning to the nearby SO130-289KL reflectance (Deplazes et al., 2013), PASOM 3 reflectance, and NGRIP stable isotope record (Andersen et al., 2004) (Table 5.1). Globorotalia events coincide with Greenland Stadials (Reichart et al., 1998; Ziegler et al., 2010) and NIOP 478 ^{14}C ages are indicated with triangles. Next to the *Globorotalia* record of NIOP 478, Br records of PASOM 3 and NIOP 478 (red) are also shown, with stars indicating the *Globorotalia* events of PASOM 3. Greenland Stadials (GS 1-21.1) are indicated in white, Greenland Interstadials in grey and with numbers.

cleaning step. First, clay particles were removed using ultrapure water, ultrasonication and methanol. Thereafter, organic particles still present were removed using a fresh alkali buffered 1% H_2O_2 solution, with NH_4OH instead of NaOH as a buffer to avoid unnecessary Na contamination. After drying, 20-40 µg per sample was weighed for stable isotopic analysis. Stable oxygen ($\delta^{18}O$) and carbon ($\delta^{13}C$) isotopes were determined with an automated carbonate device (Kiel IV, Thermo) connected to a Thermo Finnigan MAT 253 Dual Inlet Isotope Ratio Mass Spectrometer (IRMS) and reported relative to the Peedee belemnite (PDB) in standard δ notation. The NIOZ Foram house standard (NFHS-1; Mezger et al., 2016) was used for drift detection, whereas the National Bureau of Standards (NBS) 19 limestone was used as a calibration standard. The standard deviation and offset of the NBS19 standard as well as the NFHS-1 were always within 0.1‰ for $\delta^{18}O$.

To calculate SSS, a method similar to Reichart et al. (2002) has been applied. The oxygen isotopic composition of foraminiferal calcite is controlled by the calcification temperature (δ_c) as well as the $\delta^{18}O$ of the seawater (δ_w), the latter controlled by ice volume and salinity. The $\delta^{18}O$ of the seawater was obtained with the known temperature dependent isotopic fractionation relationship between seawater and calcite (Epstein et al., 1953; Shackleton, 1974), adapted by Reichart et al. (2002) to enable comparison between both records (respectively NIOP 478 and PASOM 3):

$$\Delta T_{dT} = -4.38[\Delta\delta_{ruber(dt)} - (\Delta\delta_{w\_Ice} + \Delta\delta_{w\_S})_{(dt)}] + 0.10[\Delta\delta_{ruber(dt)} - (\Delta\delta_{w\_Ice} + \Delta\delta_{w\_S})_{(dt)}]^2 \quad (1)$$

Ice volume corrections were done by directly correlating the PASOM3 record to the LR04 benthic stack (Lisiecki and Raymo, 2005), corrected for deep water temperature variability by assuming a maximum glacial-interglacial change due to ice volume of 1.2‰ (Fairbanks, 1989; Shackleton, 1987). Thereafter, SST corrections were based on measured $U^{K'}_{37}$ and foraminiferal Mg/Ca SST.

5.2.5 XRF, Reflectance and TOC

For X-Ray Fluorescence (XRF) measurements, sediment surfaces were levelled out and covered with a thin Ultralene (4 µm) film to prevent contamination and drying of the sediment surface. Thereafter, the bulk elemental composition of the sediment was determined with an irradiation area of 1.2 cm^2 and a sampling interval of 1.0 cm. Core sections were scanned using an Avaatech XRF Core Scanner (Richter et al., 2006) at the Royal NIOZ, the Netherlands, with tube voltage set-ups of 10, 30 and 50 kV and count times of 10, 10 and 40 seconds to detect both light and heavy elements. Here we

report the Br (30 kV, 10 seconds), as well as other elements as counts relative to the total counts (Weltje and Tjallingii, 2008). Sediment total reflectance (L^*) measurements were performed using line scans with a 0.1 mm resolution, of which higher values indicate lighter sediments and lower values indicate darker sediments.

For organic carbon analyses, sediment samples (~0.5 g) were freeze-dried and homogenized. After decalcification with 2 M hydrogen chloride, the samples were shaken overnight and rinsed with ultrapure water until the pH of the supernatant decreased below 5. Subsequently, samples were freeze-dried and 1-1.5 mg of sediments were transferred to tin cups organic carbon analysis. Measurements were performed with using a Flash EA 1112 Series (Thermo Scientific) analyser coupled to a Finnigan Deltaplus mass spectrometer (MS) via a Conflo II interface, with Acetanilide, benzoic acid standards and blank measurements measured at regular intervals.

5.2.6 Foraminiferal shell (trace) elements and counts

The same cleaning protocol was used as mentioned for the oxygen isotopes, with two additional steps. First, a reductive cleaning step for removal of metal (Fe, Mn) oxides was added, using a heated ammonium citrate/ammonium hydroxide solution mixed with 1.2 mL hydrazine hydroxide. After five rinsing cycles with heated ultrapure water and a gel loaded pipet tip and one cold water rinsing step to ensure no chemicals are left in the samples, samples were transferred to clean micro-centrifuge tubes. Second, adsorbed ions were removed with a leaching procedure. To do this, 250 uL of 0.001M HNO_3 was added to each sample followed by ultrasonication (degas mode, 80 kHz, 50% power) and direct removal of the acid to avoid excessive dissolution. After dissolution of the cleaned sample in 0.1 M ultragrade HNO_3, the foraminiferal elemental composition was measured on an Element 2-ICPMS at the Royal NIOZ, the Netherlands, with the isotopes of ^{23}Na, ^{24}Mg, ^{43}Ca, ^{44}Ca and ^{138}Ba being measured in low mass resolution and the ^{55}Mn and ^{43}Ca isotopes being measured in medium resolution. Samples were measured against 4 ratio calibration standards with a similar matrix, with a drift standard being measured every third sample. The monitor standards JCt-1 and NFHS-1 were included for quality control (Mezger et al., 2016; Okai et al., 2002). The RSD per measurement for all low resolution (LR) measurements was below 0.1% for all elements, except for Ba, which varied between 0.1 and 3%. The RSD for all high-resolution measurements was more variable but still below 1.3%.

Abundances of deep dwelling planktonic foraminifera (*G. truncatulinoides* and *G. crassaformis*) were quantified by counting specimens from the >150 µm fraction, to a maximum of 30 species (Reichart et al., 1998). Pteropod fragments were counted from the same fraction for all samples from PASOM3, normalized for bulk sediment weight.

5.2.7 Long chain alkenones ($U^{K'}_{37}$)

Sediments were freeze-dried and subsequently homogenized with an agate mortar. Depending on sediment availability, 9.0 to 18.0 g of sediment were analysed for alkenones as described in e.g. Lattaud et al. (2018). To summarize, sediments were extracted using an Accelerated Solvent Extractor 350 (ASE 350, DIONEX). Prior to column chromatographic separations, 3 µg of 10-nonadecanone was added for quantification of alkenones. Apolar, ketone and polar fractions were separated by column chromatography with hexane:DCM 9:1 (v:v), hexane:DCM 1:1 (v:v) and DCM:MeOH 1:1 (v:v), respectively. Ketone fractions were analysed using a Hewlett Packard 6890 gas chromatograph equipped with a flame ionization detector and helium as the carrier gas at the Royal NIOZ, the Netherlands. Peak areas of $C_{37:2}$ and $C_{37:3}$ alkenones were calculated by integration and quantified using the 10-nonadecanone as internal standard.

5.3 Results

5.3.1 XRF, TOC and pteropod counts

Four major *Globorotalia* events (15.20-17.85 ka; 36.89 ka; 38.60-40.20 and 58.20-63.75 ka) and one minor event (27.93 ka) can be distinguished for PASOM 3 (Figure 5.3). Furthermore, small peaks are found at GS6 and 7. High pteropod counts coincide with *Globorotalia* events at times of colder Greenland Stadials (respectively GS 2.1, 3 8, 12, 13, 17-19.1), but events seem to be somewhat older compared to the *Globorotalia* event at 38.6-40.2 ka. The Br record, being lower at GS's and higher at interstadials (GI's), correlates well with the reflectance record (Figure 5.3).

The pattern of the TOC (Corg%) correlates well with the reflectance record, and hence with the Greenland ice core record, being high during GI's and low during GS's. We normalized the XRF data either to Al or Ti, to prevent close sum effects (Reichart et al., 1997). Both Ba and Ti are normalized to Al to facilitate comparison to existing records, all others are normalized to Ti as this is generally more robust (Weltje and Tjallingii, 2008). The Ti/Al record corresponds well to the reflectance record, being high during GI's 2, 3, 4, 5.1, 5.2, 6, 8, 12 and 13, 14. However, during colder GS2.1 and GS3, also a few peaks in Ti/Al

are observed. Patterns in Ti/Al, Br/Ti, Ca/Ti and Ba/Al are very similar, all values being highest during the Holocene and other warm GI's (e.g. GI 1, 14 and 16). Especially from 40 ka to present, the Ca/Ti record looks similar to the Br/Ti and Ba/Al record, albeit that also cold Ca/Ti peaks are found in GS's 12, 13 and 14 which are not observed in the other records. The Ba/Al record is mainly low during GS's and higher during GI's, being most pronounced in the Holocene and GI's 2.1, 13, 14 and 16. Furthermore, also three peaks are observed during colder GS2.1, similar to peaks in Ti/Al in this time interval (Figure 5.5).

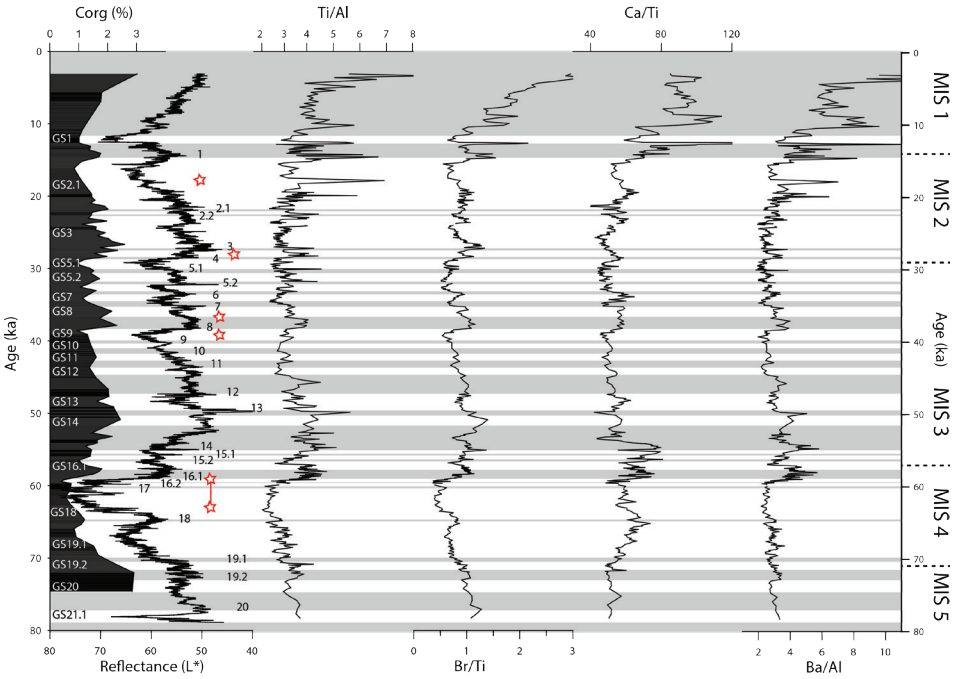

Figure 5.5. All TOC (Corg, in weight%), reflectance and XRF Ti/Al, Br/Ti, Ca/Ti and Ba/Al data for PASOM 3. Greenland Stadials (GS) are indicated in white and numbered, Interstadials are indicated in grey and also numbered (without GS) and marine isotope stages (MIS) are indicated on the right axis.

5.3.2 Foraminiferal $\delta^{18}O$, Mg/Ca and ketones

In general, the *G. ruber* oxygen isotopic record shows changes coinciding with the marine isotopic stages (MIS), and, as far as the resolution permits, also with the GS and GI pattern known from the Greenland ice core records (Figure 5.6). Values are more negative during warmer intervals (GI's) and more positive during cold intervals (GS's). Highest oxygen isotope values are observed for the Holocene, increasing from the end of GS1/Younger Dryas to present day. Almost every GI is also recognized in the *G. ruber* oxygen isotopic

record from the Arabian Sea, particularly from 42ka to present. Although in the older part of the record the oxygen isotope records of *G. ruber* and *N. dutertrei* are dissimilar, from the start of GS2.1 to present trends are comparable. Foraminiferal Mg/Ca values range from 3.3 to 5.2 mmol/mol. Temperature records obtained from Mg/Ca and $U^{K'}_{37}$ covary significantly, albeit that the correlation coefficient is low (r=0.33), and the pattern of reconstructed temperatures coincides with that expected based on our correlation to the Greenland ice core record. Some offsets are observed in timing of the onset or end of specific events, which most likely are due to the limited sampling resolution. Overall changes in temperature based on $U^{K'}_{37}$ seem larger than that observed for Mg/Ca-based temperatures (Figure 5.6).

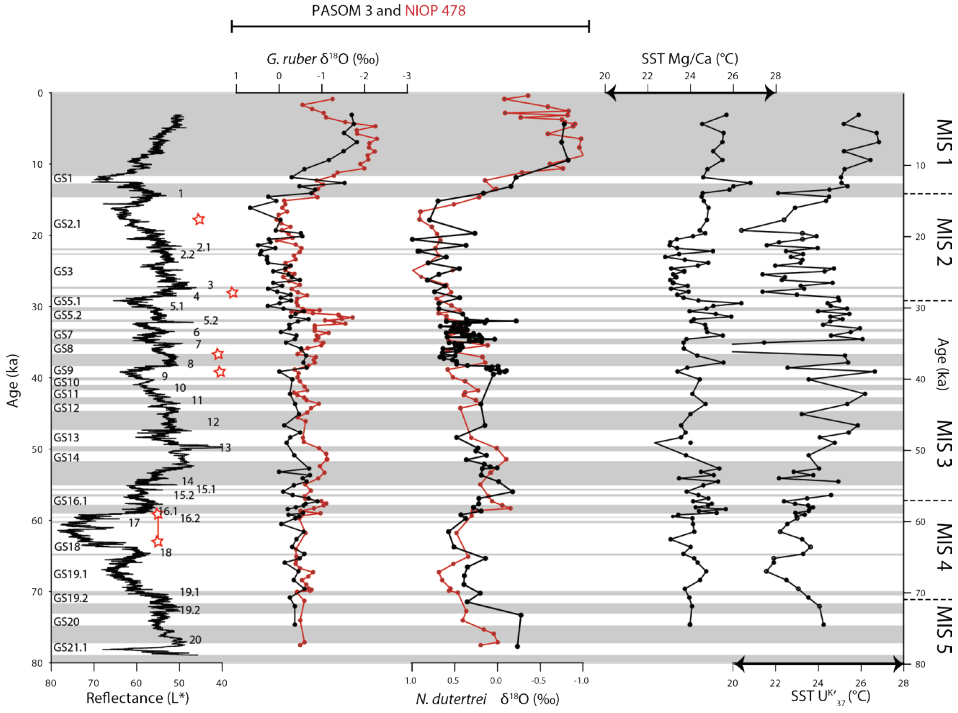

Figure 5.6. Overview of sea surface temperature (SST) proxies (foraminiferal Mg/Ca, molecular $U^{K'}_{37}$) used for this study, compared to reflectance data with stars indicating *Globorotalia*-events and $\delta^{18}O$ data of *N. dutetrei* and *G. ruber*, and the difference between NIOP 478 (red) and this study (black, PASOM 3). Greenland Stadials (GS) are indicated in white and numbered, Interstadials are indicated in grey and also numbered (without GS) and marine isotope stages (MIS) are indicated on the right axis.

5.3.3 Foraminiferal-based salinity proxies

Foraminiferal Ba/Ca values vary between 0.7 and 4 µmol/mol, with some excursions up to 36 µmol/mol (Figure 5.7). Higher values, including the larger amplitude excursions, seem to coincide mostly with the inferred warmer intervals. During the Holocene, foraminiferal shell Ba/Ca values are overall high, as well as during GI's 5.1, 4, 8, 12, 13-14, 16, and 18. However, the pattern is not consistent throughout the entire record, as lower Ba/Ca values are also observed during e.g. GI 1. Absolute Na/Ca values range from 6.4 to 10.7 mmol/mol, with lowest Na/Ca values being observed during the Holocene and at the end of GS 2.1. From GS8 to recent, the Na/Ca pattern mainly co-varies with the GI GS pattern. Clear Na/Ca peaks are also observed at GS 18, 19.1, 19.2 and 20. However, from GS 16 to GS 8, this pattern is interrupted with high values being observed during the warmer intervals GI 7, 12 and 14. After corrections for ice volume and SST (Section 4.2.4), the $\delta^{18}O$_salinity patterns co-vary with the Greenland ice core and reflectance record. Lower $\delta^{18}O$_salinity

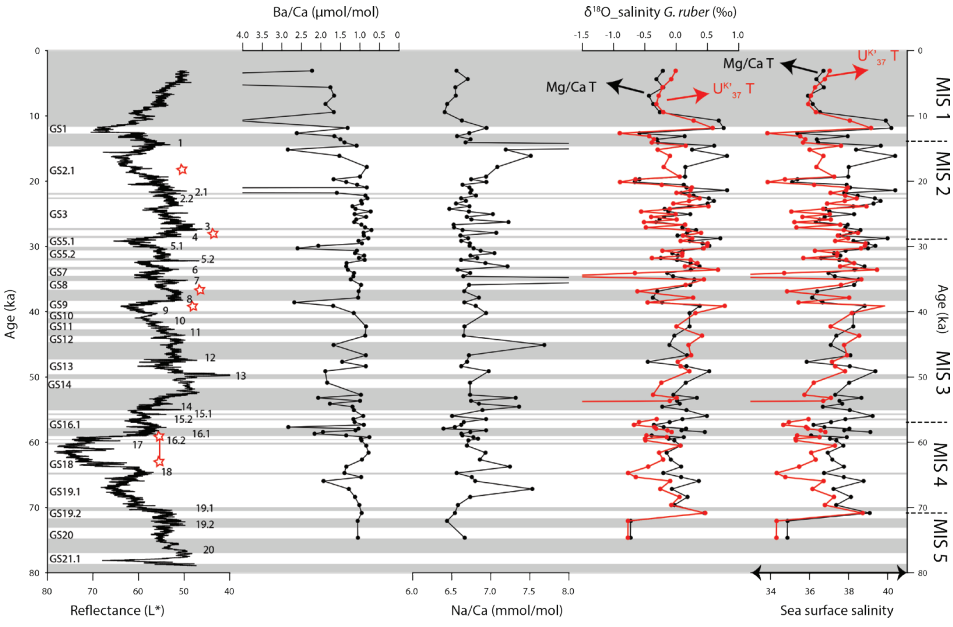

Figure 5.7. Overview of potential sea surface salinity proxies (foraminiferal Ba/Ca, Na/Ca and $\delta^{18}O$ corrected for ice volume and sea surface temperature (SST, with red: Mg/Ca SST and black $U^{K'}_{37}$ SST corrections), compared to reflectance data with stars indicating *Globorotalia*-events. Greenland Stadials (GS) are indicated in white and numbered, Interstadials are indicated in grey and also numbered (without GS) and marine isotope stages (MIS) are indicated on the right axis.

values correspond to the Holocene and warmer intervals (GI's), whereas high $\delta^{18}O$_salinity values are observed in colder intervals (GS's).

5.3.4 Oxygenation proxies

In general, XRF-based Mn/TIC (TIC: total inorganic counts) values are lower during warm intervals and higher during colder GS's (Figure 5.8). However, this pattern is not always clear and from ~42 ka to ~60 ka, peaks are correlated to warm GI's. Foraminiferal shell Mn/Ca values range between 8 µmol/mol and 0.034 mmol/mol and correlate for the upper ~50 kyr with the Greenland ice-core and reflectance record. Highest peaks occur during warmer GI's and the Holocene, albeit that for the lower part of the record also peaks are observed during cold GS 18. Foraminiferal Mn/Ca values anti-correlate

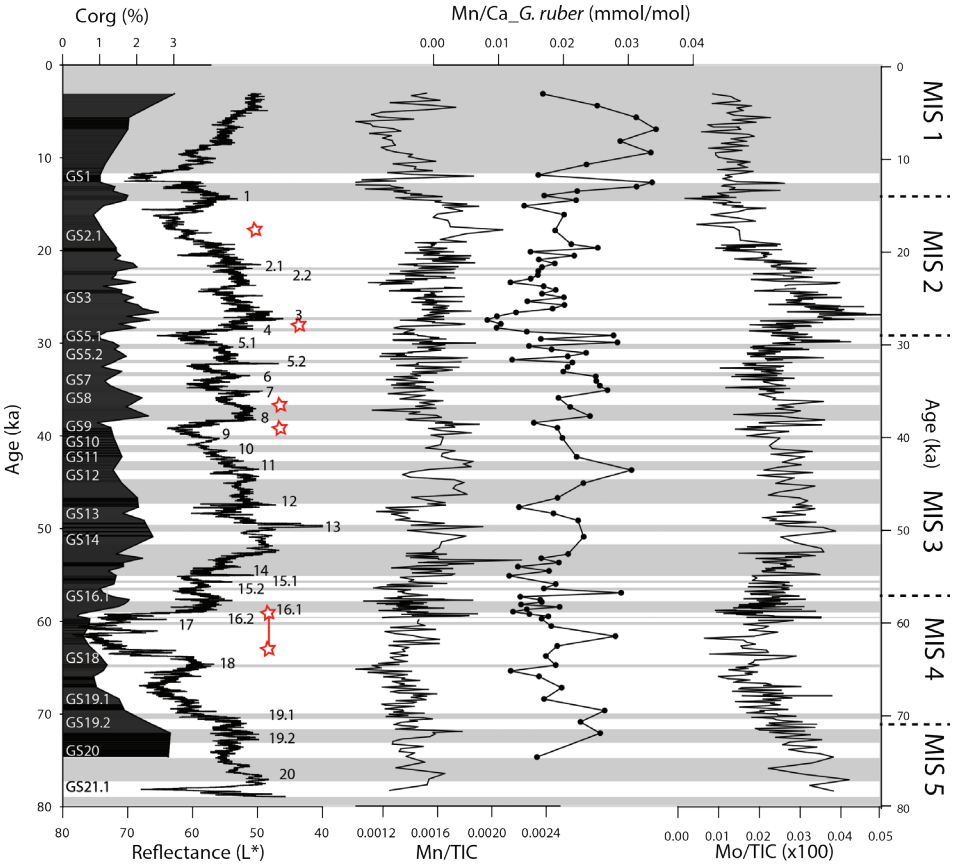

Figure 5.8. All TOC, reflectance, XRF oxygen minimum zone (OMZ) redox sensitive elements (Mn, Mo) and *G. ruber* Mn/Ca data for PASOM 3. Greenland Stadials (GS) are indicated in white and numbered, Interstadials are indicated in grey and also numbered (without GS) and marine isotope stages (MIS) are indicated on the right axis.

with XRF-based Mn/TIC values of the sediment. Mo/TIC values are noisy, but generally coincide with the reflectance pattern. Highest Mo/TIC values are found during GI's 1, 3, 5.1, 5.2, 8, 10, 13 and 20.

5.4 Discussion

The down-core pattern observed, based on reflectance, Br XRF counts and TOC, is similar to that observed in other cores in the area (e.g. Deplazes et al., 2013; Reichart et al., 1998; Von Rad et al., 1999). This allows comparing records in high resolution, also for the other proxies as they have a common age model after cross-calibrating these records. The good correlation between the PASOM 3 reflectance record and solid phase Br and Br/Ti (respectively marine versus aeolian inputs) confirms the overall marine origin of the organic matter in the darker sediments, similar to other studies (e.g. Ziegler et al., 2008; Sinninghe Damsté et al., 2002). The correlation to the Greenland ice core record shows that during GI's the SWM was intensified, resulting in darker sediments being deposited because of high upwelling-related sea surface productivity and an extended oxygen minimum zone (Reichart et al., 1998; Schulz et al., 1998). In contrast, the lighter coloured sediments deposited during GS's most likely reflect a weaker SWM (Schulz et al., 1998) and an enhanced NEM (Reichart et al., 1998). During the GS's, winter winds coming from the Asian continent were enhanced and colder, resulting in convective mixing of the upper water column in the northernmost Arabian Sea (Reichart et al., 2001). Ventilation of the local OMZ resulted in a weakening/breakdown of the OMZ (intensity) and deepening of the aragonite compensation depth (ACD; Deplazes et al., 2013; Reichart et al., 1998; Schulz et al., 1998; Von Rad et al., 1999)). This is reflected in the pteropod counts in this study, being enriched during colder Greenland Stadials (resp. GS 2.1, 3 8, 12, 13, 17-19.1) as already observed in e.g. Reichart et al. (1997) and Schulz et al. (1998). Abundances of deep dwelling planktonic foraminifera (*G. truncatulinoides* and *G. crassaformis*), representing so-called *Globorotalia* events (Reichart et al., 1998; Ziegler et al., 2010), are dependent on deep convective winter mixing, bringing juveniles to the surface to complete their life cycle (Reichart et al, 1998, and references therein). Also here, *Globorotalia* events are observed during the coldest GS's. Altogether, this shows that summer and winter monsoon intensity are anti-correlated, also on millennial time scales, with maximum winter monsoon intensity being linked to the colder phases of the Greenland ice core record and maximum summer monsoon intensity being linked to the warmer phases.

5.4.1 Proxy validation

Sea surface temperatures

The observed pattern in SST based on foraminiferal Mg/Ca and organic geochemical $U^{K'}_{37}$ correlates well with the reflectance record and hence the Greenland ice core record (Andersen et al., 2004; Rasmussen et al., 2014) (Figure 5.6). Absolute Mg/Ca values fall within the expected range based on sediment trap calibrations (e.g. Anand et al., 2003; Elderfield and Ganssen, 2000), with inferred temperatures varying between 22.3 and 26.8 °C (Anand et al., 2003). The range of reconstructed temperatures based on $U^{K'}_{37}$ have a higher amplitude compared to the Mg/Ca-based values, between 15.6 (at GS 8) and 26.9 °C, using the calibration of Müller et al. (1998). Reconstructed temperatures are colder during GS's and warmer during GI's in both the $U^{K'}_{37}$ and Mg/Ca based records. The highest calculated temperatures are observed during the Holocene and MIS3, which is especially clear from the $U^{K'}_{37}$ temperature record. Although differing in amplitude, the pattern of the reconstructed temperatures and temperature changes for Mg/Ca and $U^{K'}_{37}$ are still rather similar.

Discrepancies between proxies based on different proxy signal carriers are regularly observed and can be related to differences in e.g. growth season and/or depth habitats of the organisms involved (e.g. Sangiorgi et al., 2003; Sbaffi et al., 2001). In general, $U^{K'}_{37}$ derived SST's are lower during glacial MIS's and higher during interglacial MIS's compared to the Mg/Ca based temperatures (Figure 5.6). The observed difference in reconstructed temperatures between both records can be explained for instance by a shift in the growth season of *Emiliania huxleyi* relative to *G. ruber* (Prahl et al., 2000; Rosell-Melé and Prahl, 2013; Sangiorgi et al., 2003). Changes in monsoon intensity could affect the growth season of *E. huxleyi.* which is today associated with the early phase of the SWM (Prahl et al., 2000; Rixen et al., 2006). Presently, coccolithophorids lag the onset of the summer monsoon with about a month and precede the major diatom bloom during the summer monsoon maximum. Secondary peaks in long chain ketones are, however, also observed at the end of the summer monsoon and at the end of the winter monsoon (Prahl et al., 2000; Rixen et al., 2006). Hence a shift in *Emiliania huxleyi* blooms towards later in the summer monsoon could result in warmer temperatures being recorded, as well as that a larger part of the production being associated with summer versus winter monsoon would also increase reconstructed temperatures. This implies that maxima in summer monsoons result in temperatures being biased towards summer SST and maxima in winter monsoons resulting in a bias towards colder temperatures. Similarly, the relative fluxes of *G. ruber*

could also change between monsoon seasons and within the summer monsoon, but based on the data shown here apparently to a lesser degree.

Sea surface salinity

The salinity proxies applied here -foraminiferal Ba/Ca, Na/Ca and stable oxygen isotopes corrected for SST and ice volume- show different responses to stadial-interstadial changes (Figure 5.7). *Globigerinoides ruber* Ba/Ca suggests lower salinities during warmer GI's, whereas Na/Ca measured on the same specimens, using the calibration from Mezger et al. (2016), would suggest higher salinities during the colder GS's. The salinity and ice volume corrected oxygen isotope record co-varies with most GS's and GI's of the Greenland ice core record. The three approaches used give different results, both in the reconstructed trends and in absolute values, depending on which calibration is used.

Although the Na/Ca values measured on the Arabian Sea foraminifera are similar to those reported in Mezger et al. (2018) and Allen et al. (2016), applying the Na/Ca-SSS calibrations proposed in these papers would result in unlikely reconstructed salinities (Allen et al., 2016: 31.1-52.7; Mezger et al., 2016 : 32.9-40.5, excluding the excursion during GS 2.1, which seems an outlier). Values of Na/Ca are somewhat higher compared to the *T. sacculifer* calibration values of Bertlich et al. (2018). Whereas the Na/Ca to salinity calibration of Mezger et al. (2016) still suggested that *T. sacculifer* and *G. ruber* had similar values at the same salinity, Mezger et al. (2018) and Bertlich et al., (2018) showed an offset between these species, with *G. ruber* generally showing higher values. Hence applying the *T. sacculifer* calibration (Bertlich et al., 2018) would result in too high salinity values. Importantly, recently Mezger et al. (2019) and Mezger et al. (2018) showed that shell foraminiferal Na/Ca values are sensitive to carbonate preservation, as Na-enriched spine bases as well as the spines themselves are often lost. On longer time scales, Na within the shell might also be subject to leaching (Branson et al., 2016; Mezger et al., 2018; Yoshimura et al., 2017), albeit that this process has only been observed on time scales much longer than considered here (Yoshimura et al., 2017). Consequently, partial loss of Na-rich components, such as spines and spine bases, offsets reconstructed salinity. Although calculated salinities are offset, peaks in Na/Ca still mostly coincide with the colder GS's. Such a correlation makes sense as an intensified winter monsoon during GS's would be characterized by enhanced evaporation rates in the northern Arabian Sea and thus also higher salinities. The magnitude of these Na/Ca variations, however, might also reflect carbonate preservation. Enhanced carbonate preservation could increase the relative proportion of spine base carbonate being preserved and thus increase foraminiferal Na/

Ca values. Better calcium carbonate preservation during GS's is in line with the pteropod record showing a deepening of the ACD at those times (Figure 5.3).

Absolute Ba/Ca values are similar, or somewhat higher, compared to other studies using Ba/Ca to reconstruct river inputs (Edmond et al., 1978; Lea and Spero, 1994; Weldeab, 2007). The amount of Ba incorporated will strongly depend on local setting, as the Ba concentration in different rivers varies and hence the calibration to salinity in front of these rivers as well. With the concentration of Ba in the Indus River being unknown, we cannot calibrate our data and therefore only interpret the overall pattern. During the Holocene and other warm GI's (5.2, 12, 13, 14, 16), Ba/Ca values are high, however, for the rest of the record values are highly variable, not showing a clear correlation with the GS's or GI's known from the Greenland ice core record. This could either imply that the core location is not proximal enough to register all changes in Indus River outflow, or that not all changes in salinity are related to changes in Indus outflow. Alternatively, Indus River Ba concentrations could be relatively low, which would result in only the more prominent events being picked up by the Ba/Ca record.

Reconstructed SSS based on $\delta^{18}O_{water}$ (also referred to as $\delta^{18}O$ salinity) varies between 30.3 to 39.8 (with one outlier of 15.1) using $U^{K'}_{37}$ sea surface temperatures, or from 34.9 to 40.4 based on Mg/Ca sea surface temperatures. One would expect the most robust reconstruction based on using Mg/Ca temperatures as in that case the same proxy signal carrier (i.e. foraminifera) is used and offsets due to differences in seasonality and/or habitat are avoided. Reconstructions using either $U^{K'}_{37}$ or Mg/Ca seem, however, remarkably robust and show largely identical patterns (Figure 5.7). Highest salinities are found at the end of GS 1, decreasing during the Holocene. General patterns compare well with the reflectance record, with higher salinities during, or at the end of GS's. The most recent calculated salinities (36.7 and 37.0) fit well with current local salinity of ~36.5 (WOA09, Figure 5.1; Antonov et al., 2010; Locarnini et al., 2010). Altogether, reconstructing SSS in the Arabian Sea is still best by combining proxies ($\partial^{18}O$ and independent SST reconstructions).

OMZ intensity and dust supply

The Ba/Al and Ca/Ti XRF records, proxies for marine biological productivity (Ba/Al; Bishop, 1988; Dehairs et al., 1980; Dymond et al., 1992; Francois et al., 1995) and carbonate export productivity (Ca/Ti); Grant and Dickens, 2002), are high during warm GI's and the Holocene (Figure 5.5). This indicates that primary productivity was high during warmer

episodes (GI's) and stronger SWM's, in line with reconstructed SST's, reflectance and the TOC record. Based on Ti/Al ratios, mainly reflecting grain size (Lourens et al., 2001), dust supply was also higher during warm GI's, in contrast to what was found for the near-coast record in Reichart et al. (1997). Potentially, the location of the PASOM 3 site in the more central northern Arabian Sea is more influenced by SWM related dust, transported by the north-westerly winds overriding the Findlater jet from the North West, similar earlier suggestions by Clemens and Prell (1990) for offshore Oman.

Redox sensitive elements such as Manganese (Mn) and Molybdenum (Mo) reflect intensity of the OMZ (Schenau et al., 2002). Manganese becomes remobilized under low bottom water oxygen conditions, resulting in low sedimentary Mn concentrations in OMZ sediments and Mn enrichments in the deeper part of the basin (Schenau et al., 2002). In contrast, Mo becomes immobilized during the low oxygen conditions and is hence enriched during an intense OMZ where the OMZ impinges on the local sea floor topography. Similar to what is expected, generally higher Mn/TIC values are observed during cold GS's, and lower values at times of a stronger OMZ during warmer intervals (Figure 5.8). Mo shows more scatter but is generally higher during warm events and lower during cold events. During GS's, convective mixing of the water column due to intensified and cold NEM winds resulted in ventilation and sometimes breakdown of the OMZ. The Mo/TIC record is noisy, but the general pattern is similar to the reflectance record, showing higher Mo during low reflectance episodes. This confirms that OMZ intensity was strongest during warm GI's, and convective NEM-related convective overturning during colder intervals weakened the OMZ.

Several studies suggest that the incorporation of Mn into the shells of different foraminiferal species can be used to reconstruct past bottom water or water column oxygenation (Barras et al., 2018; Groeneveld and Filipsson, 2013; Klinkhammer et al., 2009; Koho et al., 2017; Munsel et al., 2010; Ní Fhlaithearta et al., 2010; Reichart et al., 2003; Steinhardt et al., 2014). The underlying assumption of this proxy is that during low oxygen conditions, Mn can escape at the sediment water interface into the water column (Schenau et al., 2002). In the central Arabian Sea, high foraminiferal (*G. ruber*) Mn/Ca values are observed during warmer GI's, with highest values during the Holocene. This is in line with higher Mn concentrations in the water column due to enhanced regeneration from the seafloor, but could also reflect enhanced mobilization from particles falling through the water column (Klinkhammer et al., 2009). Maximum Mn/Ca values correspond to enhanced dust inputs inferred from sedimentary Ti/Al values. Since dust input and OMZ

intensity are positively correlated, both processes might reinforce each-other. Low oxygen conditions will enhance the mobilization of Mn from the Mn-oxide/hydroxide coatings of the dust particles. Absolute Mn/Ca values are higher compared to Steinhardt et al. (2014) but similar to Klinkhammer et al. (2009). Present-day northern Arabian Sea surface Mn concentrations vary from 1.9 to 4.3 nmol/kg (translated into mmol /mol: 0.19-0.43), being up to 8 times higher compared to open ocean conditions (Saager et al., 1989). In a study of Munsel et al. (2010), it was found that the partitioning (D) of Mn in cultures of the benthic foraminiferal species *Ammonia tepida* is at least 2.4. Comparing recent Holocene *G. ruber* Mn/Ca values (up to 0.038 mmol/mol) to present-day northern Arabian Sea Mn concentrations, partitioning for this species would be between ~0.02 and 0.2. These values correspond well to earlier reported values (Barras et al., 2018; Steinhardt et al., 2014). The correlation shown here implies that Mn/Ca incorporation in the planktonic foraminifer *G. ruber* can be used to reconstruct OMZ intensity.

5.4.2 Reconstruction NE Arabian Sea hydrology

Comparison between a nearshore Pakistan record (NIOP 478, 565 mbss; Reichart et al., 2002) and the central Arabian Sea record from this study (PASOM 3, 1172 mbss) adds a spatial perspective to our observations. Reflectance, Br patterns, oxygen isotope records of *G. ruber* and *N. dutertrei* and the timing of *Globorotalia* events are similar for both records (Figure 5.4), albeit that short-lived Greenland events are more pronounced near the coast, similar to observed earlier by (Deplazes et al., 2013). Variations in SST and SSS are overall rather similar, with SSS being higher and SST lower during cold GS's and vice versa for GI's (Figure 5.7). However, the amplitude of SST and SSS variations differs between the two locations. For example, during warmer MIS's, the central Arabian Sea exhibits higher SST's (MIS 3) or similar SST's (MIS 1, 5) compared to the more nearshore SST's. During MIS's 2 and 4 SST's reconstructed for the central location are similar or colder compared to the more near shore site. This is surprising as the source for these cold events has been inferred to come from the Central Asian continent. During warmer MIS's (1, 3 and 5) (except for GI 1), salinities are similar (Holocene) or higher (MIS 3) at the central Arabian Sea, whereas during cold intervals (MIS 2, 4) SSS's are lower compared to the more near shore record. Differences in SSS and SST together determine convective overturning and hence should also be reflected in the proxies for the vertical structure of the upper water column.

The difference in oxygen isotopic composition ($\delta\delta^{18}O$) between sea surface calcifying *G. ruber* and the deeper thermocline dweller *N. dutertrei* can potentially be used to

reconstruct changes in convective overturning and/or stratification (e.g. Steinhardt et al., 2014 and references therein). When $\delta^{18}O$ values (*N. dutertrei* - *G. ruber*) become similar, this indicates that both species calcified in the same water mass and under the same conditions. Both species calcifying at the same conditions could also be due to *N. dutertrei* migrating upward in the water column because of shoaling of the thermocline. This has been observed for the Peruvian margin, where *N. dutertrei* is suggested to have changed its living depth (from ~300 to 70 meters depth) at times of increased upwelling and a more intensified OMZ (Nürnberg et al., 2015). For the Arabian Sea, the $\delta\delta^{18}O$ records are almost identical (MIS 4) or similar at the two locations for most of the last glacial cycle, albeit that variations are larger and absolute values lower for the central Arabian Sea. Importantly, high SSS's and $\delta\delta^{18}O$ values are observed in the coastal record compared to the central Arabian Sea during times characterized by a stronger NEM (e.g. MIS 2; Figure 5.9, Figure 5.10a-f). This is in line with winds coming from the Asian continents during strong NEM's at times of GS's resulting in enhanced convective mixing. Lowest temperature and strongest mixing would in that case be expected near the coast. The higher coast salinities also suggest an evaporative effect from an intensified NEM, as the driest winds resulting in most evaporation come from the continental interior. During MIS 4, and to a somewhat lesser extend also during MIS 2, $\delta\delta^{18}O$ records are similar, indicating that both species lived in the same conditions, which is in line with a homothermal upper water column (Figure 5.7, 5.8a-c). $U^{K'}_{37}$-based sea surface temperatures, however, are similar or lower in the central Arabian Sea compared to offshore Pakistan. Together with the very similar records in stable isotopes, this suggest a shift in the *E. huxleyi* growth season (Prahl et al., 2000; Sangiorgi et al., 2003). Winter $U^{K'}_{37}$ productivity might have been higher more central in the Arabian Sea during MIS 2 and 4 compared to the more coastal location offshore Pakistan (Figure 5,10a, c).

During MIS 3, in contrast, lower SST's are observed offshore Pakistan compared to the central Arabian Sea (Figure 5.9, 5.10a, b, g-j). This is in line with what would generally be expected from the impact of the cold NEM (Figure 5.8g) versus the warm SWM winds, affecting mainly the coastal and central Arabian Sea respectively. With higher summer monsoon related productivity, $U^{K'}_{37}$ temperatures would mainly reflect summer productivity in the central Arabian Sea, resulting in higher average temperatures being recorded (Figure 5.8i, j). This is also in line with other productivity proxies (sedimentary Ba/Al and Ca/Ti), showing higher overall values during MIS 3. Near the Pakistan coast, lower coastal SSS's and less variable and high $\delta\delta^{18}O$ values during this warmer time interval could partly reflect intensified outflow from the Indus River similar to Deplazes

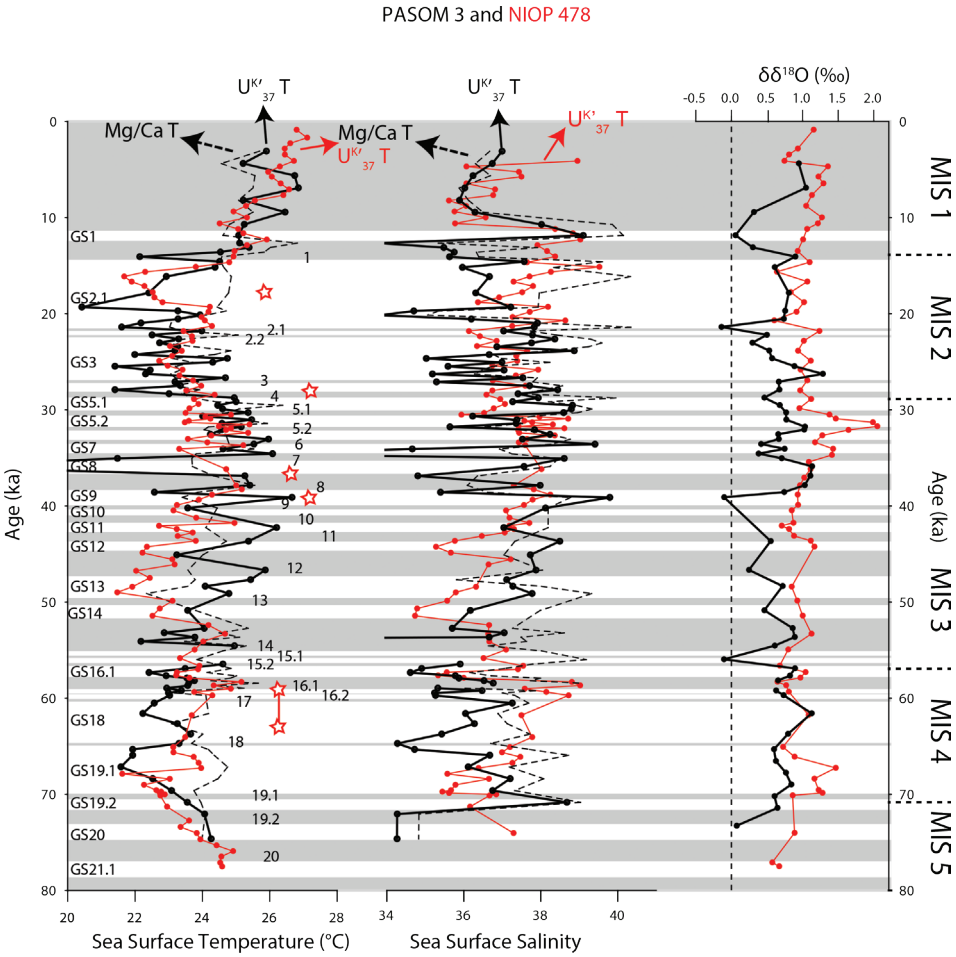

Figure 5.9. Comparison between the coastal NIOP 478 in red (Reichart et al., 2002), and offshore PASOM 3 (black, dashed: Mg/Ca-T, line: $U^{K'}_{37}$-T) reconstructed sea surface temperature (SST), difference in oxygen isotopic composition between *G. ruber* and *N. dutertrei* ($\delta\delta^{18}O$) and sea surface salinity (SSS). Greenland Stadials (GS) are indicated in white and numbered, Interstadials are indicated in grey and also numbered (without GS) and marine isotope stages (MIS) are indicated on the right axis.

et al. (2014) (Figure 5.10j). In the present-day, the Indus River is one of the largest rivers worldwide, having an annual river discharge of ~238 km^3 with highest outflow from June to September (the SWM) (Pande et al., 1994). With an intensified SWM, Indus outflow would have been enhanced, affecting mainly the near shore area.

During the Holocene, similar reconstructed SSS's and SST's across the northern Arabian Sea indicate that conditions are the same near the coast and further offshore (Figure 5.10g-

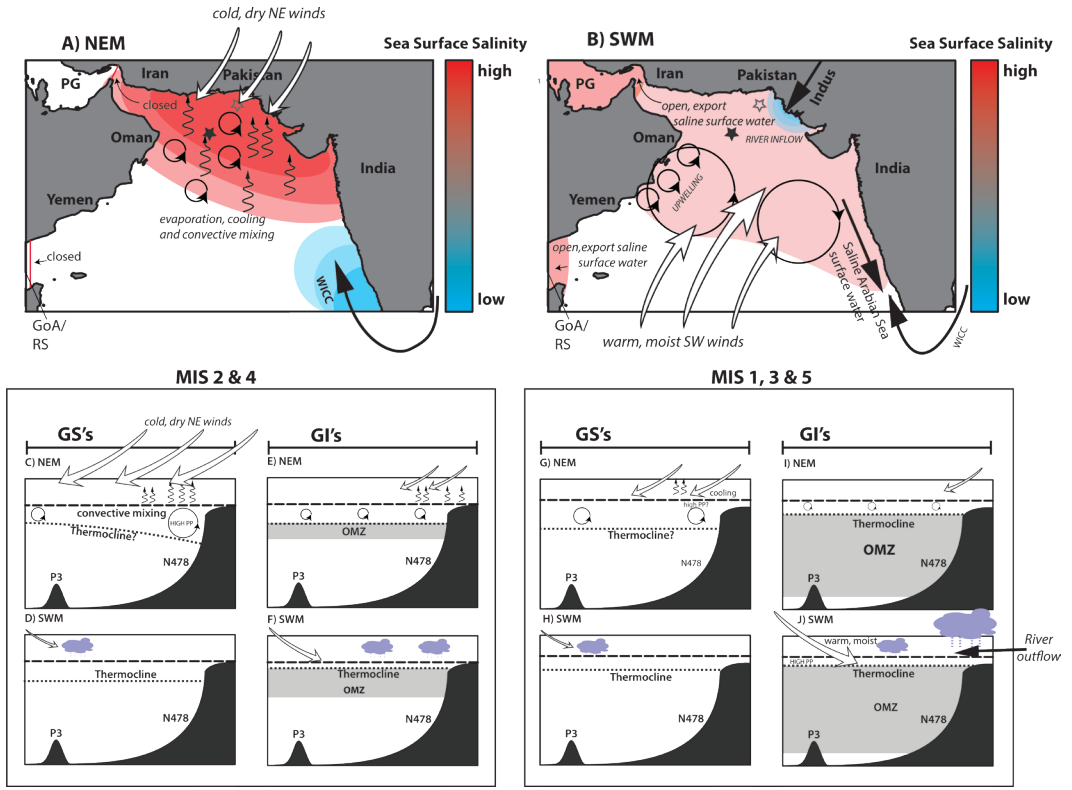

Figure 5.10. Hypothetical representation of the Northeast monsoon (NEM) and Southwest monsoon (SWM) intensity during the last glacial cycle (~75 ka-present), based on the coastal NIOP 478 (light grey star) and the central Arabian Sea PASOM 3 (dark grey filled star) record. The letters are referred to in the text, with: A) general processes affecting sea surface salinity (SSS) during Northeast monsoons (NEM's); B) general processes affecting sea surface salinity (SSS) during SWM's; C-F) scenarios of the NEM's and SWM's during MIS 2 & 4, distinguishing between Greenland Stadial (GS) and Greenland Interstadials (GI's); G-J) scenarios of the NEM's and SWM's during MIS 1, 3 & 5, distinguishing between Greenland Stadial (GS) and Greenland Interstadials (GI's) and for MIS 1, GI is referring to the Holocene.

j). However, the influence of convective winter mixing was still higher near the coast at the onset of the Holocene, as $\delta\delta^{18}O$ values were constantly higher compared to the central Arabian Sea from the Younger Dryas until ~5 ka. This delay in OMZ intensity and thus in response to insolation and global change is in line with existing monsoon reconstructions showing a large phase lag of about 6-2.7 kyr (Reichart et al., 1998; Ziegler et al., 2010). Enhanced winter mixing might thus contribute to the observed large phase lag for the summer monsoon related proxies.

Conclusions

Foraminiferal shell stable isotopes, (trace) elements, organic geochemical proxies and sedimentary (trace) elements are combined to validate proxy applications, as well as reconstructing hydrography in terms of stratification, salinity and OMZ intensity of the NE Arabian Sea. We found that the application of *G. ruber* Ba/Ca for SSS reconstructions is limited to inflow of Ba from rivers in coastal regions and is therefore not suited for the offshore location of this study. Furthermore, measured Na/Ca values are heavily impacted by preservation, albeit general patterns still follow the expected trends. Reconstructing SSS is still most robust by combining proxies ($\delta^{18}O$ and independent SST reconstructions). Reconstructed SST's show a dependency on the proxy used, with somewhat different SST estimates for $U^{K'}_{37}$ and Mg/Ca of *G. ruber* although overall trends are similar. Productivity, dust input and OMZ intensity co-vary with the SWM and are negatively correlated with the NEM. Planktonic foraminiferal Mn/Ca values, a suggested proxy for oxygenation, correlate well with OMZ intensity and are higher during warmer time intervals. Comparisons between a coastal record and the more central northern Arabian Sea show that deep convective overturning is stronger near the coast during intense NEM's. During intense SWM's, stratification is intensified near the coast reflected in lower salinities and higher $\delta\delta^{18}O$ values. This stratification is probably also enhanced by a higher Indus River input near the coast.

6

Chapter 6

Sodium incorporation into inorganic calcite and implications for the use of biogenic carbonates as a salinity proxy

Eveline M. Mezger

Laurent S. Devriendt

Ellen Olsen

James M. Watkins

Karina Kaczmarek

Gernot Nehrke

Lennart J. de Nooijer

Gert-Jan Reichart

(in preparation for submission)

Abstract

Sea surface salinity, reflecting past changes in the hydrological cycle, ice volume and together with temperature controlling the thermohaline circulation, is one of the most important, but challenging factors to reconstruct in paleoceanography. In recent years, progress has been made in developing sodium (Na) in foraminiferal calcite as a proxy for salinity. Measurements on inorganic calcites as well as cultured and field collected foraminiferal calcite show the potential of this emerging proxy, albeit that Na partitioning differs between studies. This suggests that more than one environmental parameter controls Na incorporation and hence requires quantification of the effect of individual parameters. Furthermore, Na is found to vary within foraminiferal shells, with higher concentrations in spines and spine bases. In this study, inorganic calcite precipitation experiments were performed to understand how different physico-chemical conditions drive Na incorporation during calcification. A proper understanding of the inorganic system represents a solid baseline which allows to evaluate Na/Ca in biogenic carbonates like foraminiferal calcite and to identify the processes behind the observed intra-shell variability. The effects of salinity, calcite saturation state, $[Ca^{2+}]/[CO_3^{2-}]$ stoichiometry and $[Na^{+}]/[Ca^{2+}]$ of the growth solution on Na incorporation were tested independently using two different experimental set-ups. Whereas foraminiferal shell Na partitioning increases with increasing salinities, Na partitioning in inorganically precipitated calcites was lower and did not show this effect. Therefore, foraminifera are suggested to have a strong biological control on Na incorporation in response to salinity. The difference in Na partitioning between biogenic and inorganic calcites has also been observed in previous studies for other elements (e.g. Mg) and might reflect additional physiological processes involved with the incorporation of the monovalent Na^{+} ion in biogenic calcites. Growth rate, here varied by changing the calcium concentration as well as by varying the $[Ca^{2+}]/[CO_3^{2-}]$ stoichiometry of the solution, has a substantial positive effect on Na incorporation. This is relevant for the recently suggested paleo-application of Na/Ca in reconstructing past variations in seawater $[Ca^{2+}]$, as changes in seawater $[Ca^{2+}]$ also might affect growth rate and hence Na partitioning over geological time scales.

6.1 Introduction

In paleoceanography, sea surface salinity is one of the most important, but challenging factors to reconstruct. Past salinity reflects the hydrological cycle, waxing and waning of continental ice sheets, sea ice formation and -together with temperature- the thermohaline circulation. For various environmental conditions such as temperature and sea water carbonate chemistry, (trace) elemental composition of (biogenic) calcite is employed as a proxy (Anand et al., 2003; Erez and Honjo, 1981; Hönisch et al., 2011; Kısakürek et al., 2008; Nürnberg et al., 1996; Yu, 2007), but a similar proxy approach for salinity has been lacking.

In recent years, progress has been made in developing Na in foraminiferal calcite as a proxy for salinity (Allen et al., 2016; Bertlich et al., 2018; Geerken et al., 2018; Mezger et al., 2016; Mezger et al., 2018; Wit et al., 2013). The potential of this proxy is highlighted by correlations between Na/Ca in calcite and the Na/Ca of the host solution in culturing studies on benthic foraminiferal species (Geerken et al., 2018; Wit et al., 2013), field and culture studies on planktonic foraminifera (Allen et al., 2016; Bertlich et al., 2018; Mezger et al., 2019; Mezger et al., 2016; Mezger et al., 2018) and their comparison with results from inorganic precipitation studies (Busenberg and Plummer, 1985; Ishikawa and Ichikuni, 1984; Kitano et al., 1975; White, 1978). Reported Na incorporation, however, varies between inorganic experiments, between foraminiferal species, as well as within the same species despite similar salinity conditions (Bertlich et al., 2018; Ishikawa and Ichikuni, 1984; Kitano et al., 1975; Mezger et al., 2016; Mezger et al., 2018; White, 1978). This suggests that more than one (environmental) factor determines sodium incorporation. Therefore, the influence of different environmental parameters such as the calcite saturation state (Ω), stoichiometry (Nehrke et al., 2007, Wolthers et al., 2012), growth rate and seawater $[Na^+]/[Ca^{2+}]$ (Hauzer et al., 2018) on sodium incorporation need to be assessed.

Incorporation of Na in biogenic carbonates is affected by environmental parameters as well as a biological control during biomineralization. For example, the intra-shell variability of Na seems to reflect the different processes involved during biomineralization (Branson et al., 2016; Geerken et al., 2018; Mezger et al., 2018). The intra-shell Na variations in spinose planktonic foraminifera show relatively enriched Na/Ca-values in spines and spine bases compared to the rest of the shell. Such differences could reflect differences in biogenic calcification pathways for different parts of the shell. Analogous to spine formation in sea urchins (Beniash et al., 1997), a precursor transforming into calcite could account

for the high Na/Ca values observed in foraminiferal spines. Such a precursor phase has recently been suggested by Jacob et al. (2017) to occur also during foraminiferal shell formation. For mussels, in contrast to previous studies that suggested an amorphous calcium carbonate (ACC) precursor, no such mineral phase was observed with an in vivo confocal Raman spectrometry study (Ramesh et al., 2018). Alternatively, a previously suggested impact of growth rate on element incorporation (Busenberg and Plummer, 1985) could potentially also explain observed differences in Na-incorporation .

Another unresolved issue is whether Na uptake by inorganic calcite depends on the solution Na concentration ($[Na]_w$, Ishikawa and Ichikuni, 1984), the Na/Ca concentration ratio ($([Na^+]/[Ca^{2+}])_w$; Hauzer et al., 2018) or the Na/Ca activity ratio ($(\{Na\}/\{Ca\})_w$; e.g. Wit et al. 2013). A recent study using XANES showed that Na substitutes for Ca, with the charge imbalance compensated by carbonate ion vacancies, rather than interstitially as previously suggested by Ishikawa and Ichikuni (1984). This implies that Na uptake during calcite growth would be sensitive to solution Na/Ca, rather than $[Na^+]_w$ only. Hence, the incorporation of Na should be evaluated in terms of partitioning, defined as the concentration of the (trace) element relative to $[Ca^{2+}]$ in the precipitated calcite, divided by this ratio in the growth solution (for Na: $([Na]/[Ca])_{calcite}/([Na]/[Ca])_{solution}$).

Inorganic precipitation experiments are excellently suited to isolate impacts of different carbonate system parameters. Previously performed inorganic precipitation experiments suggested that growth rate enhances incorporation of most minor and trace metals (e.g. Mg: Mavromatis et al., 2013 ; Sr: Nehrke et al., 2007; Tang et al. 2008), including Na (Busenberg and Plummer, 1985). Growth rate represents the balance between the forward (Rf, precipitation) and backward (Rb, dissolution) ratio of calcite precipitation (DePaolo, 2011). This balance is not only depending on the degree of oversaturation of the growth solution with respect to calcite (Ω), but also on the $[Ca^{2+}]/[CO_3^{2-}]$ stoichiometry of the solution (Larsen et al., 2010; Nehrke et al., 2007; Stack and Grantham, 2010) and background electrolyte ionic strength (I) (Wolthers et al., 2012). Nehrke et al. (2007) found maximum growth rates when the $([Ca^{2+}]/[CO_3^{2-}])_w$ ratio equalled one, symmetrically decreasing when this ratio decreases or increases. In this study, we attempt to disentangle the effects of seawater $[Na^+]/[Ca^{2+}]$, calcite saturation state, salinity and stoichiometry on Na incorporation by performing inorganic precipitation experiments in which these parameters are varied independently. Results are subsequently evaluated in the context of the proxy potential of Na/Ca and to understand observed differences in Na incorporation between foraminiferal shell parts.

6.2 Methodology

Three sets of inorganic growth experiments were conducted to test the effect of salinity ($[Na^+]_w$), stoichiometry ($r = [Ca^{2+}]/[CO_3^{2-}]$) and calcite saturation state (Ω, where Ω=IAP/K_{sp}, where IAP is the ion activity product and K_{sp} is the solubility product) on Na incorporation. In all experiments, calcite was precipitated at a constant temperature (25±0.5°C) and pH (8.3±0.02 or 9.8±0.3). The three series of experiments were performed with two different automated chemostat systems. One system was based on bubbling with CO_2 gas in high $[Ca^{2+}]$ waters (University of Oregon; Fig. 6.1, Section 6.2.1), whereas the other system uses calcite seeds to initiate precipitation (Royal NIOZ; Fig. 6.2, Section 6.2.2). The first set-up was used to test the effect of Na/Ca over a large range of Na concentrations (corresponding to salinities between 0-103) on Na incorporation with an r ranging from ~6,200 to ~21,000. This set-up allows establishing the Na fractionation pattern with different salinities. However, impact of solution stoichiometry could not be isolated from other parameters, therefore, a second set-up was used to quantify the impact of salinity and saturation state while keeping solution stoichiometry constant. In these experiments, the isolated effects of calcite saturation state (Ω) and $[Na^+]_w$ on $(Na/Ca)_{calcite}$ were investigated with a controlled r (~4.9, minteq.v4). Calculated solution parameters such as ionic strength (I), Ω, stoichiometry and ion activity somewhat depend on differences in complexation used in the databases underlying calculations (e.g. Farmer et al., 2019). After comparing several databases, we decided to use "minteq.v4", a database derived from MINTEQ A2 version 4 (U.S. Environmental Protection Agency, 1998; Parkhurst and Appelo, 2013), to calculate solution parameters as "MINTEQ" is commonly used in studies with ionic strengths close to seawater (Nehrke et al., 2007; Wolthers et al., 2012).

6.2.1 Unseeded salinity experiments

For the unseeded growth experiments performed at the University of Oregon, a mixture of N_2 and CO_2 (200 ppm) gas was bubbled through a constantly stirred growth solution (1700 mL), containing 30 mM $CaCl_2$, 5 mM NH_4Cl and varying [NaCl] (0-1.37 M), in $[Na^+]$ concentrations similar to a large natural salinity range from 0 to 103 (Table 6.1, Fig. 6.1, Watkins et al., 2014; Watkins et al., 2013). The experimental temperature of 25°C±0.3 was controlled by placing the glass beaker containing the growth solution inside a larger glass beaker filled with water, thermostatically controlled at 25°C±0.3 (Watlow series 93) with a heater and a chiller (Julabo FT200). The pH was monitored and controlled at 8.3±0.02 using an autotitrator (Jensen systems) with NaOH (1M) as a titrant, combined with Titronics universal burettes and an NBS-calibrated BlueLine pH combination electrode

(Schott Instruments). By adding CO_2 gas to the medium, HCO_3^- and CO_3^{2-} concentrations increase and initiate precipitation of $CaCO_3$ on the beaker walls. The CO_2 bubbling caused Ω to increase steadily until $CaCO_3$ nucleation at Ω values of ~4-13, calculated based on measured DIC and $[Ca^{2+}]$ from solution samples collected during the experiments (Table 6.1). After nucleation, Ω decreased until the system adjusted to approximately (~±0.6) steady state conditions at 2.1-6.3 (depending on the individual experiment). After each experiment, the solution was vacuum filtered through 0.45 µm filter paper (Whatman). The collected (suspended) crystals from this process were discarded, and remaining crystals attached to the bottom and sides of the beaker were rinsed at least three times with de-ionised water (resistance = 18.2 MΩ), air-dried, and then gently scraped using a plastic wiper from the walls of the beaker. Stoichiometry varied from ~6,200 to ~21,000 between experiments, calculated based on DIC measurements and an initial $[Ca^{2+}]$ of 30 mM (Table 6.1, Table S6.1). Duration of experiments varied between 41 to 93 hours. The solid phase was confirmed to be pure calcite based on X-Ray Diffraction (XRD) on a subset of experiments that span the full range of salinities.

For DIC measurements, 3.5 mL of collected solution was added by syringe through a rubber septa cap into a Helium-flushed, glass vial containing 0.1 mL of 85% orthophosphoric acid (H_3PO_4). The samples were allowed to equilibrate for over 24 hours and then analysed by continuous-flow mass spectrometry using a GasBench-DeltaV system. The approximate DIC in solution is obtained by comparing the CO_2 signal produced by the solution samples to that produced by an in-house DIC standard that is run multiple times in every batch of samples. Average calcite precipitation rates were determined (for all experiments except S2 and S3 due to logistic limitations, both corresponding to a $[Na^+]_w$ similar to a salinity of ~39) by measuring the decrease in alkalinity caused by Ca^{2+} removal. Alkalinity decrease was converted to calcification rate using the calculated surface area of calcite precipitated at the middle of each experiment (method described in Tang et al., 2008) and the molecular density of calcite as a starting point (Tang et al., 2008; Watkins et al., 2013). Alkalinity was measured by Gran titration using 0.1 M HCl as the titrant. Reported growth rates and average Ω values of each experiment are representative of steady state growth conditions rather than conditions during the initial nucleation stage. The amount precipitated during the early stage of nucleation is estimated to be ~10-30% of total precipitate mass.

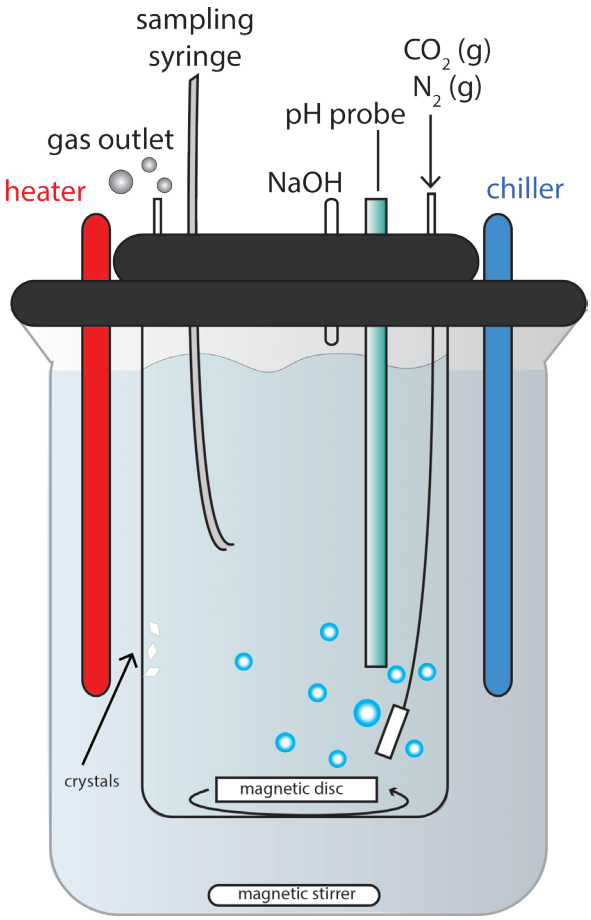

Figure 6.1. Experimental set-up for the CO2 bubbling unseeded salinity experiments, similar to Watkins et al. (2013).

6.2.2 Seeded salinity and calcite saturation state experiments

The seeded growth experiments, with $([Ca^{2+}]/[CO_3^{2-}])_w$ close to stoichiometry (±4.9 minteq. v4), were performed at the Royal NIOZ using an automated chemostat system. The effect of salinity ($[Na^+]_w$) and Ω on the amount of Na incorporated into inorganic calcite was tested in two sets of experiments. In the first set of experiments, hereafter referred to as the "Ω experiments", the $[Na^+]$ was constant at 0.47M, whereas the Ω was varied by changing $[Ca^{2+}]_w$ and $[CO_3^{2-}]_w$ simultaneously. In a second set of experiments, the $[Na^+]_w$ was varied over a range corresponding to a natural salinity range of 30-45 (e.g. Kester et al., 1967) while Ω was held constant at ~8.8 by co-varying $[Ca^{2+}]_w$ and $[CO_3^{2-}]_w$ stoichiometrically (Table 6.1). In all cases, calcite accumulation occurred via surface growth on seed material,

using seeds with no detectable [Na^+] (measured with iCap-Q-ICP-MS; method section 6.2.3). Each experiment was repeated at least once and sometimes twice. The automated chemostat system consists of a titrator (Stat Titrando, Metrohm), three burettes (Dosino, Metrohm), a combined polymer Ca electrode, a pH electrode, all driven by Tiamo 2.5 software (similar to Kaczmarek et al., 2016) (Fig. 6.2).

Before the start of each experimental run, the pH electrode was calibrated with 3 NIST-certified buffers (pH 4, 7 and 10). Furthermore, the Ca-electrode was conditioned until stabilization (i.e. a constant signal for at least 20 minutes) of the Ca-signal, which was usually achieved within 3 hours (Fig. 6.2). This was done in a solution identical to the precipitation solution and a lower DIC to avoid precipitation of $CaCO_3$. Second, 150 mL of supersaturated growth solution was mixed by combining a $CaCl_2$ solution with a $NaCO_3$ solution in a 400 mL glass beaker, both with pre-calculated [NaCl]. Thereafter, the Ca-probe was rapidly transferred from the conditioning solution into the growth solution and the system was closed air-tight with a lid including air-tight holes for the burette tips, overhead stirrer, two (Ca and pH) probes, an entrance for seeds (with a lid) and a tube connected to a balloon to compensate for overpressure (Fig. 6.2). While being stirred constantly with an overhead stirrer (~255 rpm), 5 mg of seeds (Alfa Aesar, chelometric standard, 99.95-100.05%, up to 32 μm in size) were added to the growth solution to serve as a substrate for $CaCO_3$ precipitation. Concentrations of Ca and DIC (Ω) were maintained during each experiment triggered by deviation in voltage from the initial value measured by the Ca probe, resulting in a stoichiometric addition from one burette ($CaCl_2$+NaCl) until Ca returned to the initial concentration, almost simultaneous with inorganic carbon addition from a second burette ($NaCO_3$+NaCl). A drop in pH associated with calcification triggers dropwise addition of a 0.05 M NaOH (+NaCl) solution from another burette. The total volume of [NaOH] added during the experiment was limited (up to ~2 mL per experiment), as this burette is only used to compensate for a drop in pH caused by a delay in addition between the Ca and CO_3^{2-}burettes. All burettes have $[Na^+]_w$ corresponding to the growth solution, to avoid any changes in [Na^+] due to addition of the different solutions. The rate of $CaCl_2$ and $NaCO_3$ addition typically increased slightly during an experiment, presumably related to an increase in the rate of calcite accumulation associated with increasing surface areas of growing calcite crystals. At the end of each experiment, precipitated calcite crystals were filtered immediately over a 0.2 μm filter (Whatman) connected to a pump and flushed three times with de-ionised water (18.2 MΩ). At the same time, the Ca-probe was placed directly in the drift solution, which was in composition identical to the solution at the start of the experiment, to quantify the drift

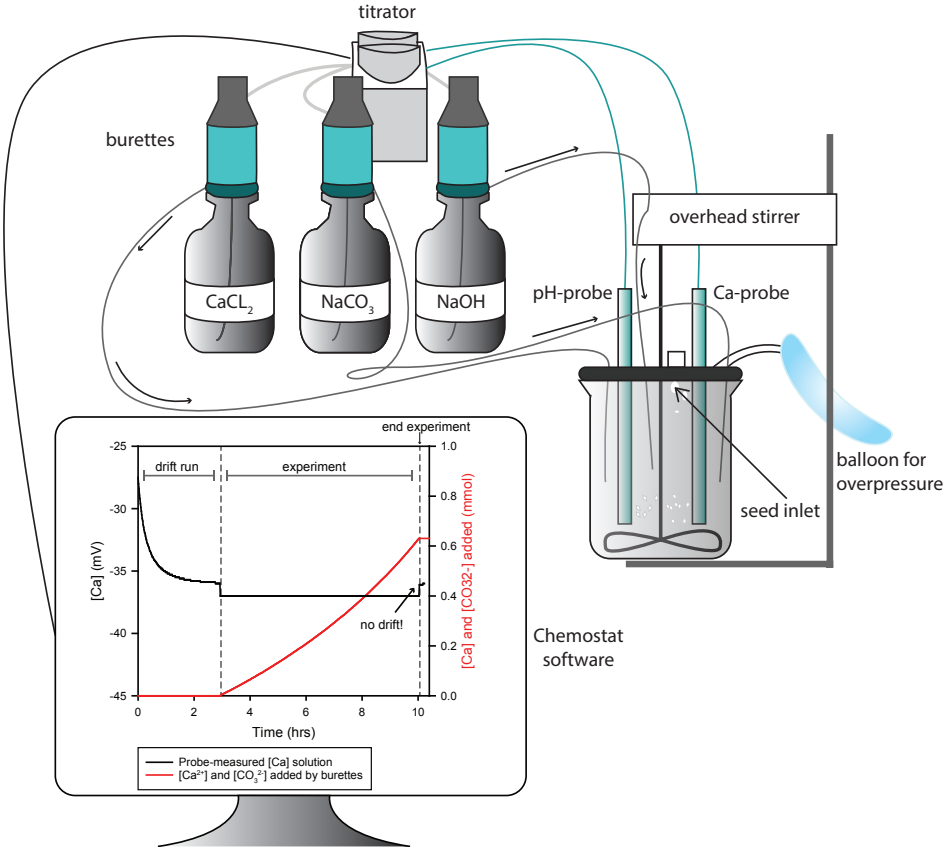

Figure 6.2. Experimental set-up of the chemostat seeded salinity and omega experiments, with an example of an experimental run. Temperature is controlled at 25°C in a thermostatically controlled room.

of the probe during the experiment. For all experiments drift was below 2% with respect to the total amount of Ca added. At the end of each run, all chemical equipment was cleaned with a weak acid, to avoid nucleation at old calcification sites in a new experiment.

The duration of experiments varied between 2 and 24 hours, depending on calcite growth rate and the amount of precipitated calcite (addition of 82-98% to the initial seed mass, for which was corrected after the analyses). After visual inspection with SEM, all minerals precipitated (rhombohedral and without the typical aragonite twins and/or needle-like aggregates) were recognized to be calcite (see Fig. S6.1). Growth rate is calculated based on the amount of Ca added, combined with the Brunauer-Emmett-Teller (BET) surface area analysis of the seed crystals used, assuming an even surface on which crystal growth

occurs laterally. The BET surface area of the seeds (0.355 m^2/g) was measured at Utrecht University with N_2 BET physisorption (TriStar 3000, V6.08A). Growth rates (log R, mol/m^2/s) were calculated as follows:

R = calcite precipitated (moles) / surface area seeds (m^2)/ duration experiment (s) (1)

The same formula was used to calculate growth rate for the CO_2 bubbling experiments, with surface areas calculated based on assumed average grain sizes during the mid-points of the experiments (similar to Watkins et al., 2013,2014).

6.2.3 Cleaning protocols and measurements

For experiments performed at the Royal NIOZ, all crystals were weighed after drying the calcite crystals in a laminar flow cabinet. However, probably not all material could be collected, as some material remained attached to the set-up, and therefore this does not necessarily represent the total precipitate weight. Hence for estimating total precipitated calcite we used the values calculated based on the added volume from the Ca burette during titration. Before measuring the Na/Ca composition of the calcite powders, a small fraction of precipitated calcite (~500-800 μg) was transferred into an acid cleaned Eppendorf tube. De-ionised water was added to the solution and the mixture ultrasonicated for two minutes, after which it was centrifuged for 60 seconds at 2000 rpm to concentrate the powder at the bottom of the vial. After removal of the supernatant with a micropipette, these steps were repeated twice as testing showed no improvement (or Na leaching, e.g. Yoshimura et al., 2017) with more rinsing steps added (see Fig. S6.2). After rinsing, the samples were dissolved in 0.1M ultrapure HNO_3.

The elemental composition of the powders was measured on a Thermo Fisher Scientific iCAP-Q-ICP-MS at the Royal NIOZ. The isotopes of ^{23}Na, ^{43}Ca, ^{44}Ca and ^{88}Sr were measured in a cycle of 1.5 minutes. Samples were measured against 4 ratio calibration standards with a similar matrix, with a drift standard measured every third sample, converting isotope counts into elemental ratios. The monitor standards JCt-1 and NFHS-1 (Mezger et al., 2016; Okai et al., 2002) were included for quality control. Elemental values were drift-corrected, even though drift was low (~1%). Accuracy based on the two quality control standards was 99±2% for Na/Ca. All measured Na/Ca element ratios for precipitated calcite are corrected for the initial mass of the seeds.

Table 6.1. Overview all experimental solution compositions, with DIC (*1,2) for the University of Oregon experiments referring to average experimental DIC conditions (*1), or nucleation DIC (*2); and (*3) referring to eliminated experiments (Section 6.2)

sample ID	Experiment	lab	pH	[Na] mol/ kgw	[Cl] mol/ kgw	[Ca] mmol/ kgw	$[DIC]_{average}$ (mmol/ kgw)*1	$[DIC]_{nucl}$ (mmol/ kgw)*2
35_1	Ω	NIOZ	9.89	0.47	0.47	1.00	1.00	-
35_2	Ω	NIOZ	9.82	0.47	0.47	0.99	0.99	-
35_4	Ω, salinity	NIOZ	10.02	0.47	0.47	1.35	1.35	-
35_6	Ω, salinity	NIOZ	9.98	0.47	0.47	1.34	1.34	-
35_7	Ω, salinity	NIOZ	9.93	0.47	0.47	1.34	1.37	-
35_8	Ω	NIOZ	10.01	0.47	0.47	1.65	1.65	-
35_9	Ω	NIOZ	10.00	0.47	0.47	1.65	1.65	-
35_10	Ω	NIOZ	9.78	0.47	0.47	0.69	0.69	-
35_11	Ω	NIOZ	9.74	0.47	0.47	0.69	0.69	-
30_1	salinity	NIOZ	9.98	0.40	0.40	1.28	1.27	-
30_2	salinity	NIOZ	9.96	0.40	0.40	1.28	1.27	-
30_4	salinity	NIOZ	9.98	0.40	0.40	1.27	1.27	-
40_1	salinity	NIOZ	9.91	0.54	0.53	1.41	1.41	-
40_2	salinity	NIOZ	9.85	0.54	0.53	1.41	1.41	-
45_1	salinity	NIOZ	9.90	0.60	0.60	1.46	1.47	-
45_2	salinity	NIOZ	9.88	0.60	0.60	1.47	1.47	-
14_5_2018 *3	Ω	NIOZ	9.93	0.47	0.47	1.20	1.20	-
15_5_2018 *3	Ω	NIOZ	9.91	0.47	0.47	1.23	1.23	-
16_5_2018_1*3	Ω	NIOZ	9.96	0.47	0.47	1.23	1.23	-
S08	unseeded	UO	8.30	*0.00*	*0.00*	30.00	0.15	0.36
S07	unseeded	UO	8.30	0.18	0.21	30.00	0.22	0.42
S05	unseeded	UO	8.30	0.35	0.38	30.00	0.18	0.58
S09	unseeded	UO	8.30	0.35	0.38	30.00	0.27	0.60
S02	unseeded	UO	8.30	0.52	0.55	30.00	0.34	0.45
S03	unseeded	UO	8.30	0.52	0.55	30.00	0.32	0.70
S10	unseeded	UO	8.30	0.69	0.73	30.00	0.31	0.70
S14	unseeded	UO	8.30	0.86	0.90	30.00	0.26	0.60
S13	unseeded	UO	8.30	1.03	1.07	30.00	0.19	0.45
S15	unseeded	UO	8.30	1.20	1.24	30.00	0.45	0.70
S12	unseeded	UO	8.30	1.37	1.41	30.00	0.34	0.80

6.3 Results

All results of the performed experiments are shown in Supporting information Figure 6.3 (Fig. S6.3), respectively the CO_2 bubbling experiments performed at University of Oregon and the chemostat experiments performed at Royal NIOZ, in separate panels as well as combined panels. All data is plotted in this Supporting information, using only the relevant parameters in the manuscript itself. The seeded experiments at $\Omega \approx 7$ are excluded from the manuscript (although still plotted in the Supporting information using separate symbols) as no Ca-probe drift run was available for these experiments. Experimental settings used are listed in Table 6.1, results are shown in the Supporting information Table 6.1 (Table S6.1). We first evaluate the impact of $([Na^+]/[Ca^{2+}])_w$, second we investigate the impact of saturation state on growth rate and partitioning and third the isolated impact of ionic strength is studied.

6.3.1 Variable $([Na^+]/[Ca^{2+}]_w$ experiments

For the variable $([Na^+]/[Ca^{2+}])_w$, unseeded experiments, measured $(Na/Ca)_{calcite}$ values are positively correlated with salinity ($[Na^+]_w$) and $[Na^+]/[Ca^{2+}]$ of the growth solution (Fig. 6.3). These experiments show similar overall growth rates (Log (R)) at -6.1±0.1 mol/m^2/s. Measured $(Na/Ca)_{calcite}$ values range from 0.12 to 1.55 mmol/mol and repeated measurements on the same sample resulted in a maximum standard deviation (SD) of 9%. The partitioning (D) of an element (El) is defined as the concentration of the El relative to $[Ca^{2+}]$ in the precipitated calcite, divided by this ratio in the growth solution. The partitioning of Na decreases (from $9.1*10^{-5}$ to $2.9*10^{-5}$) with increasing $[Na^+]/[Ca^{2+}]$ of the growth solution (Fig. 6.3). Because the incorporation of Na at a $[Na+]_w=0$ necessarily would approach zero, we also added a line going through the origin (Fig. 6.3, black dotted curve).

6.3.2 Calcite saturation state ("Ω") experiments

With increasing Ω values from 2.1 to 13, the $(Na/Ca)_{calcite}$ values increase significantly from 3.4 to 16.4 mmol/mol (Fig. 6.4a). Growth rate is positively correlated to Ω, with measured growth rates (Log(R)) varying from -4.6 to -5.9 mol/m^2/s (Fig. 6.4b). Hence, also Na partitioning (D_{Na}) increases significantly with increasing growth rate (Fig. 6.4c).

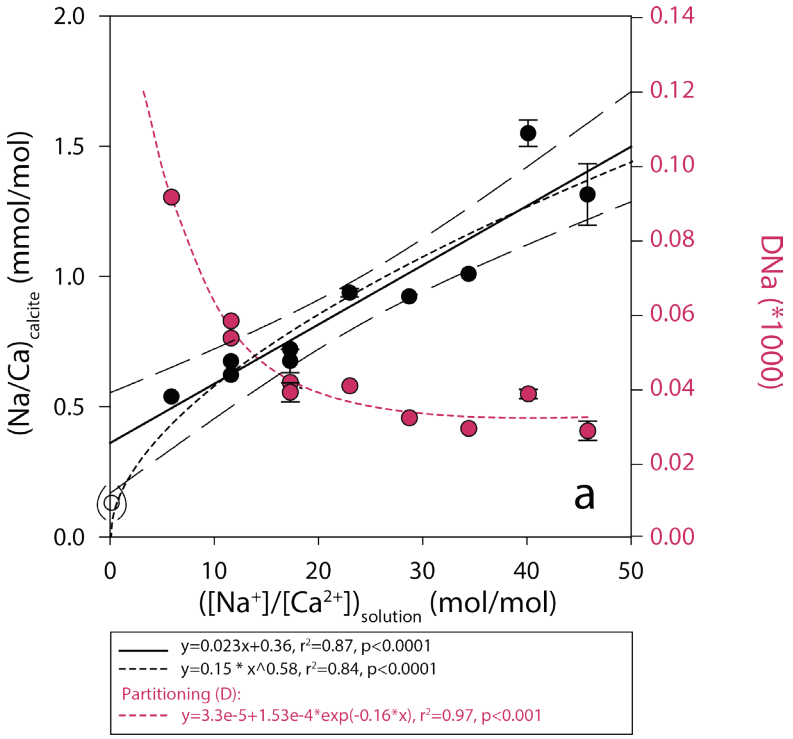

Figure 6.3. Results of the unseeded salinity experiments, with $[Na^+]/[Ca^{2+}]$ of the growth solution (also referred to in the text as $([Na^+]/[Ca^{2+}])_w$) versus Na/Ca measured in the calcite, with a linear calibration (black line) and standard deviations of measured shell Na/Ca values and 95% confidence intervals (long dashed lines), or as a power function (short dashed black line); and the partitioning (D) of Na from the growth solution into calcite for these experiments as an exponential decay function (pink dashed line) (Mewes et al., 2014). Since $[Ca^{2+}]$ of the growth solution are the same for each experiment, the X-axis can also be interpreted as the [Na] (=0.03*[Na]/[Ca]).

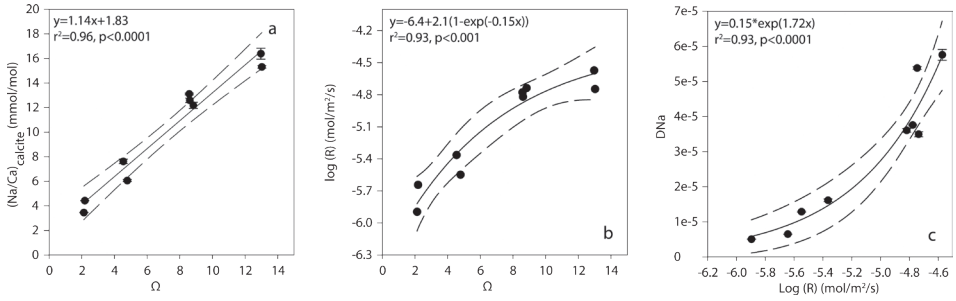

Figure 6.4. Results from omega experiments (constant [NaCl] = 0.47 M), with: a) Ω of the growth solution versus Na/Ca measured in the calcite; b) Ω of the growth solution versus measured growth rates (R); and c) measured growth rates versus partitioning (D) of Na from the growth solution into the precipitated calcite. Standard deviations of measured shell Na/Ca values and 95% confidence intervals are indicated.

6.3.3 Sodium concentration experiments

With increasing salinities ($[Na^+]_w$ from 0.4 to 0.6 M) and a constant Ω of ~8.8, the $(Na/Ca)_{calcite}$ increases, with values ranging from 11.2 to 15.7 mmol/mol (Fig. 6.5). The partitioning of Na is, however, relatively constant over the studied range (~3.7*10^{-5}), whereas precipitation rate increases slightly but not significantly (from -4.7 to -5.0 mol/m^2/s, p>0.2).

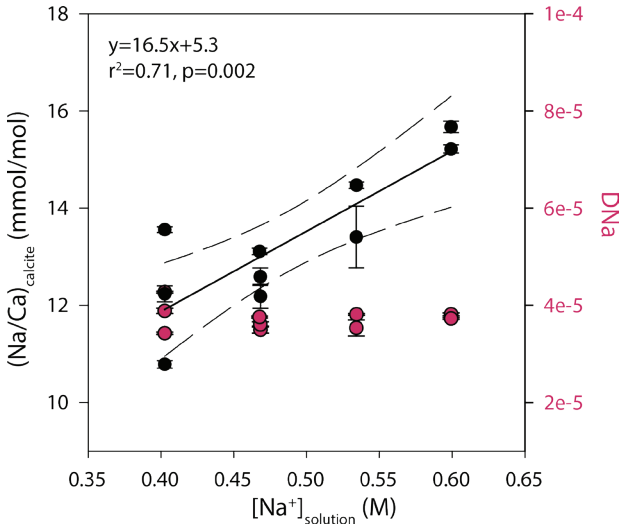

Figure 6.5. Results salinity experiments, with Na/Ca of the precipitated calcite versus [Na+] of the solution with standard deviations and 95% confidence interval indicated, and the partitioning of Na (DNa).

6.4 Discussion

Our results show that Na incorporation in inorganically precipitated calcites increases with increasing salinity, $([Na^+]/[Ca^{2+}])_w$, and/or $[Na^+]_w$ (Figs. 6.3 and 6.5). This is in line with other studies showing the dependency of Na incorporation on these parameters in other inorganically precipitated calcites (Busenberg and Plummer, 1985; Ishikawa and Ichikuni, 1984; Kitano et al., 1975), as well as in benthic and planktonic foraminifera (Allen et al., 2016; Bertlich et al., 2018; Geerken et al., 2018; Mezger et al., 2016; Wit et al., 2013). Absolute Na/Ca values differ between the two experiments in which $[Na^+]_w$ and $([Na^+]/[Ca^{2+}])_w$ were manipulated, with approximately 10 times lower $(Na/Ca)_{calcite}$ in the unseeded experiments (Fig. 6.3). Differences in $(Na/Ca)_{calcite}$ between these two sets of experiments might be related to differences in solution stoichiometry, $([Na^+]/[Ca^{2+}])_w$ and/or growth rates. For example, the $[Ca^{2+}]_w$ was higher for the unseeded experiments

to promote precipitation in the absence of a surface on which new calcite would grow (Section 6.4.1). The partitioning of Na (D_{Na}) decreases with $([Na^+]/[Ca^{2+}])_w$ in the unseeded experiments (Fig. 6.3) at lower $([Na^+]/[Ca^{2+}])_w$ values, in line with the observation that the Na/Ca-salinity calibration (Fig. 6.3) does not go through the X/Y-intercept. A similar relation was observed before for Mg/Ca in benthic foraminifera (Mewes et al., 2014). However, for Na this trend is discernible already at relatively high Na concentrations (below $[Na^+]_w$=0.52) and therefore most likely not an artefact of the non-zero X/Y-intercept regression.

Precipitation rates in our experiments are varied by changing saturation state (Ω), which are also a function of $[Ca^{2+}]/[CO_3^{2-}]$ stoichiometry (r; Nehrke et al., 2007), with highest growth rates being observed when r approaches 1 and decreasing symmetrically with in- or decreasing r. Other factors such as background electrolyte ionic strength (I), pH and temperature (T) may also have an effect on growth rate (Nehrke et al., 2007; Wolthers et al., 2012) and hence additionally affect Na-incorporation. In our experiments, variations in $[Ca^{2+}]$ of the growth solution, while maintaining r, pH, I and T, resulted in growth rates in the same order of magnitude as the study of Nehrke et al. (2007). In our study rates ranges between -6.54 (unseeded experiments) and -4.73 (seeded experiments), whereas they range from (log (R)) -6.01 up until -4.83 mol/m²/s depending on $[Ca^{2+}]/[CO_3^{2-}]$ stoichiometry and Ω in Nehrke et al. (2007).

6.4.1 Impact of growth rate

Sodium incorporation increases with precipitation rate in the experiments is which Ω was varied (Fig. 6.4). Also combining all experiments performed in this study shows that $(Na/Ca)_{calcite}$ values are positively correlated to growth rate (Fig. 6.6a), with lower growth rates resulting in lower $(Na/Ca)_{calcite}$ values (unseeded salinity experiment), higher growth rates corresponding to higher $(Na/Ca)_{calcite}$ values (seeded $[Na^+]_w$-experiment) and the Ω-experiments with varying growth rates connecting the unseeded and seeded salinity experiments (Fig. 6.6a). An impact of growth rate on element incorporation in inorganic calcite has not only been observed for Na (Busenberg and Plummer, 1985), but also for strontium (Nehrke et al., 2007; Tang et al., 2008), boron (Kaczmarek et al., 2016; Uchikawa et al., 2015), magnesium (Mavromatis et al., 2013), and many other trace elements (e.g. Lorens et al., 1981, Rimstidt et al., 1998).

Growth rate and sodium partitioning

Comparing the unseeded and seeded $[Na^+]_w$-experiments shows that the Na/Ca values in the unseeded experiments are approximately ten times lower (Fig. 6.6a). This offset is likely due to multiple fundamentally different conditions used in the two experiments, resulting in (1) differences in $[Ca^{2+}]$:$[CO_3^{2-}]$ stoichiometry (r) and thereby, precipitation rate (R) (Larsen et al., 2010; Nehrke et al., 2007; Stack and Grantham, 2010), and/or (2) the difference in $[Na^+]/[Ca^{2+}]$ of the growth solutions (Table 6.1).

First, the unseeded experiments are conducted with higher $[Ca^{2+}]$ (~20-30x) compared to the seeded experiments, whereas $[CO_3^{2-}]$ are much lower (~20x), resulting in high $([Ca^{2+}]:[CO_3^{2-}])_w$ values for the unseeded experiment of ~6,200 to ~21,000 compared to ~4.9 for the seeded growth experiments. Since crystal growth rate is controlled by $[Ca^{2+}]/[CO_3^{2-}]$ stoichiometry (r) and Ω (Larsen et al., 2010; Nehrke et al., 2007; Stack and Grantham, 2010; Wolthers et al., 2012), lower growth rates as a consequence of the rather high $([Ca^{2+}]/[CO_3^{2-}])_w$ stoichiometry might have been responsible for the observed low $(Na/Ca)_{calcite}$ (Fig. 6.4a-c, Fig. S6.4). Calculated growth rates for all experiments, plotted against Ω and r of the growth solutions, correspond well to, or are somewhat higher compared to, that of Nehrke et al. (2007) (Fig. S6.4). The slight offset between these studies could be due to differences in experimental settings, such as temperature (20°C versus 25°C for all our experiments) and ionic strength (0.1 M Na versus a range of $[Na^+]$ from 0-1.37 M in our experiments). However, the effect of stoichiometry on growth rate and Na incorporation was not tested independently here but fits well with earlier results, with r-values being either very high (r≈6,200-21,000) or close to one (seeded experiments, r≈4.9).

Secondly, the offset between the seeded and unseeded salinity experiments could also be explained by an (additional) effect of $([Na^+]/[Ca^{2+}])_w$. The $[Na^+]/[Ca^{2+}]$ of the growth solutions differed between unseeded and seeded growth experiments, being an order of magnitude lower for the unseeded salinity experiments. When correcting the relation between growth rate and $(Na/Ca)_{calcite}$ for the effect of $([Na^+]/[Ca^{2+}])_w$ by calculating D_{Na}, it becomes apparent that $([Na^+]/[Ca^{2+}])_w$ plays an important role in Na partitioning (Fig. 6.6b). The relation to growth rate is clearly not the only factor determining partitioning, as at lower $([Na^+]/[Ca^{2+}])_w$ values higher D's are observed (Fig. 6.6b).

Combined effect of growth rate and [Na+]/[Ca2+] on sodium partitioning

Our results show that both growth rate and $([Na]/[Ca])_w$ determine partitioning of Na in calcite. Previous experiments suggested that $[Ca^{2+}]$ of the solution by itself has no

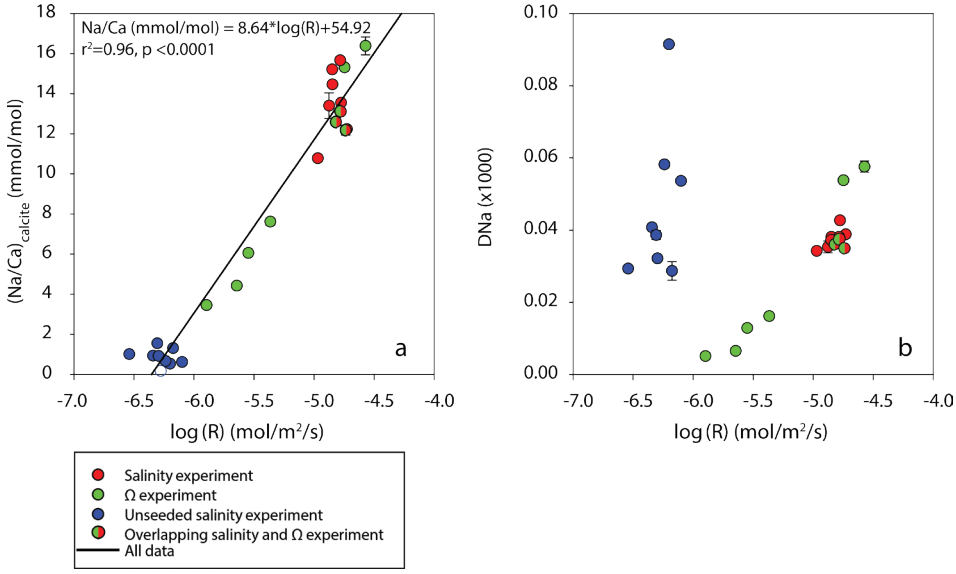

Figure 6.6. Overview of all $(Na/Ca)_{calcite}$ data from this study, explained by (a) growth rate (log (R)), and by (b) D_{Na} versus growth rate.

measurable effect on Na incorporation, and that $Na/Ca_{calcite}$ varies primarily as a function of $[Na^+]$ of the growth solution (Ishikawa and Ichikuni, 1984). This is, however, in contrast with our experiments, showing that $[Na^+]/[Ca^{2+}]$ of the solution affects Na incorporation (Figs. 6.3, 6.5 and 6.6). Although highly contrasting $([Na^+]/[Ca^{2+}])_w$ ratios were used in the seeded and unseeded experiments, the calculated partitioning was very similar (Fig. 6.6b). This implies that when investigating Na incorporation into calcites, Na partitioning rather than absolute $Na/Ca_{calcite}$ values need to be considered. The close correspondence to $([Na^+]/[Ca^{2+}])_w$ correponds to a substitution of Na for Ca, with the charge imbalance compensated by carbonate ion vacancies, as also suggested based on XANES (Yoshimura et al., 2017). In Figures 6.7 and 6.8, the combined effect of growth rate and $([Na^+]/[Ca^{2+}])_w$ is shown to explain observed pattern in partitioning. Clearly, both parameters have a significant effect on D_{Na}, albeit that more research is needed to determine the exact shape of the curves. Also towards the more extreme values of $([Na^+]/[Ca^{2+}])_w$ this relation could change.

Not only inorganic calcite precipitation studies, but also foraminiferal studies suggest a potential impact of growth rate on (trace) element incorporation. For example for strontium, incorporation into benthic foraminiferal calcites as a function of changes in

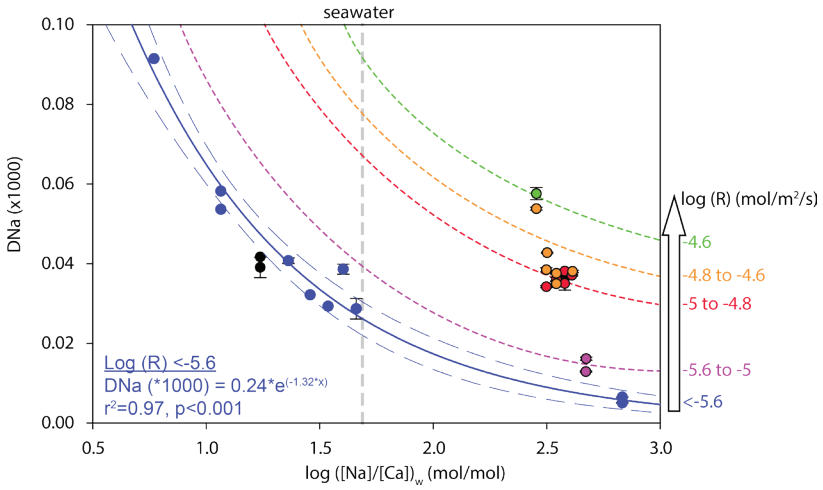

Figure 6.7. Overview of all experimental data from this study, showing the partitioning of Na (DNa), explained in terms of $[Na^+]/[Ca^+]_w$ and growth rate (R, mol/m²/s). The black dots represent data without independently determined growth rates, which are not used in the regression. The dashed lines representing different growth rates are plotted more or less parallel to the regression as a guide to the eye, as more data will be necessary to validate the suggested pattern.

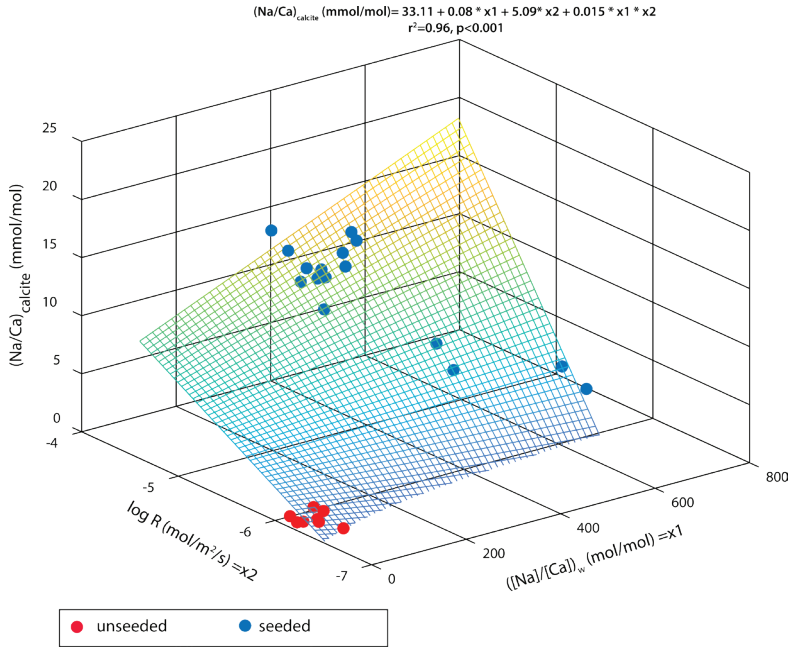

Figure 6.8. Regression surface of the combined effect of $[Na^+]/[Ca^{2+}]$ (x1 in mol/mol) and precipitation rate (x2, logR, mol/m²/s) on measured inorganic calcite Na/Ca (mmol/mol). The multiple regression analysis assumes a linear dependency of Na/Ca_{cc} on both Na/Caw and growth rate, and in addition, a dependency on their interaction. The distribution of the data on the regression surface shows that a large part of the multiple regression is an extrapolation (e.g. at highest Na/Ca_w and highest precipitation rates).

the carbonate system, suggesting a potential effect of growth rates (Dissard et al., 2010). Furthermore, the intra-shell distribution of Na in spinose planktonic foraminiferal species has also been suggested to reflect differences in growth rates, with spines high in Na being associated with areas of the test potentially characterized by higher growth rates (Mezger et al., 2019; Mezger et al., 2018).

6.4.2 Comparison to sodium in foraminiferal calcite and implications for paleoceanographic applications of foraminiferal Na/Ca

Albeit that $(Na/Ca)_{calcite}$ of both biogenic calcites (e.g. produced by foraminifera) and inorganically precipitated calcite are positively correlated to $[Na^+]_w$, the sensitivity of D_{Na} to changes in salinity differs considerably (Fig. 6.9). Whereas for foraminiferal calcite, D_{Na} values increase with increasing salinities, the partitioning is constant or decreases in precipitated calcites in growth solutions with varying ionic strength. Furthermore, D_{Na} for inorganic calcite is an order of magnitude (up to 20 times) lower compared to foraminiferal calcite. Both these observations suggest a strong organismal control on Na incorporation, also known as "vital effects" (Urey et al., 1951), which is a term that is also used for other elements and stable isotope ratios in foraminiferal calcite.

Vital effects likely cause the (chemical) conditions at the site of calcification in foraminifera to differ from those of the surrounding seawater. The underlying cellular mechanism is not fully known, but probably includes selective ion transport (Bentov and Erez, 2006; De Nooijer, 2014b; De Nooijer et al., 2009; Nehrke et al., 2007; Toyofuku et al., 2017), possibly influenced by transport of (modified) seawater to the site of calcification (vacuolization; Bentov and Erez, 2006; Erez, 2003). It is hypothesized that these processes reduce the concentrations of many elements (including Na) relative to that of calcium. At the same time, these processes also result in a highly supersaturated environment with high calcium carbonate precipitation rates as a result. This is in line with the recent observation of vaterite as a potential precursor for foraminiferal calcite (Jacob et al. 2017), which could also explain (part of) the offset in partition coefficients between inorganic precipitates and biogenic calcite.

Differences in partitioning between inorganic and biogenic calcite challenge a direct comparison between inorganically and biologically precipitated calcites. The relative complexity of foraminiferal biomineralization, however, does not mean that variability in precipitation rates are not responsible for variability in Na/Ca within specimens. Some

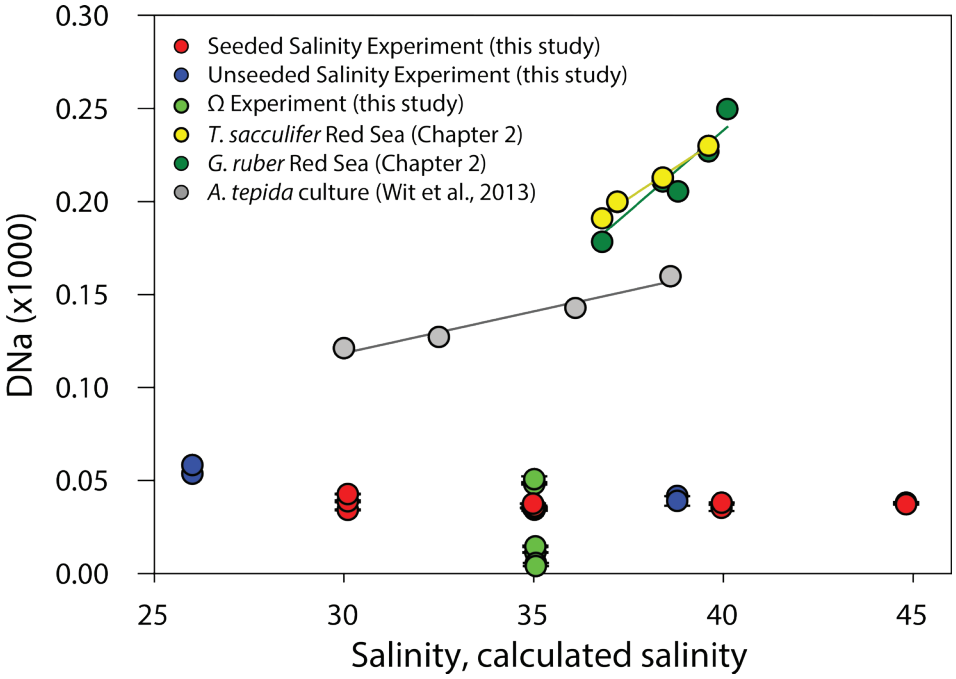

Figure 6.9. Partitioning of Na (D_{Na}) as a function of salinity (calculated from $[Na^+]$ for all experiments performed in this study, compared to previously published dependencies of foraminiferal D_{Na} on salinity (e.g. Wit et al., 2013; Mezger et al., 2016=Chapter 2).

planktonic species produce spines that are known to be enriched in Na compared to the rest of the shell (Mezger et al., 2019). In addition, bands with elevated Na/Ca are known to be present in the shells of many foraminifera (Branson et al., 2016; Geerken et al., 2018). This variability in Na/Ca within shells results in bands rich in Na, with concentrations up to 1.3 times higher in these bands compared to the carbonate in between these bands in the planktonic foraminiferal species *Orbulina universa* (Branson et al., 2016), and up to ~5 times higher in the spines (Mezger et al., 2019; 2018). Assuming that precipitation rate is largely responsible for such an offset, precipitation rate would have to change by a factor $10^{4.1}$ (from log(R)=-5.3 to -1.2) to explain the maximum observed intra-specimen variability in Na/Ca (respectively spines of 30 mmol/mol versus shells of 6 mmol/mol at a natural salinity of 35). This calculated difference in growth rate suggests that when the addition of a new chamber takes about 9 hours (Toyofuku et al., 2017), addition of a spine should be completed in less than 3 seconds, which is unlikely. Although these values exceed the calibration range presented here, the large discrepancy indicates that other

more fundamental differences must exist between shell and spine biomineralization, such as different precursor phases.

Alternatively, not precipitation rate, but Na/Ca of the calcifying fluid largely determines variability within and between foraminifera. This would be the case if foraminifera tightly control precipitation rates, for example by maintaining a constant flux of Ca^{2+} and CO_3^{2-} to the site of calcification. In this scenario, foraminiferal Na/Ca may closely reflect changes in seawater Na/Ca ratios. Sodium and calcium are considered conservative elements in ocean salinity on time scales of ~100 and ~1 Myr respectively. This implies a constant seawater concentration ratio of these elements at different salinities for at least the residence time of Ca, 1 Myr (Broecker and Peng, 1982). Over longer timescales (>1Ma), sea water $[Ca^{2+}]$ varied (e.g. Griffith et al., 2008; Ridgwell et al., 2003), with Na remaining constant over much longer time scales. Variations in sea water $[Ca^{2+}]$ mainly reflect changes in $CaCO_3$ sedimentation (Ridgwell et al., 2003), dolomitization (Holland, 2005), weathering and tectonics/seafloor spreading (Berner, 2004; Lyle, 2003). With $CaCO_3$ being the largest sink for both Ca and C, their fluxes in oceans usually co-vary. However, at times of increased weathering (glaciations) high $[Ca^{2+}]$ fluxes potentially resulted in a decoupling of the carbon and calcium flux (Heuser et al., 2005). To understand past changes in the global calcium cycle, as well as correct existing climate proxies based on El/Ca ratios in shells of marine calcifiers (e.g. Mg/Ca) for the effect of seawater $[Ca^{2+}]$ variations, an independent proxy for past seawater $[Ca^{2+}]$ variability is needed.

Recently, it has been proposed that foraminiferal shell Na/Ca values could serve as a proxy for seawater calcium concentrations (Hauzer et al., 2018). In a culturing study with benthic foraminiferal species *Operculina Ammonoides* with varying $[Ca^{2+}]$, it was found that foraminiferal Na/Ca increased with decreasing $[Ca^{2+}]$ (Hauzer et al., 2018). Such a direct and constant D would allow reconstructing past sea water Na/Ca and hence sea water Ca. Not only foraminiferal shells, but also corals were hypothesized to mainly reflect past sea water $[Ca^{2+}]$ changes over time (Gothmann et al., 2015). Our study shows, however, that increasing $[Ca^{2+}]$ relative to $[Na^+]$ of the growth solution in our Ω experiments sometimes results in higher Na incorporation. This is an indirect effect as growth rate cannot be fully decoupled from $[Ca^{2+}]$ of the seawater. Growth rate, increasing with increasing $[Ca^{2+}]$ of the growth solution and when r approaches 1 (Nehrke et al., 2007), increases D-values and hence Na incorporation (this study; Busenberg and Plummer, 1985). To untangle the effects of growth rate and $[Na^+]/[Ca^{2+}]$ of the growth solution/seawater on Na incorporation, multivariate analysis is needed (Fig. 6.8). Our

experiments, when regressed on both growth rate and $([Na^+]/[Ca^{2+}])_w$ shows that growth rate has a much larger effect on Na incorporation compared to $[Na^+]/[Ca^{2+}]$ of the growth solution. When using $(Na/Ca)_{calcite}$ to reconstruct past sea water Ca hence requires a good control on growth rates. Alternatively, with past sea water $([Na^+]/[Ca^{2+}])_w$ known, growth rates might be reconstructed from $(Na/Ca)_{calcite}$.

Conclusions

Inorganic calcite precipitation experiments were performed to test the proxy potential of foraminiferal shell Na/Ca, as well as explain intra-shell variability in Na/Ca. The effects of salinity, calcite saturation state, stoichiometry and $[Na^+]/[Ca^{2+}]$ of the growth solution were tested independently under controlled conditions in two different experimental set-ups. Inorganically precipitated calcites showed no effect of salinity, in contrast to the earlier established correlation between salinity and foraminiferal shell Na partitioning. Because also the relative incorporation of Na is much higher in the inorganic precipitates compared to foraminiferal calcite, foraminifera are suggested to exert a strong biological control on Na incorporation, possibly affected by salinity. Growth rate, here varied by changing the calcium concentration as well as by stoichiometry, has a substantial positive effect on Na incorporation. This is relevant for the recently suggested paleo-application of Na/Ca for reconstructing past variations in seawater $[Ca^{2+}]$, as changes in seawater $[Ca^{2+}]$ also might also impact growth rate.

Supporting information to Chapter 6

Supporting Table S6.1

In the next table (Table S 6.1), an overview is provided with calculated solution parameters (minteq.v4), measured Na/Ca values and partitioning (DNa) of the inorganic precipitates and calculated growth rates.

Table S6.1. Overview all minteq.v4 calculated solution parameters, measured Na/Ca_calcite values and growth rates (log (R)), where (NaCa)calcite (cc) values are corrected for initial seed mass (*1), except for (*3) experiments which were eliminated from the manuscript

sample ID	Experiment	lab	Ω	r	log(R) (mol/m2/s)	(Na/Ca) cc*[1]		SD	DNa (*10[4])	I
35_1	Ω	NIOZ	4.8	4.92	-5.55	6.06	±	0.08	0.13	0.47
35_2	Ω	NIOZ	4.5	5.20	-5.36	7.62	±	0.18	0.16	0.47
35_4	Ω, salinity	NIOZ	8.8	4.41	-4.74	12.18	±	0.25	0.35	0.47
35_6	Ω, salinity	NIOZ	8.6	4.53	-4.82	12.59	±	0.18	0.36	0.47
35_7	Ω, salinity	NIOZ	8.6	4.55	-4.78	13.11	±	0.07	0.38	0.47
35_8	Ω	NIOZ	13.0	4.46	-4.75	15.31	±	0.10	0.54	0.47
35_9	Ω	NIOZ	13.0	4.48	-4.57	16.39	±	0.45	0.58	0.47
35_10	Ω	NIOZ	2.2	5.37	-5.64	4.43	±	0.01	0.07	0.47
35_11	Ω	NIOZ	2.1	5.53	-5.90	3.45	±	0.02	0.05	0.47
30_1	salinity	NIOZ	8.9	4.32	-4.97	10.78	±	0.07	0.34	0.41
30_2	salinity	NIOZ	8.8	4.37	-4.73	12.24	±	0.16	0.39	0.41
30_4	salinity	NIOZ	8.9	4.32	-4.78	13.56	±	0.06	0.43	0.41
40_1	salinity	NIOZ	8.8	5.35	-4.88	13.41	±	0.63	0.35	0.54
40_2	salinity	NIOZ	8.5	5.54	-4.85	14.47	±	0.07	0.38	0.54
45_1	salinity	NIOZ	9.3	6.14	-4.78	15.67	±	0.12	0.38	0.60
45_2	salinity	NIOZ	9.2	6.21	-4.85	15.22	±	0.08	0.37	0.60
14_5_2018 *[3]	Ω	NIOZ	7.0	4.82	*-4.96*	*9.61*	±	0.00	0.25	0.47
15_5_2018 *[3]	Ω	NIOZ	7.1	4.75	*-4.37*	*9.33*	±	0.02	0.24	0.47
16_5_2018_1*[3]	Ω	NIOZ	7.3	4.62	*-4.54*	*8.63*	±	0.17	0.23	0.47
S08	unseeded	UO	2.8	14087	-6.27	0.13	±	-	-	0.09
S07	unseeded	UO	2.9	8005	-6.20	0.54	±	-	0.91	0.27
S05	unseeded	UO	2.1	10323	-6.10	0.62	±	-	0.54	0.44
S09	unseeded	UO	3.2	6878	-6.24	0.67	±	-	0.58	0.44
S02	unseeded	UO	3.9	6240	-	0.72	±	-	0.42	0.61
S03	unseeded	UO	3.7	6631	-	0.68	±	0.04	0.39	0.61
S10	unseeded	UO	3.6	8187	-6.34	0.94	±	0.02	0.41	0.78
S14	unseeded	UO	3.2	12023	-6.30	0.92	±	-	0.32	0.95
S13	unseeded	UO	2.5	20716	-6.54	1.01	±	-	0.29	1.12
S15	unseeded	UO	6.3	11173	-6.31	1.55	±	0.05	0.39	1.30
S12	unseeded	UO	5.1	19224	-6.17	1.31	±	0.12	0.29	1.47

Supporting Figures

Examples of the appearance of the newly precipitated calcites and seeds (the initial growth surfaces) are shown below:

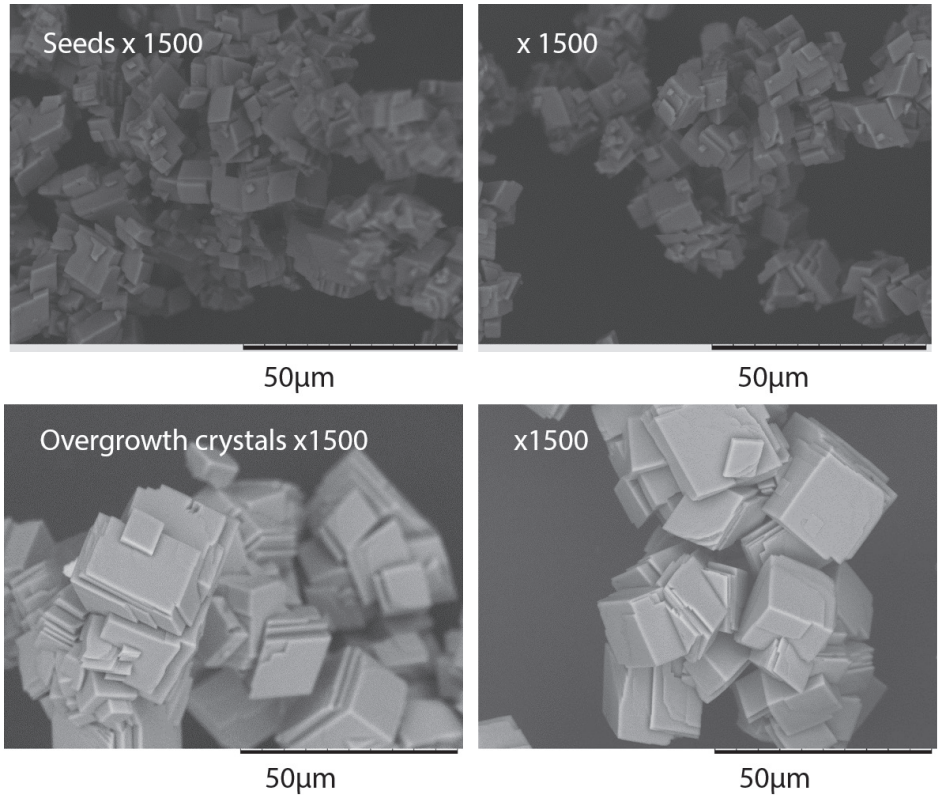

Figure S6.1. Examples of seed crystals at the start, and calcite overgrowth crystals at the end of a (seeded) experiment (35-9).

Results from the test for the cleaning protocol on sample S3 ([Na] of ~0.5) are shown below. A large step is observed from no cleaning to the first cleaning step. Additional extra steps (each step being sonication plus rinse) do not improve results, but also show that no further leaching occurs. Furthermore, no difference is found between flushing with double de-ionized water (here referred to as milli-Q) and an oversaturated $CaCO_3$ solution.

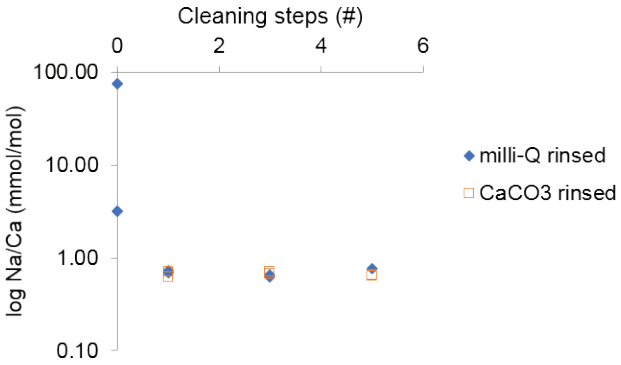

Figure S6.2. Na/Ca values of the precipitates plotted as a function of cleaning steps on sample S03 ([Na^+]=0.5).

An overview of all experiments performed for this study is shown in the next figure (Fig. S6.3), including eliminated results (white dots).

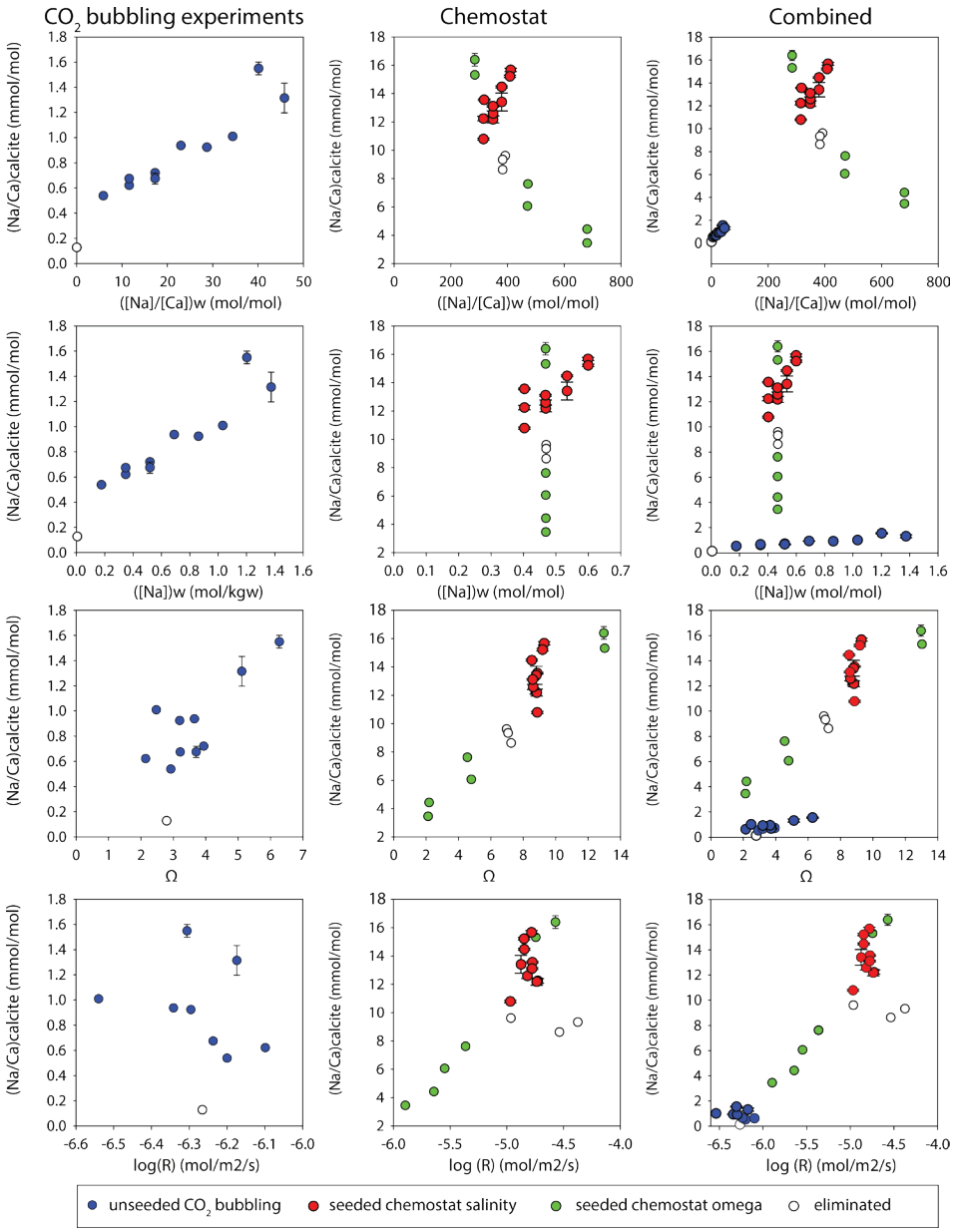

Figure S6.3. Overview all experimental results of this study.

Below, a comparison between the study of Nehrke et al. (2007) and our study, explained in terms of Ω and r, is shown (Fig. S6.4). Clearly, results are similar albeit that sometimes growth rates are somewhat higher in this study, potentially related to differences in experimental conditions (mainly ionic strenth and temperature).

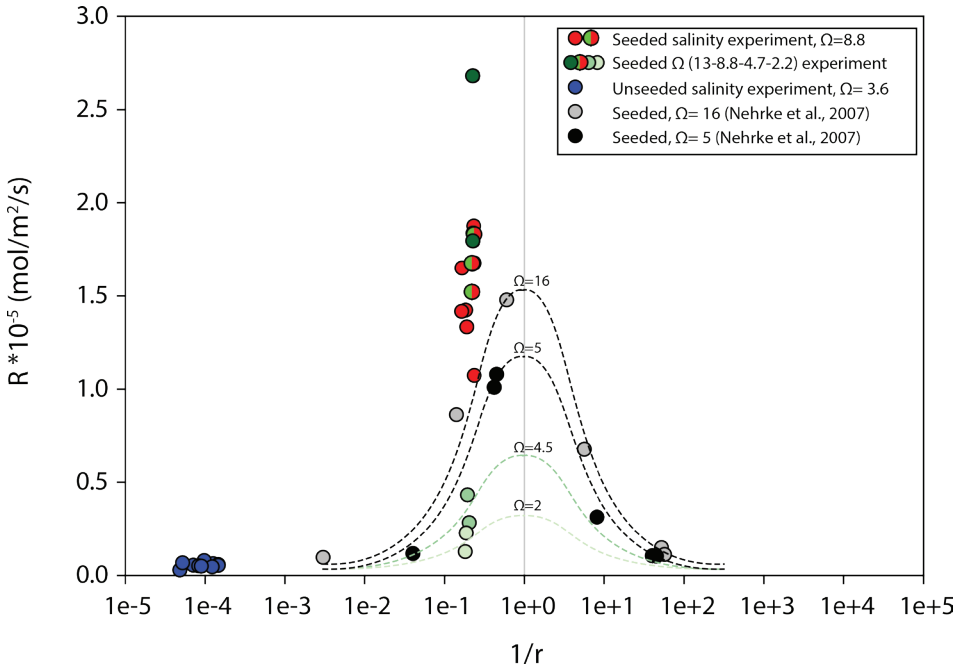

Figure S6.4. Overview of all data from this study, explained in terms of stoichiometry (1/r); growth rate (R, mol/m²/s) and calcite saturation state (Ω), compared to literature data of Nehrke et al. (2007).

References

References

Allen, K.A., Hönisch, B., Eggins, S.M., Haynes, L.L., Rosenthal, Y. and Yu, J. (2016) Trace element proxies for surface ocean conditions: A synthesis of culture calibrations with planktic foraminifera. Geochimica et Cosmochimica Acta 193, 197-221.

Altabet, M.A., Higginson, M.J. and Murray, D.W. (2002) The effect of millennial-scale changes in Arabian Sea denitrification on atmospheric CO 2. Nature 415, 159.

Anand, P., Elderfield, H. and Conte, M.H. (2003) Calibration of Mg/Ca thermometry in planktonic foraminifera from a sediment trap time series. Paleoceanography 18.

Andersen, K.K., Azuma, N., Barnola, J.-M., Bigler, M., Biscaye, P., Caillon, N., Chappellaz, J., Clausen, H.B., Dahl-Jensen, D. and Fischer, H. (2004) High-resolution record of Northern Hemisphere climate extending into the last interglacial period. Nature 431, 147.

Antonov, J., Seidov, D., Boyer, T., Locarnini, R., Mishonov, A., Garcia, H., Baranova, O., Zweng, M. and Johnson, D. (2010) World Ocean Atlas 2009, vol. 2: Salinity, edited by: Levitus. S., NOAA Atlas NESDIS 69, 184.

Auras-Schudnagies, A., D. Kroon, G. Ganssen, C. Hemleben and J. E. van Hinte (1989) Distributional pattern of planktonic foraminifers and pteropods in surface waters and top core sediments of the Red Sea, and adjacent areas controlled by the monsoonal regime and other ecological factors. Deep Sea Research Part A. Oceanographic Research Papers, 36(10), 1515-1533.

Barber, R.T., Marra, J., Bidigare, R.C., Codispoti, L.A., Halpern, D., Johnson, Z., Latasa, M., Goericke, R. and Smith, S.L. (2001) Primary productivity and its regulation in the Arabian Sea during 1995. Deep Sea Research Part II: Topical Studies in Oceanography 48, 1127-1172.

Barker, S., Greaves, M. and Elderfield, H. (2003) A study of cleaning procedures used for foraminiferal Mg/Ca paleothermometry. Geochemistry, Geophysics, Geosystems 4.

Barras, C., Mouret, A., Nardelli Maria, P., Metzger, E., Petersen, J., La, C., Filipsson, H.L. and Jorissen, F. (2018) Experimental calibration of manganese incorporation in foraminiferal calcite. Geochimica et Cosmochimica Acta.

Bé, A. W. H. (1980) Gametogenic calcification in a spinose planktonic foraminifer, *Globigerinoides sacculifer* (Brady), Marine Micropaleontology 5, 283–310.

Beniash, E., Aizenberg, J., Addadi, L. and Weiner, S. (1997) Amorphous calcium carbonate transforms into calcite during sea urchin larval spicule growth. Proceedings of the Royal Society of London B: Biological Sciences 264, 461-465.

Bentov, S. and Erez, J. (2006) Impact of biomineralization processes on the Mg content of foraminiferal shells: A biological perspective. Geochemistry, Geophysics, Geosystems 7.

Berner, R.A. (2004) A model for calcium, magnesium and sulfate in seawater over Phanerozoic time. American Journal of Science 304, 438-453.

Bernstein, R. E., P.R. Betzer, R.A. Feely, R.H. Byrne, M.F. Lamb, and A.F. Michaels, A. F.(1987) Acantharian fluxes and strontium to chlorinity ratios in the North Pacific Ocean. Science, 237(4821), 1490-1494.

Bertlich, J., Nürnberg, D., Hathorne, E.C., de Nooijer, L.J., Mezger, E.M., Kienast, M., Nordhausen, S., Reichart, G.-J., Schönfeld, J. and Bijma, J. (2018) Salinity control on Na incorporation into calcite tests of the planktonic foraminifera *Trilobatus sacculifer*–Evidence from culture experiments and surface sediments. Biogeosciences, 1-38.

Bijma, J., Erez, J. and Hemleben, C. (1990a) Lunar and semi-lunar reproductive cycles in some spinose planktonic foraminifers. Journal of foraminiferal research 20, 117-127.

Bijma, J., Faber, W. W., and Hemleben, C. (1990b) Temperature and salinity limits for growth and survival of some planktonic foraminifers in laboratory cultures, Journal of Foraminiferal Research, 20, 95-116.

Bijma, J. and Hemleben, C. (1994) Population dynamics of the planktic foraminifer *Globigerinoides sacculifer* (Brady) from the central Red Sea. Deep Sea Research Part I: Oceanographic Research Papers 41, 485-510.

Bishop, J.K. (1988) The barite-opal-organic carbon association in oceanic particulate matter. Nature 332, 341.

Böning, P. and Bard, E. (2009) Millennial/centennial-scale thermocline ventilation changes in the Indian Ocean as reflected by aragonite preservation and geochemical variations in Arabian Sea sediments. Geochimica et Cosmochimica Acta 73, 6771-6788.

Boyer, T.P. and Levitus, S. (2002) World Ocean Atlas 2001. Volume 2, Salinity.

Boyer, T., S. Levitus, H. Garcia, R.A. Locarnini, C. Stephensand J. Antonov (2005) Objective analyses of annual, seasonal, and monthly temperature and salinity for the World Ocean on a 0.25 grid. International Journal of Climatology, 25(7), 931-945.

Boyle, E.A. (1983) Manganese carbonate overgrowths on foraminifera tests. Geochimica et Cosmochimica Acta 47, 1815-1819.

Branson, O., Bonnin, E.A., Perea, D.E., Spero, H.J., Zhu, Z., Winters, M., Hönisch, B., Russell, A.D., Fehrenbacher, J.S. and Gagnon, A.C. (2016) Nanometer-Scale Chemistry of a Calcite Biomineralization Template: Implications for Skeletal Composition and Nucleation. Proceedings of the National Academy of Sciences.

Broecker, W.S. and Peng, T.-H. (1982) Tracers in the Sea.

Brown, S.J. and Elderfield, H. (1996) Variations in Mg/Ca and Sr/Ca ratios of planktonic foraminifera caused by postdepositional dissolution: Evidence of shallow Mg-dependent dissolution. Paleoceanography 11, 543-551.

Brokmann, U., M. Jacquorie, M. Talkenberg, A. Harnisch, E-W. Kreutz, D. Hülsenberg, and R. Poprawe (2002). Exposure of photosensitive glasses with pulsed UV-laser radiation. Microsystem technologies 8, 2-3, 102-104.

Brummer, G.-J.A., Hemleben, C. and Spindler, M. (1986) Planktonic foraminiferal ontogeny and new perspectives for micropalaeontology. Nature 319, 50.

Brummer, G.-J.A., Hemleben, C. and Spindler, M. (1987) Ontogeny of extant spinose planktonic foraminifera (*Globigerinidae*): a concept exemplified by *Globigerinoides sacculifer* (Brady) and *G. ruber* (D'Orbigny). Marine Micropaleontology 12, 357-381.

Busenberg, E. and Plummer, L.N. (1985) Kinetic and thermodynamic factors controlling the distribution of SO32– and Na+ in calcites and selected aragonites. Geochimica et Cosmochimica Acta 49, 713-725.

Caron, D.A., Anderson, O.R., Lindsey, J.L., Faber, W.W. and Lim, E.L. (1990) Effects of gametogenesis on test structure and dissolution of some spinose planktonic foraminifera and implications for test preservation. Marine Micropaleontology 16, 93-116.

Cember, R. P. (1988). On the sources, formation, and circulation of Red Sea deep water. Journal of Geophysical Research: Oceans. 93(C7), 8175-8191.

Clemens, S., Prell, W., Murray, D., Shimmield, G. and Weedon, G. (1991) Forcing mechanisms of the Indian Ocean monsoon. Nature 353, 720.

Clemens, S.C. and Prell, W.L. (1990) Late Pleistocene variability of Arabian Sea summer monsoon winds and continental aridity: Eolian records from the lithogenic component of deep-sea sediments. Paleoceanography 5, 109-145.

Culver, S.J. (1991) Early Cambrian foraminifera from west Africa. Science 254, 689-691.

Dansgaard, W., Johnsen, S., Clausen, H., Dahl-Jensen, D., Gundestrup, N., Hammer, C., Hvidberg, C., Steffensen, J., Sveinbjörnsdottir, A. and Jouzel, J. (1993) Evidence for general instability of past climate from a 250-kyr ice-core record. Nature 364, 218-220.

De Deckker, P. (2004). On the celestite-secreting Acantharia and their effect on seawater strontium to calcium ratios. Hydrobiologia, 517(1-3), 1-13.

Dehairs, F., Chesselet, R. and Jedwab, J. (1980) Discrete suspended particles of barite and the barium cycle in the open ocean. Earth and Planetary Science Letters 49, 528-550.

Delaney, M. L., Bé, A. W. H., and Boyle, E. A. (1985) Li, Sr, Mg, and Na in foraminiferal calcite shells from laboratory culture, sediment traps, and sediment cores. Geochimica et Cosmochimica Acta, 49, 1327-1341.

DePaolo, D.J. (2011) Surface kinetic model for isotopic and trace element fractionation during precipitation of calcite from aqueous solutions. Geochimica et Cosmochimica Acta 75, 1039-1056.

Deplazes, G., Lückge, A., Peterson, L.C., Timmermann, A., Hamann, Y., Hughen, K.A., Röhl, U., Laj, C., Cane, M.A., Sigman, D.M. and Haug, G.H. (2013) Links between tropical rainfall and North Atlantic climate during the last glacial period, Nature Geoscience, pp. 213-217.

Deplazes, G., Lückge, A., Stuut, J.B.W., Pätzold, J., Kuhlmann, H., Husson, D., Fant, M. and Haug, G.H. (2014) Weakening and strengthening of the Indian monsoon during Heinrich events and Dansgaard-Oeschger oscillations. Paleoceanography 29, 99-114.

van Dijk, I., de Nooijer, L.J. and Reichart, G.-J. (2017) Trends in element incorporation in hyaline and porcelaneous foraminifera as a function of pCO2. Biogeosciences 14, 497.

van Dijk, I., de Nooijer, L., Boer, W. and Reichart, G.-J. (2017) Sulfur in foraminiferal calcite as a potential proxy for seawater carbonate ion concentration. Earth and Planetary Science Letters 470, 64-72.

Dissard, D., Nehrke, G., Reichart, G.-J. and Bijma, J. (2010) Impact of seawater pCO2 on calcification and Mg/Ca and Sr/Ca ratios in benthic foraminifera calcite: results from culturing experiments with *Ammonia tepida*. Biogeosciences 7, 81-93.

Dueñas-Bohórquez, A., Da Rocha, R.E., Kuroyanagi, A., Bijma, J. and Reichart, G.J. (2009) Effect of salinity and seawater calcite saturation state on Mg and Sr incorporation in cultured planktonic foraminifera. Marine Micropaleontology 73, 178–189.

Dueñas-Bohórquez, A., Da Rocha, R.E., Kuroyanagi, A., Bijma, J. and Reichart, G.J. (2011) Interindividual variability and ontogenetic effects on Mg and Sr incorporation in the planktonic foraminifer *Globigerinoides sacculifer*. Geochimica et Cosmochimica Acta 75, 520-532.

Dymond, J., Suess, E. and Lyle, M. (1992) Barium in deep-sea sediment: A geochemical proxy for paleoproductivity. Paleoceanography 7, 163-181.

Edmond, J., Boyle, E., Drummond, D., Grant, B. and Mislick, T. (1978) Desorption of barium in the plume of the Zaire (Congo) River. Netherlands Journal of Sea Research 12, 324-328.

Eggins, S. M., Sadekov, A. and De Deckker, P. (2004) Modulation and daily banding of Mg/Ca in *Orbulina universa* tests by symbiont photosynthesis and respiration: a complication for seawater thermometry? Earth and Planetary Science Letters, 225(3), 411-419.

Elderfield, H. and Ganssen, G. (2000) Past temperature and d18O of surface ocean waters inferred from foraminiferal Mg/Ca ratios. Nature 405, 442-445.

Elderfield, H., Vautravers, M. and Cooper, M. (2002) The relationship between shell size and Mg/Ca, Sr/Ca, δ18O, and δ13C of species of planktonic foraminifera. Geochemistry, Geophysics, Geosystems 3, 1-13.

Emiliani, C. (1955) Pleistocene temperatures. The Journal of Geology 63, 538-578.

Epstein, S., Buchsbaum, R., Lowenstam, H. and Urey, H.C. (1951) Carbonate-water isotopic temperature scale. Geological Society of America Bulletin 62, 417-426.

Epstein, S., Buchsbaum, R., Lowenstam, H.A. and Urey, H.C. (1953) Revised carbonate-water isotopic temperature scale. Geological Society of America Bulletin 64, 1315-1326.

Erez, J. (2003) The source of ions for biomineralization in foraminifera and their implications for paleoceanographic proxies. Reviews in mineralogy and geochemistry 54, 115-149.

Erez, J. and Honjo, S. (1981) Comparison of isotopic composition of planktonic foraminifera in plankton tows, sediment traps and sediments. Palaeogeography, Palaeoclimatology, Palaeoecology 33, 129-156.

Evans, D., Erez, J., Oron, S. and Müller, W. (2015) Mg/Ca-temperature and seawater-test chemistry relationships in the shallow-dwelling large benthic foraminifera *Operculina ammonoides*. Geochimica et Cosmochimica Acta 148, 325-342.

Farmer, J.R., Branson, O., Uchikawa, J., Penman, D.E., Hönisch, B. and Zeebe, R.E. (2019) Boric acid and borate incorporation in inorganic calcite inferred from B/Ca, boron isotopes and surface kinetic modeling. Geochimica et Cosmochimica Acta 244, 229-247.

Fairbanks, R.G. (1989) A 17,000-year glacio-eustatic sea level record: influence of glacial melting rates on the Younger Dryas event and deep-ocean circulation. Nature 342, 637.

Fallet, U., Boer, W. van Assen, C. Greaves, M. and Brummer, G. J. A. (2009) A novel application of wet oxidation to retrieve carbonates from large organic-rich samples for ocean-climate research. Geochemistry, Geophysics, Geosystems, 10(8).

Fallet, U., Brummer, G. J., Zinke, J., Vogels, S., and Ridderinkhof, H. (2010) Contrasting seasonal fluxes of planktonic foraminifera and impacts on paleothermometry in the Mozambique Channel upstream of the Agulhas Current. Paleoceanography, 25.

Fehrenbacher, J. S., Spero, H. J. Russell, A. D. Vetter, L. and Eggins, S. (2015) Optimizing LA-ICP-MS analytical procedures for elemental depth profiling of foraminifera shells. Chemical Geology, 407, 2-9

Fehrenbacher, J. S., Russell, A. D., Davis, C. V., Gagnon, A. C., Spero, H. J., Cliff, J. B., Zhu, Z., and Martin, P. (2017) Link between light-triggered Mg-banding and chamber formation in the planktic foraminifera *Neogloboquadrina dutertrei,* Nature Communications.

Ferguson, J., Henderson, G., Kucera, M. and Rickaby, R. (2008) Systematic change of foraminiferal Mg/Ca ratios across a strong salinity gradient. Earth and Planetary Science Letters 265, 153-166.

Fietzke, J. and Frische, M. (2016) Experimental evaluation of elemental behavior during LA-ICP-MS: influences of plasma conditions and limits of plasma robustness. Journal of Analytical Atomic Spectrometry 31, 234-244.

Fok-Pun, L. and Komar, P.D. (1983) Settling velocities of planktonic-foraminifer: density variations and shape effects, Journal of Foraminiferal Research, pp. 60-83.

Francois, R., Honjo, S., Manganini, S.J. and Ravizza, G.E. (1995) Biogenic barium fluxes to the deep sea: Implications for paleoproductivity reconstruction. Global Biogeochemical Cycles 9, 289-303.

Gat, J. R. (1996) Oxygen and hydrogen isotopes in the hydrologic cycle. Annual Review of Earth and Planetary Sciences, 24(1), 225-262.

Geerken, E., de Nooijer, L.J., van Dijk, I. and Reichart, G.J. (2018) Impact of salinity on element incorporation in two benthic foraminiferal species with contrasting magnesium contents. Biogeosciences 15, 2205-2218.

Golani, D. (1998). Impact of Red Sea fish migrants through the Suez Canal on the aquatic environment of the Eastern Mediterranean. Bulletin Series Yale School of Forestry and Environmental Studies, 103, 375-387.

Gothmann, A.M., Stolarski, J., Adkins, J.F., Schoene, B., Dennis, K.J., Schrag, D.P., Mazur, M. and Bender, M.L. (2015) Fossil corals as an archive of secular variations in seawater chemistry since the Mesozoic. Geochimica et Cosmochimica Acta 160, 188-208.

Gordon, C., Carr, R., and Larson, R. (1970) The influence of environmental factors on the sodium and manganese content of barnacle shells. Limnology and Oceanography, 15.

Grant, K.M. and Dickens, G.R. (2002) Coupled productivity and carbon isotope records in the southwest Pacific Ocean during the late Miocene–early Pliocene biogenic bloom. Palaeogeography, Palaeoclimatology, Palaeoecology 187, 61-82.

Gray, W.R., Weldeab, S., Lea, D.W., Rosenthal, Y., Gruber, N., Donner, B. and Fischer, G. (2018) The effects of temperature, salinity, and the carbonate system on Mg/Ca in *Globigerinoides ruber* (white): A global sediment trap calibration. Earth and Planetary Science Letters 482, 607-620.

Griffith, E.M., Paytan, A., Caldeira, K., Bullen, T.D. and Thomas, E. (2008) A dynamic marine calcium cycle during the past 28 million years. Science 322, 1671-1674.

Groeneveld, J. and Filipsson, H. (2013) Mg/Ca and Mn/Ca ratios in benthic foraminifera: the potential to reconstruct past variations in temperature and hypoxia in shelf regions. Biogeosciences 10, 5125-5138.

Gupta, A.K., Anderson, D.M. and Overpeck, J.T. (2003) Abrupt changes in the Asian southwest monsoon during the Holocene and their links to the North Atlantic Ocean. Nature 421, 354.

Gupta, G., Sudheesh, V., Sudharma, K., Saravanane, N., Dhanya, V., Dhanya, K., Lakshmi, G., Sudhakar, M. and Naqvi, S. (2016) Evolution to decay of upwelling and associated biogeochemistry over the southeastern Arabian Sea shelf. Journal of Geophysical Research: Biogeosciences 121, 159-175.

Gupta, R.S. and Naqvi, S. (1984) Chemical oceanography of the Indian Ocean, north of the equator. Deep Sea Research Part A. Oceanographic Research Papers 31, 671-706.

Haake, B., Ittekkot, V., Rixen, T., Ramaswamy, V., Nair, R. and Curry, W. (1993) Seasonality and interannual variability of particle fluxes to the deep Arabian Sea. Deep Sea Research Part I: Oceanographic Research Papers 40, 1323-1344.

Hall, J.M. and Chan, L.H. (2004) Ba/Ca in Neogloboquadrina pachyderma as an indicator of deglacial meltwater discharge into the western Arctic Ocean. Paleoceanography 19.

Hathorne, E.C., James, R.H., Savage, P. and Alard, O. (2008) Physical and chemical characteristics of particles produced by laser ablation of biogenic calcium carbonate. Journal of Analytical Atomic Spectrometry 23, 240-243.

Hathorne, E. C., James, R. H., and Lampitt, R. S. (2009) Environmental versus biomineralization controls on the intratest variation in the trace element composition of the planktonic foraminifera *G. inflata* and *G. scitula*. Paleoceanography, 24.

Hathorne, E. C., A. Gagnon, T. Felis, J. Adkins, Asami, R., Boer, W., Caillon, N. Case, D., Cobb, K., Douville, M. E. and deMenocal, P. (2013) Interlaboratory study for coral Sr/Ca and other element/Ca ratio measurements. Geochemistry, Geophysics, Geosystems, 14(9), 3730-3750.

Hauzer, H., Evans, D., Müller, W., Rosenthal, Y. and Erez, J. (2018) Calibration of Na partitioning in the calcitic foraminifer Operculina ammonoides under variable Ca concentration: Toward reconstructing past seawater composition. Earth and Planetary Science Letters 497, 80-91.

Hemleben, C. (1975) Spine and pustule relationships in some recent planktonic foraminifers. Micropaleontology 21, 334–341.

Hemleben, C. and Bijma, J. (1994) Foraminiferal population dynamics and stable carbon isotopes, Carbon Cycling in the Glacial Ocean: Constraints on the Ocean's Role in Global Change. Springer, pp. 145-166.

Hemleben, C., Be, A.W., Anderson, O.R. and Tuntivate, S. (1977) Test morphology, organic layers and chamber formation of the planktonic foraminifer *Globorotalia menardii* (d'Orbigny). The Journal of Foraminiferal Research 7, 1-25.

Heuser, A., Eisenhauer, A., Böhm, F., Wallmann, K., Gussone, N., Pearson, P.N., Nägler, T.F. and Dullo, W.C. (2005) Calcium isotope (δ44/40Ca) variations of Neogene planktonic foraminifera. Paleoceanography and Paleoclimatology 20.

Hoogakker, B.A.A., Klinkhammer, G.P., Elderfield, H., Rohling , E.J. and Hayward, C. (2009) Mg/Ca paleothermometry in high salinity environments. Earth and Planetary Science Letters 284, 583-589.

Holland, H.D. (2005) Sea level, sediments and the composition of seawater. American Journal of Science 305, 220-239.

Hönisch, B., Allen, K.A., Lea, D.W., Spero, H.J., Eggins, S.M., Arbuszewski, J., deMenocal, P. and Rosenthal, Y. (2013) The influence of salinity on Mg/Ca in planktic foraminifers – Evidence from cultures, core-top sediments and complementary δ18O. Geochimica et Cosmochimica Acta 121, 196-213.

Hönisch, B., Allen, K.A., Russell, A., Eggins, S.M., Bijma, J., Spero, H.J., Lea, D.W. and Yu, J. (2011) Planktic foraminifers as recorders of seawater Ba/Ca. Marine Micropaleontology 79, 52-57.

Hülsenberg, D., Harnisch, A., and Bismarck, A. (2008) Microstructuring of glasses. Springer Berlin Heidelberg, 11-15.

Hurd, D. C. and Spencer, D. W. (1991) Marine particles: Analysis and characterization. Geophysical Monographs 63, Geophysical Union.

Imbrie, J. and Kipp, N. (1971) A new micropaleontologial method for quantitative paleoclimatology: Application to a Late Pleistocene Caribbean core. The Late Cenozoic Glacial Ages. Yale Univ. Press, New Haven 3, 71-181.

Ishikawa, M. and Ichikuni, M. (1984) Uptake of sodium and potassium by calcite. Chemical Geology 42, 137-146.

Jacob, D., Wirth, R., Agbaje, O., Branson, O. and Eggins, S. (2017) Planktic foraminifera form their shells via metastable carbonate phases. Nature Communications 8, 1265.

Jochum, K.P., Weis, U., Stoll, B., Kuzmin, D., Yang, Q., Raczek, I., Jacob, D.E., Stracke, A., Birbaum, K. and Frick, D.A. (2011) Determination of reference values for NIST SRM 610–617 glasses following ISO guidelines. Geostandards and Geoanalytical Research 35, 397-429.

Kaczmarek, K., Nehrke, G., Misra, S., Bijma, J. and Elderfield, H. (2016) Investigating the effects of growth rate and temperature on the B/Ca ratio and δ 11 B during inorganic calcite formation. Chemical Geology 421, 81-92.

Kester, D.R., Duedall, I.W., Connors, D.N., Pytkowitz, R.M. (1967) Preparation of Artificial Seawater. Limnology and Oceanography 12, 176-179.

Keul, N., Langer, G., Thoms, S., de Nooijer, L.J., Reichart, G.-J. and Bijma, J. (2017) Exploring foraminiferal Sr/Ca as a new carbonate system proxy. Geochimica et Cosmochimica Acta 202, 374-386.

Kısakürek, B., Eisenhauer, A., Böhm, F., Garbe-Schönberg and D., E., J. (2008) Controls on shell Mg/Ca and Sr/Ca in cultured planktonic foraminiferan, *Globigerinoides ruber* (white). Earth and Planetary Science Letters 273.

Kitano, Y., Okumura, M. and Idogaki, M. (1975) Incorporation of sodium, chloride and sulfate with calcium carbonate. Geochemical Journal 9, 75-84.

Klinkhammer, G.P., Mix, A.C. and Haley, B. (2009) Increased dissolved terrestrial input to the coastal ocean during the last deglaciation. Geochemistry, Geophysics, Geosystems 10.

Köhler-Rink, S. and Kühl, M. (2005) The chemical microenvironment of the symbiotic planktonic foraminifer *Orbulina universa*. Marine Biology Research, 1(1), 68-78.

Koho, K.A., De Nooijer, L.J., Fontanier, C., Toyofuku, T., Oguri, K., Kitazato, H. and Reichart, G.-J. (2017) Benthic foraminiferal Mn/Ca ratios reflect microhabitat preferences. Biogeosciences 12, 3067-3082.

Kunioka, D., Shirai, K., Takahata, N. and Yuji Sano (2006) Microdistribution of Mg/Ca, Sr/Ca, and Ba/Ca ratios in Pulleniatina obliquiloculata test by using a NanoSIMS: Implication for the vital effect mechanism. Geochemistry Geophysics Geosystems, 7, 1-11.

Labeyrie, L., Labracherie, M., Gorfti, N., Pichon, J.J., Vautravers, M., Arnold, M., Duplessy, J.C., Paterne, M., Michel, E. and Duprat, J. (1996) Hydrographic changes of the Southern Ocean (southeast Indian sector) over the last 230 kyr. Paleoceanography 11, 57-76.

Larsen, K., Bechgaard, K. and Stipp, S.L.S. (2010) The effect of the Ca2+ to CO32-activity ratio on spiral growth at the calcite {101¯ 4} surface. Geochimica et Cosmochimica Acta 74, 2099-2109.

Lattaud, J., Lo, L., Huang, J.J., Chou, Y.M., Gorbarenko, S.A., Sinninghe Damsté, J.S. and Schouten, S. (2018) A Comparison of Late Quaternary Organic Proxy-Based Paleotemperature Records of the Central Sea of Okhotsk. Paleoceanography and Paleoclimatology 33, 732-744.

Lea, D. W. (1991) Trace elements in foraminiferal calcite, In modern Foraminifera (ed. B. K. S. Gupta). Kluwer Academic Publishers.

Lea, D.W. and Boyle, E.A. (1991) Barium in planktonic foraminifera. Geochimica et Cosmochimica Acta 55, 3321-3331.

Lea, D. W., Mashiotta, T. A., and Spero, H. J. (1999): Controls on magnesium and strontium uptake in planktonic foraminifera determined by live culturing. Geochimica et Cosmochimica Acta, 63, 2369–2379.

Lea, D.W. and Spero, H.J. (1994) Assessing the reliability of paleochemical tracers: Barium uptake in the shells of planktonic foraminifera. Paleoceanography 9, 445-452.

Lewis, E. and Wallace, D.W.R., Program Developed for CO2 System calculations, ORNL/CDIAC-105, Carbon Dioxide Information Analysis Center, Oak Ridge National Laboratory, US Department of Energy, Oak Ridge, Tennessee

Li, Z., Hu, Z., Liu, Y., Gao, S., Li, M. Zong, k., Chen, H. and Hu, S. (2015) Accurate determination of elements in silicate glass by nanosecond and femtosecond laser ablation ICP-MS at high spatial resolution. Chemical Geology, 400, 11-23.

Lisiecki, L.E. and Raymo, M.E. (2005) A Pliocene-Pleistocene stack of 57 globally distributed benthic δ18O records. Paleoceanography 20.

Littlewood, J. L., Shaw, S., Peacock, C. L., Bots, P., Trivedi, D., and Burke, I. T. (2017) Mechanism of Enhanced Strontium Uptake into Calcite via an Amorphous Calcium Carbonate Crystallization Pathway, Crystal Growth & Design, 17, 1214-1223.

Locarnini, R., Mishonov, A., Antonov, J., Boyer, T., Garcia, H., Baranova, O., Zweng, M. and Johnson, D. (2010) World Ocean Atlas 2009, vol. 1, Temperature, edited by S. Levitus, 184 pp. US Gov. Print. Off., Washington, DC.

Lorens, R.B. (1981) Sr, Cd, Mn and Co distribution coefficients in calcite as a function of calcite precipitation rate. Geochimica et Cosmochimica Acta 45, 553-561.

Lourens, L.J., Wehausen, R. and Brumsack, H.J. (2001) Geological constraints on tidal dissipation and dynamical ellipticity of the Earth over the past three million years. Nature 409, 1029.

Lyle, M. (2003) Neogene carbonate burial in the Pacific Ocean. Paleoceanography and Paleoclimatology 18.

Madhupratap, M., Kumar, S.P., Bhattathiri, P., Kumar, M.D., Raghukumar, S., Nair, K. and Ramaiah, N. (1996) Mechanism of the biological response to winter cooling in the Northeast Arabian Sea. Nature 384, 549.

Mavromatis, V., Gautier, Q., Bosc, O. and Schott, J. (2013) Kinetics of Mg partition and Mg stable isotope fractionation during its incorporation in calcite. Geochimica et Cosmochimica Acta 114, 188-203.

Mertens, K. N., Bradley, L. R., Takano, Y., Mudie, P. J., Marret, F., Aksu, A. E., Hiscott, R. N., Verleye, T. J., Mousing, E. A., and Smyrnova, L. L. (2012): Quantitative estimation of Holocene surface salinity variation, Quaternary Science reviews 39, 45-59.

Mewes, A., Langer, G., De Nooijer, L.J., Bijma, J. and Reichart, G.J. (2014) Effect of different seawater Mg2+ concentrations on calcification in two benthic foraminifers. Marine Micropaleontology 113, 56-64.

Mezger, E.M., de Nooijer, L.J., Bertlich, J., Bijma, J., Nürnberg, D. and Reichart, G.J. (2019) Planktonic foraminiferal spine versus shell carbonate Na incorporation in relation to salinity. Biogeosciences 16, 1147-1165.

Mezger, E.M., Nooijer, L.J., Boer, W., Brummer, G.J.A. and Reichart, G.J. (2016) Salinity controls on Na incorporation in Red Sea planktonic foraminifera. Paleoceanography 31, 1562-1582.

Mezger, E.M., Nooijer, L.J., Siccha, M., Kucera, M. and Reichart, G.-J. (2018) Taphonomic and ontogenetic effects on Na/Ca and Mg/Ca in spinose planktonic foraminifera from the Red Sea. Geochemistry, Geophysics, Geosystems 19, 4174-4194.

Morcos, S. A. (1970) Physical and chemical oceanography of the Red Sea., Oceanography and Marine Biology Annual Review, 8(73), 202.

Morse, J.W., Arvidson, R.S. and Lüttge, A. (2007) Calcium Carbonate Formation and Dissolution. Chemical Reviews 107, 342-381.

Müller, P.J., Kirst, G., Ruhland, G., Von Storch, I. and Rosell-Melé, A. (1998) Calibration of the alkenone paleotemperature index U 37 K' based on core-tops from the eastern South Atlantic and the global ocean (60 N-60 S). Geochimica et Cosmochimica Acta 62, 1757-1772.

Munsel, D., Kramar, U., Dissard, D., Nehrke, G., Berner, Z., Bijma, J., Reichart, G.-J. and Neumann, T. (2010) Heavy metal incorporation in foraminiferal calcite: results from multi-element enrichment culture experiments with *Ammonia tepida*. Biogeosciences 7, 2339-2350.

Naqvi, S., Noronha, R., Somasundar, K. and Gupta, R.S. (1990) Seasonal changes in the denitrification regime of the Arabian Sea. Deep Sea Research Part A. Oceanographic Research Papers 37, 593-611.

Nehrke, G., Keul, N., Langer, G., De Nooijer, L., Bijma, J. and Meibom, A. (2013) A new model for biomineralization and trace-element signatures of Foraminifera tests. Biogeosciences 10, 6759-6767.

Nehrke, G., Reichart, G.J., Van Cappellen, P., Meile, C. and Bijma, J. (2007) Dependence of calcite growth rate and Sr partitioning on solution stoichiometry: Non-Kossel crystal growth. Geochimica et Cosmochimica Acta 71, 2240-2249.

Ní Fhlaithearta, S., Reichart, G.J., Jorissen, F.J., Fontanier, C., Rohling, E., Thomson, J. and De Lange, G. (2010) Reconstructing the seafloor environment during sapropel formation using benthic foraminiferal trace metals, stable isotopes, and sediment composition. Paleoceanography and Paleoclimatology 25.

de Nooijer, L. J., Hathorne, E. C. Reichart, G. J. Langer G.,and Bijma, J. (2014a) Variability in calcitic Mg/Ca and Sr/Ca ratios in clones of the benthic foraminifer *Ammonia tepida*, Marine Micropaleontology, 107, 32-43.

de Nooijer, L.J., Langer, G., Nehrke, G. and Bijma, J. (2009) Physiological controls on seawater uptake and calcification in the benthic foraminifer *Ammonia tepida*. Biogeosciences 6, 2669-2675.

de Nooijer, L.J., Reichart, G.-J., Dueñas-Bohórquez, A., Wolthers, M., Ernst, S., Mason, P. and Van der Zwaan, G. (2007) Copper incorporation in foraminiferal calcite: results from culturing experiments. Biogeosciences 4, 493-504.

de Nooijer, L.J., Spero, H.J., Erez, J., Bijma, J., Reichart, G.J. (2014b) Biomineralization in perforate foraminifera. Earth-Science Reviews 135, 48-58.

de Nooijer, L.J., Toyofuku, T., Kitazato, H. (2009) Foraminifera promote calcification by elevating their intracellular pH. Proceedings of the National Academy of Sciences 106, 15374-15378.

North, N. A. (1974) Pressure dependence ot SrSO4 solubility. Geochimica et Cosmochimica Acta, 38(7), 1075-1081.

Nürnberg, D., Bijma, J. and Hemleben, C. (1996) Assessing the reliability of magnesium in foraminiferal calcite as a proxy for water mass temperatures. Geochimica et Cosmochimica Acta 60, 803-814.

Nürnberg, D., Böschen, T., Doering, K., Mollier-Vogel, E., Raddatz, J. and Schneider, R. (2015) Sea surface and subsurface circulation dynamics off equatorial Peru during the last~ 17 kyr. Paleoceanography and Paleoclimatology 30, 984-999.

Odum, H.T. (1951) Notes on the strontium contain of seawater, celestite Radiolaria and strontianite snail shell. Science, 114, 211–213.

Okai, T., Suzuki, A., Kawahata, H., Terashima, S. and Imai, N. (2002) Preparation of a New Geological Survey of Japan Geochemical Reference Material: Coral JCp-1. Geostandards and Geoanalytical Research 26, 95-99.

Okumura, M. and Y. Kitano (1986) Coprecipitation of alkali metal ions with calcium carbonate. Geochimica et Cosmochimica Acta, 50(1), 49-58.

Pachauri, R.K., Allen, M.R., Barros, V.R., Broome, J., Cramer, W., Christ, R., Church, J.A., Clarke, L., Dahe, Q. and Dasgupta, P. (2014) Climate change 2014: synthesis report. Contribution of Working Groups I, II and III to the fifth assessment report of the Intergovernmental Panel on Climate Change. IPCC.

Palmer, M., Brummer, G., Cooper, M., Elderfield, H., Greaves, M., Reichart, G., Schouten, S. and Yu, J. (2010) Multi-proxy reconstruction of surface water pCO 2 in the northern Arabian Sea since 29ka. Earth and Planetary Science Letters 295, 49-57.

Pande, K., Sarin, M., Trivedi, J., Krishnaswami, S. and Sharma, K. (1994) The Indus River system (India-Pakistan): Major-ion chemistry, uranium and strontium isotopes. Chemical Geology 116, 245-259.

Parkhurst, D.L. and Appelo, C. (2013) Description of input and examples for PHREEQC version 3: a computer program for speciation, batch-reaction, one-dimensional transport, and inverse geochemical calculations. US Geological Survey.

Pawlowski, J., Holzmann, M., Berney, C., Fahrni, J., Gooday, A.J., Cedhagen, T., Habura, A. and Bowser, S.S. (2003) The evolution of early Foraminifera. Proceedings of the National Academy of Sciences 100, 11494-11498.

Por, F. D. (2012) Lessepsian migration: the influx of Red Sea biota into the Mediterranean by way of the Suez Canal (Vol. 23). Springer Science & Business Media

Prahl, F. and Wakeham, S. (1987) Calibration of unsaturation patterns in long-chain ketone compositions for palaeotemperature assessment. Nature 330, 367-369.

Prahl, F.G., Dymond, J. and Sparrow, M.A. (2000) Annual biomarker record for export production in the central Arabian Sea. Deep Sea Research Part II: Topical Studies in Oceanography 47, 1581-1604.

van Raden, U.J., Groeneveld, J., Raitzsch, M. and Kucera, M. (2011) Mg/Ca in the planktonic foraminifera *Globorotalia inflata* and *Globigerinoides bulloides* from Western Mediterranean plankton tow and core top samples. Marine Micropaleontology 78, 101-112.

Ramesh, K., Melzner, F., Griffith, A.W., Gobler, C.J., Rouger, C., Tasdemir, D. and Nehrke, G. (2018) In vivo characterization of bivalve larval shells: a confocal Raman microscopy study. Journal of The Royal Society Interface 15, 20170723.

Rasmussen, S.O., Bigler, M., Blockley, S.P., Blunier, T., Buchardt, S.L., Clausen, H.B., Cvijanovic, I., Dahl-Jensen, D., Johnsen, S.J. and Fischer, H. (2014) A stratigraphic framework for abrupt climatic changes during the Last Glacial period based on three synchronized Greenland ice-core records: refining and extending the INTIMATE event stratigraphy. Quaternary Science Reviews 106, 14-28.

Reichart, G.-J., Den Dulk, M., Visse, H.J., Van der Weijden, C.H. and Zachariasse, W.J. (1997) A 225 kyr record of dust supply, paleoproductivity and the oxygen minimum zone from the Murray Ridge (northern Arabian Sea). Palaeogeography, Palaeoclimatology, Palaeoecology 134, 149-169.

Reichart, G.-J., Jorissen, F., Anschutz, P. and Mason, P.R. (2003) Single foraminiferal test chemistry records the marine environment. Geology 31, 355-358.

Reichart, G.-J., Lourens, L. and Zachariasse, W. (1998) Temporal variability in the northern Arabian Sea Oxygen Minimum Zone (OMZ) during the last 225,000 years. Paleoceanography 13, 607-621.

Reichart, G.-J., Brinkhuis, H., Huiskamp, F. and Zachariasse, W.J. (2004) Hyperstratification following glacial overturning events in the northern Arabian Sea. Paleoceanography 19.

Reichart, G.-J., Nortier, J., Versteegh, G. and Zachariasse, W.J. (2002) Periodical breakdown of the Arabian Sea oxygen minimum zone caused by deep convective mixing. Geological Society, London, Special Publications 195, 407-419.

Reimer, P.J., Bard, E., Bayliss, A., Beck, J.W., Blackwell, P.G., Ramsey, C.B., Buck, C.E., Cheng, H., Edwards, R.L. and Friedrich, M. (2013) IntCal13 and Marine13 radiocarbon age calibration curves 0–50,000 years cal BP. Radiocarbon 55, 1869-1887.

Richter, T.O., Van der Gaast, S., Koster, B., Vaars, A., Gieles, R., de Stigter, H.C., De Haas, H. and van Weering, T.C. (2006) The Avaatech XRF Core Scanner: technical description and applications to NE Atlantic sediments. Geological Society, London, Special Publications 267, 39-50.

Ridgwell, A.J., Kennedy, M.J. and Caldeira, K. (2003) Carbonate deposition, climate stability, and Neoproterozoic ice ages. Science 302, 859-862.

Rimstidt, J.D., Balog, A. and Webb, J. (1998) Distribution of trace elements between carbonate minerals and aqueous solutions. Geochimica et Cosmochimica Acta 62, 1851-1863.

Rink, S., Kühl, M., Bijma, J. and Spero, H. J. (1998). Microsensor studies of photosynthesis and respiration in the symbiotic foraminifer *Orbulina universa*, Marine Biology, 131(4), 583-595.

Rixen, T., Goyet, C. and Ittekkot, V. (2006) Diatoms and their influence on the biologically mediated uptake of atmospheric CO 2 in the Arabian Sea upwelling system. Biogeosciences 3, 1-13.

Rixen, T., Haake, B. and Ittekkot, V. (2000) Sedimentation in the western Arabian Sea the role of coastal and open-ocean upwelling. Deep Sea Research Part II: Topical Studies in Oceanography 47, 2155-2178.

Rodriguez-Blanco, J.D., Shaw, S. and Benning, L.G. (2011) The kinetics and mechanisms of amorphous calcium carbonate (ACC) crystallization to calcite, via vaterite. Nanoscale 3, 265-271.

Rohling, E.J. (1994) Glacial conditions in the Red Sea. Paleoceanography 9, 653-660.

Rohling, E. J., and Bigg, G. R. (1998) Paleosalinity and d180: A critical assessment. J. Geophys. Res, 103, 1307-1318.

Rohling, E. J. (2007) Progress in paleosalinity: Overview and presentation of a new approach, Paleoceanography, 22, 1-9.

Rosell-Melé, A. and Prahl, F.G. (2013) Seasonality of UK' 37 temperature estimates as inferred from sediment trap data. Quaternary Science Reviews 72, 128-136.

Rostek, F., Bard, E., Beaufort, L., Sonzogni, C. and Ganssen, G. (1997) Sea surface temperature and productivity records for the past 240 kyr in the Arabian Sea. Deep Sea Research Part II: Topical Studies in Oceanography 44, 1461-1480.

Rucker, J. B., and Valentine, J. W. (1961) Salinity response of trace element concentration in *Crassostrea virginica*, Nature, 190, 1099-1100.

Russell, A. D., Hönisch, B., Spero, H. J. and Lea, D. W. (2004) Effects of seawater carbonate ion concentration and temperature on shell U, Mg, and Sr in cultured planktonic foraminifera. Geochimica et Cosmochimica Acta, 68(21), 4347-4361.

Saager, P.M., De Baar, H.J. and Burkill, P.H. (1989) Manganese and iron in Indian Ocean waters. Geochimica et Cosmochimica Acta 53, 2259-2267.

Sadekov, A. Y., Eggins, S. M., and De Deckker, P. (2005) Characterization of Mg/Ca distributions in planktonic foraminifera species by electron microprobe mapping. Geochemistry, Geophysics, Geosystems, 6.

Sadekov, A. Y., Eggins, S.M., De Deckker, P., and Kroon, D. (2008) Uncertainties in seawater thermometry deriving from intratest and intertest Mg/Ca variability in Globigerinoides ruber. Paleoceanography, 23(1).

Sarmiento, J.L. and N. Gruber (2006), Ocean Biogeochemical Dynamics, Princeton University Press.

Sangiorgi, F., Capotondi, L., Combourieu Nebout, N., Vigliotti, L., Brinkhuis, H., Giunta, S., Lotter, A.F., Morigi, C., Negri, A. and Reichart, G.J. (2003) Holocene seasonal sea-surface temperature variations in the southern Adriatic Sea inferred from a multiproxy approach. Journal of Quaternary Science 18, 723-732.

Sbaffi, L., Wezel, F.C., Kallel, N., Paterne, M., Cacho, I., Ziveri, P. and Shackleton, N. (2001) Response of the pelagic environment to palaeoclimatic changes in the central Mediterranean Sea during the Late Quaternary. Marine Geology 178, 39-62.

Schenau, S., Reichart, G.-J. and De Lange, G. (2002) Oxygen minimum zone controlled Mn redistribution in Arabian Sea sediments during the late Quaternary. Paleoceanography and Paleoclimatology 17.

Schiebel, R., and Hemleben, C. (2017) Planktic foraminifers in the modern ocean. Springer.

Schlitzer, R. (2007) Ocean data view. http://odv. awi. de.

Schouten, S., Hopmans, E. C., Schefuß, E., and Sinninghe Damste, J. S. (2002) Distributional variations in marine crenarchaeotal membrane lipids: a new tool for reconstructing ancient sea water temperatures?. Earth and Planetary Science Letters, 204, 265-274.

Schouten, S., Ossebaar, J., Schreiber, K., Kienhuis, M., Langer, G., Benthien, A. and Bijma, J. (2006) The effect of temperature, salinity and growth rate on the stable hydrogen isotopic composition of long chain alkenones produced by *Emiliania huxleyi* and *Gephyrocapsa oceanica*. Biogeosciences 3, 113-119.

Schulte, S., Rostek, F., Bard, E., Rullkötter, J. and Marchal, O. (1999) Variations of oxygen-minimum and primary productivity recorded in sediments of the Arabian Sea. Earth and Planetary Science Letters 173, 205-221.

Schulz, H., von Rad, U. and Erlenkeuser, H. (1998) Correlation between Arabian Sea and Greenland climate oscillations of the past 110,000 years. Nature 393, 54.

Schulz, H., von Rad, U. and Ittekkot, V. (2002) Planktic foraminifera, particle flux and oceanic productivity off Pakistan, NE Arabian Sea: modern analogues and application to the palaeoclimatic record. Geological Society, London, Special Publications 195, 499-516.

Schulz, H., Von Rad, U. and Von Stackelberg, U. (1996) Laminated sediments from the oxygen-minimum zone of the Northeast Arabian Sea. Geological Society, London, Special Publications 116, 185-207.

Van Sebille, E., Scussolini, P., Durgadoo, J.V., Peeters, F.J., Biastoch, A., Weijer, W., Turney, C., Paris, C.B. and Zahn, R. (2015) Ocean currents generate large footprints in marine palaeoclimate proxies. Nature communications 6, 6521.

Segev, E. and Erez, J. (2006) Effect of Mg/Ca ratio in seawater on shell composition in shallow benthic foraminifera. Geochemistry Geophysics Geosystems 7, 1-8.

Shackleton, N. (1974) Attainment of isotopic equilibrium between ocean water and the benthonic foraminifera genus *Uvigerina*: isotopic changes in the ocean during the last glacial.

Shackleton, N. (1987) Oxygen isotopes, ice volume and sea level. Quaternary Science Reviews 6, 183-190.

Siccha, M., Trommer, G., Schulz, H., Hemleben, C., and Kucera, M. (2009): Factors controlling the distribution of planktonic foraminifera in the Red Sea and implications for the development of transfer functions, Marine Micropaleontology, 72, 146-156.

Sinninghe Damsté, J.S.S., Rijpstra, W.I.C. and Reichart, G.-j. (2002) The influence of oxic degradation on the sedimentary biomarker record II. Evidence from Arabian Sea sediments. Geochimica et Cosmochimica Acta 66, 2737-2754.

Sofianos, S. S., W. E. Johns and S. P. Murray (2002), Heat and freshwater budgets in the Red Sea from direct observations at Bab el Mandeb, Deep-Sea Research, 2(49), 1323-1340.

Spero, H. (1988) Ultrastructural examination of chamber morphogenesis and biomineralization in the planktonic foraminifer *Orbulina universa*. Marine Biology 99, 9-20.

Spero, H. J., Eggins, S. M., Russell, A. D., Vetter, L., Kilburn, M. R., and Hönisch, B. (2015) Timing and mechanism for intratest Mg/Ca variability in a living planktic foraminifer. Earth and Planetary Science Letters, 409, 32-42.

Spezzaferri, S., Kucera, M., Pearson, P.N., Wade, B.S., Rappo, S., Poole, C.R., Morard, R. and Stalder, C. (2015) Fossil and Genetic Evidence for the Polyphyletic Nature of the Planktonic Foraminifera" *Globigerinoides*", and Description of the New Genus Trilobatus. PLoS One 10.

Stack, A.G. and Grantham, M.C. (2010) Growth rate of calcite steps as a function of aqueous calcium-to-carbonate ratio: independent attachment and detachment of calcium and carbonate ions. Crystal Growth & Design 10, 1409-1413.

Steinhardt, J., Cléroux, C., Ullgren, J., de Nooijer, L., Durgadoo, J.V., Brummer, G.-J. and Reichart, G.-J. (2014) Anti-cyclonic eddy imprint on calcite geochemistry of several planktonic foraminiferal species in the Mozambique Channel. Marine Micropaleontology 113, 20-33.

Steinhardt, J., de Nooijer, L. J., Brummer, G. J., and Reichart, G. J. (2015) Profiling planktonic foraminiferal crust formation. Geochemistry, Geophysics, Geosystems, 16, 2409-2430.

Steinke, S., Chiu, H. Y., Yu, P. S., Shen, C. C., Löwemark, L., Mii, H. S., and Chen, M. T. (2005) Mg/Ca ratios of two *Globigerinoides ruber* (white) morphotypes: Implications for reconstructing past tropical/subtropical surface water conditions. Geochemistry, Geophysics, Geosystems, 6.

Stuiver, M., Reimer, P. and Reimer, R. (2017) CALIB 7.1 [WWW program].

Swallow, J. (1984) Some aspects of the physical oceanography of the Indian Ocean. Deep Sea Research Part A. Oceanographic Research Papers 31, 639-650.

Takahashi, K. and Be, A.W.H. (1984) Planktonic foraminifera: factors controlling sinking speeds. Deep Sea Research Part A. Oceanographic Research Papers 31, 1477-1500.

Tang, J., Dietzel, M., Böhm, F., Köhler, S.J. and Eisenhauer, A. (2008) Sr2+/Ca2+ and 44Ca/40Ca fractionation during inorganic calcite formation: II. Ca isotopes. Geochimica et Cosmochimica Acta 72, 3733-3745.

Thompson, P. R., Bé, A.W., Duplessy, J. C. and Shackleton, N. J. (1979) Disappearance of pink-pigmented *Globigerinoides ruber* at 120,000 yr BP in the Indian and Pacific Oceans. Nature, 280, 554-558.

Toyofuku, T., Matsuo, M.Y., De Nooijer, L.J., Nagai, Y., Kawada, S., Fujita, K., Reichart, G.-J., Nomaki, H., Tsuchiya, M. and Sakaguchi, H. (2017) Proton pumping accompanies calcification in foraminifera. Nature Communications 8, 14145.

Uchikawa, J., Penman, D.E., Zachos, J.C. and Zeebe, R.E. (2015) Experimental evidence for kinetic effects on B/Ca in synthetic calcite: implications for potential B (OH) 4– and B (OH) 3 incorporation. Geochimica et Cosmochimica Acta 150, 171-191.

Urey, H.C., Lowenstam, H.A., Epstein, S. and McKinney, C.R. (1951) Measurement of paleotemperatures and temperatures of the Upper Cretaceous of England, Denmark, and the southeastern United States. Geological Society of America Bulletin 62, 399-416.

Vasiliev, I., Mezger, E. M., Lugli, S., Reichart, G.-J., Manzi, V., and Roveri, M. (2017) How dry was the Mediterranean during the Messinian salinity crisis?. Palaeogeography, Palaeoclimatology, Palaeoecology, 471, 120-133.

Verleye, T. J., Mertens, K. N., Young, M. D., Dale, B., McMinn, A., Scott, L., Zonneveld, K. A., and Louwye, S. (2012): Average process length variation of the marine dinoflagellate cyst Operculodinium centrocarpum in the tropical and Southern Hemisphere Oceans: assessing its potential as a palaeosalinity proxy, Marine Micropaleontology, 86, 45-58.

De Villiers, S., Greaves, M., and Elderfield, H. (2002) An intensity ratio calibration method for the accurate determination of Mg/Ca and Sr/Ca of marine carbonates by ICP-AES. Geochemistry, Geophysics, Geosystems, 3(1).

Von Rad, U., Schaaf, M., Michels, K.H., Schulz, H., Berger, W.H. and Sirocko, F. (1999) A 5000-yr record of climate change in varved sediments from the oxygen minimum zone off Pakistan, Northeast Arabian Sea. Quaternary research 51, 39-53.

Wakeham, S.G., Peterson, M.L., Hedges, J.I. and Lee, C. (2002) Lipid biomarker fluxes in the Arabian Sea, with a comparison to the equatorial Pacific Ocean. Deep Sea Research Part II: Topical Studies in Oceanography 49, 2265-2301.

Wang, L. (2000) Isotopic signals in two morphotypes of *Globigerinoides ruber* (white) from the South China Sea: implications for monsoon climate change during the last glacial cycle. Palaeogeography, Palaeoclimatology, Palaeoecology, 161(3).

Watkins, J.M., Hunt, J.D., Ryerson, F.J. and DePaolo, D.J. (2014) The influence of temperature, pH, and growth rate on the δ 18 O composition of inorganically precipitated calcite. Earth and Planetary Science Letters 404, 332-343.

Watkins, J.M., Nielsen, L.C., Ryerson, F.J. and DePaolo, D.J. (2013) The influence of kinetics on the oxygen isotope composition of calcium carbonate. Earth and planetary science letters 375, 349-360.

Webster, P.J., Magana, V.O., Palmer, T., Shukla, J., Tomas, R., Yanai, M. and Yasunari, T. (1998) Monsoons: Processes, predictability, and the prospects for prediction. Journal of Geophysical Research: Oceans 103, 14451-14510.

Weldeab, S., Lea, D.W., Schneider, R.R., Andersen, N. (2007) 155,000 Years of West African Monsoon and Ocean Thermal Evolution. Science 316, 1303-1307.

Weltje, G.J. and Tjallingii, R. (2008) Calibration of XRF core scanners for quantitative geochemical logging of sediment cores: theory and application. Earth and Planetary Science Letters 274, 423-438.

White, A.F. (1978) Sodium coprecipitation in calcite and dolomite. Chemical Geology 23, 65-72.

Wilson, S., Koenig, A. and Orklid, R. (2008) Development of microanalytical reference material (MACS-3) for LA-ICP-MS analysis of carbonate samples. Geochimica et Cosmochimica Acta Supplement 72, A1025.

Wit, J.C., De Nooijer, L., Wolthers, M. and Reichart, G.-J. (2013) A novel salinity proxy based on Na incorporation into foraminiferal calcite. Biogeosciences 10, 6375–6387.

Wit, J.C., Reichart, G.J., Jung, J.A., Kroon, A. (2010) Approaches to unravel seasonality in sea surface temperatures using paired single-specimen foraminiferal d18O and Mg/Ca analyses. Paleoceanography 25, 1-15.

Wolthers, M., Nehrke, G., Gustafsson, J.P. and Van Cappellen, P. (2012) Calcite growth kinetics: Modeling the effect of solution stoichiometry. Geochimica et Cosmochimica Acta 77, 121-134.

Wyrtki, K. (1973) Physical oceanography of the Indian Ocean. In'The Biology of the Indian Ocean'. (Eds B. Zeitzschel and SA Gerlach.) pp. 18-36. Springer-Verlag: Berlin.

Wyrtki, K., Bennett, E.B. and Rochford, D.J. (1971) Oceanographic atlas of the international Indian Ocean expedition.

Yoshimura, T., Tamenori, Y., Suzuki, A., Kawahata, H., Iwasaki, N., Hasegawa, H., Nguyen, L.T., Kuroyanagi, A., Yamazaki, T. and Kuroda, J. (2017) Altervalent substitution of sodium for calcium in biogenic calcite and aragonite. Geochimica et Cosmochimica Acta 202, 21-38.

Yu, J., Elderfield, H. and Hönisch, B. (2007) B/Ca in planktonic foraminifera as a proxy for surface seawater pH. Paleoceanography 22.

Zachos, J., Pagani, M., Sloan, L., Thomas, E., and Billups, K. (2001) Trends, rhythms, and aberrations in global climate 65 Ma to present. Science, 292, 686-693.

Zahn, R. and Mix, A.C. (1991) Benthic foraminiferal δ18O in the ocean's temperature-salinity-density field: Constraints on Ice Age thermohaline circulation. Paleoceanography 6, 1-20

Zahran, M. A. (2010) Climate-Vegetation: Afro-Asian Mediterranean and Red Sea Coastal Lands (Vol. 4). Springer Science & Business Media.

Zhao, L., Schöne, B. R., Mertz-Kraus, R., and Yang, F. (2017) Insights from sodium into the impacts of elevated pCO 2 and temperature on bivalve shell formation. Journal of Experimental Marine Biology and Ecology, 486, 148-154.

Ziegler, M., Jilbert, T., de Lange, G.J., Lourens, L.J. and Reichart, G.J. (2008) Bromine counts from XRF scanning as an estimate of the marine organic carbon content of sediment cores. Geochemistry, Geophysics, Geosystems 9.

Ziegler, M., Lourens, L.J., Tuenter, E., Hilgen, F., Reichart, G.J. and Weber, N. (2010) Precession phasing offset between Indian summer monsoon and Arabian Sea productivity linked to changes in Atlantic overturning circulation. Paleoceanography 25.

Addendum

Concluding remarks

Nederlandse samenvatting

Dankwoord

Curriculum Vitae

Bibliography

Concluding remarks

This thesis focuses on understanding of foraminiferal shell Na/Ca and the development of this ratio as a paleoceanographic proxy. In particular, I aimed to assess the possibility of using the incorporation of Na in the calcite of foraminiferal shells to reconstruct past changes in seawater salinity. Salinity is considered one of the most important, but challenging parameters to reconstruct in paleoceanography. Changes in salinity reflect the hydrological cycle (e.g. the balance between precipitation and evaporation) and on longer timescales the waxing and waning of continental ice sheets, sea ice formation and regional and global circulation of water masses. Together with temperature, salinity controls the density of seawater, driving large scale ocean circulation (the thermohaline circulation). Therefore, reconstructing past changes in salinity is essential in understanding past climate and the role ocean circulation played therein.

From all ions dissolved in seawater, sodium and chlorine are most abundant. Despite their abundance, the concentrations in which they are incorporated into foraminiferal shell calcite and the mechanisms involved are largely unexplored. Existing calibrations for Na incorporation on foraminiferal shells focused on benthic species (Wit et al., 2013), which are here complemented by those for planktonic foraminifera (Chapter 2), as these are more often used in paleoceanographic reconstructions. Furthermore, I studied the inter- and intra-specimen and species variability (Chapters 3 and 4); the influence of other physical and chemical factors on Na incorporation (Chapter 6) and tested the validity of this novel proxy by applying it to a record covering the last ~80 kyrs (Chapter 5).

For the first field calibration of planktonic foraminiferal Na/Ca to salinity, *Globigerinoides ruber* and *Trilobatus sacculifer* specimens are collected from the surface water of the Red Sea. It is found that *G. ruber* and *T. sacculifer* shell Na/Ca values, measured with laser ablation (LA)-Q-ICP-MS, co-vary with changes in salinity, albeit with a low sensitivity and a high inter- and intra-shell variability (Chapter 2). Whereas in this study as well as other culturing studies (Allen et al., 2016; Wit et al., 2013), foraminiferal shell Na partitioning ($D_{Na}=([Na]/[Ca])_{calcite}/([Na]/[Ca])_{solution}$) increases with increasing salinities, D_{Na} for inorganically precipitated calcites is lower and does not show such an effect (Chapter 6). Therefore, foraminifera are suggested to exert a strong biological control on Na incorporation in response to salinity. This implies that large inter specific differences could exist in Na incorporation.

For validation of this Na-salinity proxy, the effect of transport through the water column upon settling at the sediment surface is quantified. Shell Na/Ca values are sensitive to preservation, as the presence or absence of spines are found to significantly affect the average shell Na composition (Chapters 3 and 4). This is relevant for the paleo-application of this newly developed proxy, as a better preservation of spines might also result in higher Na/Ca values independent of salinity variations (Chapter 5). Whereas the LA-Q-ICP-MS measured average shell Na/Ca values decrease with increasing water depth, probably related to spine loss (Chapter 3), shell-only Na/Ca values (excluding spine and spine base regions) measured with Electron Probe microanalyses (EPMA) seem relatively robust (Chapter 4). Comparing both shell and spine Na/Ca values with salinity shows that shell chemistry records salinity, albeit with a low sensitivity (Chapter 4). Such a low slope and intra-shell inhomogeneity would require novel analytical approaches for the robust application of this proxy.

In addition to salinity and preservation, also growth rate, influenced by saturation state (Ω) as well as $[Na^+]/[Ca^{2+}]$ of the growth solution, might affect calcite Na/Ca substantially (Chapter 6). Based on inorganic precipitation experiments, it is found that growth rate positively affects Na incorporation. Growth rate might particularly affect the shell elemental composition on timescales longer than 1 Ma, as Ca -influencing growth rate- is no longer considered a conservative element on these time scales. For proxy applications, foraminiferal culturing studies should be performed to test the effect of growth rate on Na incorporation and whether salinity influences growth rate.

To conclude, these field studies and experiments aimed at increasing our understanding of foraminiferal shell Na/Ca and the potential of this ratio as a proxy for salinity. Although all these studies showed additional constraints on the application of Na/Ca as a salinity proxy, the shell-only Na/Ca signal is robust and can be used to reconstruct (large) changes in salinity. Furthermore, results in this thesis show that the foraminiferal Na/Ca and variability therein can only be understood by acknowledging that calcification and element partitioning is a biological process. In particular, comparison of inorganic studies with foraminiferal geochemistry can show the extent of this biological (versus purely chemical) signal in Na/Ca. This thesis highlights the potential role of precipitation in this respect and, likely related to that, differences within the foraminiferal shell (i.e. spines). It is unlikely that only Na incorporation is affected by these processes and therefore, simultaneous analysis of several elements may further constrain our understanding of growth rates, salinity and foraminiferal intra-shell morphology.

Nederlandse samenvatting

De aarde is voor 71% bedekt met water, waarvan de oceaan 96.5% van al het water op aarde bevat. Deze oceaan speelt een belangrijke rol in veel fysische, chemische en biologische processen op aarde en met name in het klimaatsysteem vanwege de bufferende werking in de koolstof cyclus en als transport route voor warmte. Vanaf het begin van de industriële revolutie heeft het verbranden van fossiele brandstoffen voor grootschalige koolstofdioxide (CO_2) uitstoot gezorgd. Koolstofdioxide is een belangrijk broeikasgas en haar toegenomen concentratie in de atmosfeer leidt tot opwarming van de aarde en daarmee het smelten van de ijskappen met uiteindelijk zeespiegelstijging tot gevolg. Verder zorgt de opname van CO_2 in de oceaan, die daarin een grote rol speelt (30% van de CO_2 die uitgestoten is sinds de industriële revolutie is inmiddels opgenomen door de oceaan), voor zogenaamde oceaanverzuring, die grote consequenties heeft voor het leven in de zee. Oceaanonderzoek is daarom van belang om de toekomst van onze planeet ten tijde van deze klimaatveranderingen beter te kunnen begrijpen en voorspellen.

Onderzoek naar het klimaat in het verleden (paleoklimatologie) en de oceaan in het verleden (paleoceanografie) geeft waardevolle informatie over het functioneren van ons klimaatsysteem en de rol van oceanen hierin. Door te kijken naar veranderingen die in het verleden hebben plaatsgevonden, kunnen we begrijpen hoe de verschillende processen met elkaar samenhangen, alsmede veranderingen in de toekomst beter voorspellen. Omdat het niet mogelijk is om op geologische en ook kortere pre-instrumentale tijdschalen verschillende klimaatfactoren, zoals temperatuur, zeeniveau, ijsvolume of zoutgehalte van de zee, direct te meten, gebruiken we zogenaamde proxies. Een proxie is een meetbare grootheid, zoals de chemische samenstelling van sedimenten of foraminiferen, die gebruikt kan worden om te benaderen omgevingsfactoren uit het verleden te reconstrueren. Vaak worden hiervoor kalkschaaltjes van foraminiferen gebruikt: ééncellige mariene organismes, die schaaltjes maken van kalk, sedimentdeeltjes of organisch materiaal (polysacchariden). Voor de eerste groep geldt dat de chemische samenstelling van deze kalkschaaltjes covarieert vaak met de leefomgeving waarin deze is gevormd. Deze kalkschaaltjes zijn gevonden tot ~500 miljoen jaar geleden, waardoor ze dan ook als een waardevol klimaatarchief worden beschouwd.

Voor de toepassing in paleoceanografisch en -klimatologisch onderzoek zijn verschillende proxies ontwikkeld, gebaseerd op de (spoor-)element of isotoop samenstelling van de schaaltjes van foraminiferen. Tijdens de vorming van een foraminiferen schaaltje,

bestaande uit verschillende kamers die periodiek worden gebouwd, komen allerlei elementen vanuit het zeewater in dat kalk terecht. Zodoende reflecteert de chemische samenstelling van het schaaltje van een foraminifeer de concentraties van deze elementen in het zeewater, maar ook de fysische en chemische omstandigheden tijdens kalkvorming. Zo is gebleken dat bijvoorbeeld de hoeveelheid magnesium (Mg) die wordt ingebouwd toeneemt met temperatuur. De hoeveelheid mangaan in het kalk (doorgaans uitgedrukt als mangaan/calcium) om het zuurstofgehalte van de zeebodem of de waterkolom te reconstrueren; zwavel/Ca en strontium/Ca als proxies voor zeewater carbonaat chemie, en de zuurstof isotoop samenstelling ($\delta^{18}O$) van kalkschaaltjes van foraminiferen voor reconstructies van temperatuur, continentaal ijsvolume en het zoutgehalte van de zee.

De inbouw van natrium in de kalkschaaltjes van foraminiferen en het effect van omgevingsinvloeden

Het zoutgehalte van de zee (saliniteit) wordt beschouwd als een van de belangrijkste, maar ook meest uitdagende factoren om te reconstrueren in de paleoceanografie. Veranderingen in saliniteit komen vooral door verschuivingen in de hydrologische cyclus (bijvoorbeeld de balans tussen neerslag en verdamping), maar op langere tijdschalen ook door het smelten of aangroeien van land- en zee-ijs en de regionale en mondiale circulatie van watermassa's. Samen met temperatuur bepaalt het zoutgehalte de dichtheid van zeewater, die de oceaancirculatie bepaalt en daarmee ook de verspreiding van warmte en zuurstof op aarde. Van alle ionen die opgelost zijn in zeewater, komen natrium (Na) en chloride het meest voor. Dit proefschrift richt zich op de kalibrering, validatie en toepassing van Na/Ca gemeten in kalkschaaltjes van foraminiferen als een mogelijke proxie voor saliniteit. Bestaande kalibraties voor benthische soorten (op/in het sediment levende foraminiferen) worden uitgebreid naar planktonische soorten, aangezien deze meestal worden gebruikt voor paleoceanografisch onderzoek om oppervlaktewater mileufactoren te reconstrueren.

Kalibrering

In hoofdstuk 2 wordt de eerste veld-kalibratie van Na/Ca gemeten in kalkschaaltjes van planktonische foraminiferen gepresenteerd. De inbouw van natrium in de schaaltjes van benthische en planktonische soorten uit laboratium kweek-studies bleek al een veelbelovende onafhankelijke proxie voor saliniteit, maar een kalibratie gebaseerd op de natuurlijke omgeving ontbrak nog. De Rode Zee is hiervoor een geschikte locatie, aangezien deze gekenmerkt wordt door een grote saliniteitsgradiënt tussen ~36 en 40 (gram opgelost zout per liter). Levende individuen van twee planktonische soorten, *Trilobatus sacculifer* en *Globigerinoides ruber*, zijn verzameld uit het oppervlaktewater van

de Rode Zee, en de chemische samenstelling is gemeten met laser ablatie ICP-MS. Laser ablatie ICP-MS is een techniek die metingen kan uitvoeren op zeer weinig materiaal, en daardoor dus ook goed de variatie in chemische samenstelling binnen één kalkschaaltje kan laten zien. Zowel *T. sacculifer* als *G. ruber* laten een toename zien in Na/Ca waardes met toenemend zoutgehalte van de Rode Zee, hoewel met grote inter- en intra-individuele variaties. Absolute Na/Ca waardes en ook de helling van de kalibraties zijn gelijk voor beide soorten, al wijkt *T. sacculifer* af in het noordelijkste traject. Mogelijk komen de individuen in het uiterste noorden (gedeeltelijk) uit een ander gebied (de Middellandse Zee), met andere temperaturen en zoutgehaltes, en moeten ze daarom buiten beschouwing worden gelaten voor deze kalibratie. Vergeleken met de eerdergenoemde Na/Ca-saliniteits kalibraties van planktonische en benthische soorten gekweekt in het laboratium in andere studies, wijken de gemeten waardes van deze studie af door een hogere gevoeligheid voor veranderingen in saliniteit en ook hogere absolute Na/Ca waardes. Dit kan komen door: 1) verschillen in biomineralisatie tussen soorten; 2) additionele effecten van andere covariërende omgevingsfactoren in de Rode Zee, zoals temperatuur, en 3) de aan- of afwezigheid van stekels (zie hoofdstuk 3). Het effect van de tegengestelde saliniteits- en temperatuurgradiënt in de Rode Zee (optie 2) is ook zichtbaar in de gemeten Mg/Ca waardes van dezelfde individuen, die geen reactie laten zien op toenemende temperatuur door het dempende effect van saliniteit op Mg inbouw.

Validatie

Toepassing van deze Na/Ca-gebaseerde saliniteits proxie vereist ook onderzoek naar het potentiële effect van neerwaards transport door de waterkolom tot aan begraving op de zeebodem op de concentratie Na in het kalk. Voor paleoceanografische en -klimatologische reconstructies worden immers niet levende individuen gebruikt, maar schaaltjes uit lagen sediment afgezet door de tijd op de zeebodem. In hoofdstuk 3 worden Na/Ca waardes van individuen van dezelfde soorten als in hoofdstuk 2 uit de waterkolom van de Rode Zee tussen 0 en 500 meter diepte vergeleken met waardes van individuen verzameld op de zeebodem, vooral kijkend naar chemische veranderingen tijdens de levenscycli van deze soorten (ontogenie) en na het overlijden (taphonomie). De veranderingen tussen de verschillende dieptes en van het oppervlaktewater naar de zeebodem tonen aan dat Na/Ca waardes van de kalkschaaltjes voor beide soorten afnemen met toenemende diepte totdat de oppervlakte van de zeebodem wordt bereikt. Deze afname in Na/Ca waardes wordt waarschijnlijk veroorzaakt door het verlies van stekels, die relatief hoge Na/Ca hebben, tijdens het levenscyclus voorafgaand aan- of tijdens reproductie (gametogenese) terwijl de kalkschaaltjes zinken door de waterkolom. Daarnaast nemen Mg/Ca waardes,

gemeten aan dezelfde individuen, toe met diepte. Dit is waarschijnlijk gerelateerd aan de afzetting van een laag gametogenetisch (GAM) kalk over de kalkschaaltjes, hoog in Mg/Ca maar min of meer gelijk in Na/Ca aan de rest van het schaaltje. Dit hoofdstuk toont aan dat zowel het verlies van stekels als de afzetting van GAM kalk tijdens verschillende levensfases een aanzienlijk effect hebben op gemiddelde (spoor) element samenstellingen in kalkschaaltjes van foraminiferen.

In hoofdstuk 4 wordt de verdeling van Na binnen een kalkschaaltje gekwantificeerd, gericht op de relatieve bijdrages van het schaaltje zelf (zonder stekels), stekels buiten het kalkschaaltje, de basis van stekels in het kalkschaaltje die soms achterblijft na reproductie en de organische laagjes op het totale gemeten Na/Ca signaal. Voordat een nieuwe kamer wordt toegevoegd aan een kalkschaaltje, vormt het organisme een organisch laagje buiten zijn protoplasma, die zorgt voor een semi-afgesloten ruimte: de plaats van kalkvorming. Vanaf deze organische laag vindt neerslag van kalk aan beide kanten plaats. De chemische samenstelling op deze plaats van kalkvorming is nog vrijwel onbekend, maar wordt waarschijnlijk grotendeels beïnvloed door selectief transport van ionen en mogelijk ook door transport van (aangepast) zeewater naar deze locatie. Tijdens de vorming van elke nieuwe kamer, vormt zich ook een dun laagje kalk over de oude kamers wat ook zorgt voor gelaagdheid in elementen-inbouw. Eerdere studies toonden al aan (onder andere hoofdstuk 3) dat Na/Ca concentraties in kalkschaaltjes kunnen variëren, bijvoorbeeld in laagjes en door verschillen tussen stekel-regio's en het schaaltje zelf. In deze studie worden de technieken 'Electron Probe Microanalysis (EPMA)' toegepast om deze variaties te kunnen kwantificeren en de gevoeligheid van Na/Ca ingebouwd in verschillende onderdelen van kalkschaaltjes voor veranderende zoutgehaltes te kunnen meten. Hieruit is gebleken dat regio's met hoge Na/Ca waardes, zoals stekels en de basis van stekels, gevoelig kunnen zijn voor veranderingen in samenstelling door taphonomie, terwijl de Na/Ca samenstelling van de schaaltjes zelf erg robuust blijkt. Het effect van Na/Ca in organische lagen is minimaal op de totale gemeten Na/Ca waardes. Van alle onderdelen van de kalkschaaltjes blijkt dat alleen de chemische samenstelling van de schaaltjes zelf (dus zonder de stekels) het saliniteits-signaal weergeeft, zij het met een relatief lage gevoeligheid.

In hoofdstuk 6 worden resultaten beschreven van experimenten, waarin we niet-biologisch kalk hebben neergeslagen onder gecontroleerde omstandigheden in het laboratorium. In dit hoofdstuk testen we het proxie potentieel van Na/Ca in calciet, en proberen we de variatie binnen kalkschaaltjes uit te leggen door middel van de relaties gevonden voor inorganisch neergeslagen kalk. De effecten van saliniteit, de verzadigingsgraad (Ω), de

verhouding tussen Ca en carbonaat ($[Ca^{2+}]/[CO_3^{2-}]$ stoichiometrie) en $[Na^+]/[Ca^{2+}]$ van de groeioplossing zijn onafhankelijk getest in twee verschillende opstellingen. De partitie van Na, beschreven als de hoeveelheid Na ingebouwd in kalk gedeeld door de hoeveelheid Na in de groeioplossing, is lager bij inorganisch kalk dan bij foraminiferen en bleef, in tegenstelling tot wat gevonden is bij foraminiferen, constant over een breed spectrum van saliniteiten van de groeioplossing. Dit geeft aan dat foraminiferen een extra biologische mechanisme hebben tijdens kalkvorming, dat reageert op veranderingen in saliniteit. Verder is er ontdekt dat de groeisnelheid van kalk, in deze experimenten aangepast door veranderingen in Ω en $[Na^+]/[Ca^{2+}]$, een positieve invloed heeft op natrium inbouw. Al deze bevindingen hebben we gecombineerd in een generiek model, dat als basis voor evaluaties van Na/Ca variaties in biogeen kalk kan worden gebruikt. Implicaties voor het gebruik van Na/Ca gemeten in foraminiferen als potentiële proxie voor saliniteit zijn dat het effect van groeisnelheid op Na niet genegeerd kan worden, die afhangt van $[Ca^{2+}]$ van het zeewater. Dit is ook relevant voor de recent gesuggereerde paleo-toepassing van Na/Ca om variaties in de Ca concentratie van zeewater te reconstrueren op tijdschalen langer dan 1 miljoen jaar geleden, aangezien veranderingen in $[Ca^{2+}]$ in zeewater mogelijk ook invloed hebben op groeisnelheid.

Toepassing

De eerste toepassing van de Na/Ca-saliniteitsproxie wordt beschreven in hoofdstuk 5. Verschillende traditionele en nieuwere proxies worden uitgetest en vergeleken op een sedimentkern uit het noordoosten van de Arabische Zee, waarvan de sedimenten zijn afgezet tussen ~80 duizend jaar geleden en nu. De chemische samenstelling van het sediment, stabiele isotopen en (spoor) elementen gemeten aan kalkschaaltjes van foraminiferen en organisch geochemische proxies, zijn gecombineerd om oppervlaktewater temperatuursveranderingen, saliniteiten en de intensiteit van de zuurstof minimum zone (ZMZ) te reconstrueren. Al deze milieufactoren zijn gerelateerd aan veranderingen in de relatieve intensiteit van de zomer- en wintermoessons in dit gebied. Om saliniteit te reconstrueren zijn drie verschillende methodes getest, allen gemeten aan kalkschaaltjes van *G. ruber*: 1) de Na/Ca-saliniteitsproxy; 2) de ratio tussen barium (Ba) en Ca als een proxie voor zoetwater aanvoer van rivieren, en; 3) de zuurstof isotoopsamenstelling ($\delta^{18}O$), gecorrigeerd voor oppervlaktewater temperatuur en ijsvolume. Hoewel Na/Ca waardes wel het verwachte patroon volgen, blijken deze ook erg beïnvoed te zijn door de aan- of afwezigheid van stekels. Verder wordt de toepassing van *G. ruber* Ba/Ca gelimiteerd door de toevoer van Ba door rivieren in kustgebieden, waardoor deze proxie niet van toepassing is voor de offshore locatie van deze kern. Daarom blijft de beste methode om saliniteit te

reconstrueren in deze kern toch de combinatie tussen $\delta^{18}O$ en een onafhankelijke methode om deze proxie te corrigeren voor temperatuursveranderingen. Gereconstrueerde oppervlaktewater temperaturen zijn sterk afhankelijk van de gebruikte methode: Mg/Ca gemeten aan foraminiferen geven een jaarlijks gemiddelde temperatuur weer, terwijl de moleculaire 'index van onverzadiging' van alkenonen ($U^{k'}_{37}$) meer seizonale temperaturen weergeeft door een verschuiving in productiviteit van de organismes die deze moleculen maken. Het signaal van de gesuggereerde proxie voor het zuurstofgehalte in de waterkolom, Mn/Ca in planktonische foraminiferen, correleert goed met de intensiteit van de ZMZ en is hoger tijdens warme periodes.

Dankwoord

Gert-Jan, allereerst wil ik jou bedanken. Het is het einde van een tijdperk en een 'kibbelend huwelijk', en ik zal je dan ook erg gaan missen op persoonlijk vlak en op de werkvloer. We hebben veel samen meegemaakt, vanaf mijn Aardwetenschappen bachelor tot nu. We hebben de hele wereld samen overgereisd voor veldwerken naar Spanje en Italië, maar ook voor congressen in Frankrijk (Angers, Parijs), Oostenrijk (Wenen) en Amerika (San Francisco), naar verschillende instituten in Duitsland, op Pelagia cruises op de Zwarte Zee en Middellandse Zee en de Urbino summerschool in Italië. Heel erg bedankt voor de vele kansen en mogelijkheden die je me geboden hebt, ik waardeer alles wat je voor me gedaan hebt en onze samenwerking enorm. Hopelijk komen we elkaar dan ook weer tegen in de toekomst.

Lennart, bedankt voor je fijne begeleiding, creatieve ideeën en je eindeloze geduld met het doorlezen van manuscripten en de discussies over de verschillende onderwerpen. Je hebt me erg veel geleerd over de wondere wereld van foraminiferen en jouw unieke invalshoek motiveerde me anders naar dingen te kijken. Het was een eer om met je te mogen werken.

Members of the dissertation committee, thank you for taking the time to read and evaluate this thesis.

Ook wil ik graag iedereen bedanken met wie ik samengewerkt heb. Bedankt aan alle co-auteurs die al eerder in dit proefschrift vermeld staan, voor jullie inzet, hulp en inzichten die de hoofdstukken erg verbeterd hebben. Met name dank aan Geert-Jan voor het delen van je kennis en vele prettige discussies over foraminiferen. Laurent, merci pour notre coopération et bonne chance avec la poursuite de nos expériences scientifiques.

Bedankt aan Wim, Patrick, Bas, Bob, Sharyn, Karel, Piet, Rineke (allen NIOZ), Serguei, Tilly, Leonard en Beatriz (Universiteit Utrecht): zonder jullie had ik geen data om mee te werken. Bedankt voor het meedenken en het onmogelijke soms mogelijk maken. Ook bedankt voor alle crew van de Pelagia en andere cruises die genoemd staan in deze thesis, dankzij jullie heb ik geweldige data kunnen gebruiken.

Bedankt aan al mijn fijne collega's van het NIOZ en de personeelsvereniging, die ik helaas niet allemaal persoonlijk kan benoemen. Met name mijn Ocean Systems afdeling (OCS), heden en verleden, heeft mijn tijd bijzonder prettig en gezellig gemaakt. Mijn lieve kantoorgenoot Ulrike, bedankt voor de fijne gesprekken, etentjes bij jou en David en goede

afleiding. My OCS co-PhD's Esmee, Siham, Linda, Sofia, Stanley, Mathijs, Kristin, Alice, Indah, Coral and Sabine: thank you for the great time and support, you can do it! Ook natuurlijk mega bedankt voor alle steun, gesprekken en hulp aan Henko, Jan-Berend, Femke, Sabine, Rick, Laura, Michèlle, Sven, Hans, Rob, Loes en de rest van de afdeling. Tijdens de Zwarte Zee cruise aan het begin van mijn promotie heb ik veel fijne mensen leren kennen (Nikki, Fatimah, Matthias, Tom, Peter, Sander, Lorendz en Jan-Dirk), bedankt daarvoor.

Toen ik net naar Texel verhuisde, zag ik erg op tegen het leven op een eiland. Mede dankzij de nieuwe vriendschappen viel dat echter reuze mee! Siem en Rineke, bedankt voor de kopjes thee, de altijd open deur en jullie geweldige hulp met verhuizingen. Surfmeisjes van boven de Spar, Selma, Pasquale, Anouk en Carola, bedankt voor de gezellige tijd en dat jullie mijn ogen openden voor het mooie wat Texel te bieden heeft. Suzanne, ook al leerden we elkaar pas later kennen, daar ben ik reuze blij mee! Hans V., Marcel, Bas en Annelous, bedankt voor de gezellige avonden, wandelingen en fijne gesprekken. Ook bedankt aan mede Potvissers en 'buren' (Nel, Marten, Sigrid, Lise, Diana, Alejandro etc.), die het wonen op Texel erg fijn maakten.

Mijn lieve stoere paranimfen, Carola en Furu, ik voel me vereerd dat jullie me bij willen staan op deze bijzondere dag. Jullie zijn in korte tijd erg belangrijk voor me geworden als goede vriendinnen en ik bewonder jullie enorm!

Willem, Connie en Willemijn, mijn tweede gezin en thuis, bedankt voor jullie warmte en eeuwige steun. Wieke, bedankt voor de gezellige afleiding en een luisterend oor. En natuurlijk mijn lieve vrienden en vriendinnen Rutchanna, Marieke, Sanne, Jan-Hendrik, Bibian en Mischa, ik ben jullie eindeloos dankbaar. Thom Palstra, bedankt voor je goede advies die me op het juiste pad heeft gebracht.

Bedankt ook aan mijn familie: Jose en Michèle, Michiel en Willy en Rob. Met name dank aan Opa en Oma, die altijd met veel interesse al mijn verhalen over Texel en mijn proefschrift hebben aangehoord.

Marc, mijn steun en toeverlaat, mijn Texel en mijn vrije tijd, bedankt voor je liefde en aanwezigheid. Ook bedankt aan je lieve ouders.

En als laatste dank aan Marlies, mijn moeder en rots in de branding, die altijd voor mij klaar staat met een luisterend oor en wijze adviezen.

Curriculum Vitae

Eveline Maryse Mezger was born the 11th of August 1989 in Nijmegen, the Netherlands. She graduated from secondary school (VWO, Gymnasium) at the 'Stedelijk Gymnasium Nijmegen' in 2007. Thereafter, she enrolled in the Bachelor Earth Sciences at Utrecht University and graduated 'with merit' in 2010. In the same year, she started her MSc degree in 'Biogeology' at Utrecht University, from which she graduated 'cum laude' in 2013. Her MSc thesis was titled 'How dry was the Messinian Salinity Crisis? - A molecular biogeochemical study of the Eraclea Minoa (Sicily) section, Italy -'. This MSc research was followed-up by an internship at Shell, in which she learned many high-tech organic geochemical techniques. In 2013, she started as a PhD candidate at the Royal Netherlands Institute for Sea Research (NIOZ), supervised by Prof. dr. Gert-Jan Reichart and dr. Lennart de Nooijer. During her PhD, she focused on the foraminiferal Na/Ca (salinity) proxy potential. She participated in two scientific cruises and the Urbino Summer School for Paleoclimatology (2014).

Bibliography

1. **Mezger, E.M.**, De Nooijer, L.J., Bertlich, J., Bijma, J., Nürnberg, D. and Reichart, G.-J (2019) Planktonic foraminiferal spine versus shell carbonate Na incorporation in relation to salinity. Biogeosciences 16: 1147-1165.

2. **Mezger, E.M.**, De Nooijer, L.J., Siccha, M., Brummer, G.-J.A., Kucera, M. and Reichart, G.-J. (2018) Taphonomic and ontogenetic effects on Na/Ca and Mg/Ca in spinose planktonic foraminifera from the Red Sea. Geochemistry, Geophysics, Geosystems 19: 4174-4194.

3. Bertlich, J., Nürnberg, D., Hathorne, E.C., de Nooijer, L.J., **Mezger, E.M.**, Kienast, M., Nordhausen, S., Reichart, G.-J., Schönfeld, J., and Bijma, J. (2018) Salinity control on Na incorporation into calcite tests of the planktonic foraminifera *Trilobatus sacculifer* – Evidence from culture experiments and surface sediments. Biogeosciences 15: 5991-6018.

4. Vasiliev, I., **Mezger, E.M.**; Lugli, S., Reichart, G.-J., Manzi, V. and Roveri, M. (2017) How dry was the Mediterranean during the Messinian salinity crisis?. Palaeogeography, Palaeoclimatology, Palaeoecology 471: 120-133.

5. **Mezger, E.M.**, de Nooijer, L.J., Boer, W., Brummer, G.-J.A. and Reichart, G.-J. (2016) Salinity controls on Na incorporation in Red Sea planktonic foraminifera. Paleoceanography 31(12): 1562–1582.

Under review or in preparation for submission

6. **Mezger, E.M.**, Erdem, Z., Lattaud, J., Van Erk, M., Schouten, S., and Reichart, G.-J. Arabian Sea salinity and temperature changes over the last glacial cycle and impact on the oxygen minimum zone. *Under review in Palaeogeography, Palaeoclimatology, Palaeoecology.*

7. **Mezger, E.M.**, Devriendt, L.S., Olsen, E., Watkins, J.M., Kaczmarek, K., Nehrke, G., De Nooijer, L.J. and Reichart, G.-J. Sodium incorporation into inorganic calcite and implications for the use of biogenic carbonates as a salinity proxy. *in prep.*

8. Erdem, Z., Lattaud, J., Van Erk, M., **Mezger, E.M.**, Reichart, G.-J., Lückge, A., Sinninghe Damsté, J.S., Schouten, S. Applicability of the long chain diols as sea surface temperature and upwelling proxies in the Arabian Sea. *in prep.*

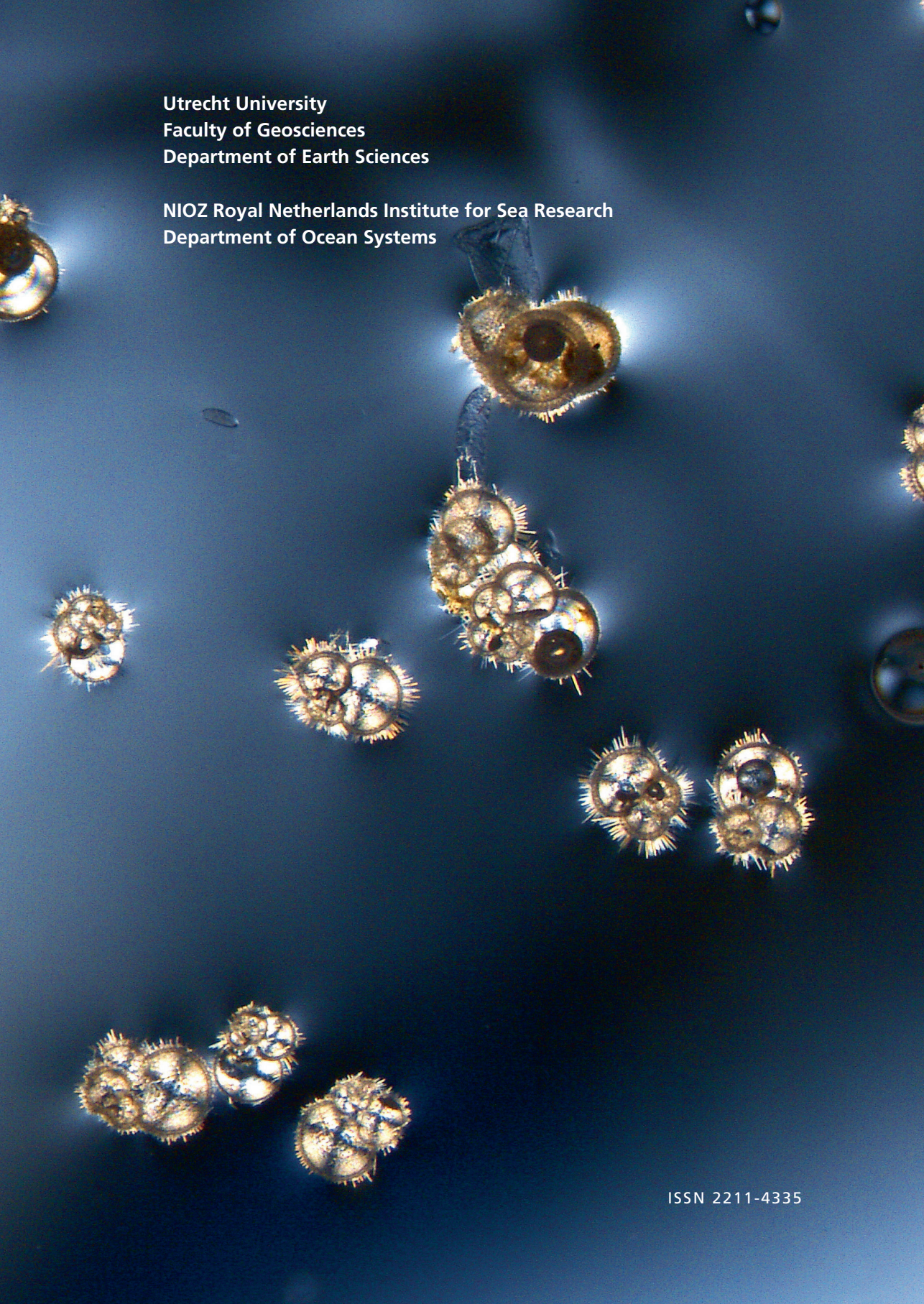

Utrecht University
Faculty of Geosciences
Department of Earth Sciences

NIOZ Royal Netherlands Institute for Sea Research
Department of Ocean Systems

ISSN 2211-4335